



N7627214

**CORRELATION STUDY OF THEORETICAL AND
EXPERIMENTAL RESULTS FOR SPIN TESTS OF A
1/10 SCALE RADIO CONTROL MODEL**

GRUMMAN AEROSPACE CORP., BETHPAGE, N.Y

JUL 1976

CORRELATION STUDY OF THEORETICAL AND EXPERIMENTAL
RESULTS FOR SPIN TESTS OF A $\frac{1}{10}$ -SCALE RADIO CONTROL MODEL

JULY 1976

by

William Bihrlle, Jr.

Prepared Under Contract NAS 1-13578

for

Langley Research Center

National Aeronautics and Space Administration

by

Grumman Aerospace Corporation

Bethpage, New York



ABSTRACT

A correlation study has been conducted to determine the ability of current analytical spin prediction techniques to predict the flight motions of a current fighter airplane configuration during the spin entry, the developed spin, and the spin recovery motions. The airplane math model used aerodynamics measured on an exact replica of the flight test model using conventional static and forced-oscillation wind-tunnel test techniques and a recently developed rotation-balance test apparatus capable of measuring aerodynamics under steady spinning conditions. An attempt was made to predict the flight motions measured during stall/spin flight testing of an unpowered, radio-controlled model designed to be a $\frac{1}{10}$ -scale, dynamically-scaled model of a current fighter configuration. Comparison of the predicted and measured flight motions showed that while the post-stall and spin entry motions were not well-predicted, the developed spinning motion (a steady flat spin) and the initial phases of the spin recovery motion were reasonably well predicted. The study clearly demonstrated the need to model the effects of spin rotation rate on the aerodynamics, the large influence of the pitch damping coefficient on the developed spin, and the extreme sensitivity of the predicted model motions to control timing and phasing.

SUMMARY

The NASA Langley Research Center has a broad research program designed to advance the state-of-the-art in the area of stall/spin technology. A major requirement in this area is to develop and validate reliable theoretical methods for the prediction and analysis of airplane stall/spin characteristics. The present study was performed as the final phase of a two-part study to determine factors which influence the correlation between predicted and measured airplane

spin motions and to actually correlate analytically predicted spin motions with flight motions measured on a radio-controlled, dynamically-scaled drop-model of a current fighter airplane. This final study concentrated on the correlation between predicted and measured flight motions and considered the spin entry, the developed spin, and the spin-recovery motions. The airplane math model used in the study was based on the full, nonlinear equations of motion and employed aerodynamics measured in low-speed wind-tunnel tests on an exact replica of the $\frac{1}{10}$ -scale model used in the flight tests. These aerodynamic data were obtained from conventional static and forced-oscillation test techniques and from a recently developed rotation-balance test apparatus capable of measuring the effect of spin rotation rate on airplane aerodynamics. Extensive analysis was made of the measured aerodynamics to develop a comprehensive aerodynamic model of the airplane. Control time histories taken from the model flight test results were used in the analytical model to attempt to calculate the stall, spin-entry, developed spin, and recovery motions measured in the radio-controlled drop-model tests. The calculated results were correlated with the flight test results.

Results of the study showed that the model developed-spin motion (a flat, steady spin) and the early phases of the spin-recovery motion were reasonably well predicted but that the spin-entry and complete spin-recovery motions were not as well predicted. The high degree of correlation obtained was only possible when the effects of rotation rate on the model aerodynamics were included - that is, when rotation-balance data were used. In that regard, it was also noted that the phases of the motion which were not well predicted were the flight regions for which rotary aerodynamic characteristics had to be assumed. The predicted model motions were found to be very sensitive to small changes in the timing and phasing of the control inputs. The character of the

calculated developed spin motion was found to be sensitive to the value of the pitch-damping coefficient. Finally, the lack of good body attitude information on the flight model was found to be a severe handicap in determining the proper initial conditions to use in the analytical study since the initial attitudes assumed were found to dramatically effect the spin entry motion.

CONTENTS

	PAGE
SUMMARY -----	i
INTRODUCTION -----	1
TECHNICAL APPROACH -----	4
Radio Control Model Time Histories -----	4
Aerodynamic Model -----	5
Inertia and Mass Data -----	8
Analytical Technique -----	9
RESULTS AND DISCUSSION -----	12
CONCLUDING REMARKS -----	16
REFERENCES -----	18
LIST OF FIGURES -----	19
APPENDICES -----	36
Appendix A: Equations of Motion and Associated Formulas -----	36
Appendix B: Symbols -----	39
Appendix C: Aerodynamic Data Employed in Investigation -----	47
Appendix D: Basis of Aerodynamic Model -----	77

INTRODUCTION

The Langley Research Center has a broad research program designed to advance the state-of-the-art in the area of stall/spin technology. One major requirement existing in this area is the development and validation of reliable theoretical methods for prediction and analysis of stall/spin characteristics. Although theoretical studies have been made in the past, no concentrated nor continuing effort has been made to rigorously validate the analytical techniques employed in these studies. In view of the urgent need for valid theoretical techniques, this study was performed as a step toward advances in this area.

The present investigation is the second phase of a two-part study directed toward determining the correlation between theoretically predicted and experimentally measured spinning motions of a $\frac{1}{10}$ -scale, unpowered, radio-controlled, dynamically ballasted, drop model of a current fighter configuration. In the first phase, developed spin motions obtained with theoretical models based on conventional aerodynamics were compared with motions based on rotary (rotation balance) aerodynamics and factors, such as possible errors in aerodynamics and mass characteristics, control time histories, etc., which might influence the correlation between predicted and measured airplane spin motions were examined. This previous study reported in reference 1, which dealt primarily with the developed spin, presented the following conclusions, and consequently dictated the technical approach employed in the present study:

- The spinning motion can be acutely sensitive to a small change in the application of the spin entry controls. Since the control phasing required to trigger a radical change in the spin behavior of the

airplane cannot be predicted at this time, flight recorded control time histories must be faithfully duplicated during an experimental-analytical correlation study.

- The spinning motion, both the incipient and developed phases, are sensitive to the location of the center of gravity but are not significantly affected by reasonable errors incurred in measuring airplane inertias.
- The damping in pitch derivative, C_{m_q} , has a significant influence on all phases of the spinning motion. The magnitude of the static yawing moment in the 50 to 90 degree angle-of-attack range appreciably affects the incipient spin but only slightly affects the developed spin.
- No spin can be computed using the conventional analytical technique when the dynamic (forced-oscillation) derivative C_{m_q} , C_{n_r} or C_{l_r} is unstable in the angle of attack region for spin equilibrium. When the contribution of the dynamic derivatives are limited to the oscillatory component of the total angular rates, a spin can be computed which, however, does not match the experimentally determined spin motion.
- The spin computed with rotary data duplicated the developed spin obtained in the spin tunnel. Whereas, the spin computed in the conventional manner with static aerodynamic data was considerably less severe. It is indicated, therefore, that the aerodynamic moments generated in the spin due to steady rotational flow, as measured by a rotation-balance, are indeed significant.

- It appears that static aerodynamic derivatives can be extracted from rotation-balance data. It may be possible, therefore, to simply add the aerodynamics associated with steady rotation flow to the conventional aerodynamic model.

The present investigation completed the two-phase study by determining the degree of correlation that can be obtained with measured flight motions by using a theoretical model based on the use of rotary, static and dynamic aerodynamics according to the technical approach identified in the first-phase study. To minimize Reynold's number effects, the experimental motion and measured aerodynamics were obtained with the same model.

TECHNICAL APPROACH

Radio Control Model Time Histories

The objective of the present study was to correlate analytically predicted model motions with the flight motions measured on a remotely-controlled, unpowered model launched from a helicopter and controlled from a ground-based pilot station. In this free-flight model technique, the model is launched and then controls are applied to force the model into the stall angle of attack range and possibly into a spinning motion. The test technique is used at the Langley Research Center for stall/spin testing. Parameters recorded during a typical flight include airspeed, angle of attack, angle of sideslip, the three body axis angular rates, and the control surface positions. Attitude angles are not currently measured. Using this model test procedure, the complete flight history of a vehicle entering a spin can be obtained, including the post-stall, the incipient spin, the developed spin, and the spin recovery motions.

Ideally, for the purposes of a correlation study, one would like to have numerous flights wherein the pilot attempts to repeat the same spin-entry maneuver with the model to establish the repeatability of the model motions and to determine if the model exhibits any aerodynamic asymmetries which may make it more prone to spin in a particular direction. These repeated flights were not possible in the present study and therefore only one model flight was obtained which clearly exhibited the spin-entry, spinning, and spin-recovery motions of interest in this study. The time-history obtained during this flight is presented in figure 1, and this is the flight which this study attempted to analytically predict using the same control inputs that were applied to the flight model. The values of α , β , and V presented in figure 1 are referenced to the airplane

center of gravity and were computed by transferring the values measured at the model nose boom using the formulas in appendix A, where the values of ΔX , ΔY , and ΔZ were 5.17, 0.39, and 0. feet, respectively.

Aerodynamic Model

A large quantity of measured aerodynamic data, including static, dynamic, and rotary types, has been obtained on the subject model configuration at low speeds. A summary of the data available is presented in Table I showing the range of test variables covered. As can be seen, the data available were restricted in several variables. For instance, the rotation balance data was not measured below $\alpha=55^\circ$ and complete data were not available on each control surface for its full deflection range at high angles of attack. By comparing the measured model flight excursions shown in figure 1 with the aerodynamic data available (shown in Table I), it can be seen that the aerodynamics were not measured to cover all of the angles of attack, sideslip angles and control deflections experienced in flight. Acknowledging these data limitations, an effort was made to construct the best aerodynamic model possible from the available data. Probably the most severe limitation in aerodynamic data was with the rotation balance (or rotary) data which was restricted to only four control configurations and to angles of attack above 55° .

The aerodynamic data referred to in Table I was extensively analyzed and combined, as discussed in appendix D, to develop the final aerodynamic model used for the analytical predictions. The aerodynamics used for the final model are presented in appendix C. These data represent the clean, $\frac{1}{10}$ -scale model configuration used in the radio-controlled model flight test. All the data presented in appendices C and D were reduced to standard coefficient form on the basis of the following geometric characteristics:

TABLE I: SUMMARY OF AVAILABLE AERODYNAMIC DATA FOR CONSTRUCTING AERODYNAMIC MODEL

	(a) LRC 30'x60' ROTATION BALANCE DATA	(b) LRC 12' STATIC FORCE DATA
	LRC 30'x60' STATIC FORCE DATA	LRC 30'x60' FORCED OSCILLATION
	DATA RN=.47x10 ⁶	DATA RN=.33x10 ⁶
	α = 0 to 90°	α = 0 to 90°
	β = -40 to 40°	β = 0°
	ref. center @ 16.25c	ref. center @ 31.55c
δ _a =0	δ _R =0	X
δ _a =-12	δ _R =0	X
δ _a =0	δ _R =30	
δ _a =0	δ _R =-30	X
δ _a =12	δ _R =0	X
δ _a =-12	δ _R =0	X
δ _a =0	δ _R =0	X
δ _a =0	δ _R =-30	X
δ _a =5	δ _R =0	X
δ _a =-5	δ _R =0	X
δ _a =5	δ _R =-30	X
δ _a =-5	δ _R =30	X

a) Data obtained clockwise and counterclockwise for $\frac{a}{2V}$ values of .0493, .1030, .1523, .2015, .2553 and .3045 at β = 0 and 5°.

b) Only lateral - directional data measured.

$$S = 5.65 \text{ ft.}^2 \quad \bar{c} = 11.76 \text{ in.} \quad b = 6.41 \text{ ft.}$$

The data of Appendix C were transferred during the computation of time histories to a 20 percent \bar{c} moment reference center to correspond with the flight model center-of-gravity location.

The static and rotary aerodynamic data measured on this particular model configuration indicate that aerodynamic derivatives such as $C_{l_{\beta}}$, $C_{n_{\beta}}$, $C_{m_{i_s}}$, etc. can be obtained from the rotary data in a manner similar to that used with static data. Also, for this particular configuration, these derivatives and the longitudinal aerodynamics did not appear to vary greatly with rotation rate. Therefore, the conventional method of representing the longitudinal aerodynamics and the stability and control derivatives was used and the measured changes in the lateral-directional aerodynamics due to rotation rate were included in an incremental form. Although this approach seemed reasonably valid for the particular configuration under study, it may not be valid for any airplane since rotary aerodynamics are known to be highly configuration dependent. However, if such a method can be used, as done here, it is very convenient since one can employ all of the static aerodynamic data available, and one can develop an aerodynamic model which can transition from the static aerodynamics valid at low rotation rates to the rotary aerodynamics needed at the high rotation rates and angles of attack associated with the spin entry and developed spin. Moreover, if the static control data can be used, much more flexibility is available in simulating complex control time histories, and one is not restricted to the particular control configurations tested on the rotation balance. In view of the above discussion, the following aerodynamic model was selected for this study.

$C_{n_{\delta_R}}, C_{l_{\delta_R}}, C_{y_{\delta_R}}$	(α, β)
$C_{n_{\delta_a}}, C_{l_{\delta_a}}, C_{y_{\delta_a}}$	(α, β)
C_N, C_c, C_y	(α, β, i_s)
C_m, C_n, C_l	(α, β, i_s)
$C_{y_{rot}}$	$(\alpha, \frac{nb}{2V}, i_s)$
$C_{n_{rot}}, C_{l_{rot}}$	$(\alpha, \frac{nb}{2V}, i_s)$
$C_{N_q}, C_{y_r}, C_{y_p}$	(α)
$C_{m_q}, C_{n_r}, C_{l_p}$	(α)
C_{l_r}, C_{n_p}	(α)

Two aerodynamic models were employed herein which differed only in respect to the dynamic derivatives selected from Appendix C. One model employed the dynamic derivatives that were experimentally obtained in the Langley full-scale tunnel facility at a nondimensional forced-oscillation frequency of $\frac{\omega \bar{c}}{2V} = .047$ and the other used estimated dynamic derivatives. Unless noted otherwise, the experimental derivatives were always employed in this study.

The data presented in Appendix C were inputted into the computer in tabular form. Values for control settings other than those presented were obtained by linear interpolation. By tabulating C_m, C_n and C_c as a function of α and β for $i_s = 0$ and -30° , the stabilizer control derivatives $C_{m_{i_s}}, C_{N_{i_s}}$ and $C_{c_{i_s}}$ were not required. Interpolation of these tables would not incur errors except at low α where the tail is stalled for an $i_s = -30^\circ$ setting—a flight condition not to be simulated during this investigation. If an angle of attack/or side-

slip angle were computed momentarily which was greater or less than those available in the tables, the last values used would be maintained until the computed angle fell within the confines of the available data.

The ability of this aerodynamic model to represent the radio control model requires that three assumptions be made. To wit:

- 1) Rotation balance data does not change appreciably at lower angles of attack from that measured at 55° angle of attack.
- 2) Control characteristics for this configuration are not influenced by rotational flow.
- 3) The wing-mounted, upper surface spoiler used on the radio-control model had a negligible influence at high angles of attack.

Inertia and Mass Data

The following weight and inertia characteristics were used to represent the model:

Weight = 145.12 lbs

Center of gravity location = $0.20 \bar{c}$

$$I_x = 1.805 \text{ slug-ft}^2 \quad I_{xz} = 0.$$

$$I_y = 7.326 \text{ slug-ft}^2$$

$$I_z = 9.388 \text{ slug-ft}^2$$

These model values therefore represent a model which has relatively more mass in the fuselage than the wings, as indicated by the inertia parameters, i.e.,

$$\frac{I_x - I_y}{mb^2} = -.0298, \quad \frac{I_y - I_z}{mb^2} = -.0111, \quad \frac{I_z - I_x}{mb^2} = .0409.$$

Analytical Technique

This study required the computation of large angle motions using a large angle, six-degree-of-freedom, plotted output digital computer program with nonlinear, multifunctioned aerodynamic coefficients. This program solved the equations of motion and associated formulas presented in Appendix A as discussed in Reference 1.

Forty-second time histories presented herein were calculated employing the control time histories shown in Figure 1 for the radio-control model. Each time history is presented in a figure consisting of two 11" x 17" pages and each page contains the following variables plotted versus time.

Page 1	Page 2
α	p
β	q
V_R	r

It was felt that the spinning motion was sufficiently illustrated by describing the relative wind vector at the center of gravity on the first page and the angular velocities about the axes having their origin at the center of gravity on the second page.

Unless noted otherwise, the following initial values at time equal zero seconds was employed for these studies.

H_0	4250 ft	p	- 0.41	rad/sec
V_R	110.2 ft/sec	q	0	rad/sec
γ	-60.1 deg	r	0	rad/sec
α	26.0 deg	ϕ	-50.8	deg
β	0 deg	θ	-50.0	deg
δ_a	0 deg	ψ	0	deg
δ_R	0 deg	i_s	-1.8	deg

All of these values except for the Euler angles which are discussed later, were obtained from the flight records at a time equal 0 seconds as shown in Figure 1 which was the time at which the drop model was assumed to be out of the flow field of the helicopter.

RESULTS AND DISCUSSION

The study of reference 1 had conclusively demonstrated the need for and the adequacy of the mathematical model used herein. The aerodynamic model was the best that could be developed under the constraints discussed in the Technical Approach and Appendix D. Obviously, the level of confidence in the validity of the aerodynamic model was considerably less than in the mathematical model. The various parameters that were investigated, therefore, and discussed herein are identified in the List of Figures on page 19.

The ability to compute the flight recorded motion shown in Figure 1 when experimental and estimated dynamic (forced-oscillation) derivatives were used is shown in Figures 2 and 3, respectively. It can be seen that the experimental dynamic derivatives resulted in a considerably more oscillatory motion, which appears to diverge, than was evidenced by the radio-control model. When the estimated dynamic derivatives were employed, the computed motion was appreciably different in that the amplitudes of the oscillation were greatly reduced. In fact, the amplitudes in p , q , α and β were even less than was realized with the radio-control model. And, in this instance, the maximum magnitude of r was greater and the vehicle did not quite recover using the radio-control model recovery control time histories.

As shown in Appendix C, there is an appreciable difference between the experimental and estimated dynamic derivatives. However, since reference 1 had shown C_{m_q} to be of paramount importance and the magnitude for the experimental and estimated derivative was approximately -2 and -17, respectively above $\alpha = 75^\circ$, only the magnitude of the experimental C_{m_q} derivative was modified such that its value was -12 at and above $\alpha = 75^\circ$. As shown in Figure 4, with this one change

incorporated in the experimentally determined aerodynamics model, the build-up in the oscillation shown in Figure 2 is eliminated and the oscillatory motion obtained between 12 and 24 seconds approximates the frequencies and amplitudes of the recorded radio-control model values. Consequently, the average values in β , p and q agree well, although the computed average α value is slightly less than the flight value (i.e., 87° and 91° for the computed and flight motions, respectively). Also, the flight recorded velocity and number of turns (turns not presented herein) were duplicated during the computed motion. It should be noted that when the computed α trace oscillated to a peak value of 97° , only the aerodynamic values realized at $\alpha = 90^\circ$ were employed throughout the time periods α exceeded 90° . This being the case since no aerodynamic data were available for angles of attack above 90° . Consequently, not matching the average oscillatory flight value of 91° is not surprising.

Although the flight recorded spin and recovery motions were computed reasonably well, the incipient spin motion (i.e., from unstalled flight to a flat spin condition) that takes place in approximately the first 12 seconds after control movements are initiated does not correlate with the radio control time history.

As mentioned previously, the flight attitude angles were unknown. Unfortunately, it was found that the initial motion was highly dependent on the assumed initial values for the attitude angles θ and ϕ . For instance, large oscillations in α resulting in negative angles of attack for which no aerodynamic data was available and a full 360° roll could be computed during this time depending on the assumed initial values for θ and ϕ . Since many combinations of these attitude angles are possible, the first combination which resulted in no violent α upset was used throughout the study even though they probably did

not represent the flight values the drop model had assumed at the time control movements were initiated. An error in the initial velocity can also produce this type of problem.

Although it was known that the initial values of θ and ϕ could critically influence the resulting incipient spin motion, concern still existed relative to the differences between the flight recorded and computed motion. Consequently, other factors were examined. For instance, knowing the importance of changes in control deflection, the stabilator deflection was increased from -12 to 20° between 6.80 and 12.18 seconds. The motion computed with this control change is presented in Figure 5. A significant delay in the time for r to increase was realized such that the magnitude of r attained at the time of applying recovery controls was reduced from 13.4 to 11.6 rad/sec. Although this value is closer to the flight recorded value of 12 rad/sec, the overall r trace correlation is further degraded.

It was also thought that the computed r trace during the incipient spin phase was the consequence of applying arbitrarily the rotational flow characteristics obtained at $\alpha = 55^\circ$ to lower angles of attack. The effect of limiting the influence of rotational flow to angles of attack above 55° was, therefore, investigated. It was found that in this instance the incipient spin phase correlation deteriorated as did the recovery phase (compare Fig. 1 with Fig. 6). It was indicated, therefore, that rotational flow effects are important below $\alpha = 55^\circ$ and that in the future rotational flow data should be obtained down to at least 30° angle of attack.

The control time history employed on the radio control model did not trigger a spin in the shortest time possible nor was the flat spin completely stabilized (relative to yaw rate) before recovery controls were applied. This

situation was realized while examining the effect of changing the stabilator deflection between 6.80 and 12.18 seconds. It was observed that when the stabilator deflection was increased from -12 to -25° during this time period, the incipient spin motion did not culminate in a flat spin to the right as the model did. However, when the recovery controls were introduced beginning at 17.9 secs. (which previously resulted in a recovery from a right spin), the vehicle went very rapidly from a post-stall gyration motion to a spin to the left. The resulting motion which ensues when the recovery time history is introduced at $t = 0$ seconds is shown in Figure 7. Also, the initial values in this instance were

V_R	161.8 ft/sec	p	-1.57 rad/sec
γ	-48.5 deg	q	0 rad/sec
α	0 deg	r	0 rad/sec
β	8.1 deg	ϕ	-82.5 deg
		θ	-56.5 deg

which were the values existing at 17.9 seconds in the above described motion. It will be noted that some of these values are different from those previously employed. As can be seen in Figure 7, the duration of the incipient spin phase has been considerably reduced and, as shown, the shape of the r trace is more closely simulated in this instance. This may be the result of assuming different initial values for θ , ϕ and V and/or the fact that very little time is spent in this instance below $\alpha = 55^{\circ}$ for which rotational data had to be assumed.

CONCLUDING REMARKS

This correlation study was conducted to determine what degree of correlation could be obtained between analytically predicted stall/spin motions and motions measured during flight tests of an unpowered, remotely-controlled scale model of a current fighter configuration. The emphasis in the study was to determine if the use of rotation balance aerodynamic data would provide improved correlation. Due to time limitations, only one model flight time history was available for the correlation study. This fact prevented this study from determining the degree of repeatability of flight motions that could be obtained in the model flights. The lack of this information prevents an evaluation of possible errors in correlation due to such factors as model aerodynamic asymmetries and small variations in control deflection timing.

The results of the correlation study showed that the aerodynamic model formulated to use the rotation balance aerodynamics was necessary to obtain the best possible prediction of the model flight motions. Specifically, the correlation was best for the developed spin motion and relatively poor for the spin entry and final phase of the recovery motion. In this regard, it would appear desirable to measure rotational flow effects down to lower angles of attack than is presently done, at least down to near $\alpha = 30^\circ$. Furthermore, more work is needed to refine the aerodynamic model needed to represent the motions occurring during the spin-entry motion. Several other important factors identified in the correlation study included:

- (1) A dominant effect of the value of the damping parameter

$C_{m\dot{q}}$ in the developed spin region.

- (2) A major influence of the initial values of the Euler angles used at the initiation of the motion calculation - these results indicate that it is necessary to accurately know the initial flight attitude of the vehicle when trying to analytically predict the motions. Therefore, the attitude angles of the flight vehicle must be accurately known.

In summary, the major result of this correlation study is that rotation balance aerodynamic data are needed to formulate a useful analytical model for spin calculations. Shortcomings of previous analytical correlation efforts, which attempted to use the conventional static and dynamic stability derivatives, were probably ultimately related to the omission of rotary aerodynamics. A final caution to the reader regarding the application of these results to other vehicle configurations is that it is well-known that the rotation balance aerodynamics measured to date on a range of airplane configurations show the rotary aerodynamics to be quite configuration dependent. For instance, configurations other than the one studied herein may very well exhibit variations in both static stability and control power with rate of rotation. Therefore, due caution should be taken in extending the assumptions of this study to different configurations without careful study of the particular data.

REFERENCES

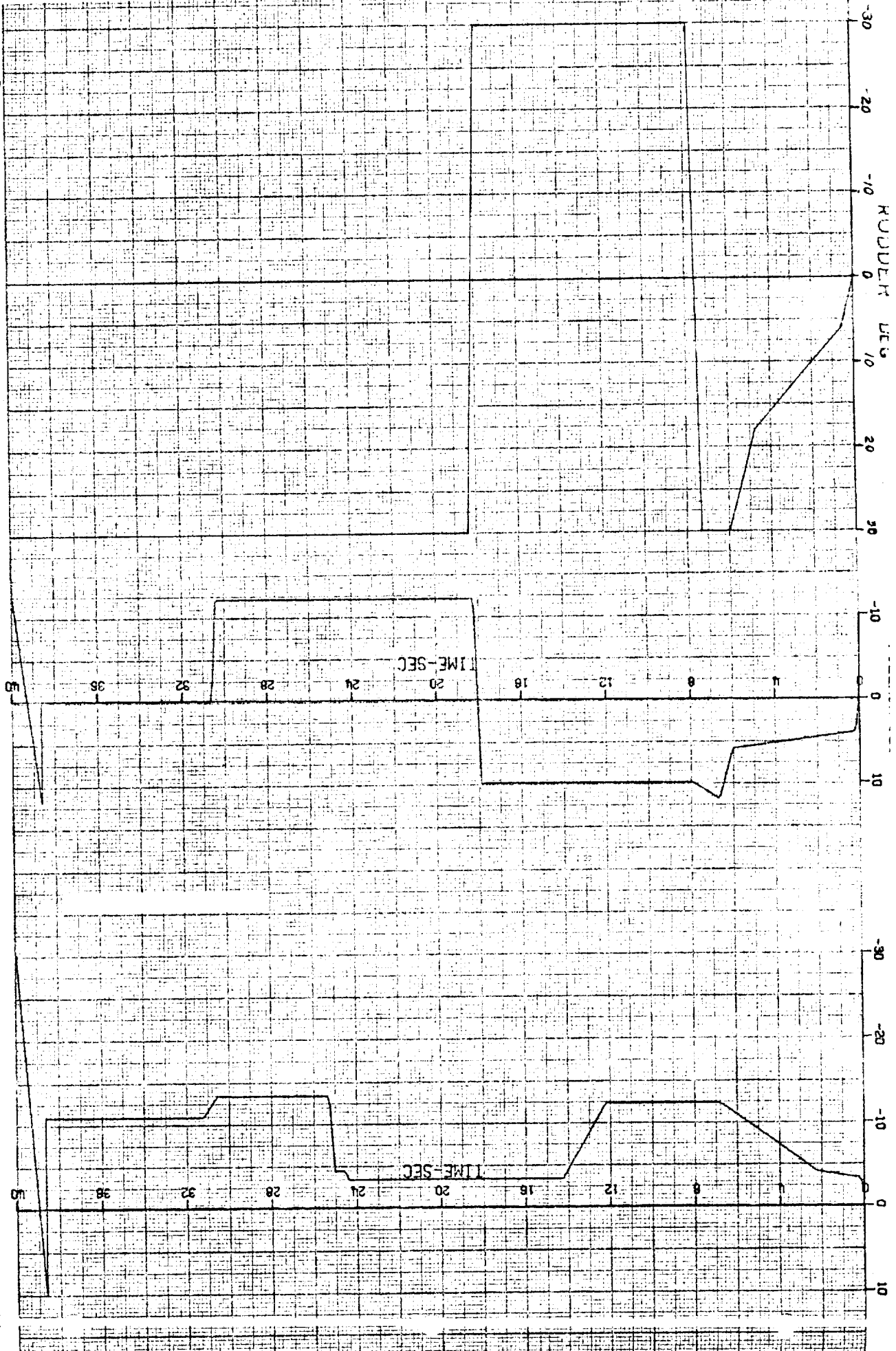
1. Bihrlle, William Jr. and Barnhart, Billy: Effects of Several Factors on Theoretical Predictions of Airplane Spin Characteristics. NASA CR-132521, 1974.
2. Mechtly, E.A.: The International System of Units - Physical Constants and Conversion Factors (Revised). NASA SP-7012, 1969.

LIST OF FIGURES

Figure No.		Page
1	Time history of flight recorded radio-control model motion.	20
2	Motion computed using experimental dynamic derivatives.	23
3	Motion computed using estimated dynamic derivatives.	25
4	Motion computed when experimental C_{m_q} modified (i.e., $C_{m_q} = -12$ at $\alpha \geq 75^\circ$).	27
5	Motion computed when stabilator deflection increased from -12 to -20° between 6.80 and 12.18 secs. ($C_{m_q} = -12$ at $\alpha \geq 75^\circ$).	29
6	Motion computed when rotary aerodynamics employed only at $\alpha \geq 55^\circ$ ($C_{m_q} = -12$ at $\alpha \geq 75^\circ$).	31
7	Motion computed when some initial conditions and the control time histories were changed ($C_{m_q} = -12$ at $\alpha = 75^\circ$).	33

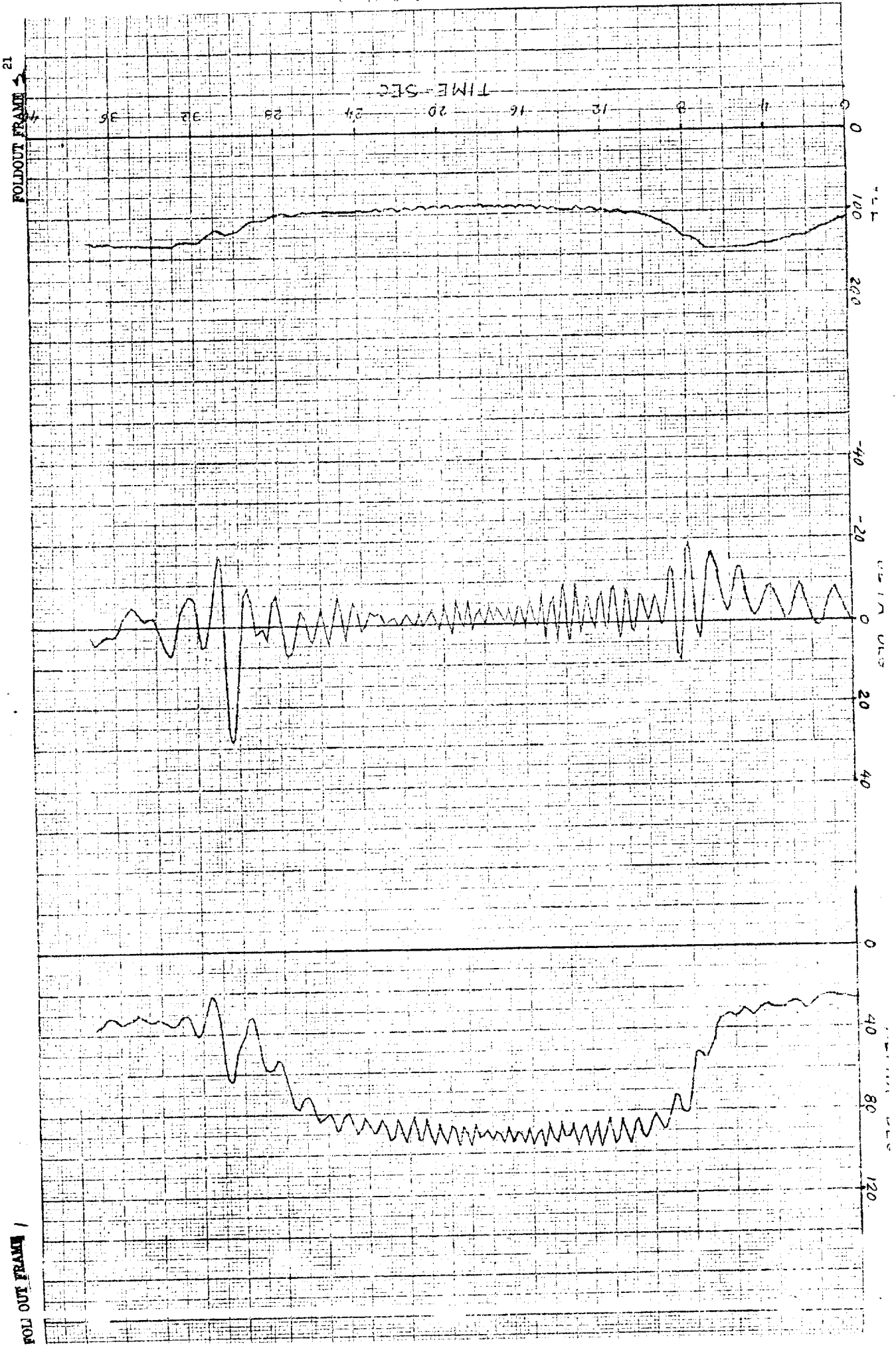
Figure 1. Time history of flight recorded radio-control model motion.

FOLDOUT FRAME 20 1



FOLDOUT FRAME /

Figure 1. Continued.

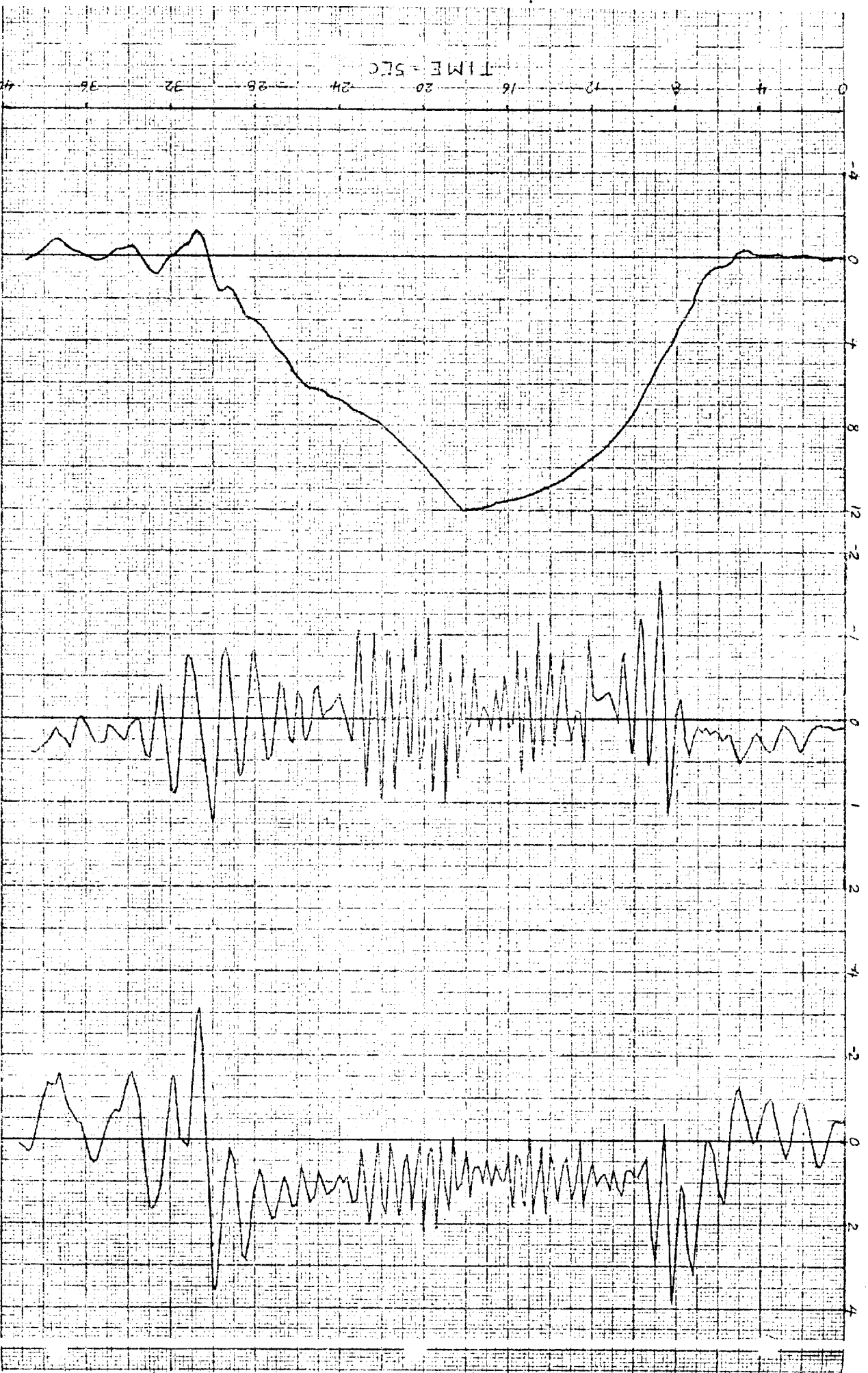


FOLDOUT FRAME 21

FOLD OUT FRAME /

FOLDOUT FRAME 22

TIME - SEC



FO DOUT FRAME 1

Figure 2. Motion computed using experimental dynamic derivatives.

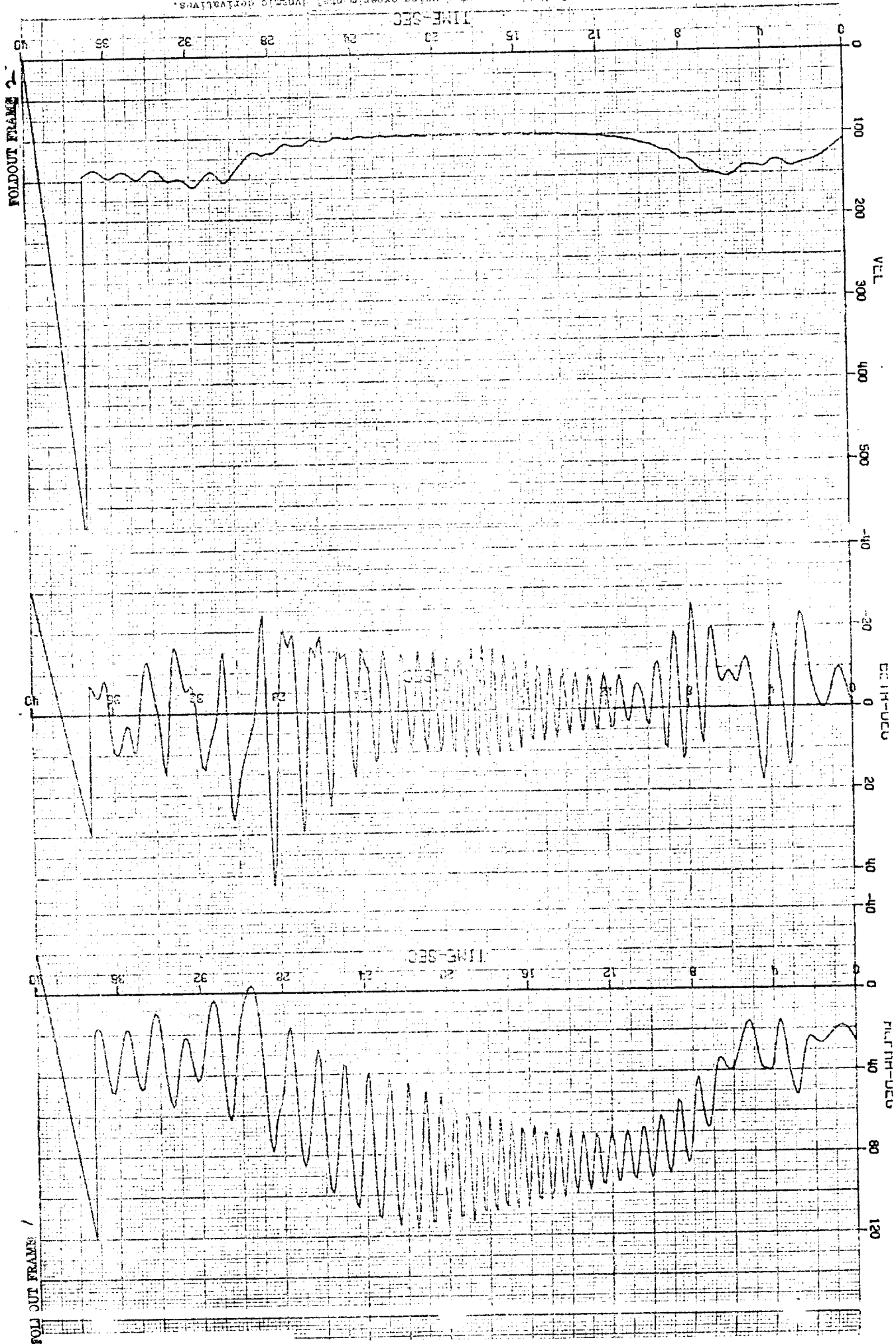


Figure 2. Concluded.

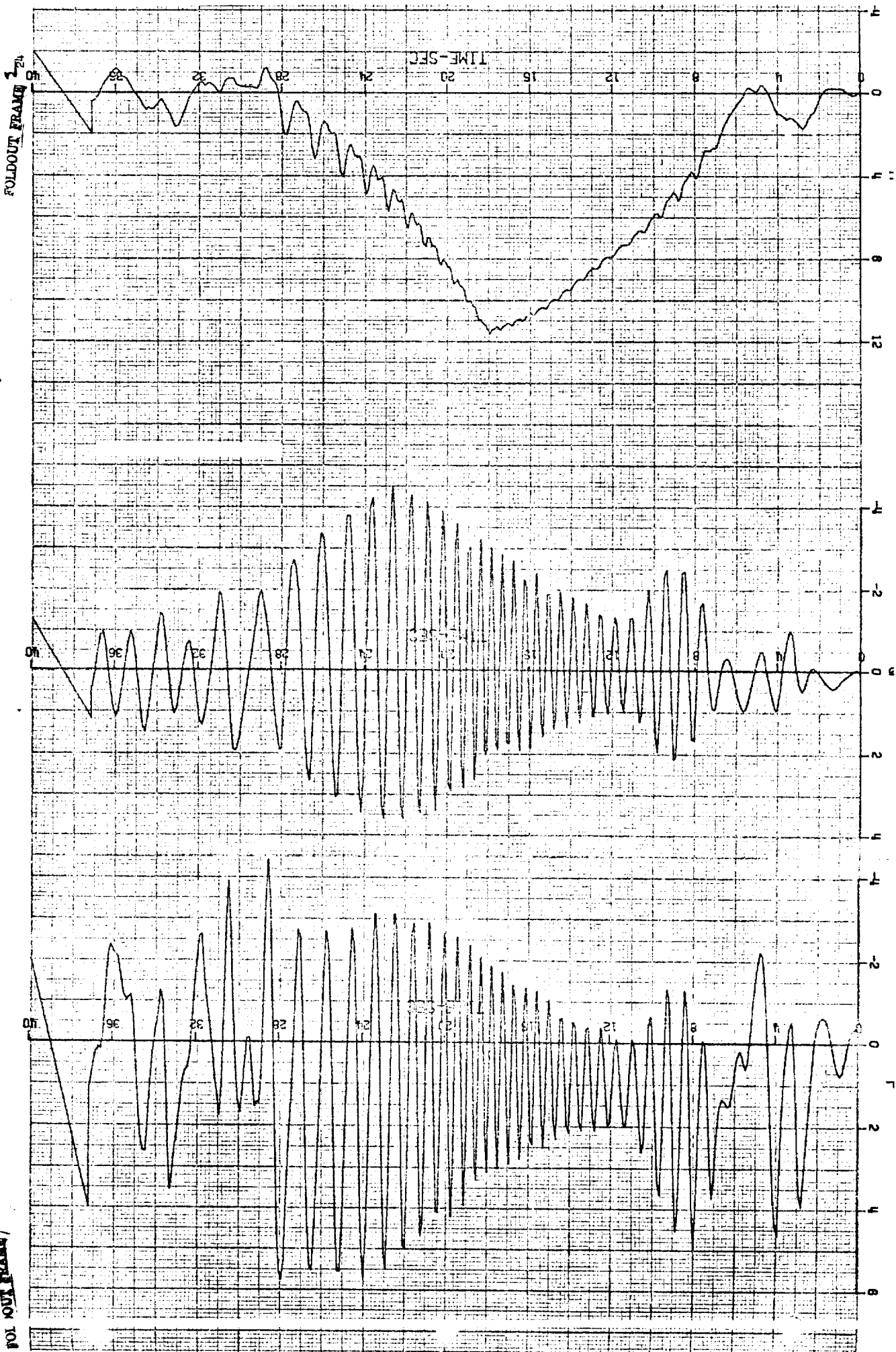
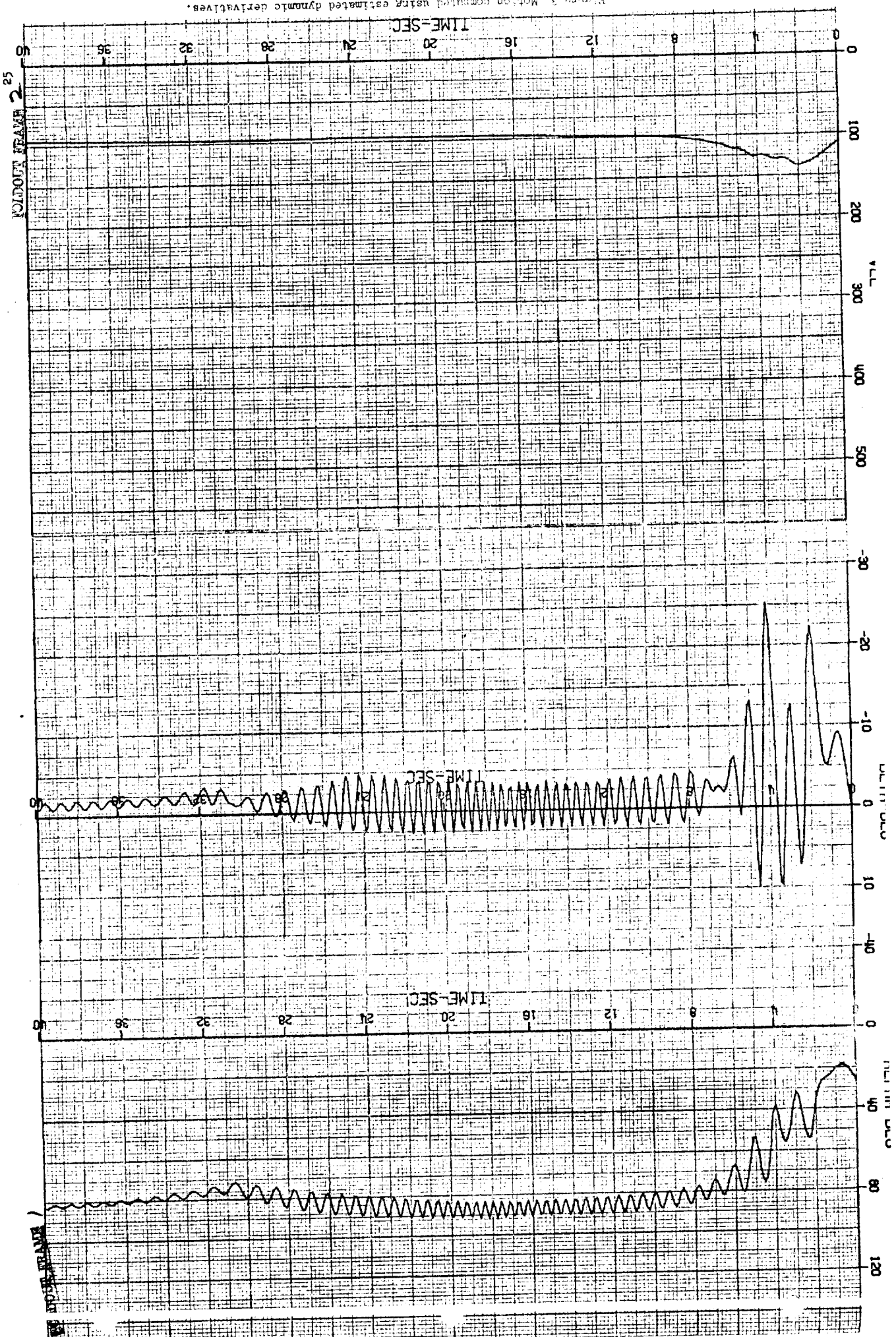


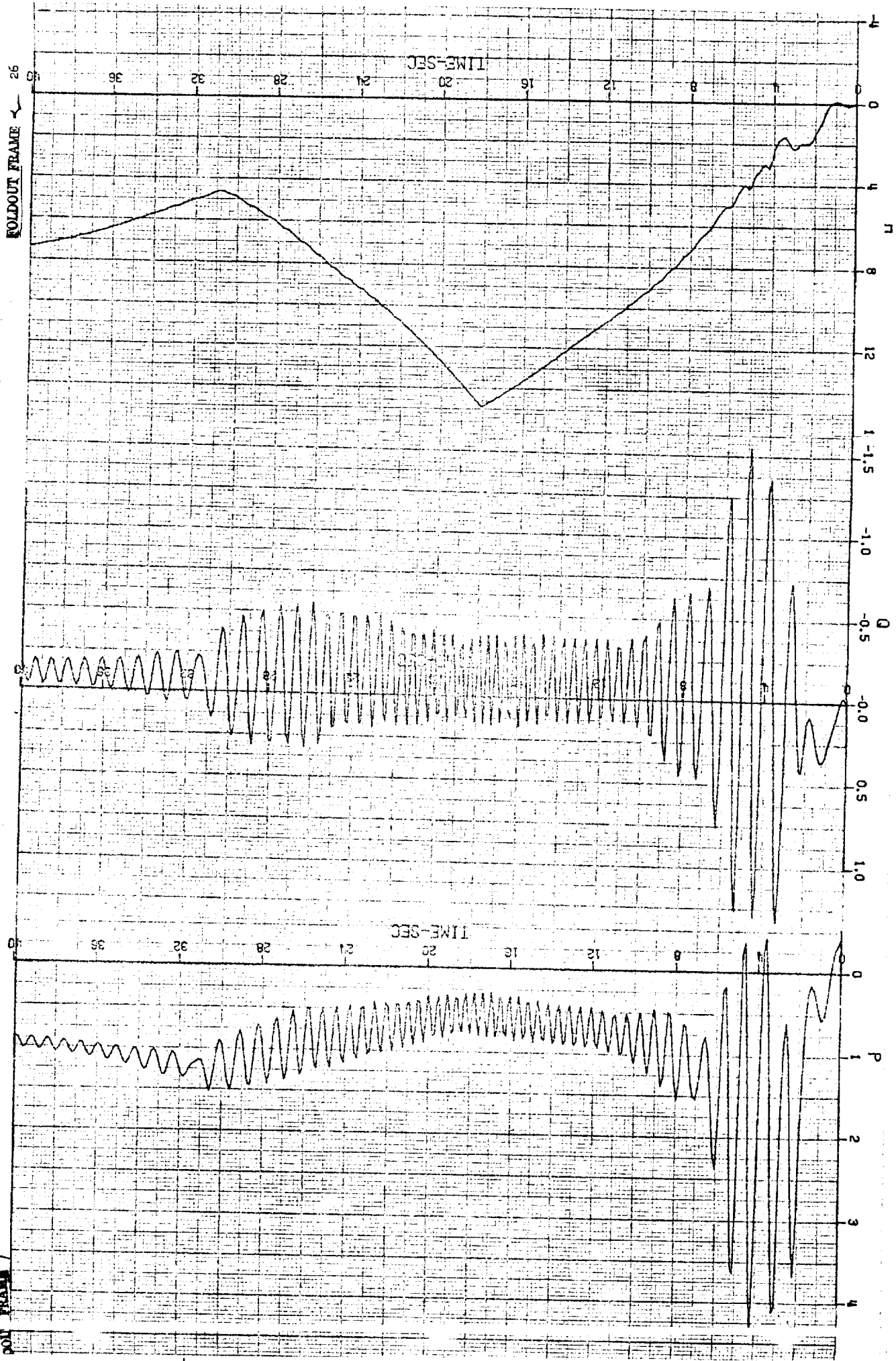
Figure 3. Motion computed using estimated dynamic derivatives.



WILDOUT FRAME 2 25

WILDOUT FRAME 1 25

FOLDOUT FRAME 26



FOLDOUT FRAME 26

Figure 4. Motion computed when experimental C_m^q modified (i.e. $C_m^q = -12$ at $\alpha = 75^\circ$).

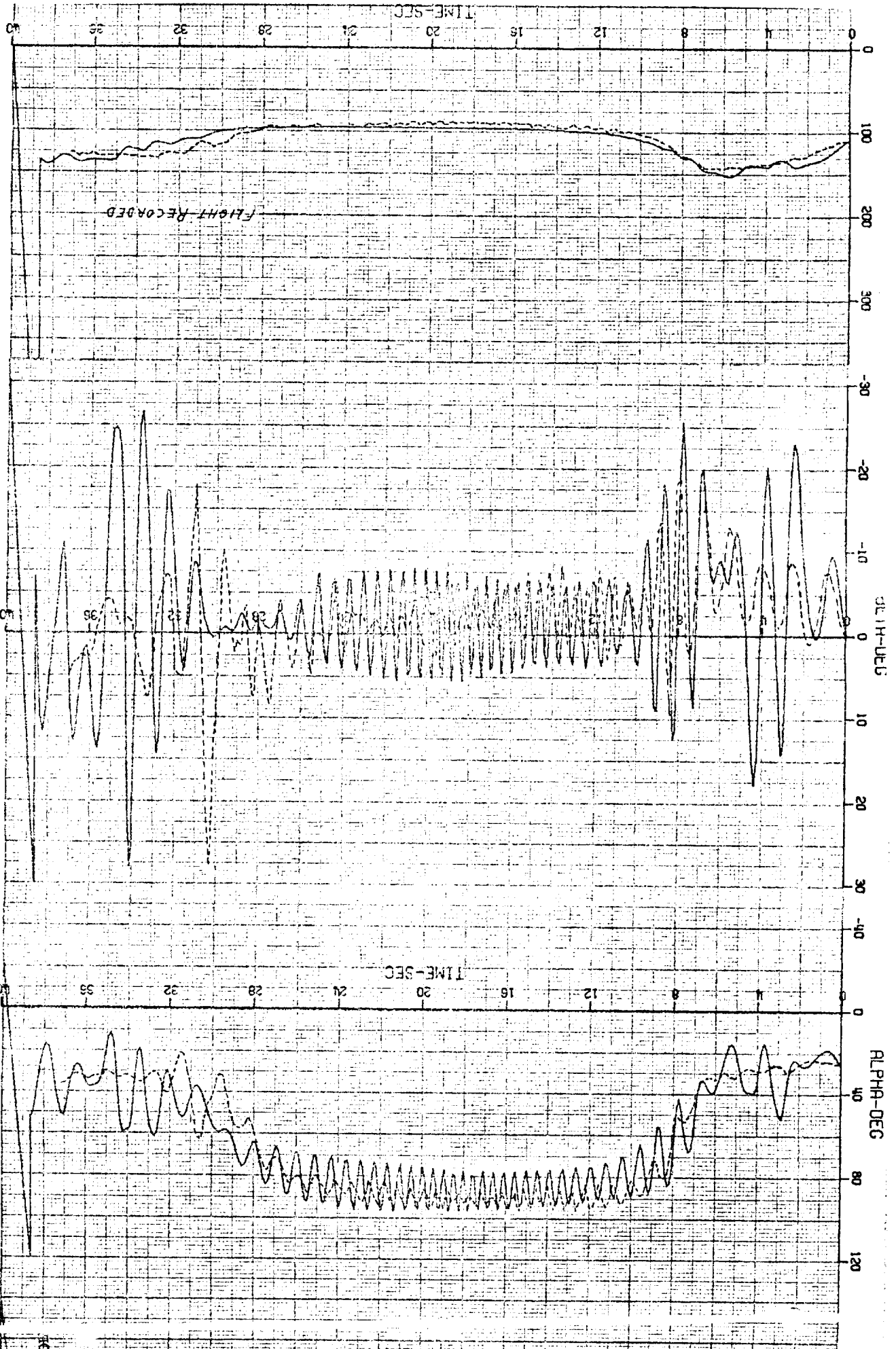


Figure 4. Concluded.

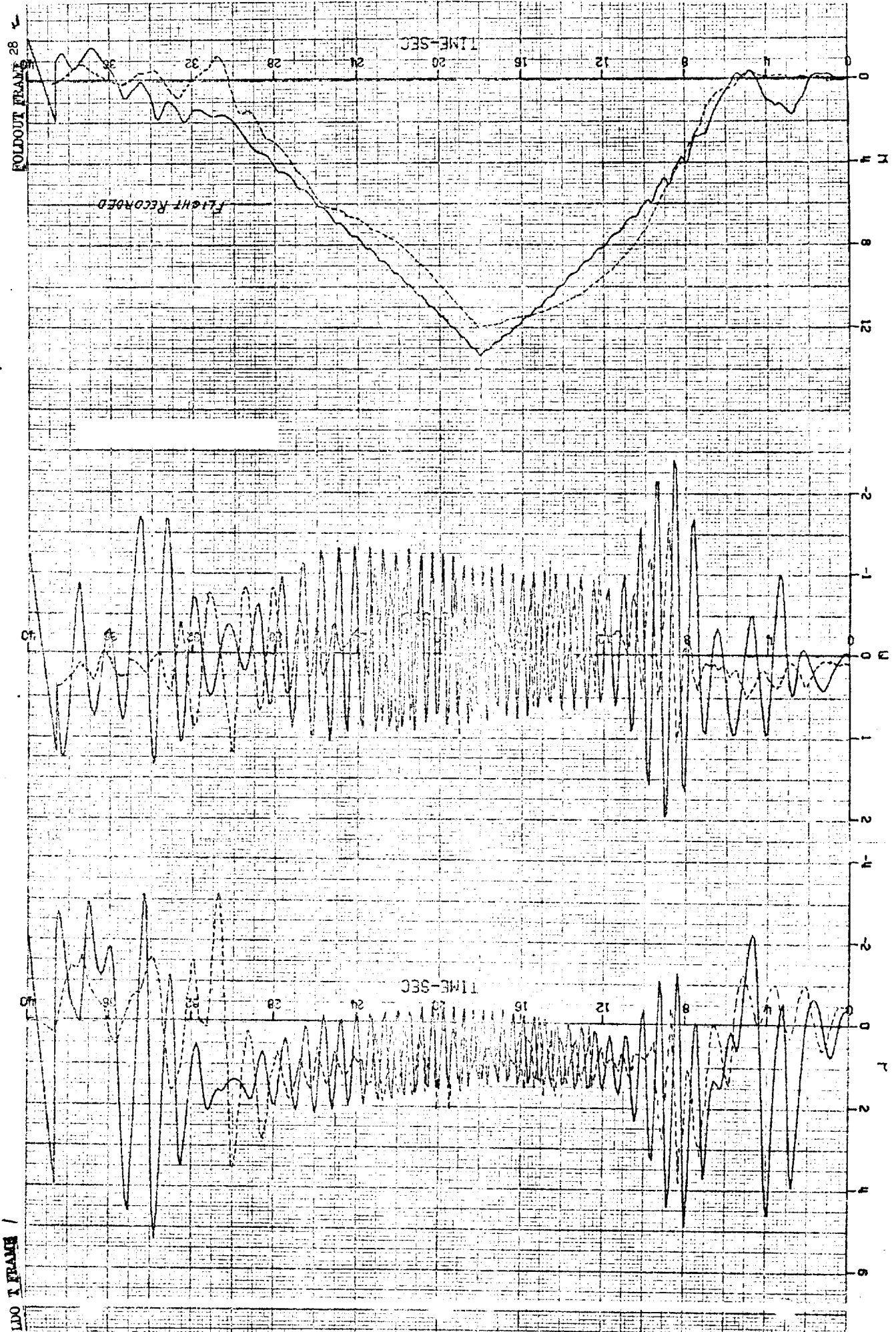
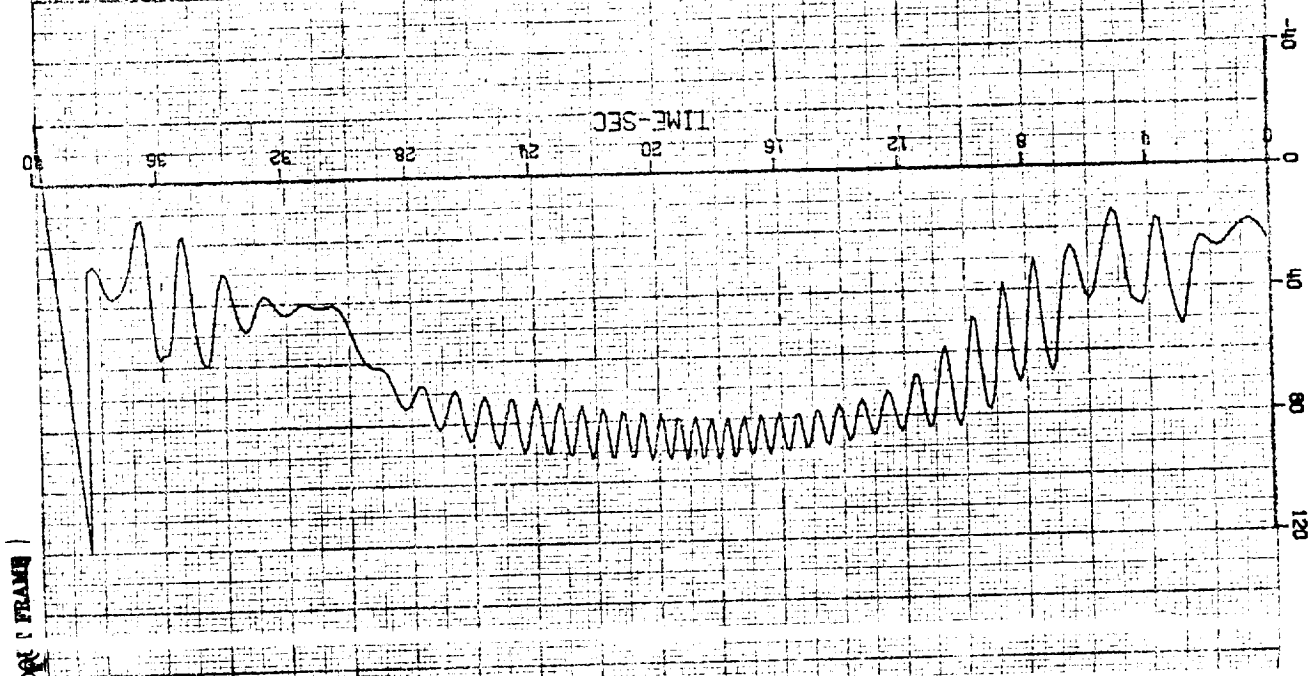
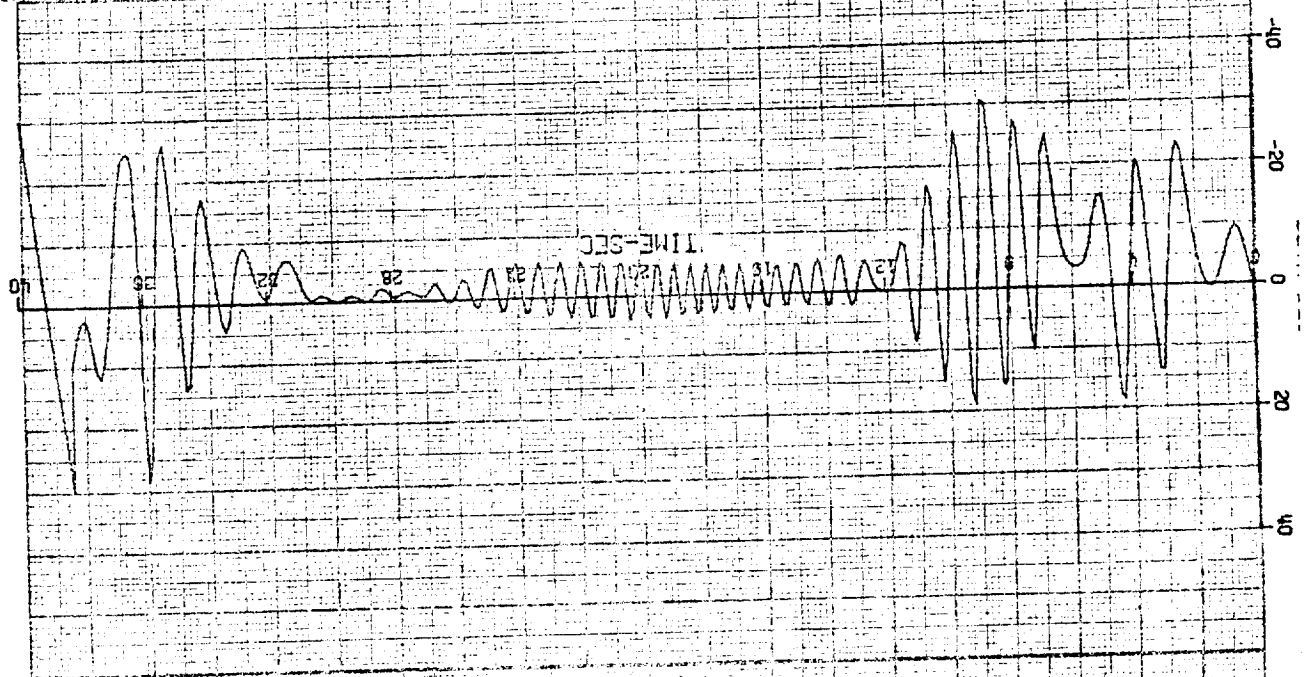
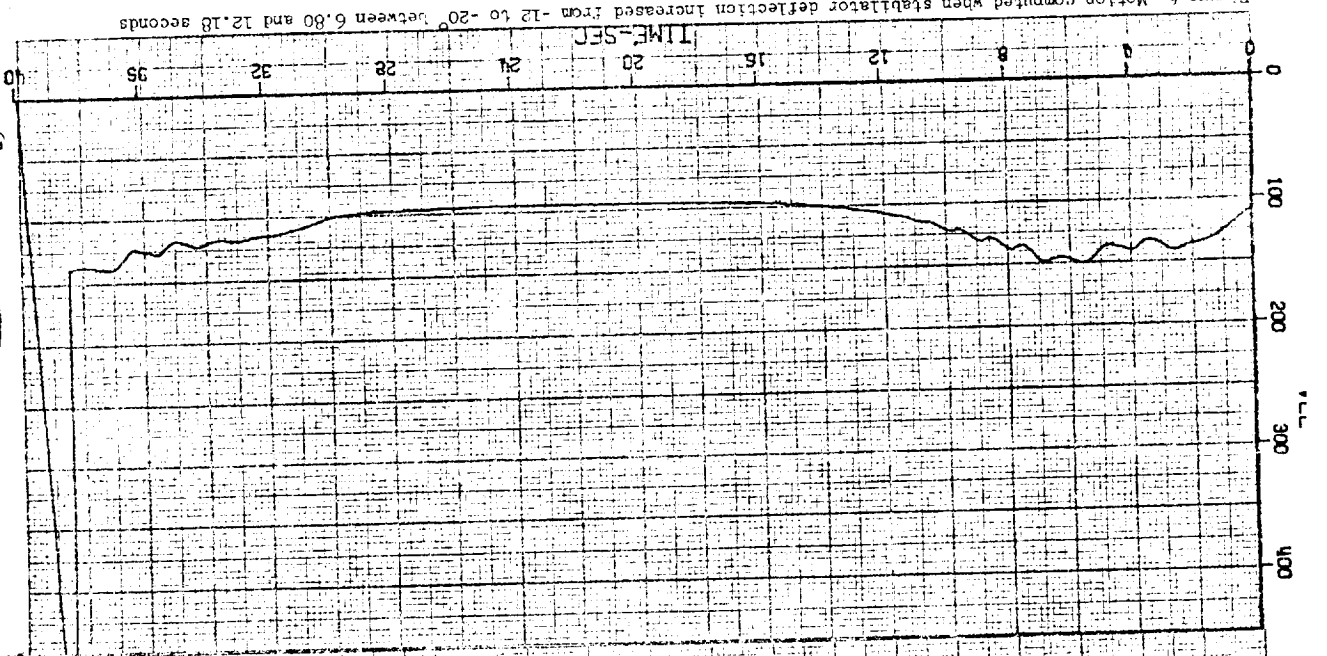


Figure 5. Motion computed when stabilator deflection increased from -12° to -20° between 6.80 and 12.18 seconds ($C_m = -12$ at $\alpha = 75^\circ$)

FRAME 2-29



FRAME 2-30

Figure 5. Continued.

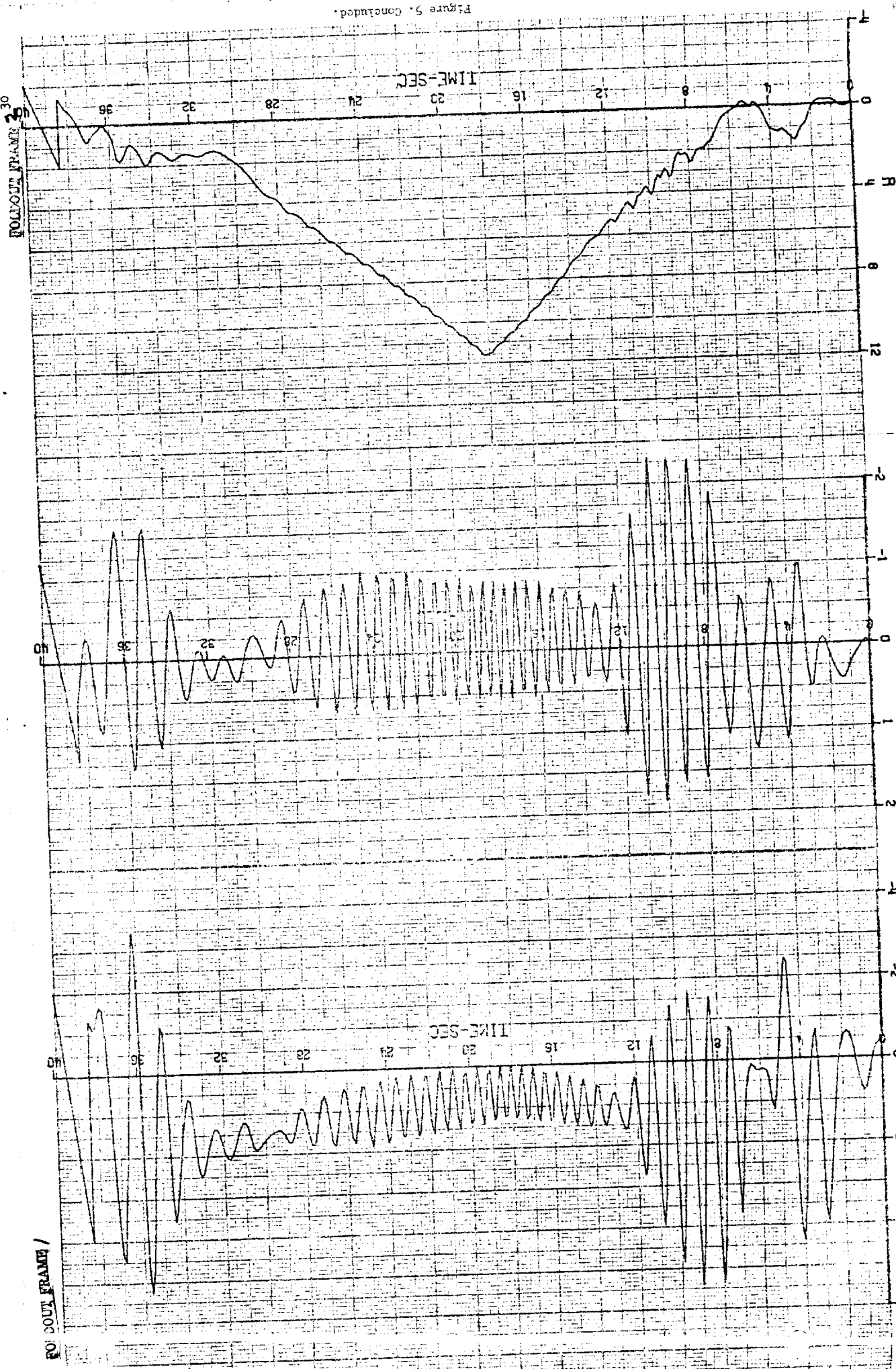
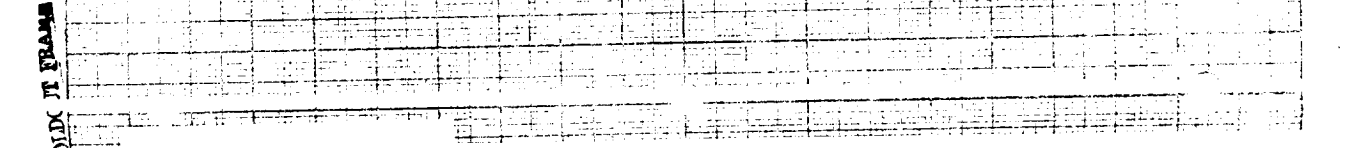
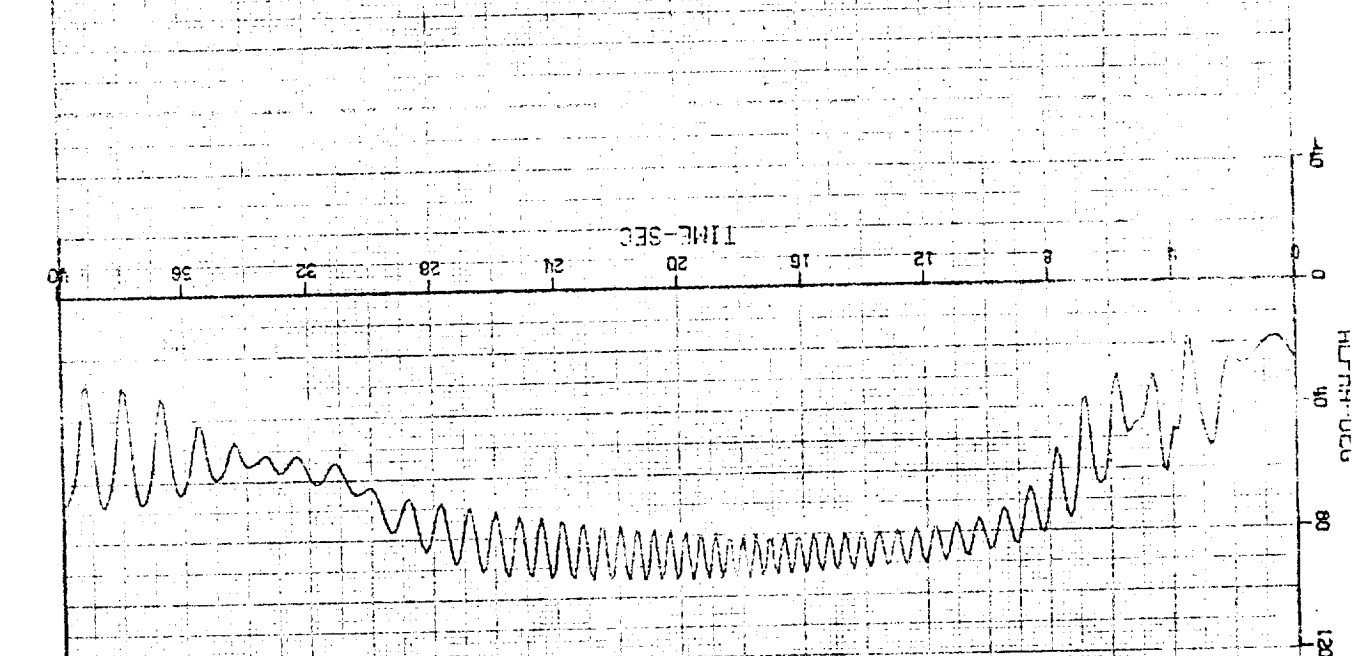
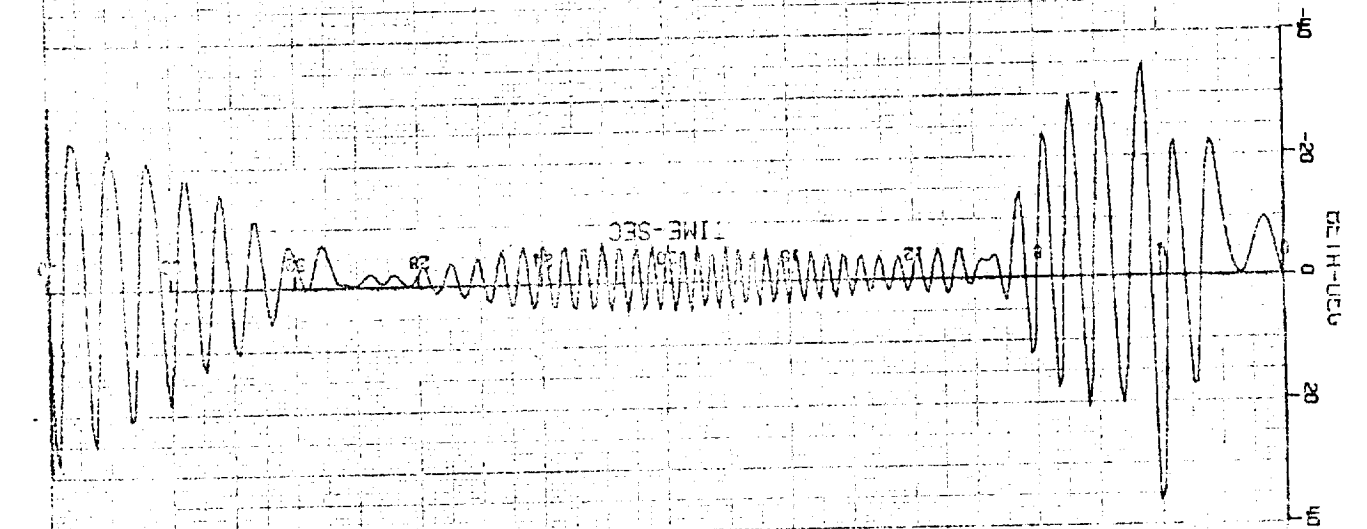
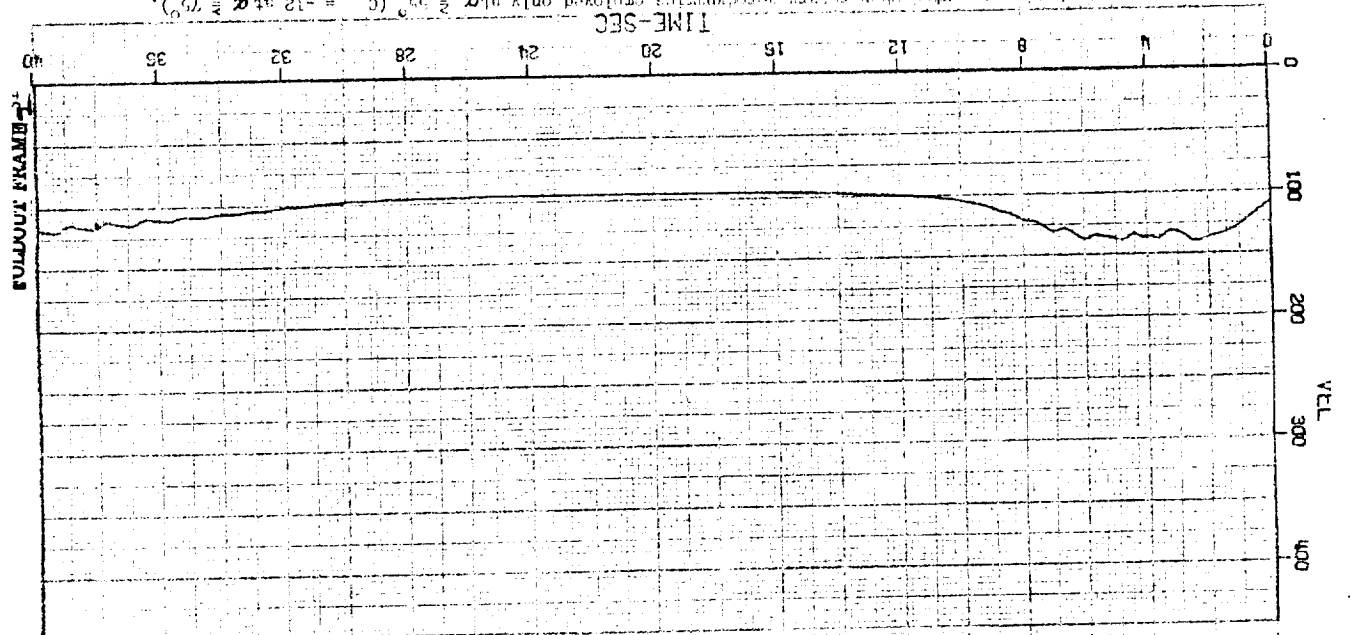


Figure 10 Motion counter when rotary accelerometers employed only at $\alpha = -12$ at $\theta = 75^\circ$.

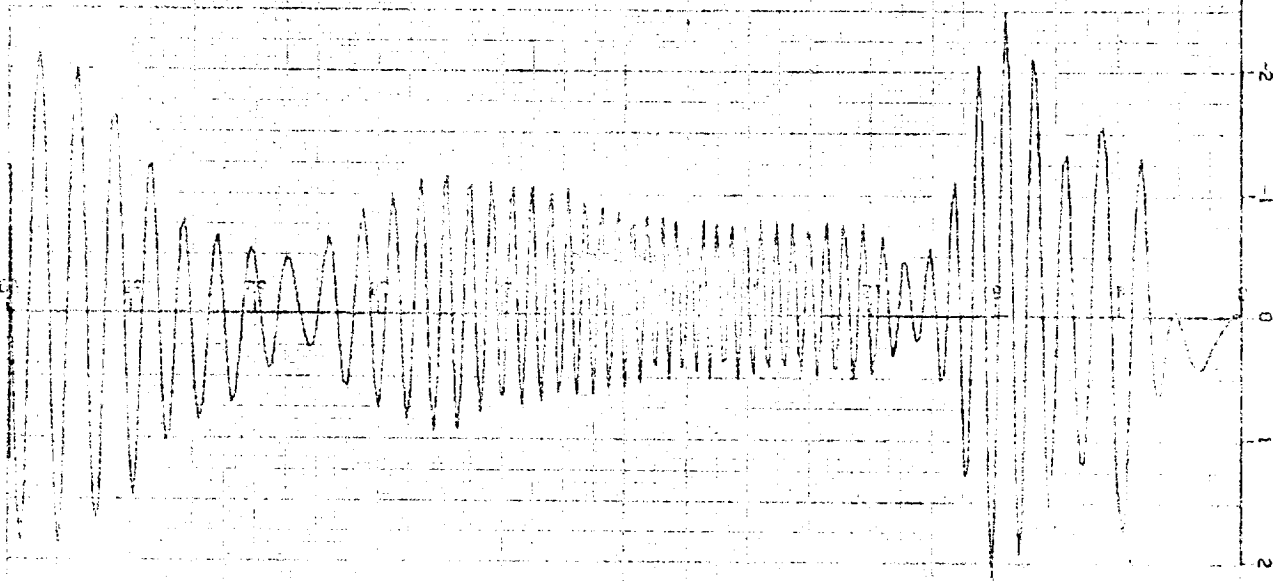
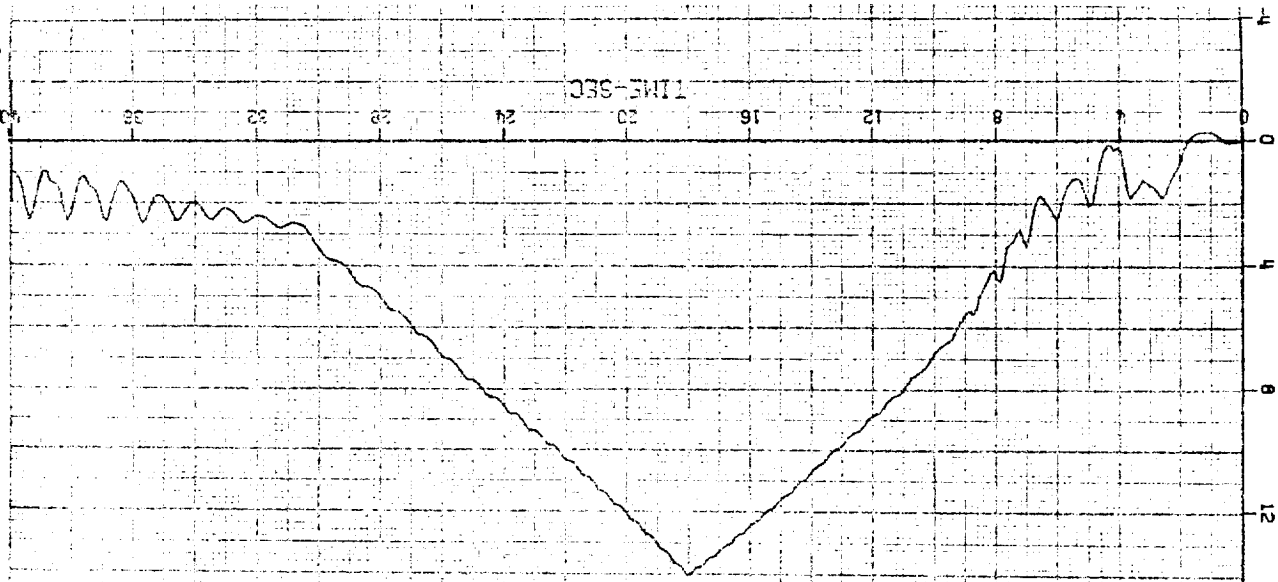


FOLDOUT FRAME 32 1

Figure 6. Concluded.

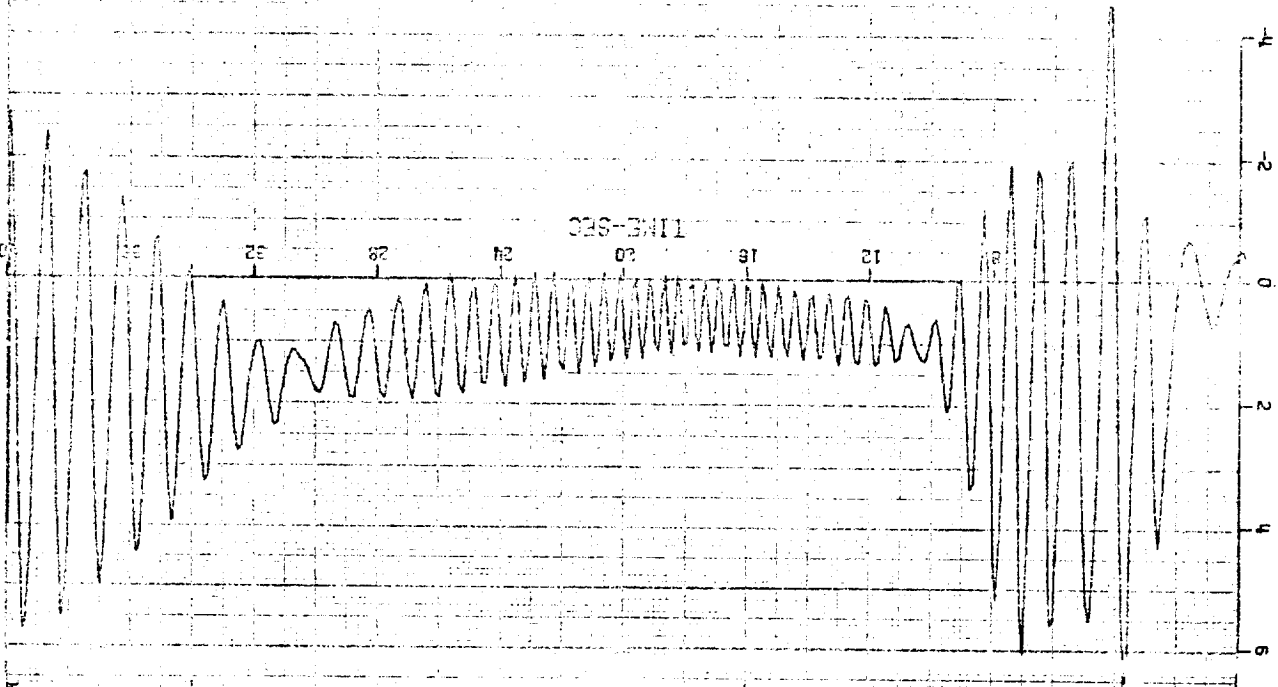
TIME-SEC

0 4 8 12 16 20 24 28 32 36



TIME-SEC

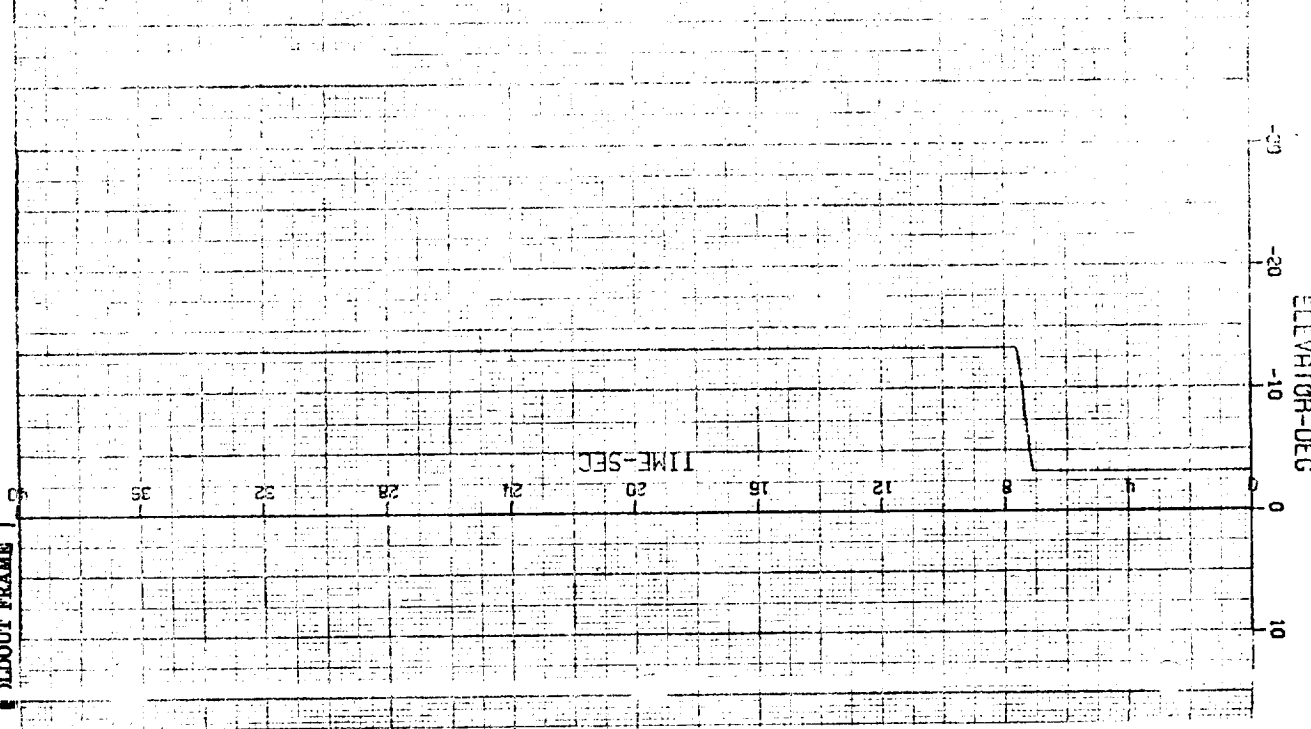
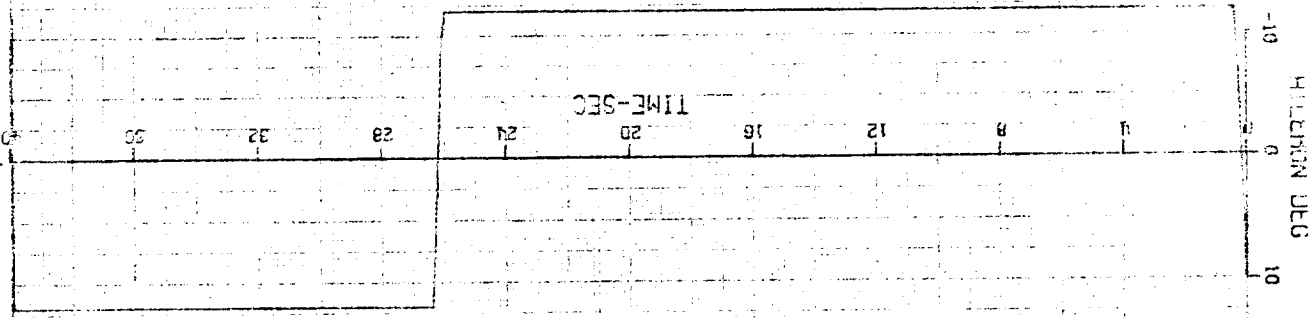
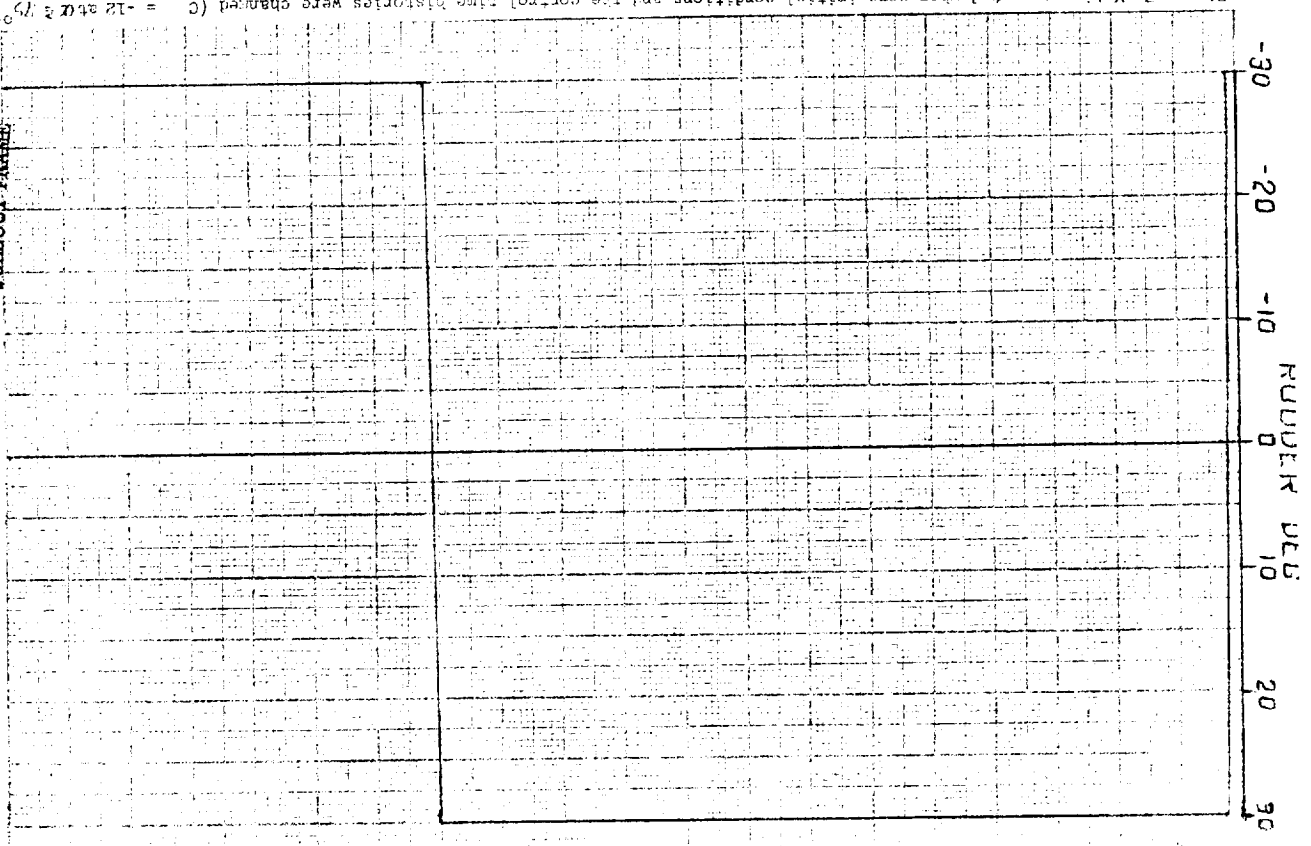
0 4 8 12 16 20 24 28 32 36



FOLDOUT FRAME 1

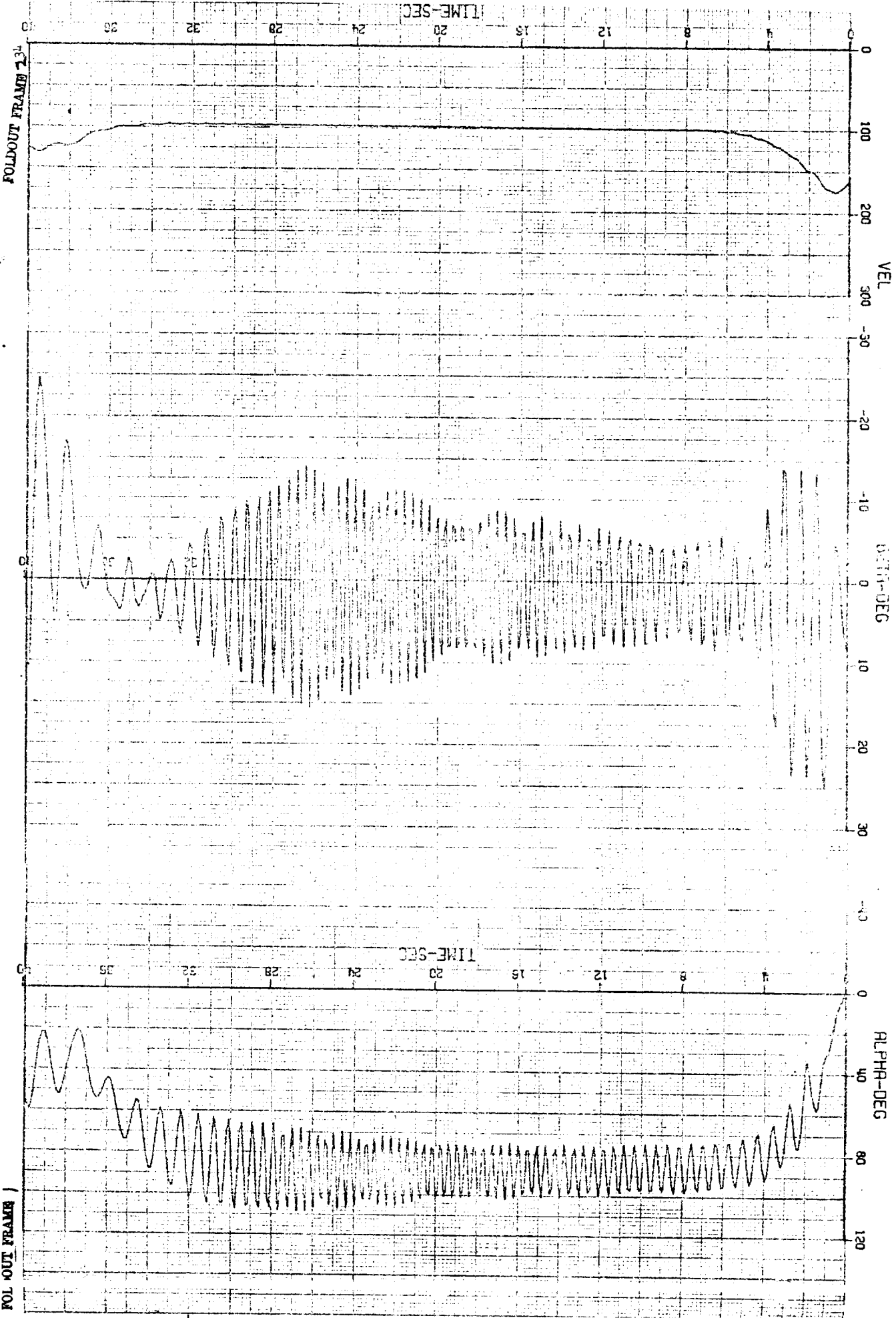
Figure 7. Motion computed when some initial conditions and the control time histories were changed ($C_m = -12$ at $\alpha = 17^\circ$).

FOLDOUT FRAME 233



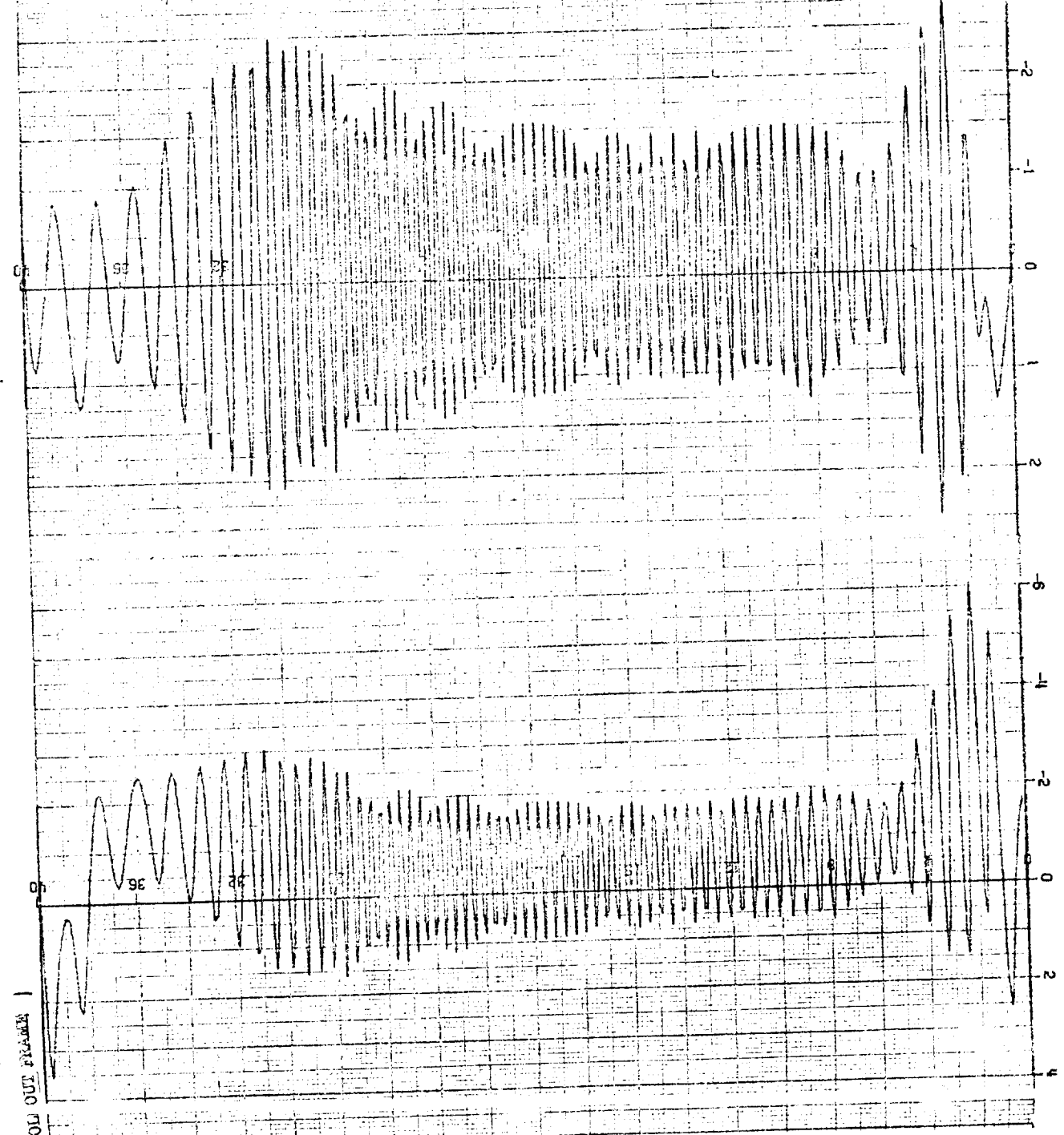
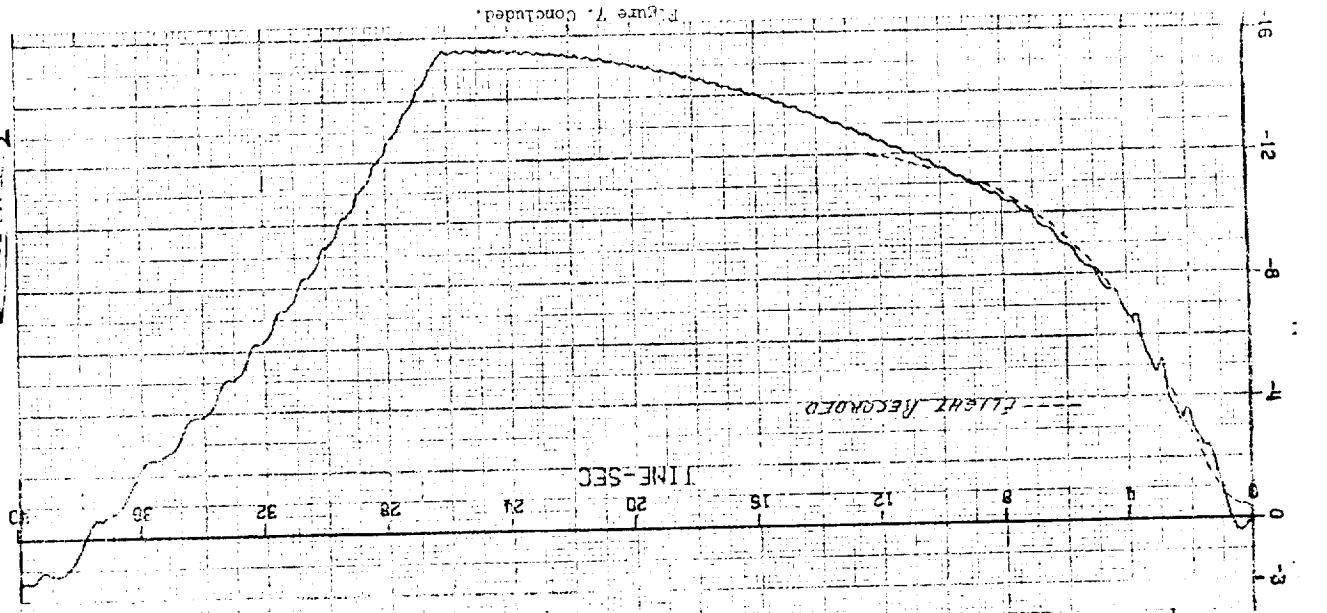
FOLDOUT FRAME 1

Figure 7. Continued.



FOOTAGE 17. 35

Figure 7. Concluded.



FOOTAGE 17. 36

APPENDIX A

EQUATIONS OF MOTION AND ASSOCIATED FORMULAS

The dynamical equations required to specify the translational and rotational motions of a rigid body moving through space are described in this appendix. The familiar six degree of freedom differential equations representing linear and angular accelerations of a moving body axis system having its origin at the aircraft center of mass are presented below.

$$\dot{u} = -g \sin \theta_e + vr - wq + \frac{\Sigma F_x^{\text{aero}}}{m}$$

$$\dot{v} = g \cos \theta_e \sin \phi_e + wp - ur + \frac{\Sigma F_y^{\text{aero}}}{m}$$

$$\dot{w} = g \cos \theta_e \cos \phi_e + uq - vp + \frac{\Sigma F_z^{\text{aero}}}{m}$$

$$\dot{p} = \frac{I_y - I_z}{I_x} qr + \frac{I_{xz}}{I_x} (\dot{r} + pq) + \frac{\Sigma L^{\text{aero}}}{I_x}$$

$$\dot{q} = \frac{I_z - I_x}{I_y} pr - \frac{I_{xz}}{I_y} (p^2 - r^2) + \frac{\Sigma M^{\text{aero}}}{I_y}$$

$$\dot{r} = \frac{I_x - I_y}{I_z} pq + \frac{I_{xz}}{I_z} (\dot{p} - qr) + \frac{\Sigma N^{\text{aero}}}{I_z}$$

In addition, the following formulas were used:

$$\alpha = \tan^{-1} \left(\frac{w}{u} \right)$$

$$\beta = \sin^{-1} \left(\frac{v}{V_R} \right)$$

$$V_R = \sqrt{u^2 + v^2 + w^2}$$

$$n = \sqrt{p^2 + q^2 + r^2}$$

$$\text{Turns in spin} = \frac{\int \dot{\psi}_e dt}{2\pi}$$

$$\dot{\psi}_e = \frac{\dot{\phi}_e - p}{\sin \theta_e}$$

$$\phi_e = \sin^{-1} \left(\frac{\sin \phi}{\cos \theta_e} \right)$$

$$\dot{\theta}_e = q \cos \phi_e - r \sin \phi_e$$

$$\dot{\phi}_e = p + r \tan \theta_e \cos \phi_e + q \tan \theta_e \sin \phi_e$$

$$p = p_r + p_o$$

$$q = q_r + q_o$$

$$r = r_r + r_o$$

These total angular velocities (p , q , r) consist of steady rotation (p_r , q_r , r_r) components upon which oscillatory (p_o , q_o , and r_o) components are superimposed. These components are defined as follows:

$$\begin{aligned} p_r &= -\dot{\psi}_e \sin \theta_e & p_o &= \dot{\phi}_e \\ q_r &= \dot{\psi}_e \cos \theta_e \sin \phi_e & q_o &= \dot{\theta}_e \cos \phi_e \\ r_r &= \dot{\psi}_e \cos \theta_e \cos \phi_e & r_o &= -\dot{\theta}_e \sin \phi_e \end{aligned}$$

For the aerodynamic model, the following total derivatives were used:

$$C_N^1 = C_N + C_{Nq} \frac{q_o \bar{c}}{2V}$$

$$C_c^1 = C_c$$

$$C_y^1 = C_y + C_{y\delta_a} \delta_a + C_{y\delta_R} \delta_R + C_{y_{rot}} + C_{y_r} \frac{r_o b}{2V} + C_{y_p} \frac{p_o b}{2V}$$

$$C_l^1 = C_l + C_{l\delta_a} \delta_a + C_{l\delta_R} \delta_R + C_{l_{rot}} + C_{l_r} \frac{r_o b}{2V} + C_{l_p} \frac{p_o b}{2V}$$

$$C_n^1 = C_n + C_{n_{\delta_a}} \delta_a + C_{n_{\delta_R}} \delta_R + C_{n_{rot}} + C_{n_r} \frac{r_{ob}}{2V} + C_{n_p} \frac{p_{ob}}{2V}$$

$$C_m^1 = C_m + C_{m_q} \frac{q_o \bar{c}}{2V}$$

Note:

The values of $C_{y_{rot}}$, $C_{l_{rot}}$ and $C_{n_{rot}}$ are obtained from rotary balance data using the values of p_r , q_r and r_r to compute $\frac{nb}{2V}$ as

$$\left(\frac{nb}{2V} \right)^2 = p_r^2 + q_r^2 + r_r^2$$

The following formulas were used to compute α and β at the nose boom vane location.

$$u_{Boom} = u + \Delta z \cdot q - \Delta y \cdot r$$

$$v_{Boom} = v + \Delta x \cdot r - \Delta z \cdot p$$

$$w_{Boom} = w - \Delta x \cdot q + \Delta y \cdot p$$

$$V_{Boom}^2 = u_{Boom}^2 + v_{Boom}^2 + w_{Boom}^2$$

$$\alpha_{Boom} = \tan^{-1} \frac{w_{Boom}}{u_{Boom}}$$

$$\beta_{Boom} = \sin^{-1} \frac{v_{Boom}}{V_{Boom}}$$

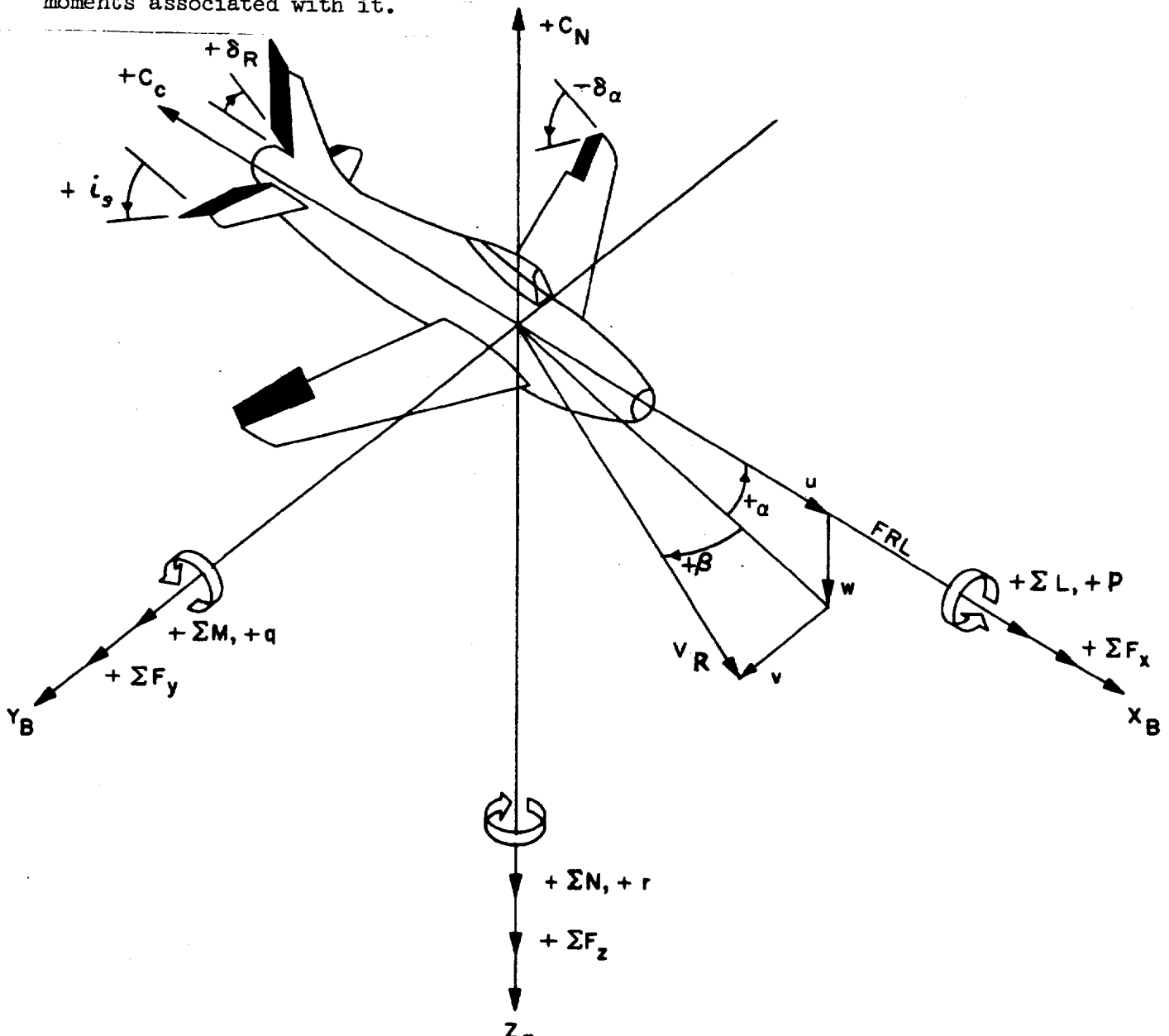
where Δz , Δx and Δy are the distance between center of gravity and boom vane location.

APPENDIX B

SYMBOLS

Measurements and calculations were made in the U.S. Customary Units. Factors for converting these units to the International Systems of Units may be found in reference 2.

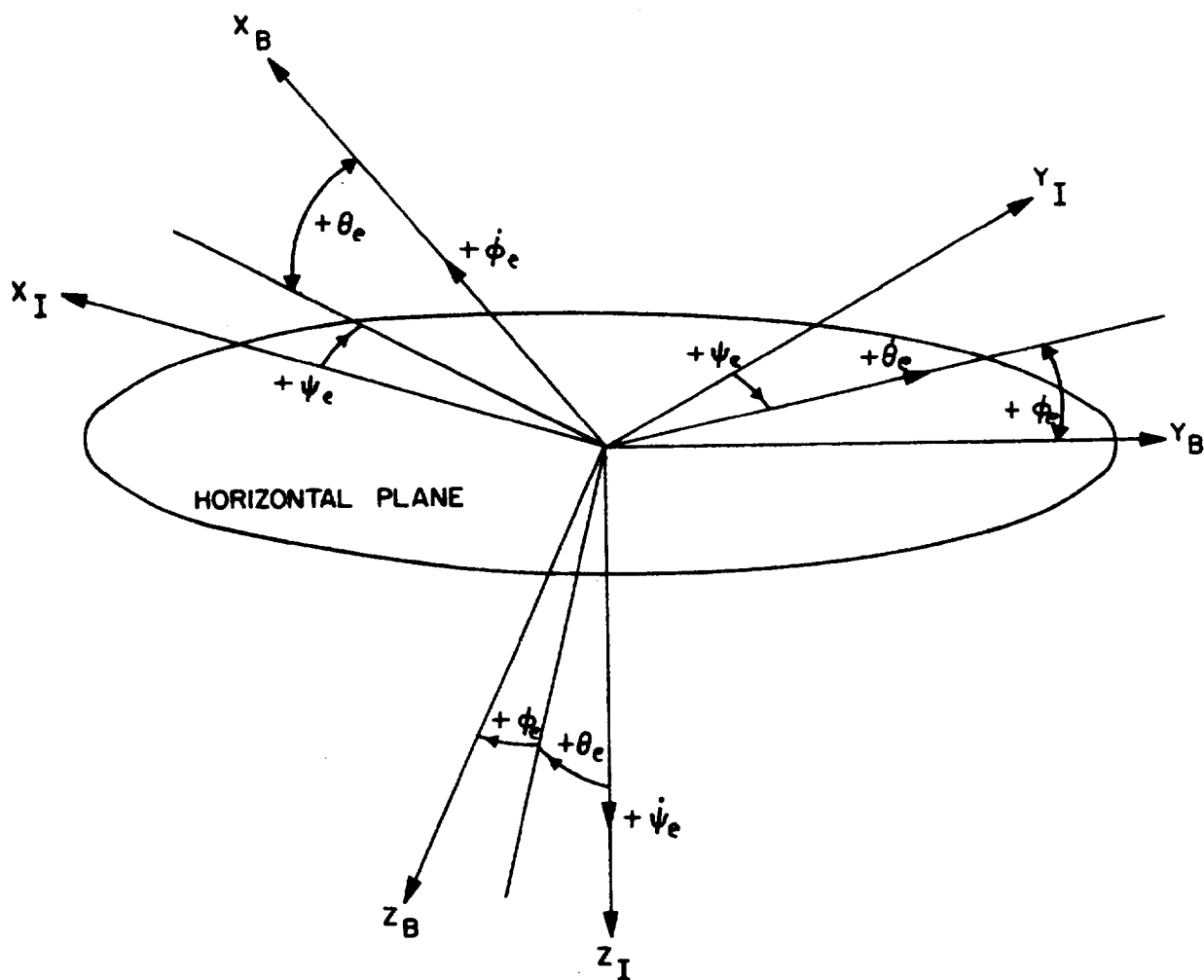
The Body Axes System is used with the origin of the axes system located at the aircraft center of gravity. The X axis is parallel to the aircraft Fuselage Reference Line (FRL) and is positive forward, the Y axis is positive towards the right wing tip and the Z axis is positive downward. The following illustration shows this axis system and the positive direction of the angles, forces and moments associated with it.



In the following definitions a dot (.) over a quantity denotes one differentiation with respect to time and a zero subscript (o) denotes the initial value of the quantity.

X_I, Y_I, Z_I , inertial axes

X_B, Y_B, Z_B body axes



BODY AXIS SYSTEM LOCATED IN INERTIAL SPACE
 POSITIVE DIRECTION OF EULER ANGLES AND RATES

I_x, I_y, I_z	moments of inertia about the X, Y and Z body axes, respectively	slug-ft ²
I_{xz}	product of inertia, positive when the principle X axis is inclined below the X body axis at the aircraft nose	slug-ft ²
m	aircraft mass (=W/g)	slug's
W	aircraft weight (=mg)	lbs
S	wing area	ft ²
b	wing span	ft
\bar{c}	wing mean aerodynamic chord	ft
W/S	wing loading	lb/ft ²
$(I_y - I_z)/mb^2$	inertia rolling moment parameter	-
$(I_z - I_x)/mb^2$	inertia pitching moment parameter	-
$(I_x - I_y)/mb^2$	inertia yawing moment parameter	-
t	time	sec
ρ	atmospheric density	slug/ft ³
\bar{q}	dynamic pressure = $\left(\frac{\rho V_R^2}{2}\right)$	lb/ft ²
H	vertical height	ft
α	angle of attack	deg
β	angle of sideslip	deg
θ_e, ϕ_e, ψ_e	Euler angles	deg
ϕ	angle between Y body axis and horizontal measured in vertical plane, positive for erect spins when right wing is downward and for inverted spins when left wing is downward	deg

γ	flight path angle, measured in a vertical plane between the horizontal plane and the resultant velocity vector, positive when the resultant velocity vector points above the horizontal plane	deg
δ_a	differential horizontal tail deflection (half angle), positive to produce left rolling moment	deg
i_s	control deflection-stabilizer, positive direction trailing edge down	deg
δ_R	control deflection-rudder, positive direction trailing edge left	deg
V_R	total linear velocity vector	ft/sec
V	free-stream velocity	ft/sec
u, v, w	components of the total linear velocity vector (V_R) along the X, Y and Z body axes, respectively	ft/sec
$\dot{u}, \dot{v}, \dot{w}$	components of the relative linear acceleration vector along the X, Y and Z body axes, respectively	ft/sec ²
p, q, r	components of the total angular velocity vector along the X, Y and Z body axes, respectively	radians/sec
ω	frequency of forced-oscillation tests	radians/sec
Ω	total angular velocity vector	radians/sec

g	acceleration due to gravity	ft/sec ²
$F_{x_{aero}}, F_{y_{aero}}, F_{z_{aero}}$	components of the aerodynamic forces along the X, Y and Z body axes, respectively	lbs
$L_{aero}, M_{aero}, N_{aero}$	components of the aerodynamic moments about the X, Y and Z body axes, respectively	ft/lbs
T	total engine thrust force	lbs
$C_c^l = \frac{-F_{x_{aero}}}{\bar{q} S}$	total chordwise force coefficient, positive along the negative X body axis	
$C_y^l = \frac{F_{y_{aero}}}{\bar{q} S}$	total sideforce coefficient, positive along the positive Y body axis	
$C_N^l = \frac{-F_{z_{aero}}}{\bar{q} S}$	total normal force coefficient, positive along the negative Z body axis	
$C_l^l = \frac{L_{aero}}{\bar{q} S b}$	total rolling moment coefficient, positive direction of moment drives the right wing tip down	
$C_m^l = \frac{M_{aero}}{\bar{q} S \bar{c}}$	total pitching moment coefficient about the aerodynamic center, positive direction of moment drives the nose up	
$C_n^l = \frac{N_{aero}}{\bar{q} S b}$	total yawing moment coefficient, positive direction of moment drives the nose right	
$C_c(\alpha, \beta, i_s)$	variation in chordwise force coefficient due to angle of attack, sideslip angle and stabilizer deflection	
$C_y(\beta, \alpha)$	variation in side force coefficient due to sideslip angle and angle of attack	

$C_{y_{rot}} (\dot{\alpha}b/2V, \alpha, i_s)$	variation in side force coefficient due to rate of rotation, angle of attack and stabilizer deflection
$C_N (\alpha, \beta, i_s)$	variation in normal force coefficient due to angle of attack, sideslip angle and stabilizer deflection
$C_l (\beta, \alpha, i_s)$	variation in rolling moment coefficient due to sideslip angle, angle of attack and stabilizer deflection
$C_{l_{rot}} (\dot{\alpha}b/2V, \alpha, i_s)$	variation in rolling moment coefficient due to rate of rotation, angle of attack, and stabilizer deflection
$C_m (\alpha, \beta, i_s)$	variation in pitching moment coefficient due to angle of attack, sideslip angle and stabilizer deflection
$C_n (\beta, \alpha, i_s)$	variation in yawing moment coefficient due to sideslip angle, angle of attack and stabilizer deflection
$C_{n_{rot}} (\dot{\alpha}b/2V, \alpha, i_s)$	variation in yawing moment coefficient due to rate of rotation, angle of attack, and stabilizer deflection
$C_{y_{\delta_a}} (\alpha, i_s)$	variation in $\frac{\partial C_y}{\partial \delta_a}$ due to angle of attack and stabilizer deflection, per deg
$C_{l_{\delta_a}} (\alpha, i_s)$	variation in $\frac{\partial C_l}{\partial \delta_a}$ due to angle of attack and stabilizer deflection, per deg
$C_{n_{\delta_a}} (\alpha, i_s)$	variation in $\frac{\partial C_n}{\partial \delta_a}$ due to angle of attack and stabilizer deflection, per deg
$C_{y_{\delta_R}} (\alpha, i_s)$	variation in $\frac{\partial C_y}{\partial \delta_R}$ due to angle of attack and stabilizer deflection, per deg

$C_{l_{\delta_R}}(i_s, \alpha, \beta)$ variation in $\frac{\partial C_l}{\partial \delta_R}$ due to stabilizer deflection, angle of attack and sideslip angle, per deg

$C_{n_{\delta_R}}(i_s, \alpha, \beta)$ variation in $\frac{\partial C_n}{\partial \delta_R}$ due to stabilizer deflection, angle of attack and sideslip angle, per deg

$C_Z = -C_N$ per deg

$C_X = -C_C$ per deg

$C_{y_p} = \frac{\partial C_y}{\partial \frac{pb}{2V_R}}$ per radian

$C_{l_p} = \frac{\partial C_l}{\partial \frac{pb}{2V_R}}$ per radian

$C_{n_p} = \frac{\partial C_n}{\partial \frac{pb}{2V_R}}$ per radian

$C_{N_q} = \frac{\partial C_N}{\partial \left(\frac{q\bar{c}}{2V_R}\right)}$ per radian

$C_{m_q} = \frac{\partial C_m}{\partial \left(\frac{q\bar{c}}{2V_R}\right)}$ per radian

$C_{y_r} = \frac{\partial C_y}{\partial \left(\frac{rb}{2V_R}\right)}$ per radian

$C_{l_r} = \frac{\partial C_l}{\partial \left(\frac{rb}{2V_R}\right)}$ per radian

$C_{n_r} = \frac{\partial C_n}{\partial \left(\frac{rb}{2V_R}\right)}$ per radian

APPENDIX C

AERODYNAMIC DATA EMPLOYED IN INVESTIGATION

LIST OF FIGURES

Figure No.	Title	Page
C-1	Effect of angle of attack and sideslip angle on normal-force coefficient when $i_s = 0^\circ$.	50
C-2	Effect of angle of attack and sideslip angle on normal-force coefficient when $i_s = -30^\circ$.	51
C-3	Effect of angle of attack and sideslip angle on chordwise force coefficient when $i_s = 0^\circ$.	52
C-4	Effect of angle of attack and sideslip angle on chordwise force coefficient when $i_s = -30^\circ$.	53
C-5	Effect of angle of attack and sideslip angle on side-force coefficient when $i_s = 0^\circ$ and -30° .	54
C-6	Effect of angle of attack and sideslip angle on pitching-moment coefficient when $i_s = 0^\circ$.	55
C-7	Effect of angle of attack and sideslip angle on pitching-moment coefficient when $i_s = -30^\circ$.	56
C-8	Effect of angle of attack and sideslip angle on rolling-moment coefficient when $i_s = 0^\circ$ and -30° .	57
C-9	Effect of angle of attack and sideslip angle on yawing-moment coefficient when $i_s = 0^\circ$ and -30° .	
	a) $\beta = 10^\circ$ and 20°	58
	b) $\beta = 30^\circ$ and 40°	59
C-10	Effect of angle of attack and sideslip angle on directional - control characteristics when $i_s = 0^\circ$.	
	a) C_n	60
	b) C_l	61
	c) C_y	62
C-11	Effect of angle of attack and sideslip angle on lateral-control characteristics when $i_s = 0^\circ$ and -30° .	
	a) C_n	63
	b) C_l	64
	c) C_y	65

LIST OF FIGURES (Continued)

Figure No.	Title	Page
C-12	Effect of rotation rate and angle of attack on side-force coefficient when $i_s = 0^\circ$ and -30° .	66
C-13	Effect of rotation rate and angle of attack on rolling-moment coefficient when $i_s = 0^\circ$.	67
C-14	Effect of rotation rate and angle of attack on rolling-moment coefficient when $i_s = -30^\circ$.	68
C-15	Effect of rotation rate and angle of attack on yawing-moment coefficient when $i_s = 0^\circ$ and -30° .	69
C-16	Effect of angle of attack and forced-oscillation frequency on normal-force coefficient due to pitch rate.	70
C-17	Effect of angle of attack and forced-oscillation frequency on side-force coefficient due to roll and yaw rate.	71
C-18	Effect of angle of attack and forced-oscillation frequency on damping derivatives.	
	a) C_{mq}	72
	b) C_{lp}	73
	c) C_{nr}	74
C-19	Effect of angle of attack and forced-oscillation frequency on cross derivatives.	
	a) C_{np}	75
	b) C_{lr}	76

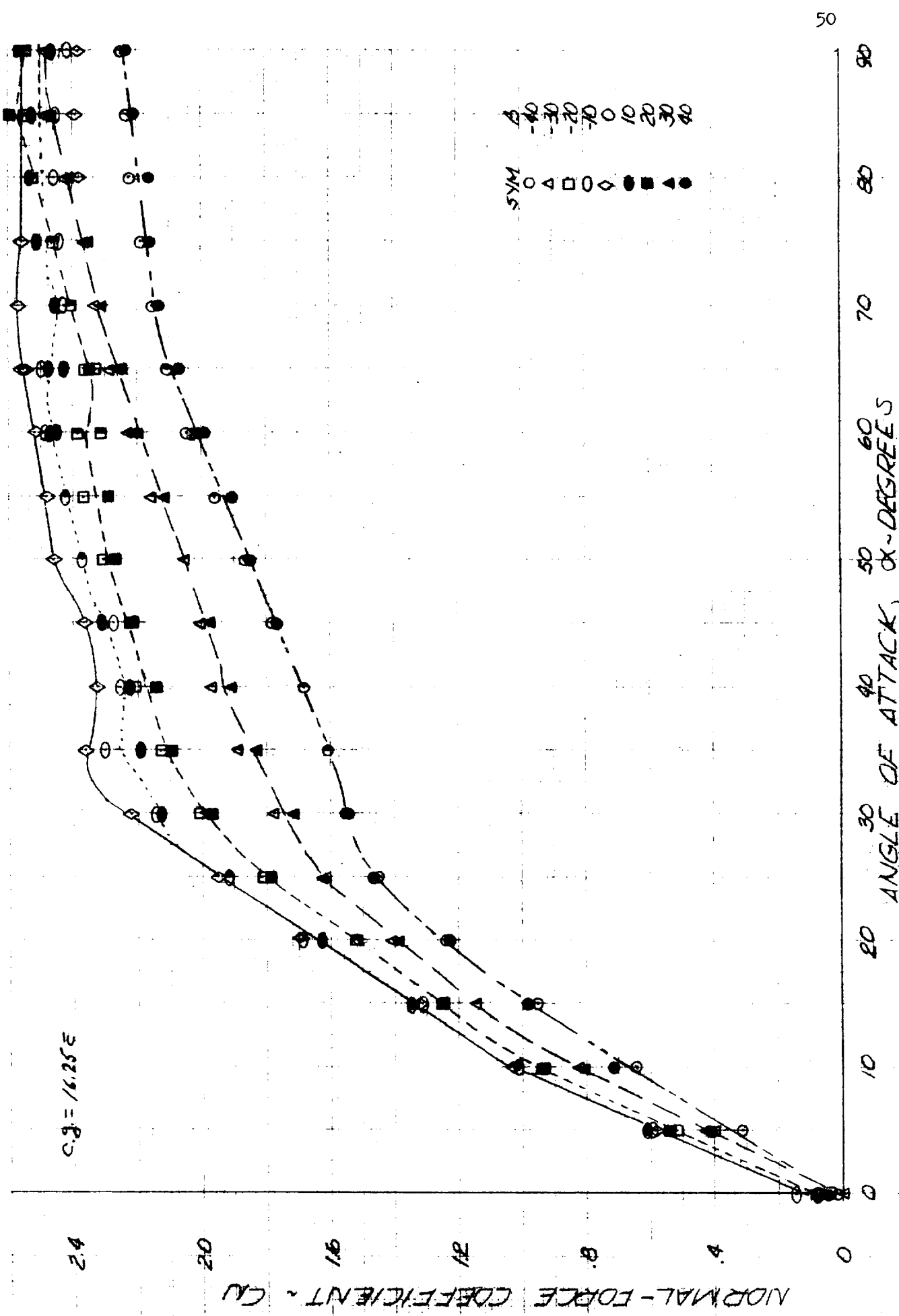


Figure C-1. Effect of angle of attack and sideslip angle on normal-force coefficient when $i_s = 0^\circ$.

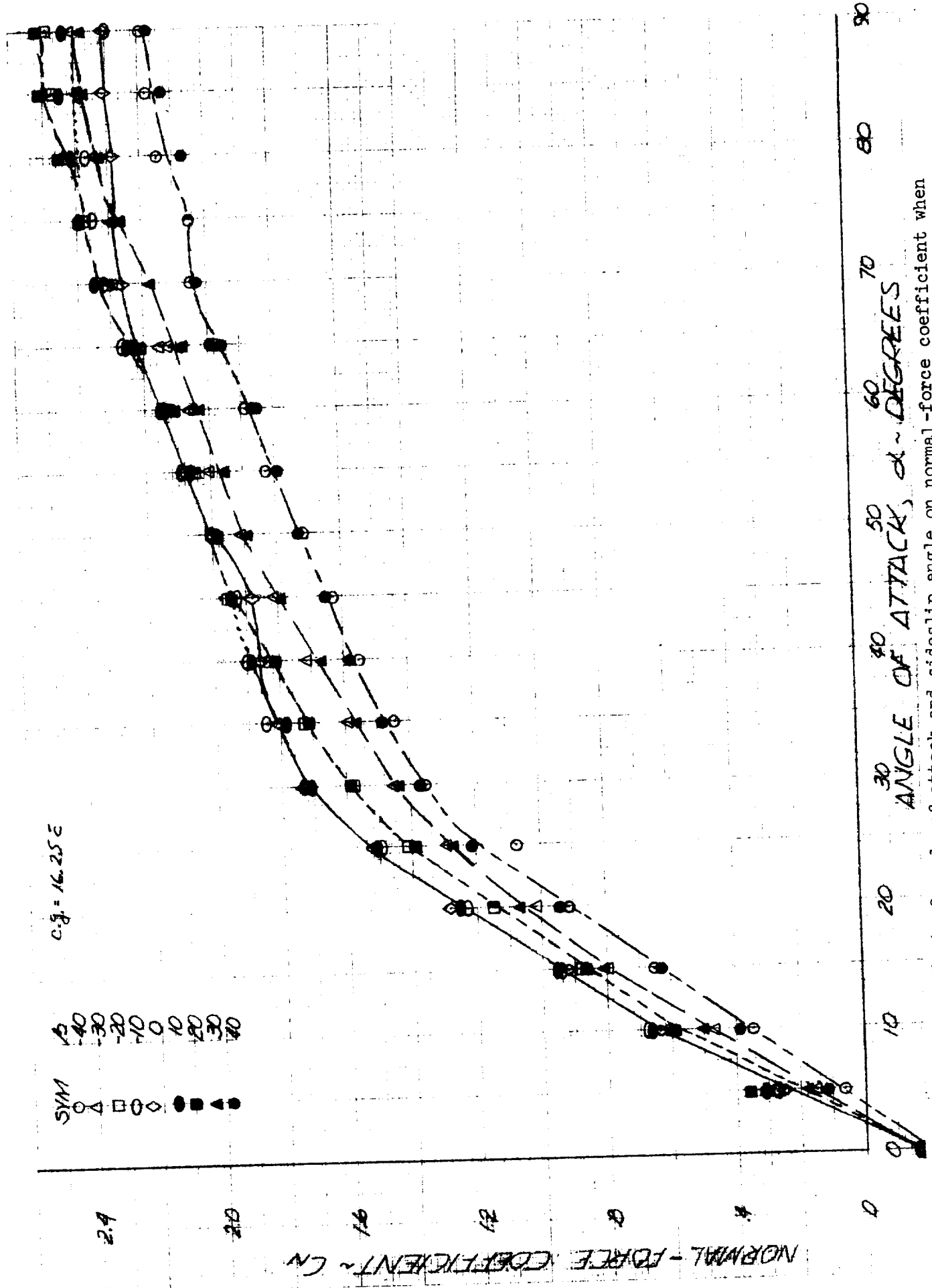


Figure C-2. Effect of angle of attack and sideslip angle on normal-force coefficient when $i_s = -30^\circ$.

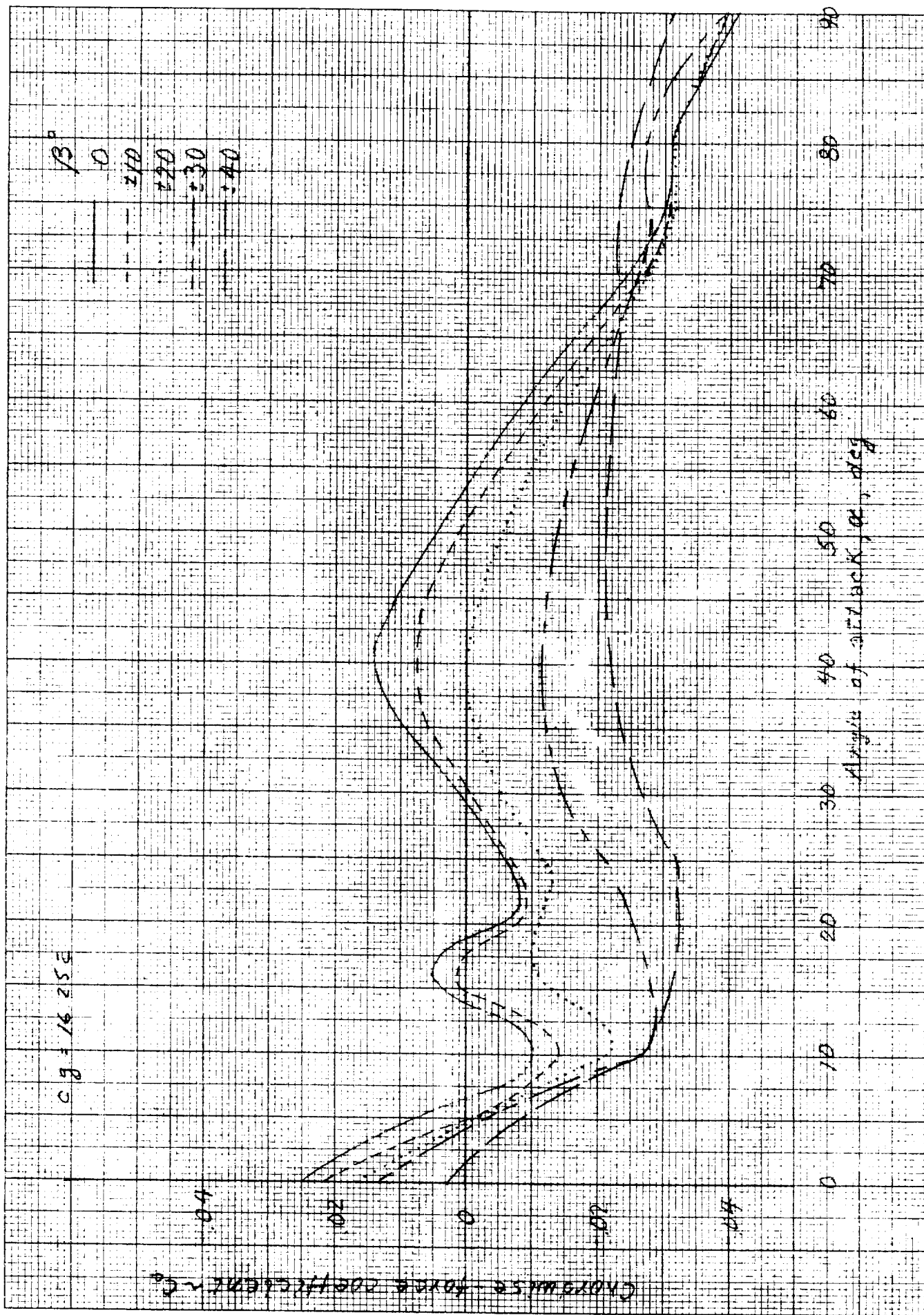
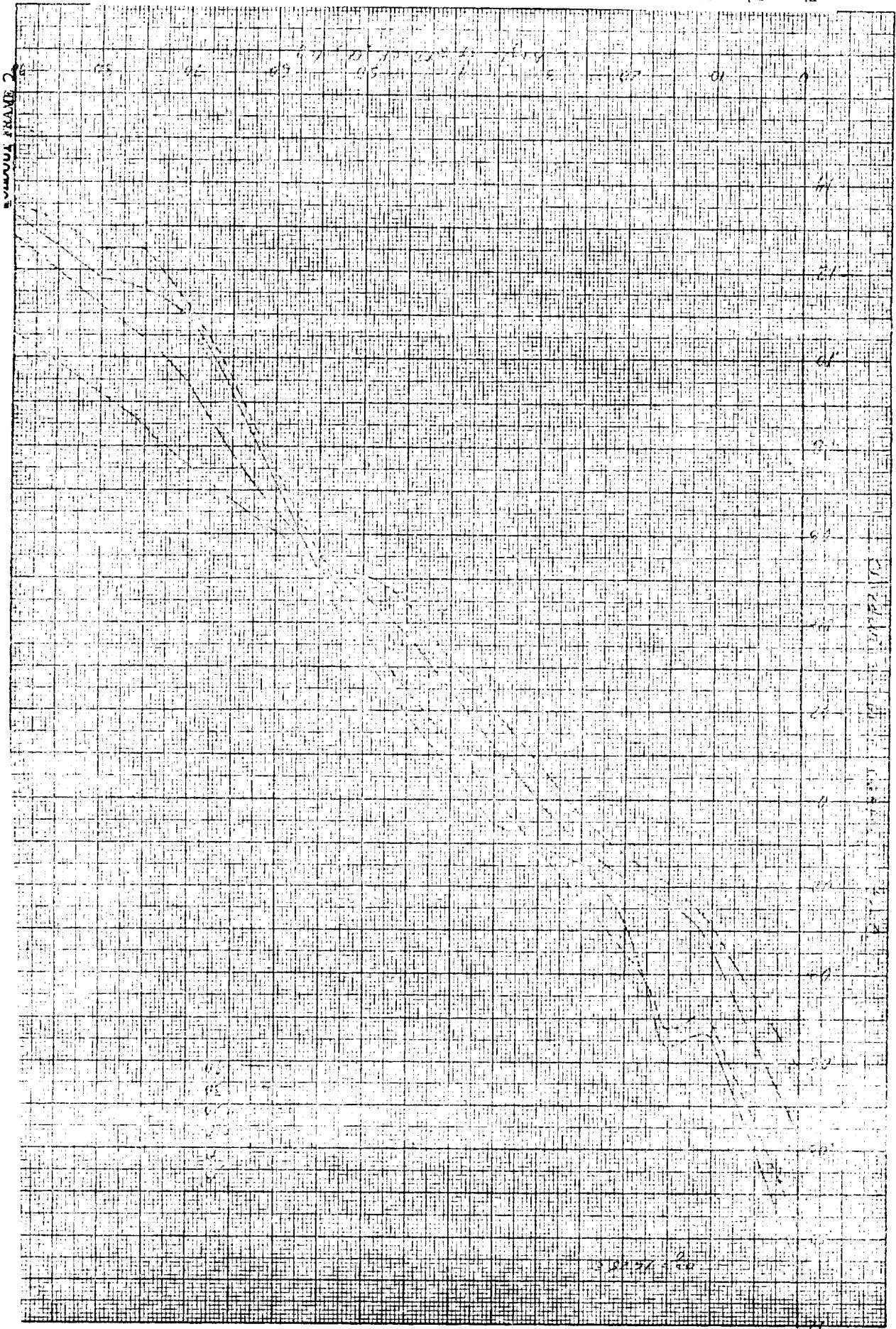


Figure C-3. Effect of angle of attack and sideslip angle on chordwise-force coefficient when $i_s = 0^\circ$.

Figure C-4. Effect of angle of attack and sideslip angle on chordwise-force coefficient when $\alpha = -30^\circ$.



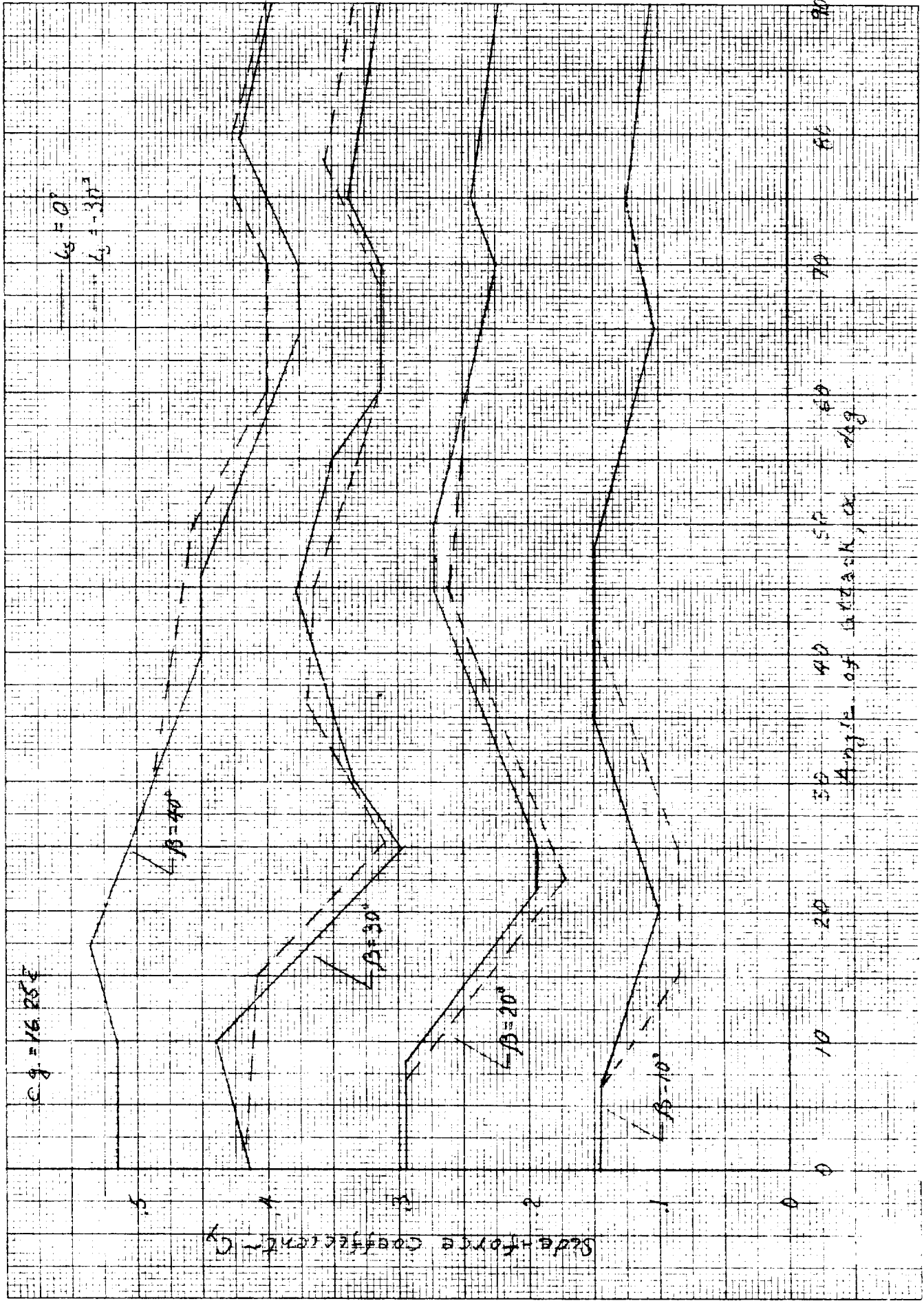


Figure C-5. Effect of angle of attack and sideslip angle on side-force coefficient when $i_s = 0^\circ$ and -30° .

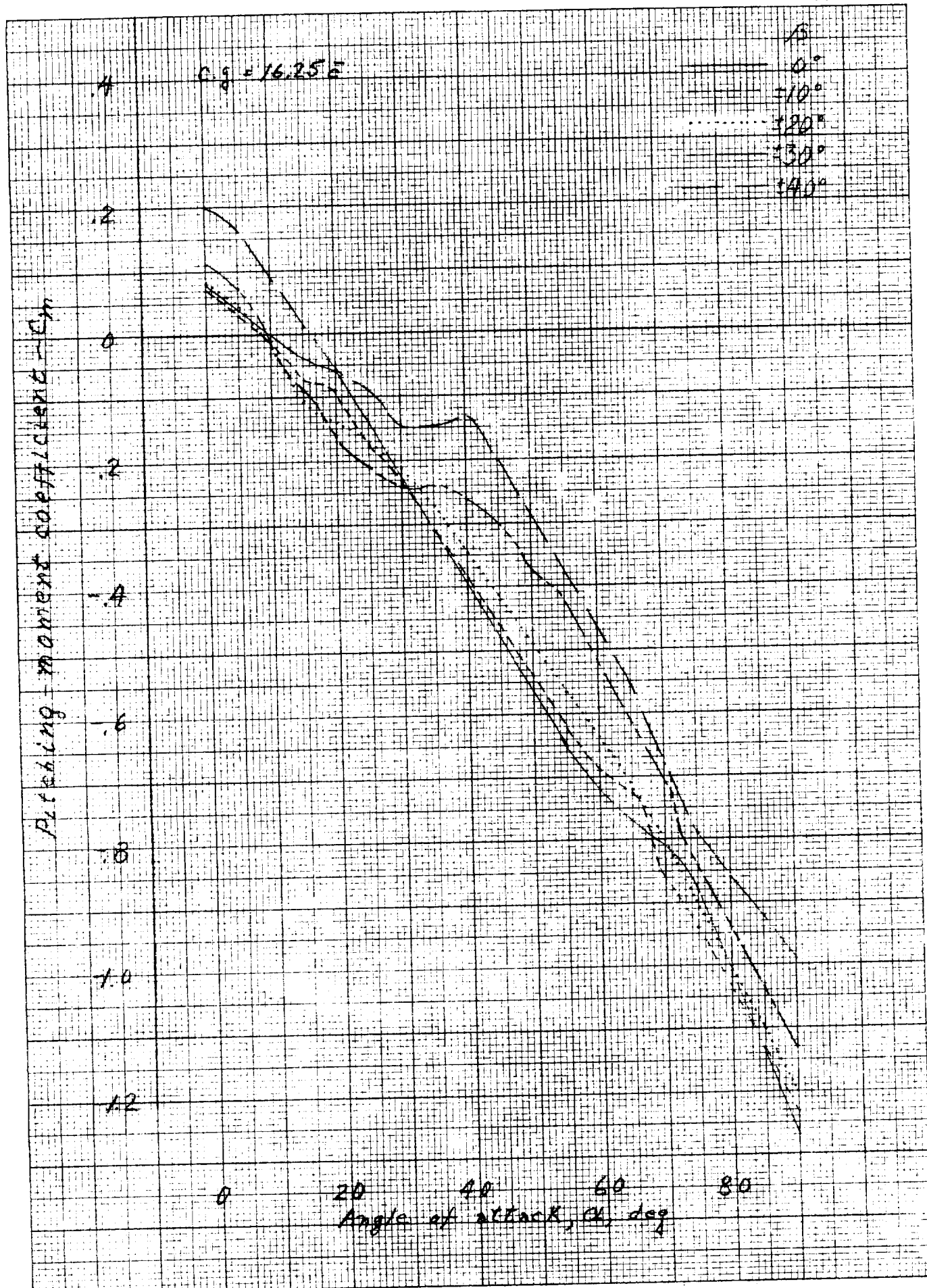


Figure C-6. Effect of angle of attack and sideslip angle on pitching moment coefficient when $\beta_s = 0^\circ$.

NO 1023

NO 10
RESEARCH
CH
LUS. CO. MADE

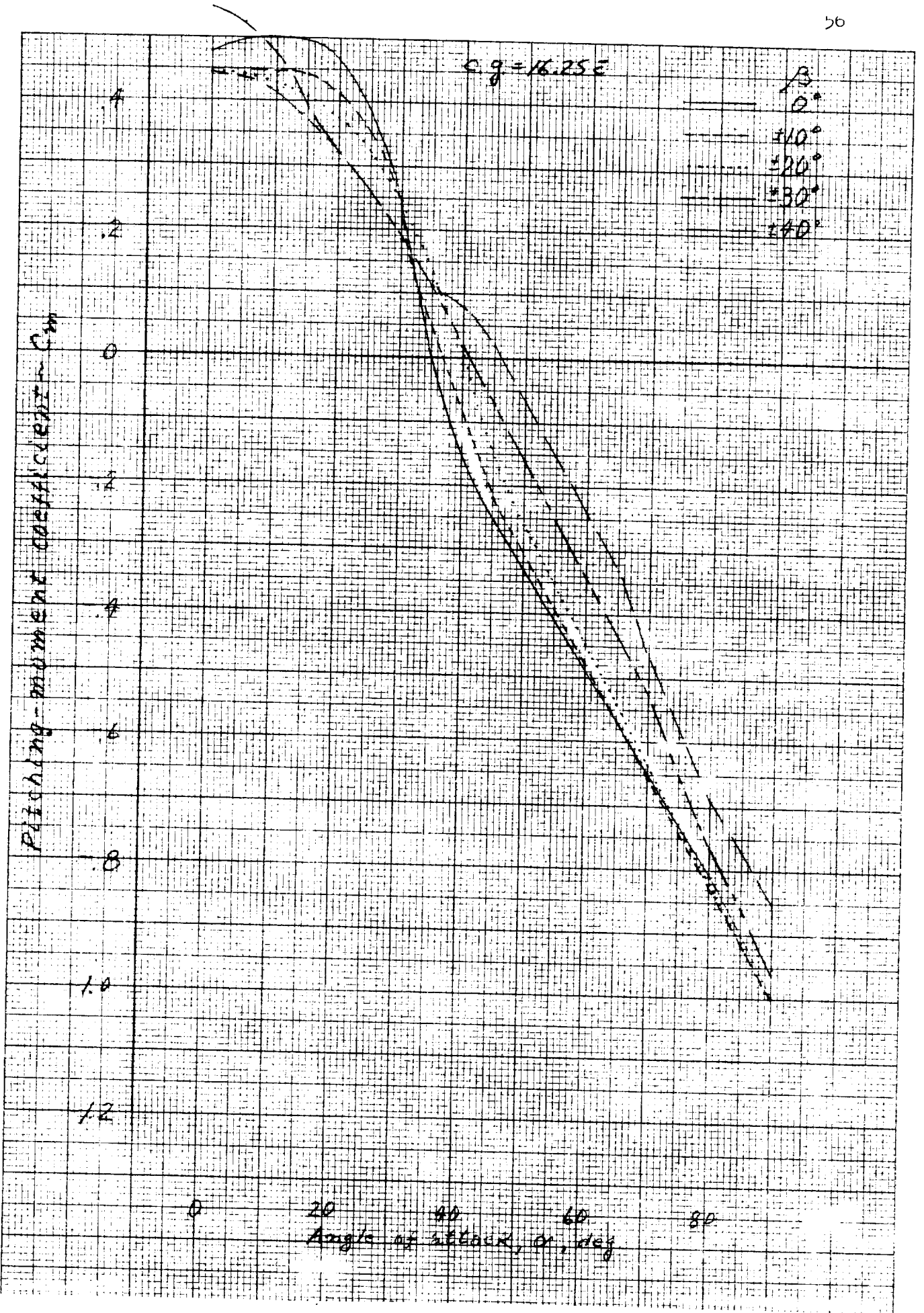


Figure C-7. Effect of angle of attack and sideslip angle on pitching moment when $\beta_s = -30^\circ$.

C.g. = 16.25%

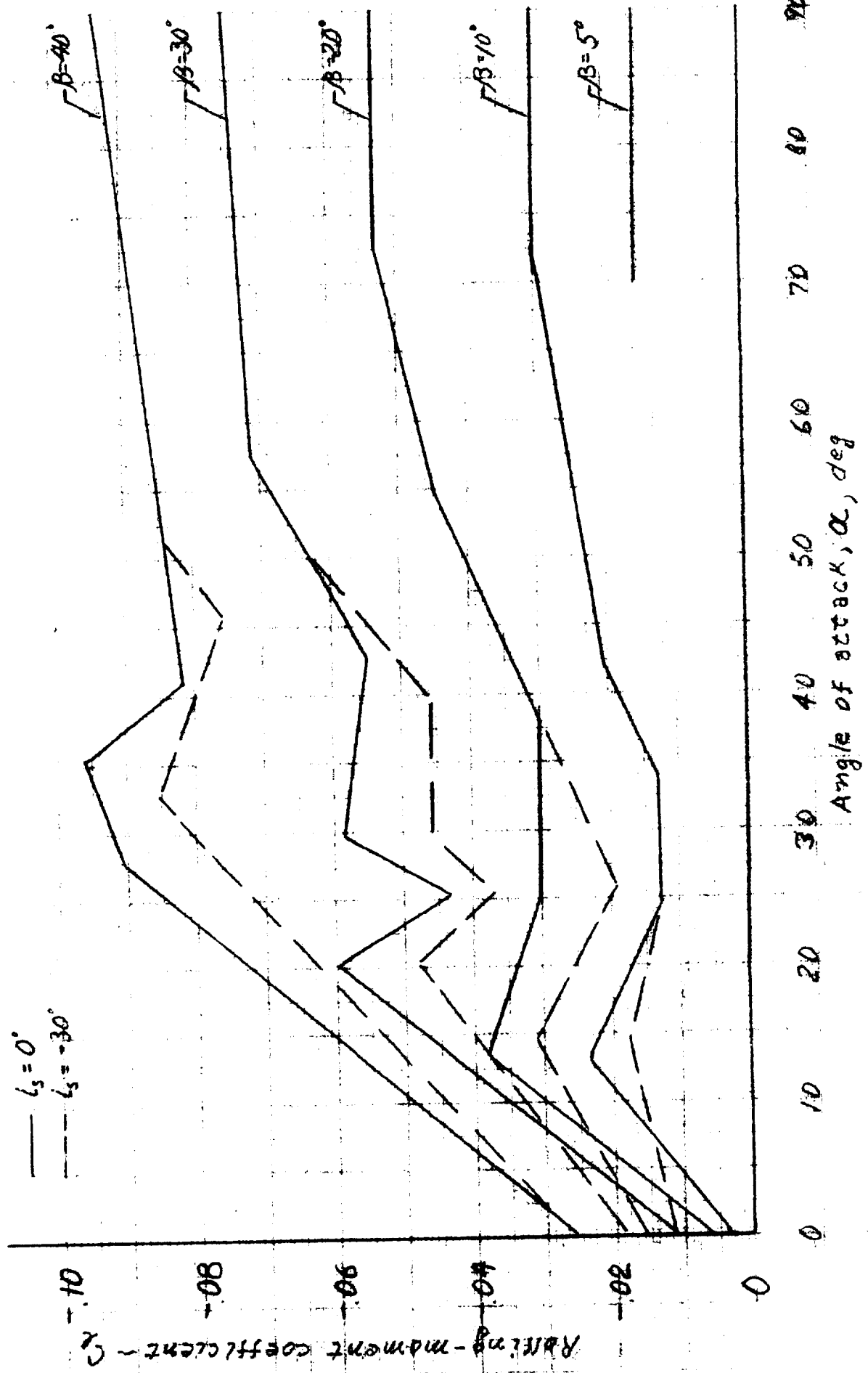


Figure C-8. Effect of angle of attack and sideslip angle on rolling-moment coefficient when $i_s = 0^\circ$ and -30° .

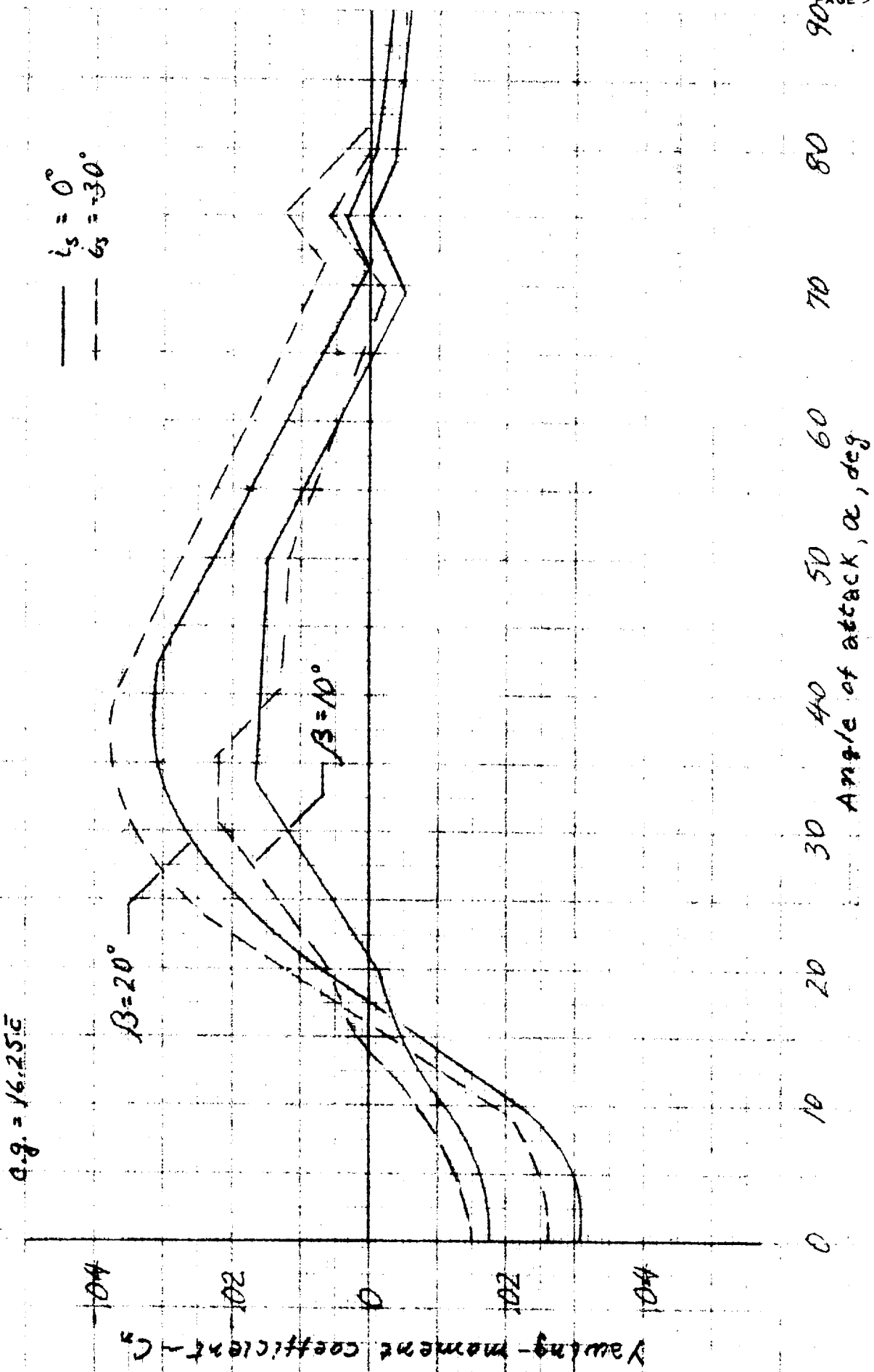


Figure C-9. Effect of angle of attack and sideslip angle on yawing-moment coefficient when $i_s = 0^\circ$ and -30° .

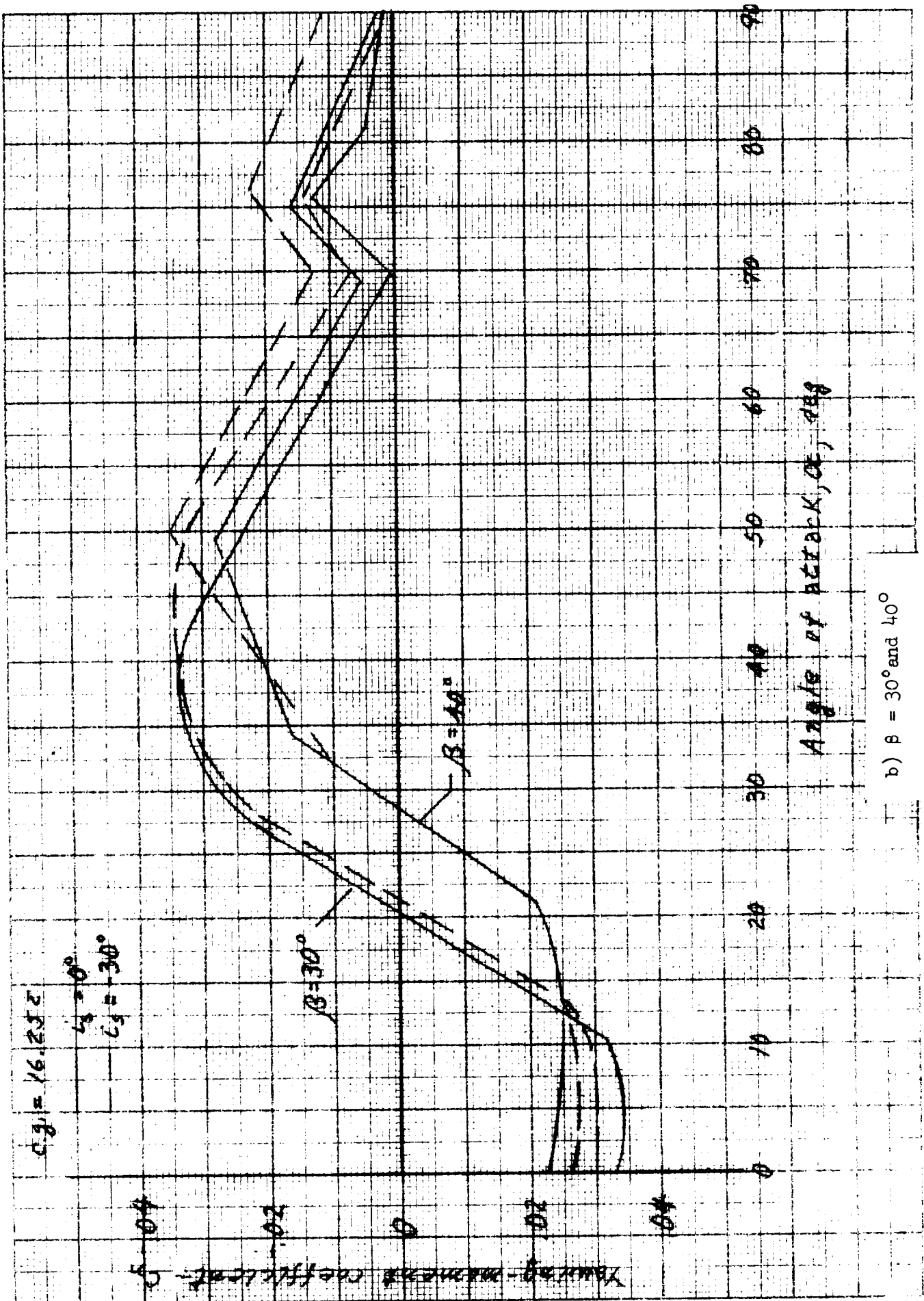


Figure C-9. Concluded.

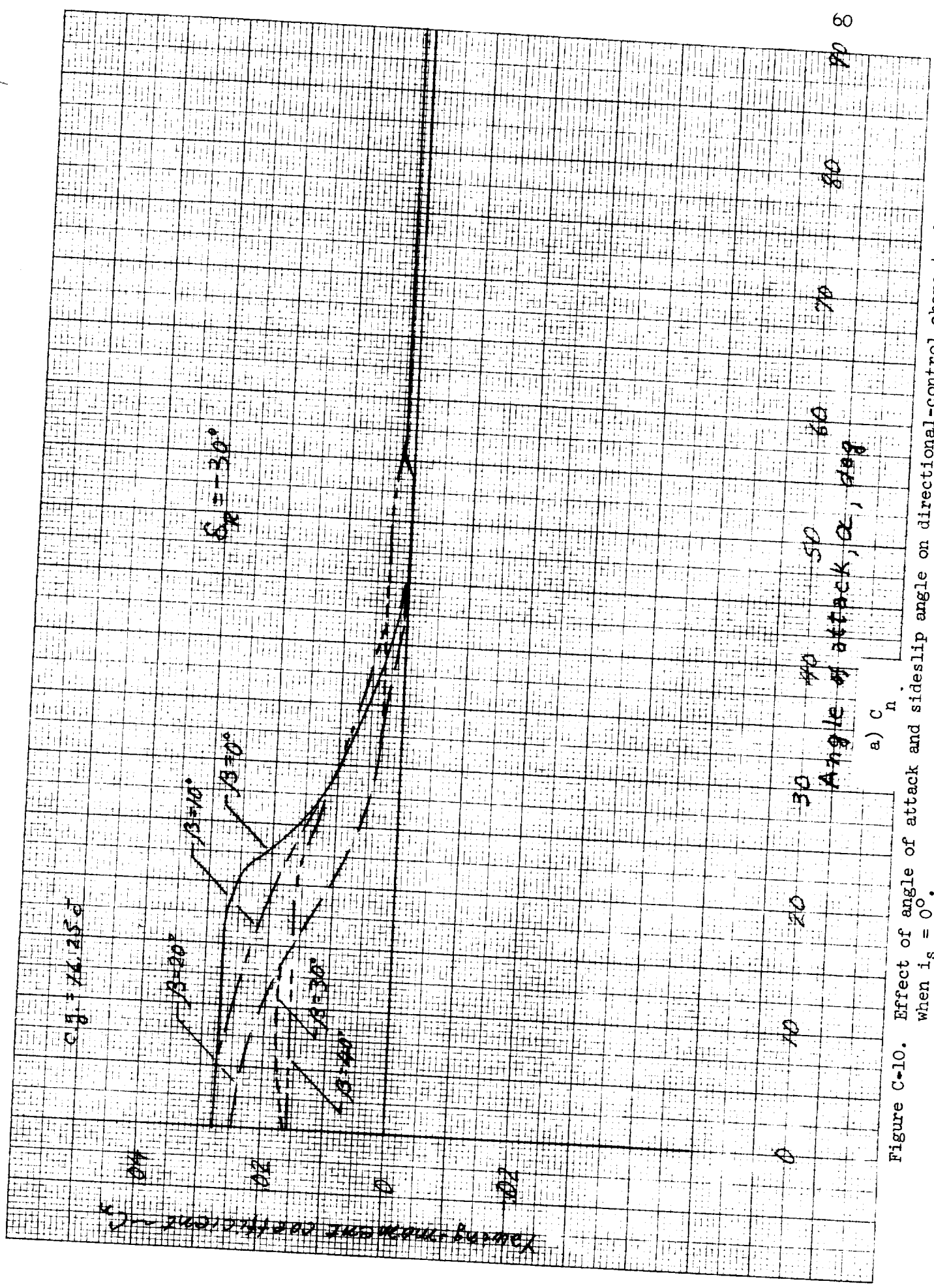


Figure C-10. Effect of angle of attack and sideslip angle on directional-control characteristics when $i_s = 0^\circ$.

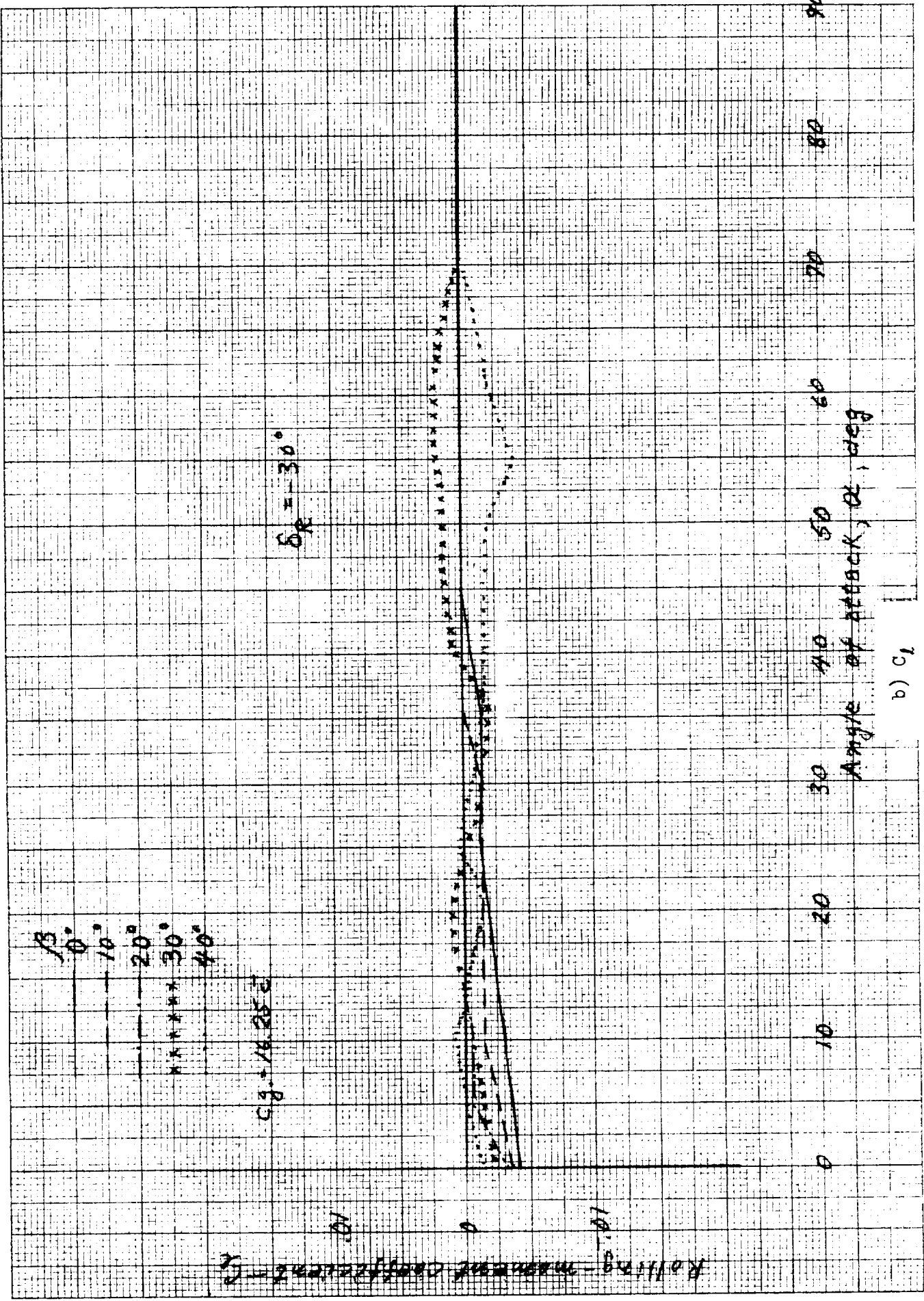
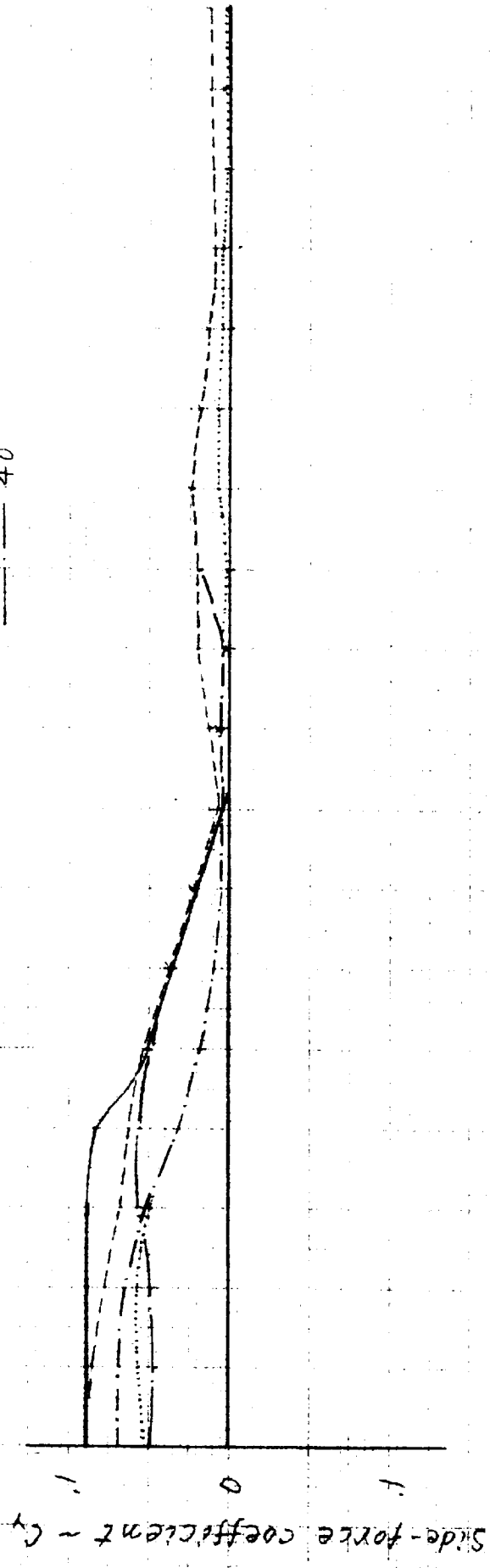


Figure C-10. Continued.

β°
0
10
20
30
40

$C_g = 16.25e$



Angle of attack, α , deg

c) C_y

Figure C-10. Concluded.

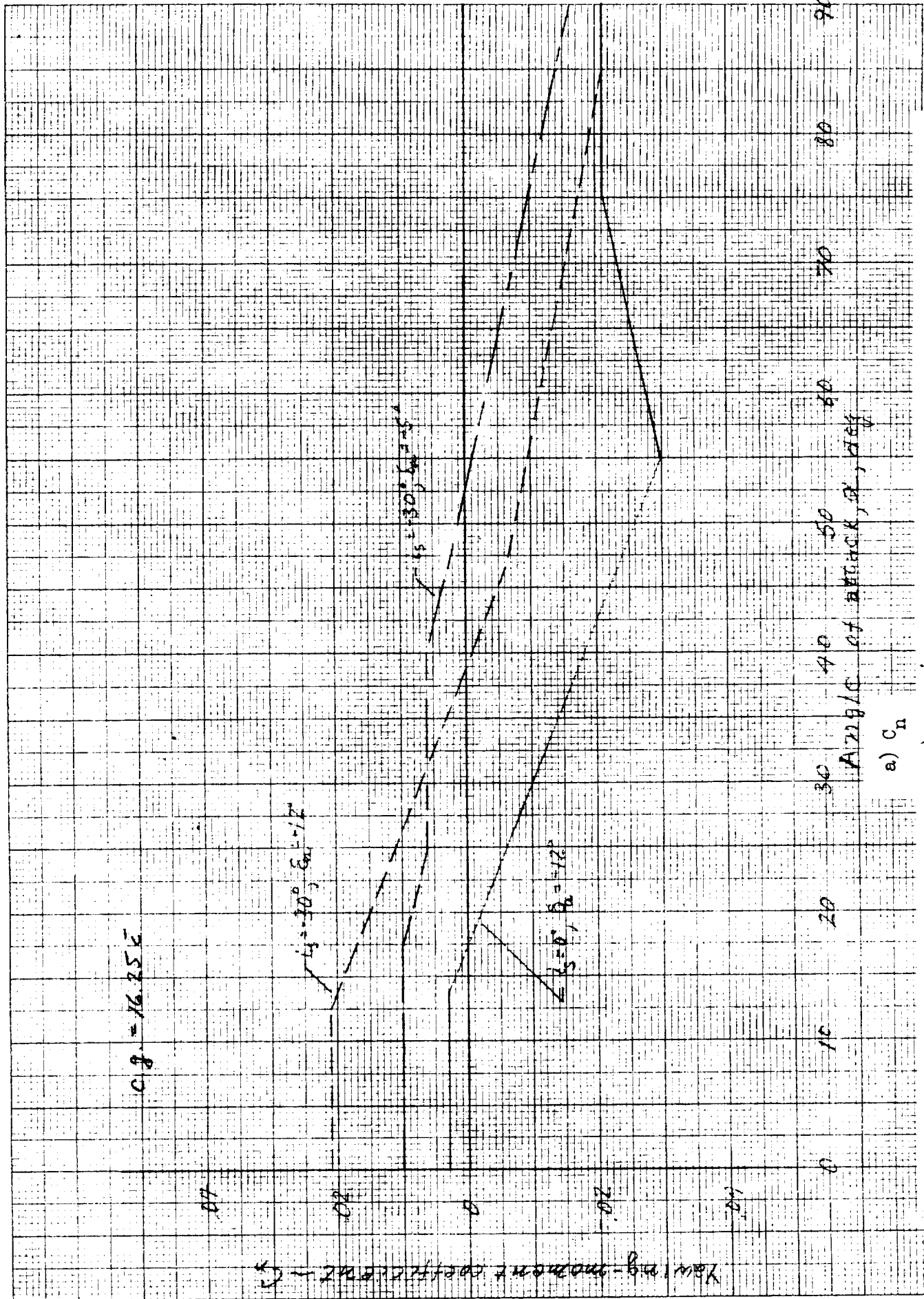


Figure C-11 Effect of angle of attack and sideslip angle on lateral-control characteristics when $i_s = 0^\circ$ and -30° .

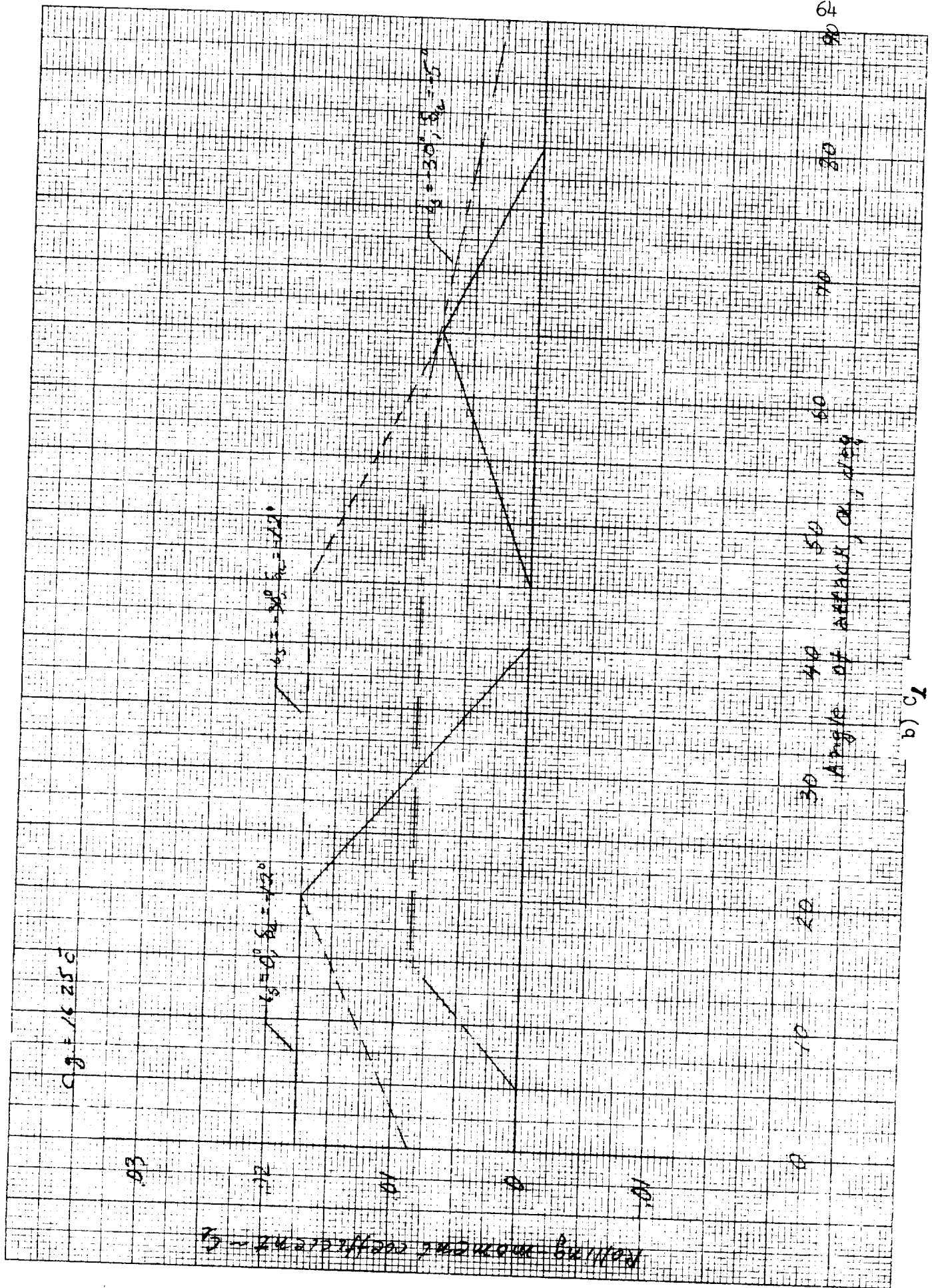
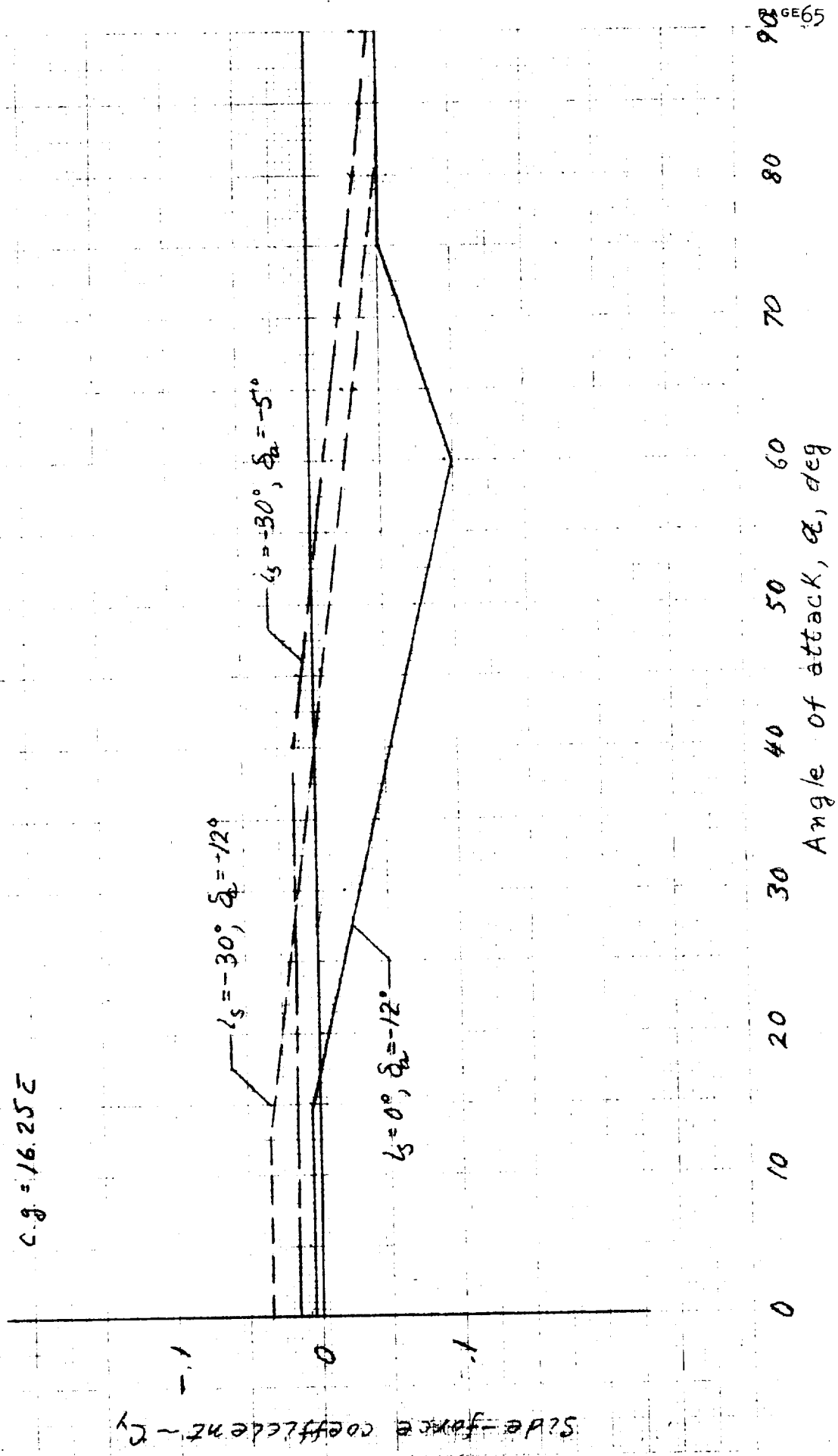


Figure C-11. Continued.



c) C_y
 Figure C-11. Concluded.

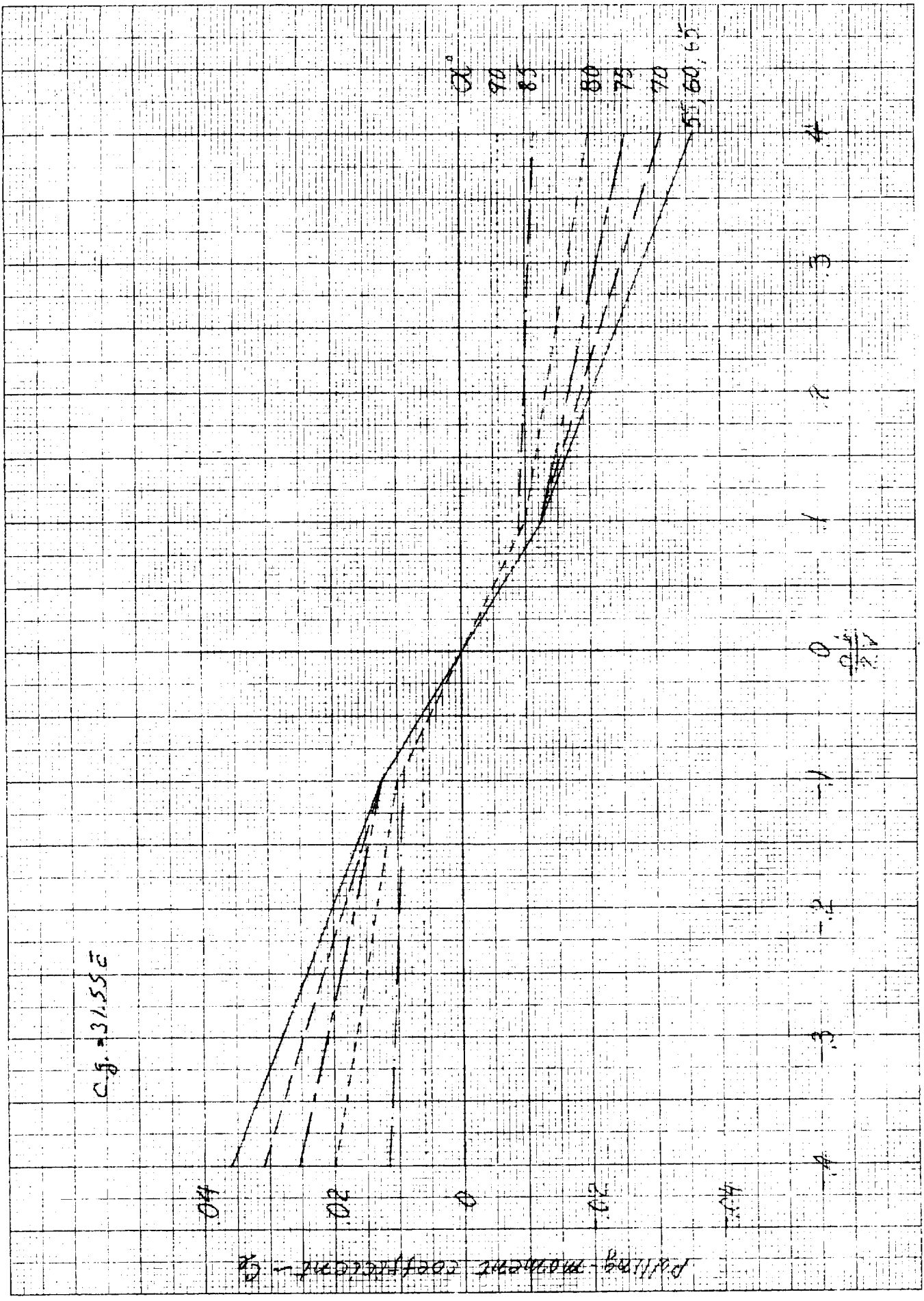


Figure C-13. Effect of rotation rate and angle of attack on rolling-moment coefficient when $i_s = 0^\circ$.

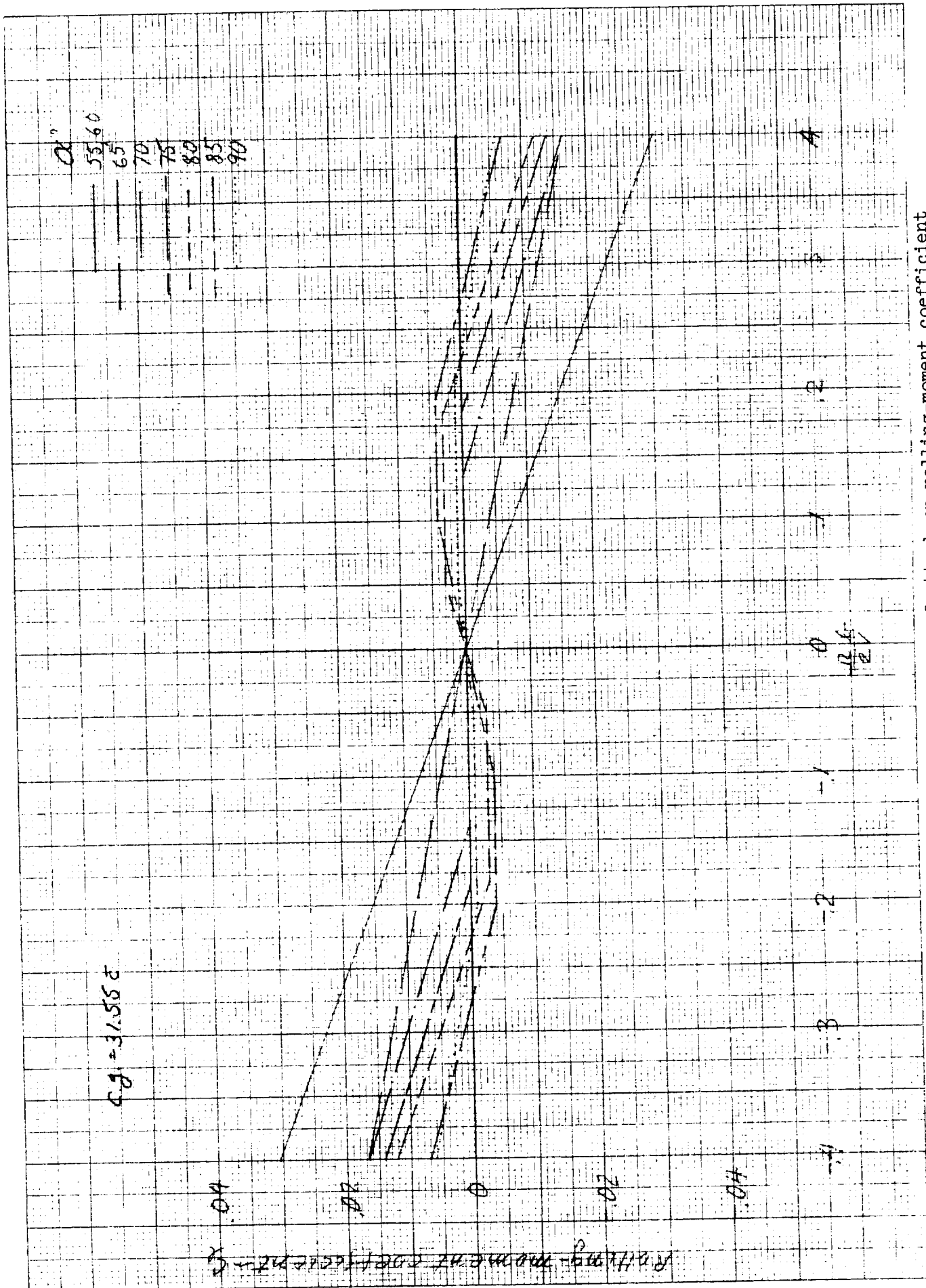


Figure C-14. Effect of rotation rate and angle of attack on rolling-moment coefficient when $i_s = -30^\circ$.

46 1323

K&L
10.7, 10.1, 10.4, 10.8, 10.9, 10.10, 10.11, 10.12, 10.13, 10.14, 10.15, 10.16, 10.17, 10.18, 10.19, 10.20, 10.21, 10.22, 10.23, 10.24, 10.25, 10.26, 10.27, 10.28, 10.29, 10.30, 10.31, 10.32, 10.33, 10.34, 10.35, 10.36, 10.37, 10.38, 10.39, 10.40, 10.41, 10.42, 10.43, 10.44, 10.45, 10.46, 10.47, 10.48, 10.49, 10.50, 10.51, 10.52, 10.53, 10.54, 10.55, 10.56, 10.57, 10.58, 10.59, 10.60, 10.61, 10.62, 10.63, 10.64, 10.65, 10.66, 10.67, 10.68, 10.69, 10.70, 10.71, 10.72, 10.73, 10.74, 10.75, 10.76, 10.77, 10.78, 10.79, 10.80, 10.81, 10.82, 10.83, 10.84, 10.85, 10.86, 10.87, 10.88, 10.89, 10.90, 10.91, 10.92, 10.93, 10.94, 10.95, 10.96, 10.97, 10.98, 10.99, 11.00

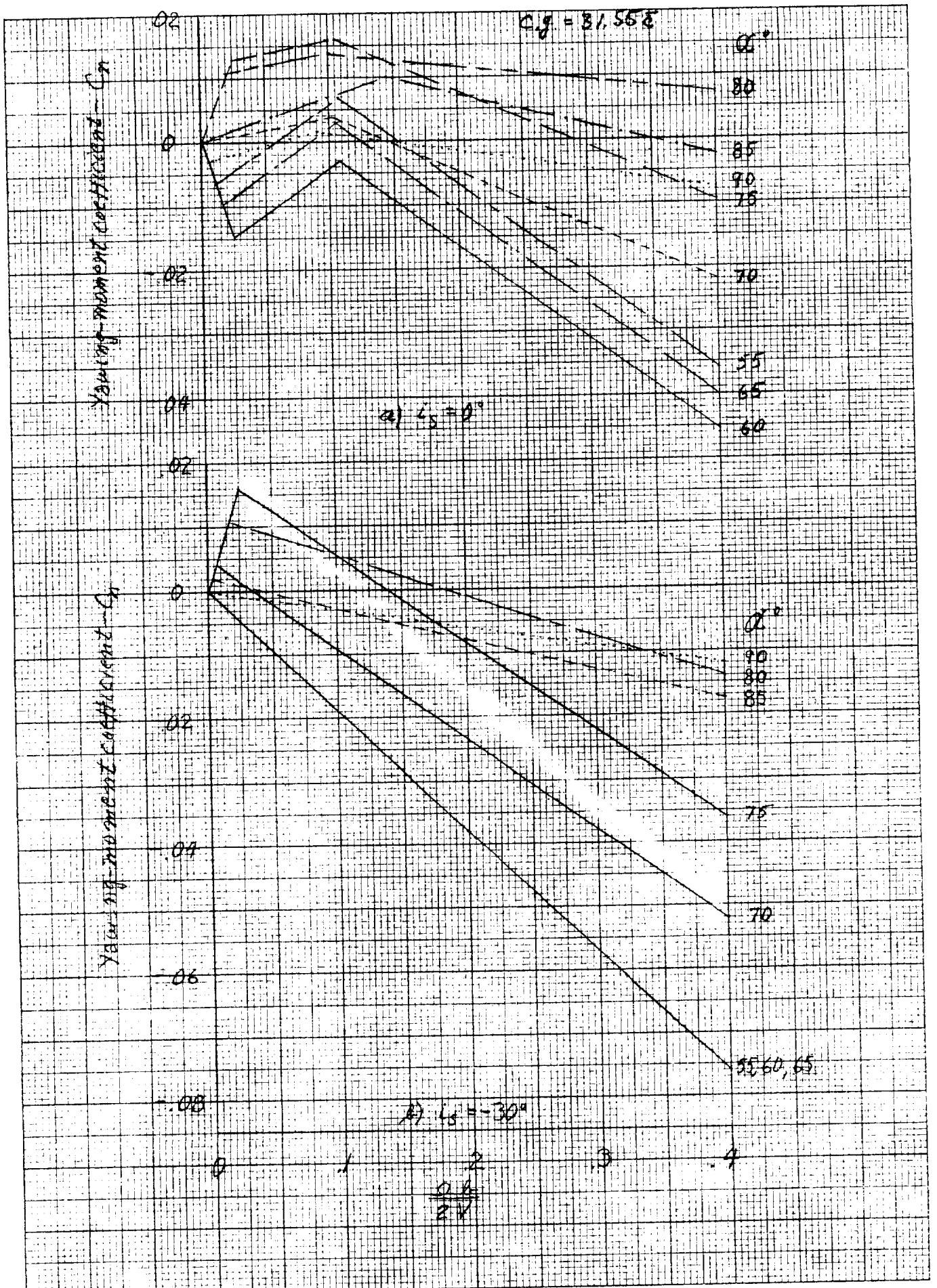


Figure C-15 Effect of rotation rate and angle of attack on yawing-moment coefficient when $i_s = 0^\circ$ and -30° .

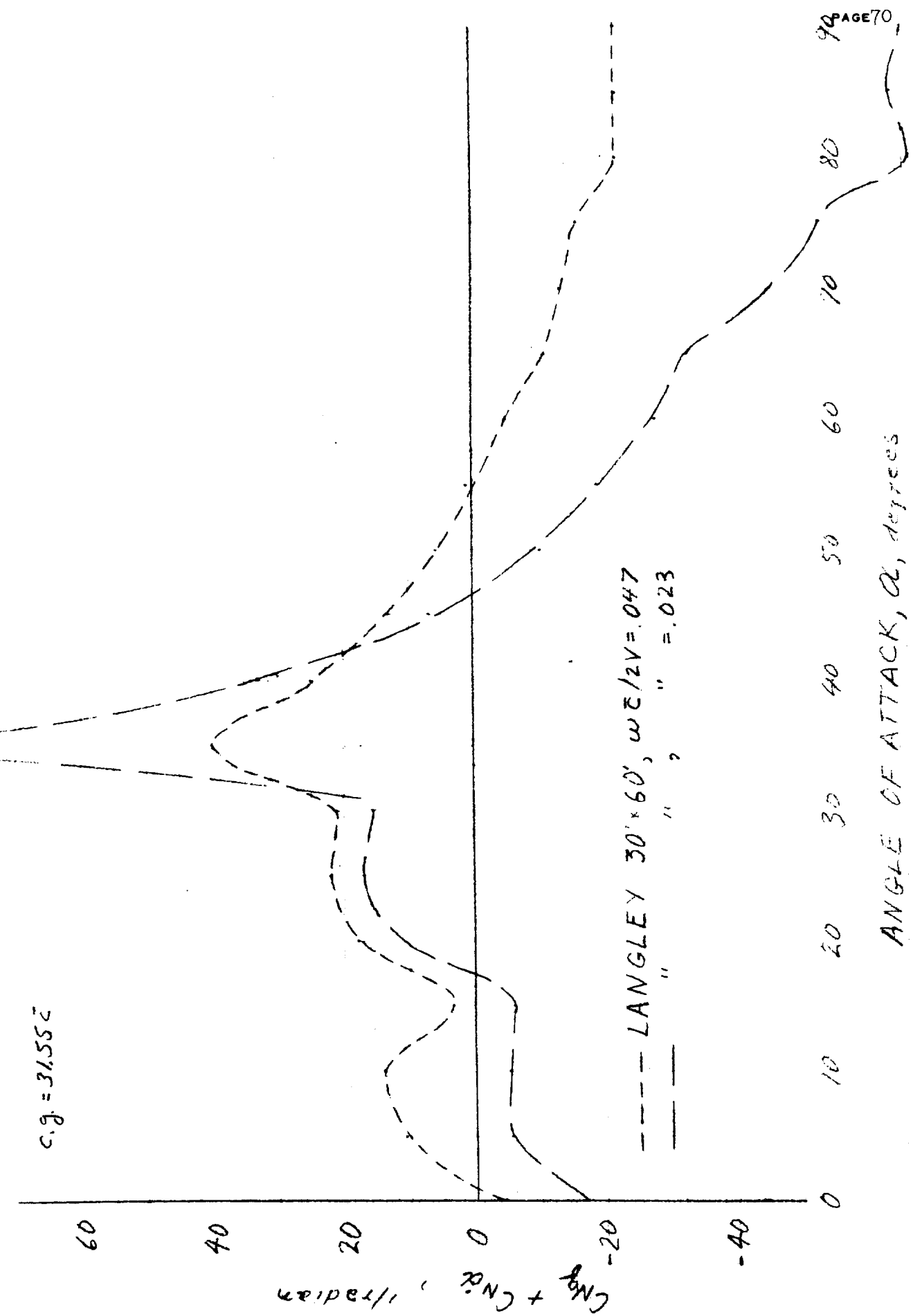


Figure C-16. - Effect of angle of attack and forced-oscillation frequency on normal-force coefficient due to pitch rate.

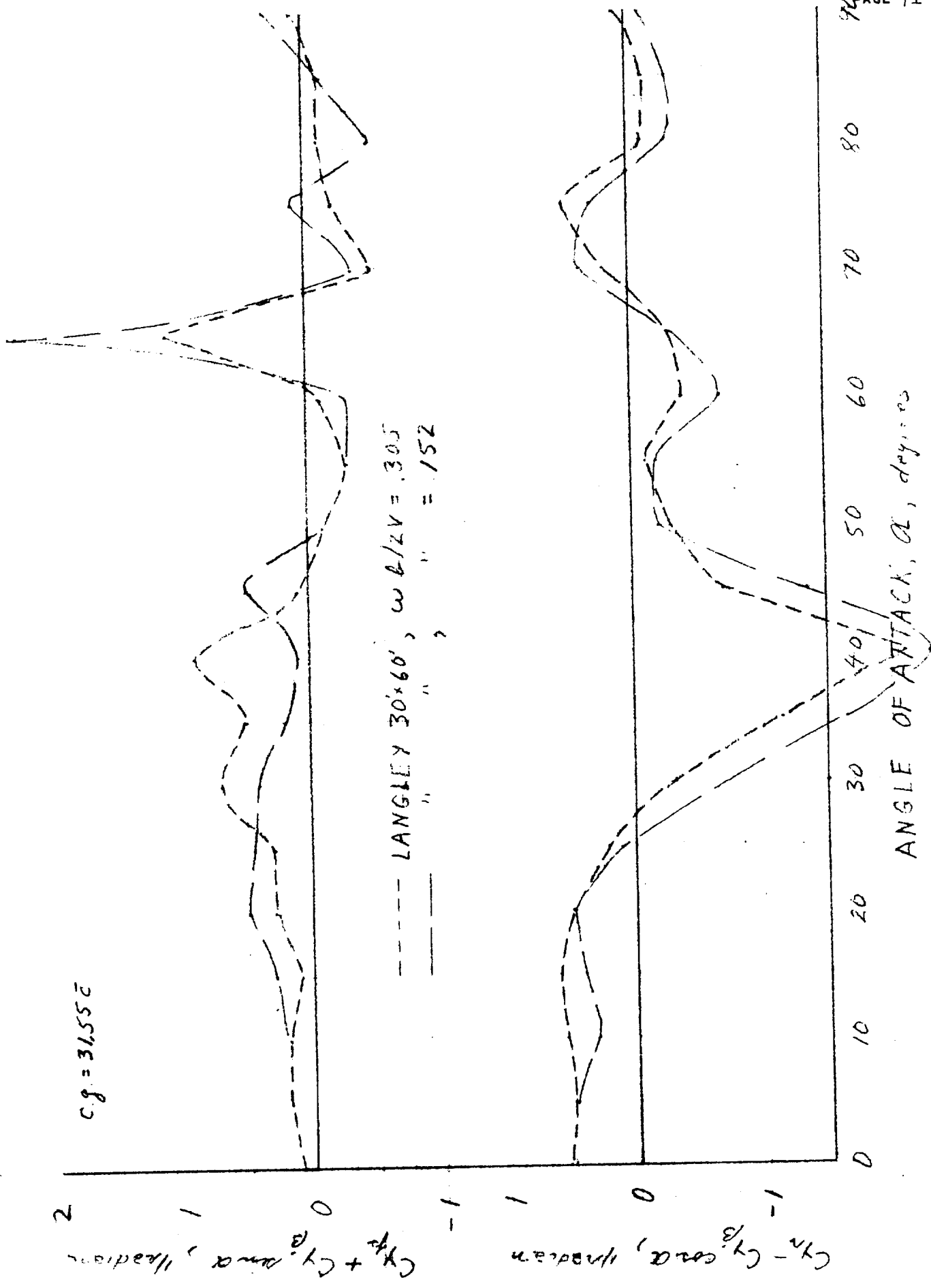
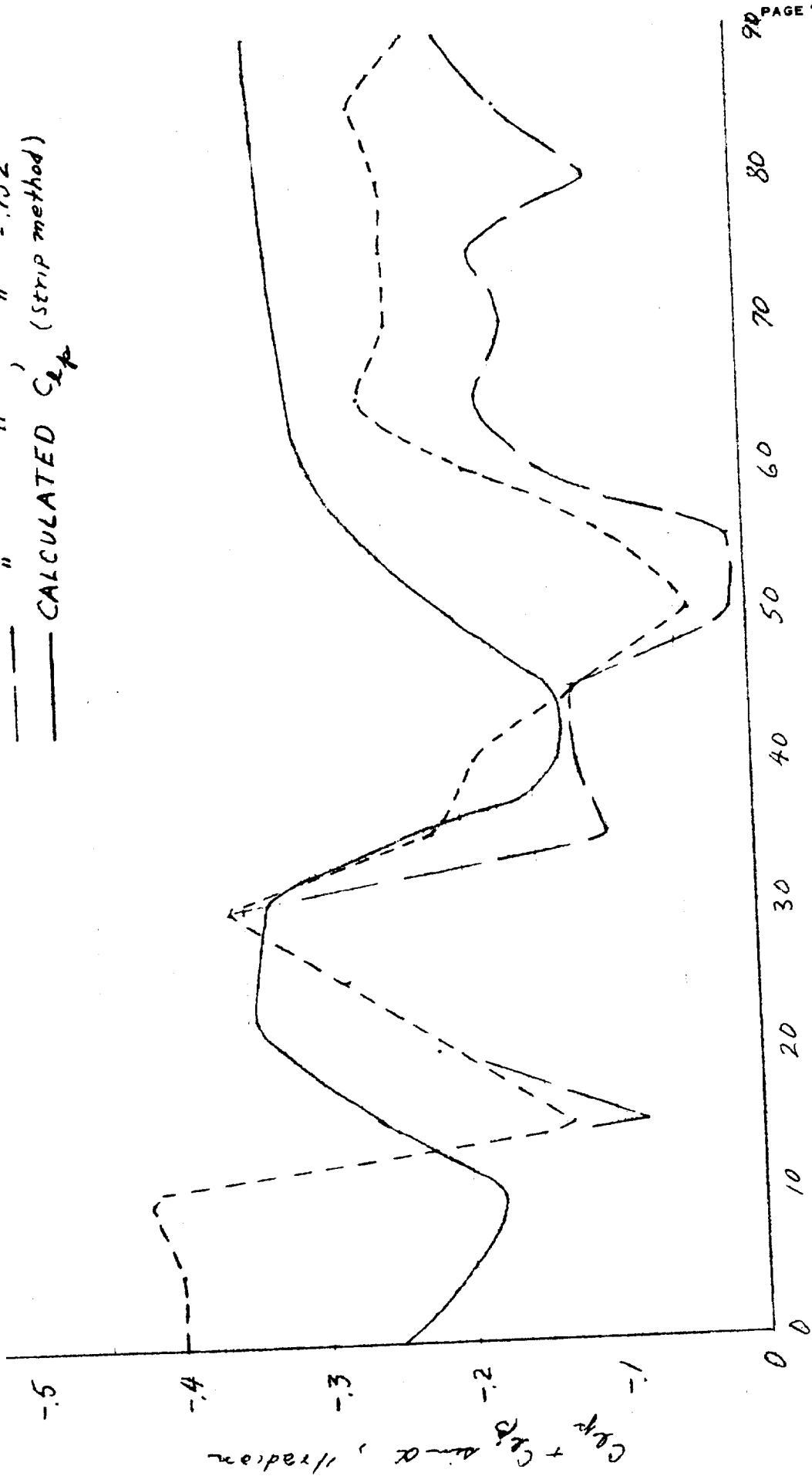


Figure C-17. - Effect of angle of attack and forced-oscillation frequency on side-force coefficient due to roll and yaw rate.

C.G. = 31.55%

--- LANGLEY 30'x60', $wA/RV = .305$
--- " " " " = .152
--- CALCULATED C_{Lp} (strip method)



ANGLE OF ATTACK, α , degrees

b) C_{Lp}

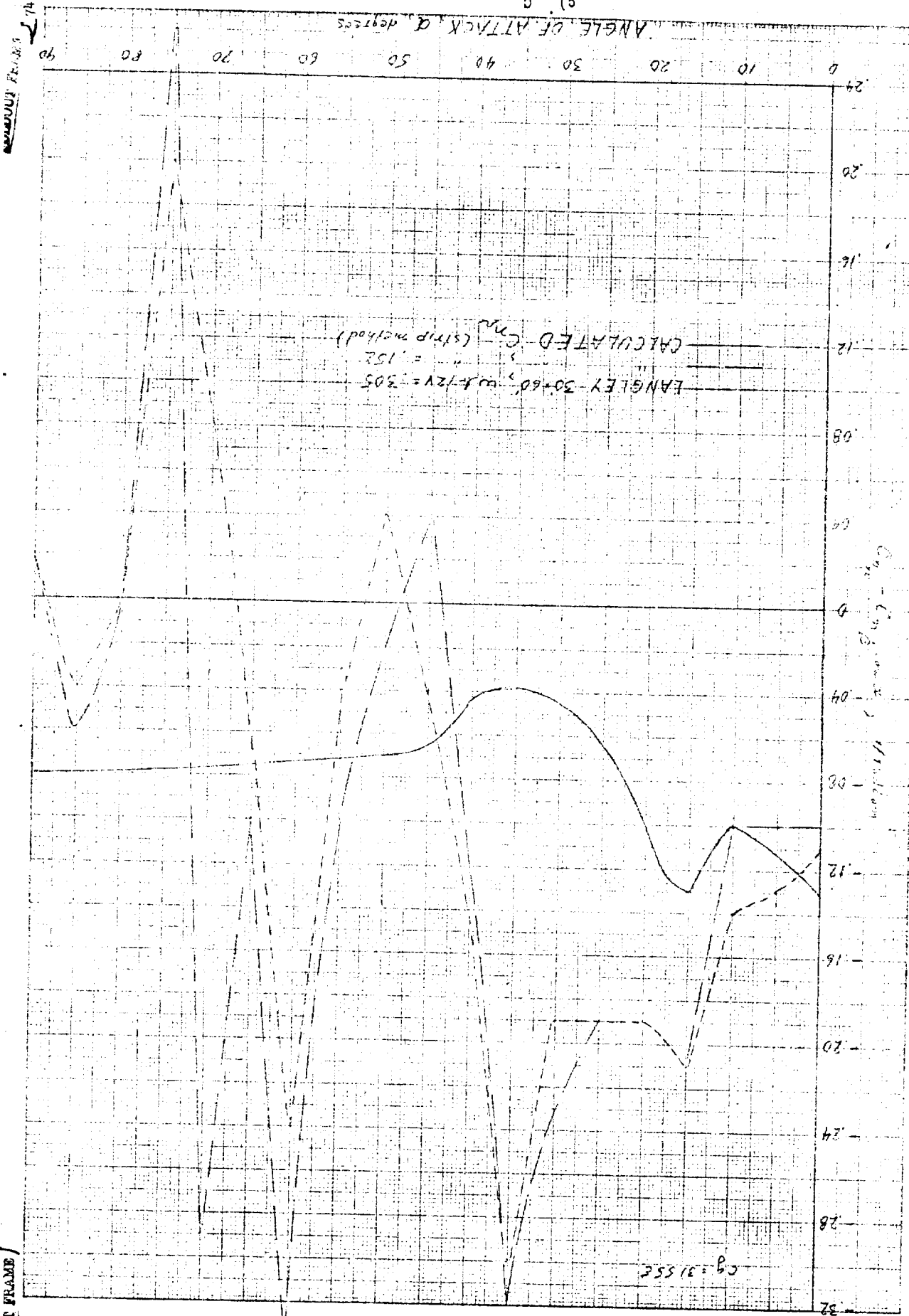
Figure C-18. - Continued.

Figure C-18. - Concluded.

(c) α_n
 ANGLE OF ATTACK α , degrees

LANGLEY-30x60, $\omega = 121 = 305$
 " " " " = 152
 CALCULATED C_m (strip method)

$C_g = 31.55$



FOLDOUT FRAME

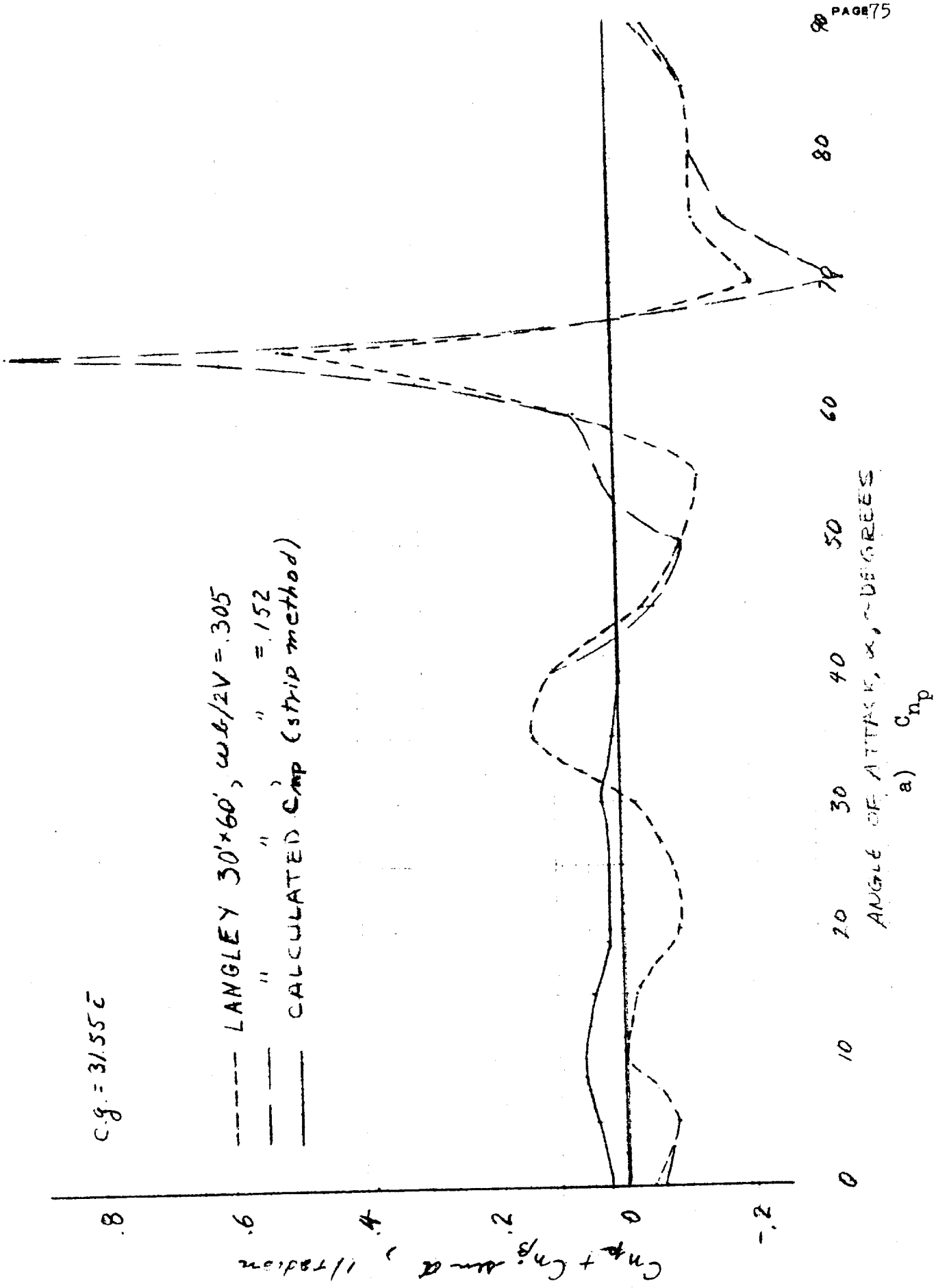


Figure C-19. - Effect of angle of attack and forced-oscillation frequency on cross derivatives.

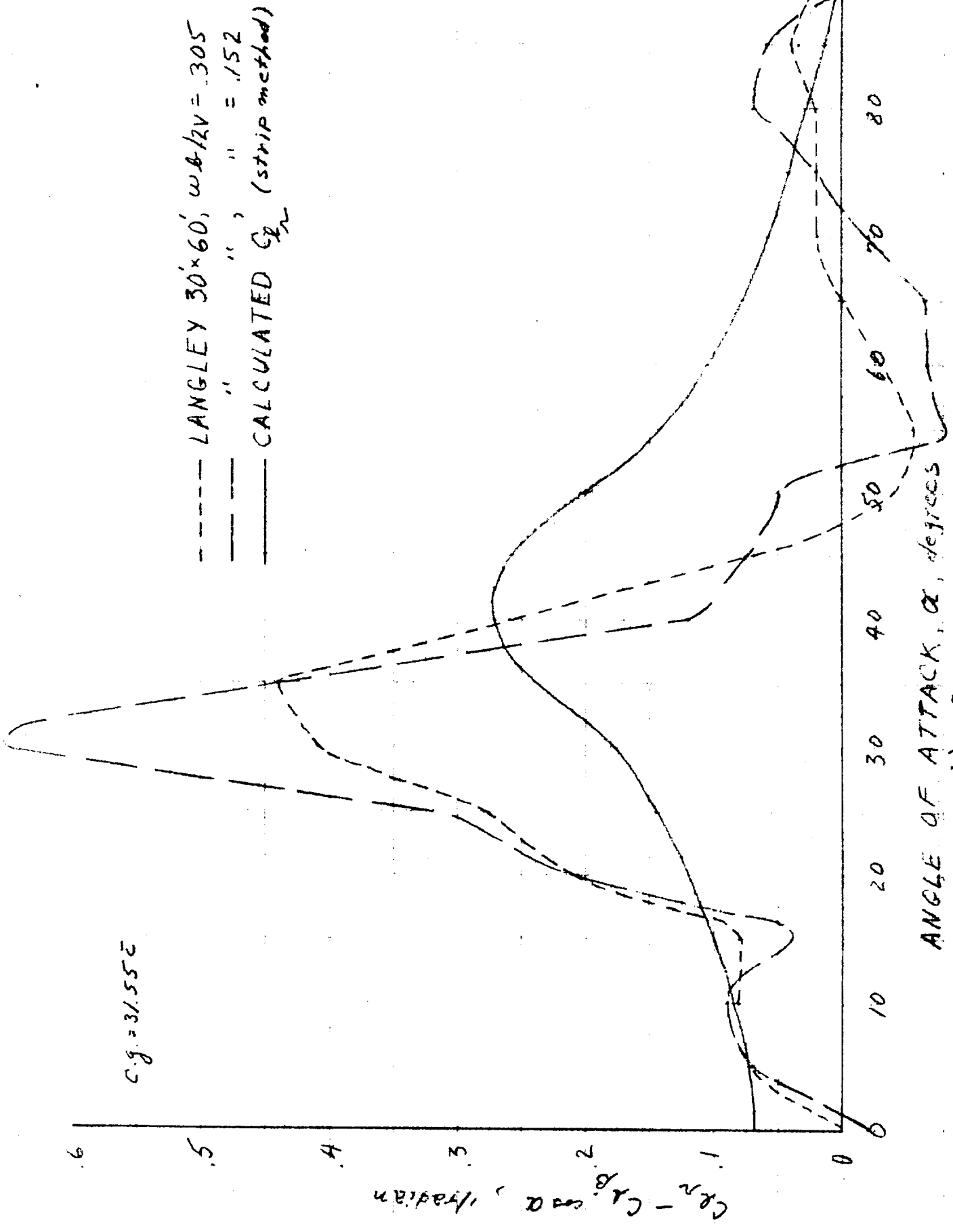


Figure C-19. - Concluded.

APPENDIX D
BASIS OF AERODYNAMIC MODEL

A considerable amount of effort was expended in defining the aerodynamic model presented in Appendix C. This effort basically involved the following three tasks:

- 1) Analyze the Langley full-scale tunnel data to identify the significant parameters affecting the aerodynamic characteristics and extract the most valid model from these data.
- 2) Validate the use of Langley 12-foot data for modeling control characteristics not directly available from Langley full-scale tunnel tests.
- 3) Identify model required to represent rotational rate effects.

Langley Full-Scale Tunnel Data

Figures D-1 through D-7 identify the influence that angle of attack, sideslip angle and control configuration may have on the longitudinal, lateral and directional stability characteristics. It can be seen from these figures that the stability characteristics are significantly effected by α , β and stabilizer deflection and not by the rudder or differential tail setting. The variation of C_l , C_n , and C_y with α and β presented in Appendix C was obtained, therefore, by fairing through the data obtained for the different control configurations associated with a $i_s = 0$ or -30° setting.

The curves of Figures D-4 through D-7 were obtained from Figures D-8 through D-25. These later figures present rolling- and yawing-moment and side-force versus α for various β angles and control configurations. In all instances, the sign of the force or moment was reversed for positive β values. (The closeness of the corresponding positive and negative β data for lateral controls neutral, as well as the data points for $\beta = 0^\circ$ themselves, demonstrate model symmetry.) Curves were then faired between the plotted positive and negative data point. These curves were then assembled and compared in Figures D-4 through D-7. Fairing the data in this manner allows one to eliminate the control

moment and force increments and to examine the effects of control deflection on stability. Therefore, the absolute increments due to control deflections do not appear in Figures D-4 to D-7.

Rudder and differential tail control characteristics at sideslip angles were also determined from these figures by taking at a given α one half the incremental value between corresponding positive and negative sideslip data points from the appropriate control configuration figure. (The value for $\beta = 0^\circ$ could of course be read directly off the figure.) These control characteristics were then compared with the values obtained by subtracting the neutral controls configuration data from the subject control configuration data.

Langley 12-Foot Low Speed Tunnel Data

Given below are the control configurations for which lateral-directional data were available from the Langley full-scale (30'x60') and 12' facilities.

LRC - 30'x 60'			LRC - 12'		
* $i_s = 0^\circ$	$\delta_a = 0^\circ$	$\delta_R = 0^\circ$	$i_s = 0^\circ$	$\delta_a = 0^\circ$	$\delta_R = 0^\circ$
$i_s = 0^\circ$	$\delta_a = -12^\circ$	$\delta_R = 0^\circ$	$i_s = 0^\circ$	$\delta_a = -12^\circ$	$\delta_R = 0^\circ$
$i_s = 0^\circ$	$\delta_a = 0^\circ$	$\delta_R = -30^\circ$	$i_s = 0^\circ$	$\delta_a = 0^\circ$	$\delta_R = -30^\circ$
$i_s = 0^\circ$	$\delta_a = 0^\circ$	$\delta_R = 30^\circ$			
* $i_s = -30^\circ$	$\delta_a = 0^\circ$	$\delta_R = 0^\circ$			
* $i_s = -30^\circ$	$\delta_a = 5^\circ$	$\delta_R = -30^\circ$			
			$i_s = -30^\circ$	$\delta_a = 0^\circ$	$\delta_R = -30^\circ$
			$i_s = -30^\circ$	$\delta_a = 5^\circ$	$\delta_R = 0^\circ$
			$i_s = -30^\circ$	$\delta_a = -5^\circ$	$\delta_R = 0^\circ$
			$i_s = -23^\circ$	$\delta_a = 12^\circ$	$\delta_R = 0^\circ$
			$i_s = -23^\circ$	$\delta_a = -12^\circ$	$\delta_R = 0^\circ$

*Also rotary balance data available from $\alpha = 55$ to 90° .

As can be seen, the isolated effect of rudder and differential tail deflection at

high values of stabilizer setting were not available from the 30'x60' facility. Consequently, it was desired to employ the available 12' control configuration data in this area.

The curves presented in Figures 26 and 27 were prepared using the same technique described above for the Langley full scale (30'x60') data analysis. It can be seen from these figures that, as was the case for the 30'x60' data, the rudder and differential tail did not effect the lateral-directional stability characteristics. However, the rolling and yawing moment characteristics obtained in the 30'x60' and 12' facilities for the identical $i_s = 0^\circ$ control configurations (presented in Figures D-28 and 29, respectively) do not correlate well over some angle of attack regions. That is, less lateral stability in the $\alpha = 25$ to 40° region and less directional stability above $\alpha = 30^\circ$, especially at high β values, is realized in the LRC 12' facility. Obviously, some model-tunnel wall interference effects were encountered with the $\frac{1}{10}$ - scale model. It was decided, therefore, not to use the 12' data directly but to obtain incremental effects due to control deflection and to determine the influence of stabilizer setting on other control characteristics. It was found that rudder control characteristics obtained from both facilities did indeed compare favorably (see Figure D-30) and it was shown that the i_s setting did not influence rudder power (see Figure D-31). The differential tail control power from both facilities was also in good agreement but i_s settings (as shown in Appendix C) had an appreciable influence on the control power.

Rotary Balance Data

Rotary balance data presented in reference 1 for clockwise and counter clockwise rotation $\frac{\Omega}{2V}$ values of .0493, .1030, .1523, .3015, .2553 and .3045 at α and β values of 55, 60, 65, 70, 75, 80, 85 and 90° and 0 and 5° , respectively, were analyzed for the following available control configurations:

$$\begin{aligned}
 i_s, \delta_a, \delta_R &= 0^\circ \\
 i_s &= -30^\circ, \delta_a = 0^\circ, \delta_R = 0^\circ \\
 i_s &= -30^\circ, \delta_a = 5^\circ, \delta_R = -30^\circ \\
 i_s &= -30^\circ, \delta_a = -5^\circ, \delta_R = 30^\circ
 \end{aligned}$$

By connecting the clockwise and counter clockwise data points with a straight line segment, forces and moments at $\frac{\Omega b}{2V} \neq 0$ were determined. The static longitudinal characteristics obtained from the rotary balance data using this procedure are presented in Figure D-32. The $i_s = 0$ and -30° control configuration data of Figure D-32 are compared in Figure D-33 with static test data. It can be seen that although the C_m , C_N and C_c variations with α are approximately the same (also illustrated in Figure D-34 which compares the control characteristics), they are displaced by approximately a constant value. The magnitude of C_m and C_N being less and C_c greater for the coefficients extracted from rotary balance data when compared with the static test data. Since the longitudinal characteristics were invariant for this configuration with rate of rotation, these incremental effects would have been experienced between no rotation and an $\frac{\Omega b}{2V}$ value of .0493 (first test point). This did not seem probable, therefore, these incremental effects were not included in the aerodynamic model. It was found that the lateral and directional stability characteristics were in fair agreement (see Figure D-35) with the values established during the static tests.

The longitudinal characteristics for this model were found to be essentially invariant with rate of rotation and, therefore, it was not necessary to include any effect of rotation rate in the longitudinal aerodynamic model. This was not the case relative to C_n , C_l and C_y . To establish the influence of rotation rate, the $\beta = 0^\circ$ counter clockwise data vs $\frac{\Omega b}{2V}$ were fitted over the clockwise data points and the same procedure was applied separately to the $\beta = 5^\circ$ data. Then the $+\frac{\Omega b}{2V}$ data for $\beta = 5^\circ$ were adjusted by the incremental value obtained between $\beta = 0$ and 5° at $\frac{\Omega b}{2V} = 0$

and superimposed on the $\beta = 0^\circ$ data. Therefore, four sets of data points vs $\frac{\Omega b}{2V}$ were available for each angle of attack and control configuration through which slopes could be drawn. It was found that all the $i_s = -30^\circ$ control configurations has the same rotation rate characteristics which, however, were different from the $i_s = 0^\circ$ characteristics. Consequently, rotation flow models are presented in Appendix C for both $i_s = 0$ and -30° settings.

LIST OF FIGURES

Figure No.	Title	Page
	LANGLEY FULL-SCALE TUNNEL DATA	
D-1	Effect of control configuration on longitudinal characteristics, $\beta=0^\circ$.	
	a) C_N	87
	b) C_m	88
	c) C_c	89
D-2	Effect of sideslip angle on normal-force coefficient for various control configurations.	
	a) $i_s, \delta_a, \delta_R = 0^\circ$ (See Figure C-1)	50
	b) $i_s = -30^\circ, \delta_a, \delta_R = 0^\circ$ (See Figure C-2)	51
	c) $i_s = -30^\circ, \delta_a = 5^\circ, \delta_R = -30^\circ$	90
D-3	Effect of sideslip angle on pitching-moment coefficient for various control configurations.	
	a) $i_s, \delta_a, \delta_R = 0^\circ$	91
	b) $i_s = -30^\circ, \delta_a, \delta_R = 0^\circ$	92
	c) $i_s = -30^\circ, \delta_a = 5^\circ, \delta_R = -30^\circ$	93
D-4	Effect of $i_s=0^\circ$ control configurations on yawing-moment characteristics.	
	a) $\beta = 10^\circ, 20^\circ$	94
	b) $\beta = 30^\circ, 40^\circ$	95
D-5	Effect of $i_s = -30^\circ$ control configurations on yawing moment characteristics.	
	a) $\beta=10^\circ, 20^\circ$	96
	b) $\beta=30^\circ, 40^\circ$	97
D-6	Effect of control configuration on rolling-moment characteristics.	
	a) $i_s = 0^\circ$ configurations	98
	b) $i_s = -30^\circ$ configurations	99
D-7	Effect of control configuration on side-force characteristics.	
	a) $i_s = 0^\circ$ configurations	100
	b) $i_s = -30^\circ$ configurations	101

LIST OF FIGURES (Continued)

Figure No.	Title	Page
D-8	Effect of angle of attack and sideslip angle on yawing-moment coefficient for configuration i_s , δ_a , $\delta_R = 0^\circ$.	
	a) $\beta = 0^\circ, \pm 10^\circ, \pm 20^\circ$	102
	b) $\beta = 0^\circ, \pm 30^\circ, \pm 40^\circ$	103
D-9	Effect of angle of attack and sideslip angle on yawing-moment coefficient for configuration $i_s = -30^\circ$; $\delta_a, \delta_R = 0^\circ$.	
	a) $\beta = 0^\circ, \pm 10^\circ, \pm 20^\circ$	104
	b) $\beta = 0^\circ, \pm 30^\circ, \pm 40^\circ$	105
D-10	Effect of angle of attack and sideslip angle on yawing-moment coefficient for configuration $i_s, \delta_R = 0^\circ$; $\delta_a = -12^\circ$.	
	a) $\beta = 0^\circ, \pm 10^\circ, \pm 20^\circ$	106
	b) $\beta = 0^\circ, \pm 30^\circ, \pm 40^\circ$	107
D-11	Effect of angle of attack and sideslip angle on yawing-moment coefficient for configuration $i_s = -30^\circ, \delta_a = 5^\circ, \delta_R = -30^\circ$.	
	a) $\beta = 0^\circ, \pm 10^\circ, \pm 20^\circ$	108
	b) $\beta = 0^\circ, \pm 30^\circ, \pm 40^\circ$	109
D-12	Effect of angle of attack and sideslip angle on yawing-moment coefficient for configuration $i_s, \delta_a = 0^\circ$; $\delta_R = 30^\circ$.	
	a) $\beta = 0^\circ, \pm 10^\circ, \pm 20^\circ$	110
	b) $\beta = 0^\circ, \pm 30^\circ, \pm 40^\circ$	111
D-13	Effect of angle of attack and sideslip angle on yawing-moment coefficient for configuration $i_s, \delta_a = 0^\circ$; $\delta_R = -30^\circ$.	
	a) $\beta = 0^\circ, \pm 10^\circ, \pm 20^\circ$	112
	b) $\beta = 0^\circ, \pm 30^\circ, \pm 40^\circ$	113
D-14	Effect of angle of attack and sideslip angle on rolling-moment coefficient for configuration $i_s, \delta_a, \delta_R = 0^\circ$.	114

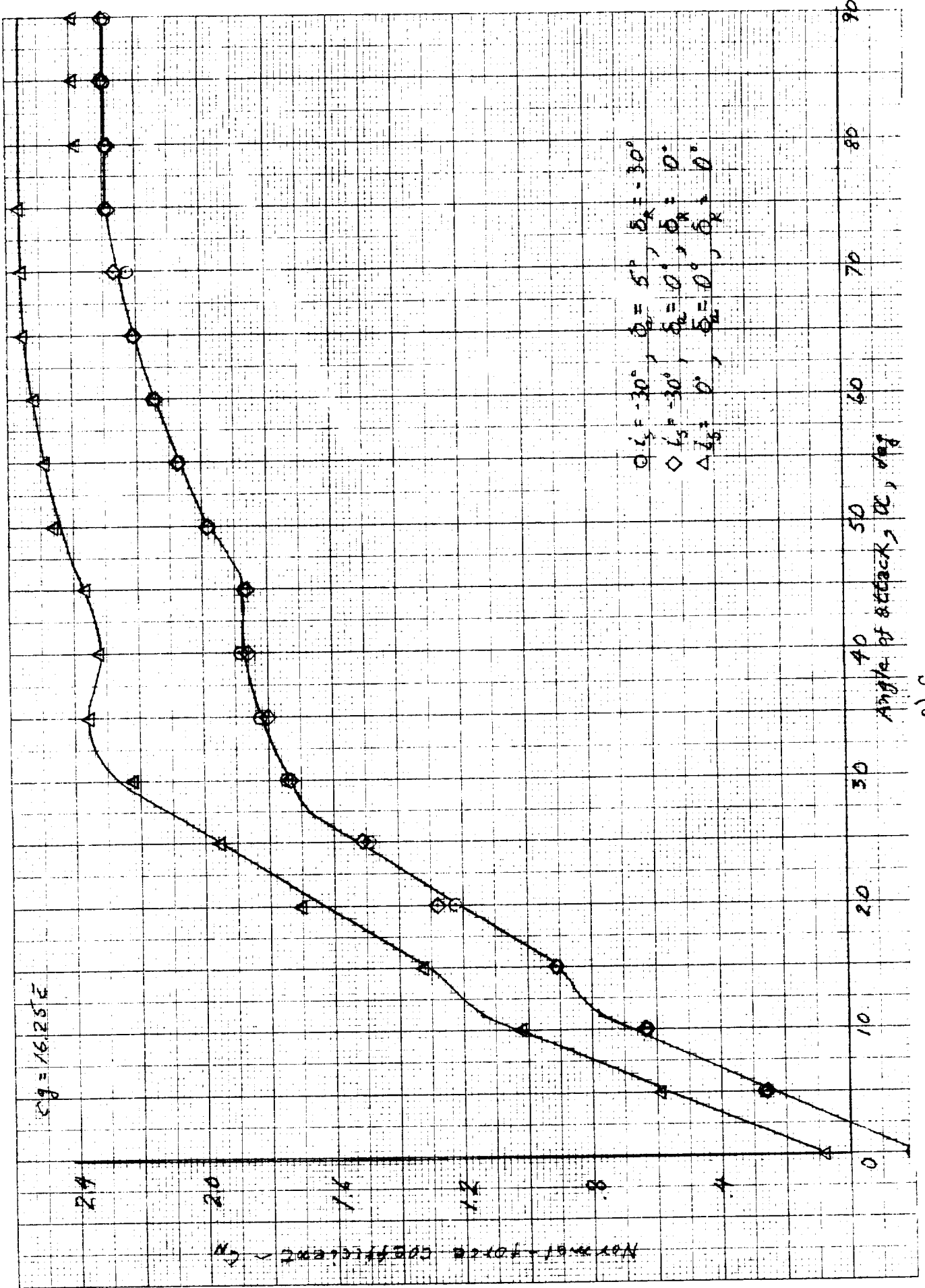
LIST OF FIGURES (Continued)

Figure No.	Title	Page
D-15	Effect of angle of attack and sideslip angle on rolling-moment coefficient for configuration $i_s = -30^\circ$; $\delta_a, \delta_R = 0^\circ$.	115
D-16	Effect of angle of attack and sideslip angle on rolling-moment coefficient for configuration $i_s, \delta_R = 0^\circ$; $\delta_a = -12^\circ$.	116
D-17	Effect of angle of attack and sideslip angle on rolling-moment coefficient for configuration $i_s = -30, \delta_a = 5^\circ, \delta_R = -30^\circ$.	117
D-18	Effect of angle of attack and sideslip angle on rolling-moment coefficient for configuration $i_s, \delta_a = 0^\circ; \delta_R = 30^\circ$.	118
D-19	Effect of angle of attack and sideslip angle on rolling-moment coefficient for configuration $i_s, \delta_a = 0^\circ; \delta_R = -30^\circ$.	119
D-20	Effect of angle of attack and sideslip angle on side-force coefficient for configuration $i_s, \delta_a, \delta_R = 0^\circ$.	120
D-21	Effect of angle of attack and sideslip angle on side-force coefficient for configuration $i_s = -30^\circ; \delta_a, \delta_R = 0^\circ$.	121
D-22	Effect of angle of attack and sideslip angle on side-force coefficient for configuration $i_s, \delta_R = 0^\circ; \delta_a = 12^\circ$.	122
D-23	Effect of angle of attack and sideslip angle on side-force coefficient for configuration $i_s = -30, \delta_a = 5^\circ, \delta_R = -30^\circ$.	123
D-24	Effect of angle of attack and sideslip angle on side-force coefficient for configuration $i_s, \delta_a = 0^\circ; \delta_R = 30^\circ$.	124
D-25	Effect of angle of attack and sideslip angle on side-force coefficient for configuration $i_s, \delta_a = 0^\circ; \delta_R = -30^\circ$.	125
	LANGLEY 12-FOOT LOW SPEED TUNNEL DATA	
D-26	Effect of control configuration on yawing-moment characteristics.	
	a) $i_s = 0^\circ$ configurations	126
	b) i_s deflected configurations	127

LIST OF FIGURES (Continued)

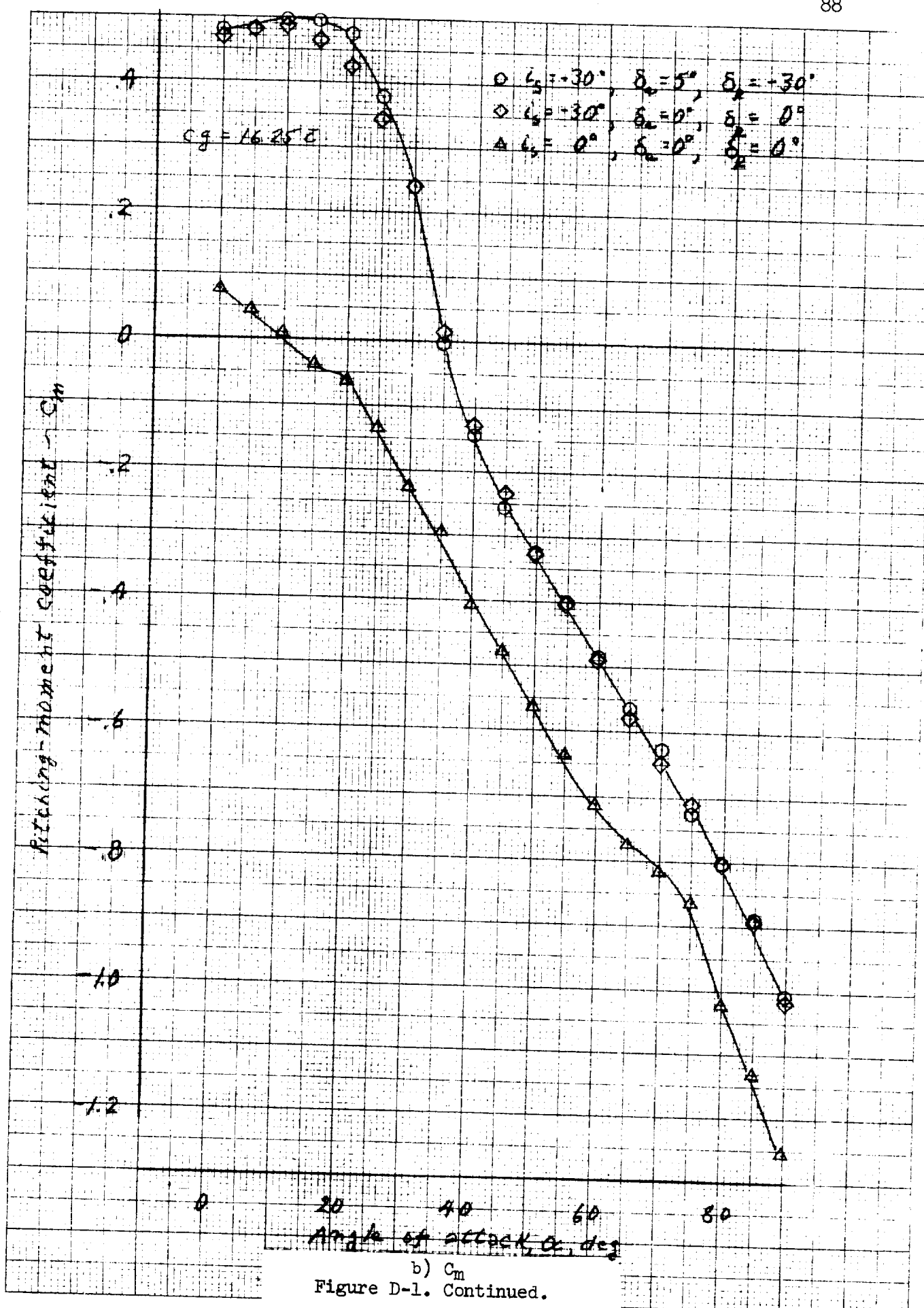
Figure No.	Title	Page
D-27	Effect of control configuration on rolling-moment characteristics.	
	a) $i_s = 0^\circ$ configurations	128
	b) i_s deflected configuration	129
D-28	Comparison between rolling-moment characteristics obtained in LRC 30' x 60' and 12' facilities for various control configurations.	
	a) $i_s, \delta_a, \delta_R = 0^\circ$	130
	b) $i_s, \delta_a = 0^\circ; \delta_R = -30^\circ$	131
	c) $i_s = 0^\circ, \delta_a = -12^\circ, \delta_R = 0^\circ$	132
D-29	Comparison between yawing-moment characteristics obtained in LRC 30' x 60' and 12' facilities for various control configurations.	
	a) $i_s, \delta_a, \delta_R = 0^\circ$	133
	b) $i_s, \delta_a = 0^\circ; \delta_R = -30^\circ$	134
	c) $i_s = 0^\circ, \delta_a = -12^\circ, \delta_R = 0^\circ$	135
D-30	Comparison between rudder effectiveness obtained in LRC 30' x 60' and 12' facilities. $\delta_R = -30^\circ$.	136
D-31	Comparison between rudder effectiveness obtained at different stabilizer incidence in LRC 12' facility. $\delta_R = -30^\circ$.	137
LANGLEY FULL-SCALE TUNNEL ROTARY BALANCE DATA		
D-32	Static longitudinal characteristics obtained from rotation balance data faired through $\frac{Qb}{2V} = 0$ for various control configurations.	
	a) C_N	138
	b) C_c	139
	c) C_m	140
D-33	Comparison between static longitudinal characteristics obtained	

		Page
	from static and rotation balance data at a stabilizer incidence of 0 and 30°.	
	a) C_N	141
	b) C_c	142
	c) C_m	143
D-34	Comparison between static longitudinal control power obtained from static and rotation balance data.	144
D-35	Comparison between static lateral-directional characteristics obtained from static and rotation balance data. $i_s = -30^\circ$.	145

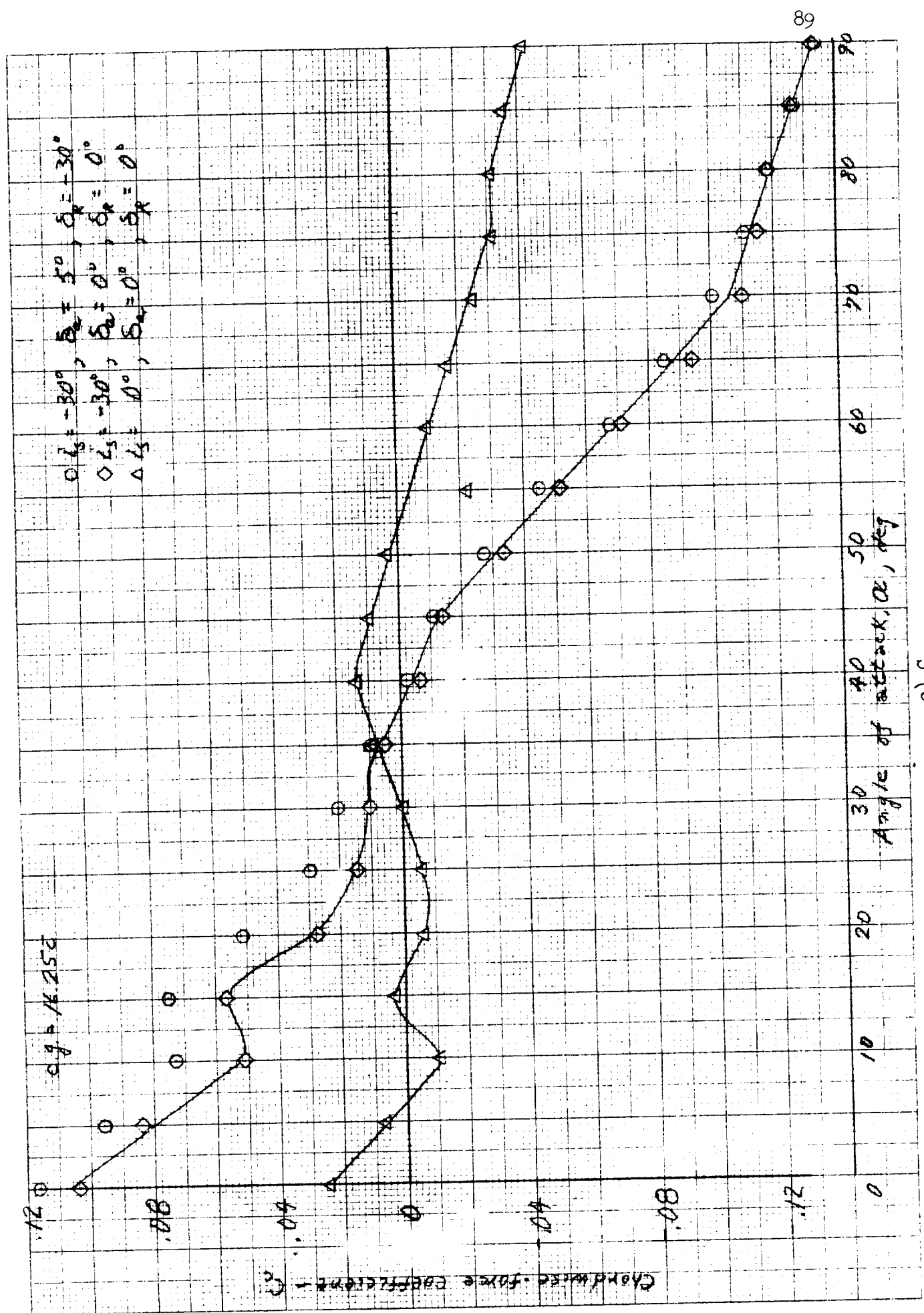


e) CN Figure D-1. Effect of control configuration on longitudinal characteristics, $\beta = 0^\circ$.

46 1327



b) C_m
Figure D-1. Continued.



c) C_c
Figure D-1. Concluded.

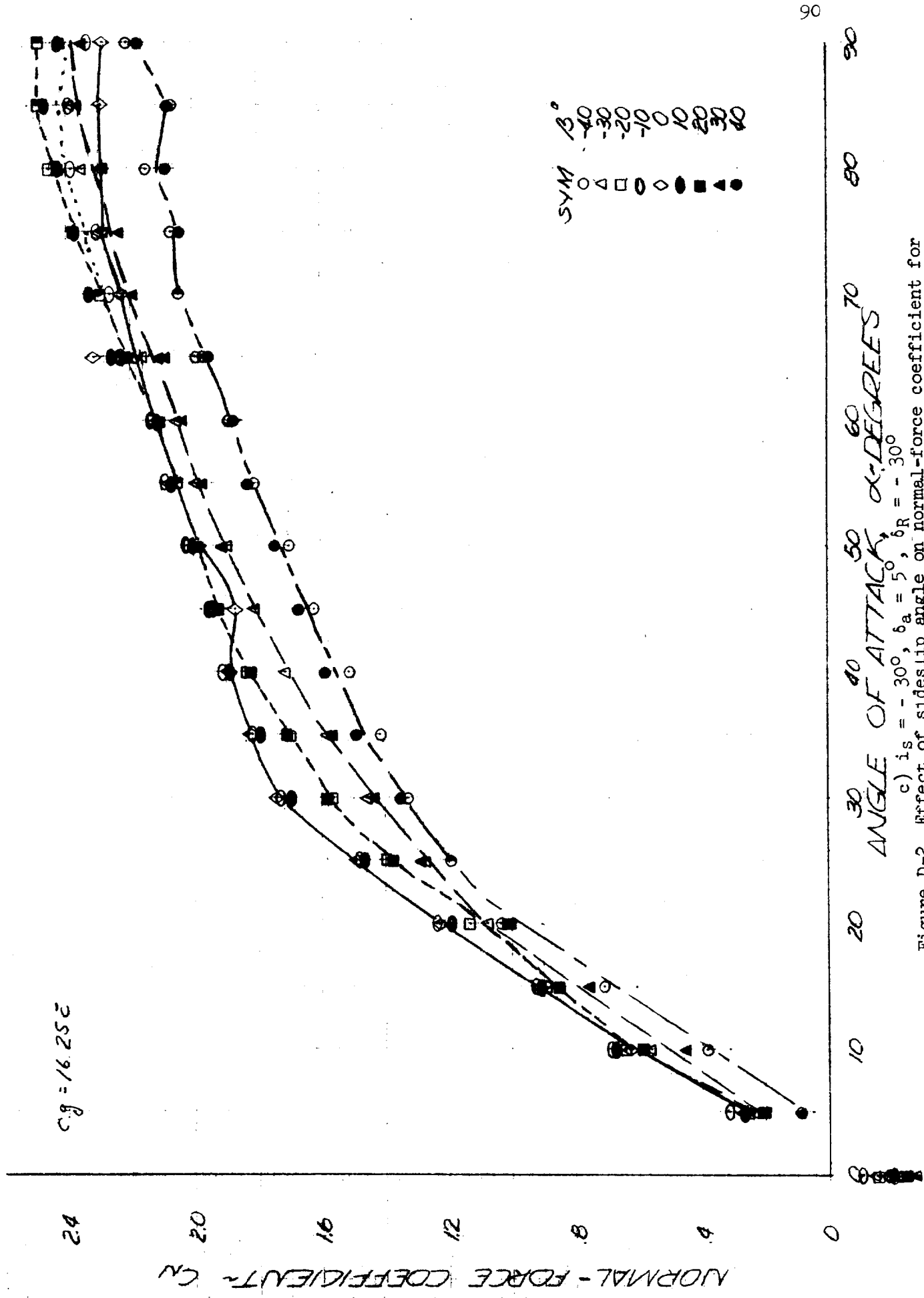


Figure D-2. Effect of sideslip angle on normal-force coefficient for various control configurations.

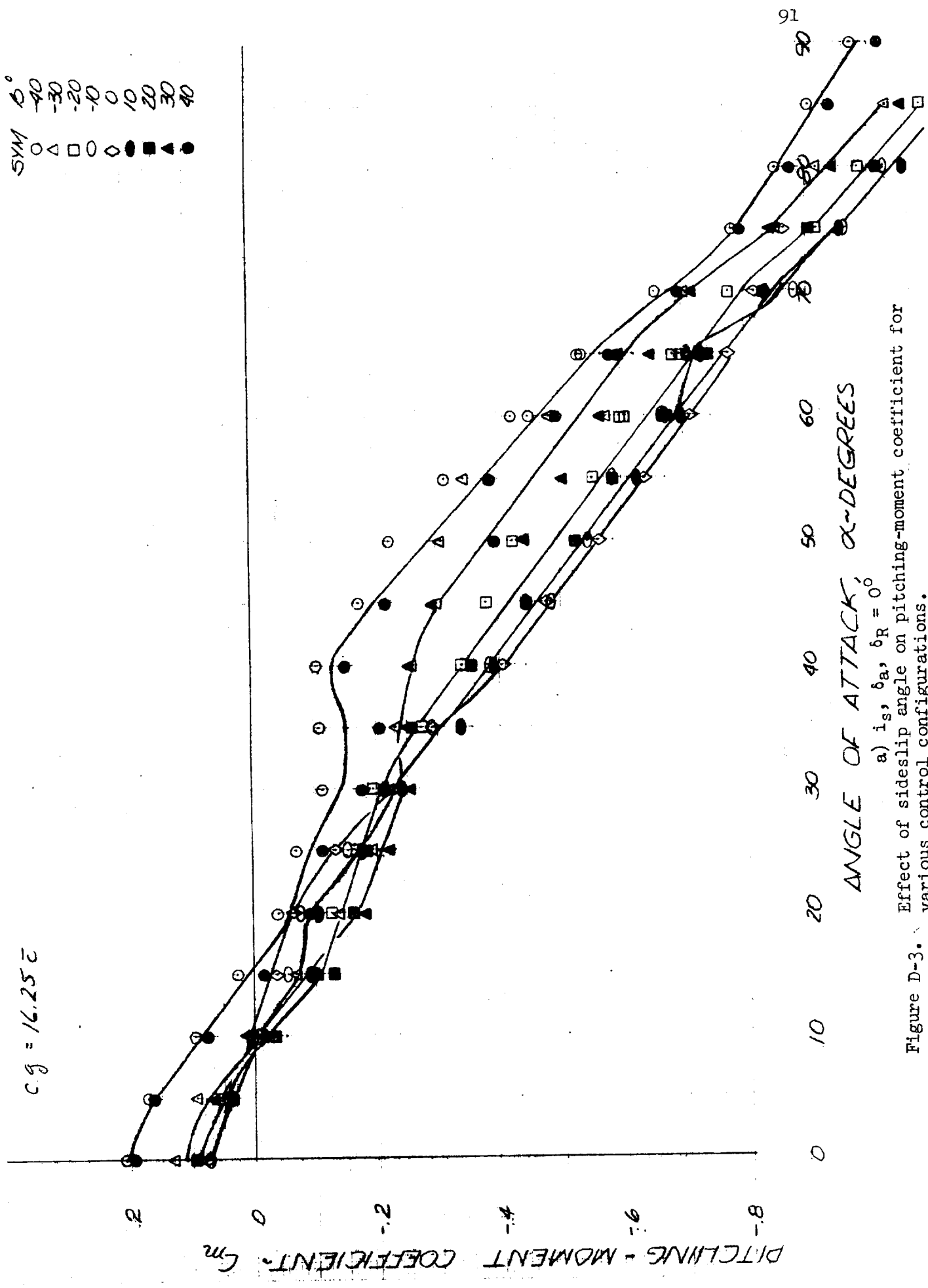
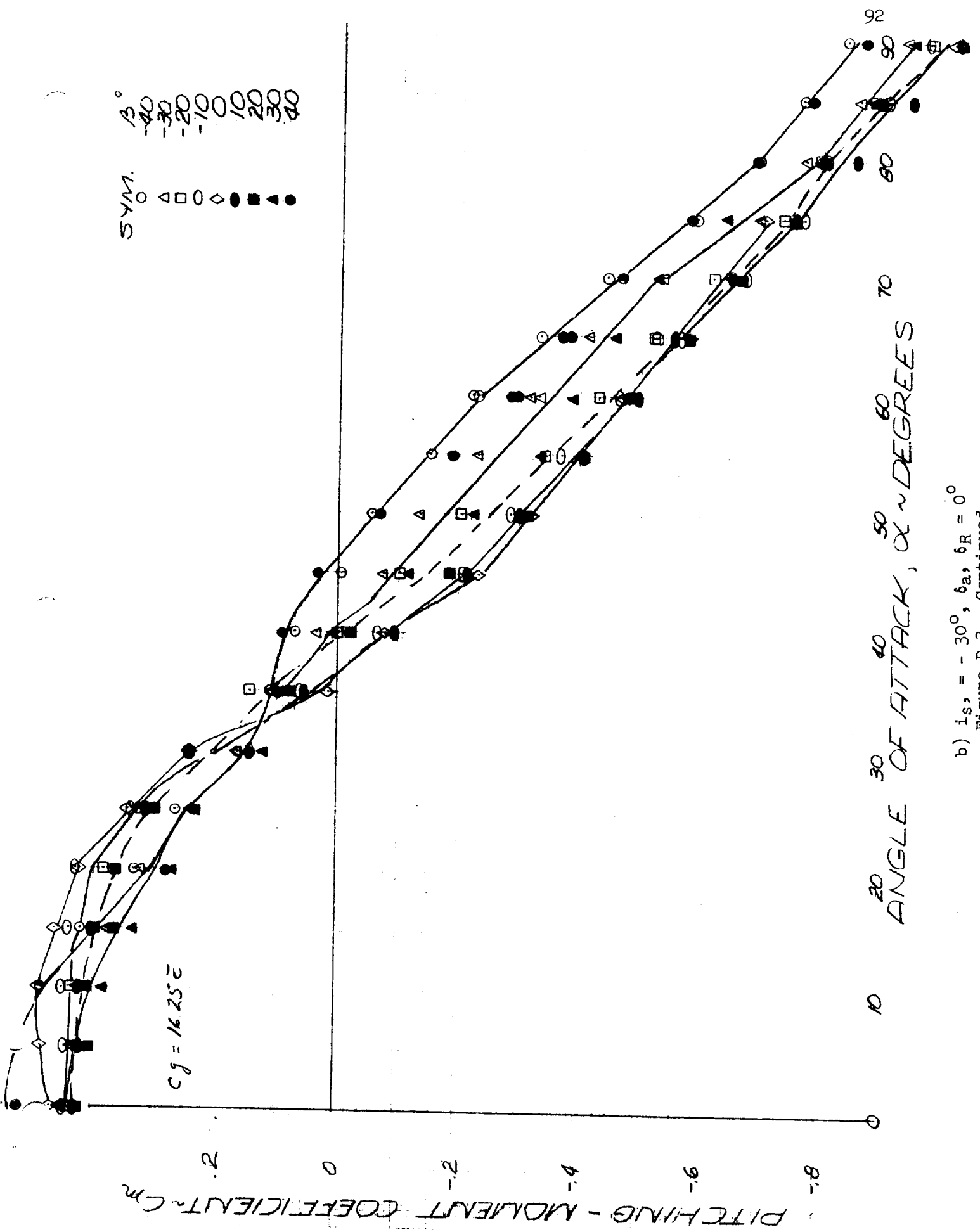
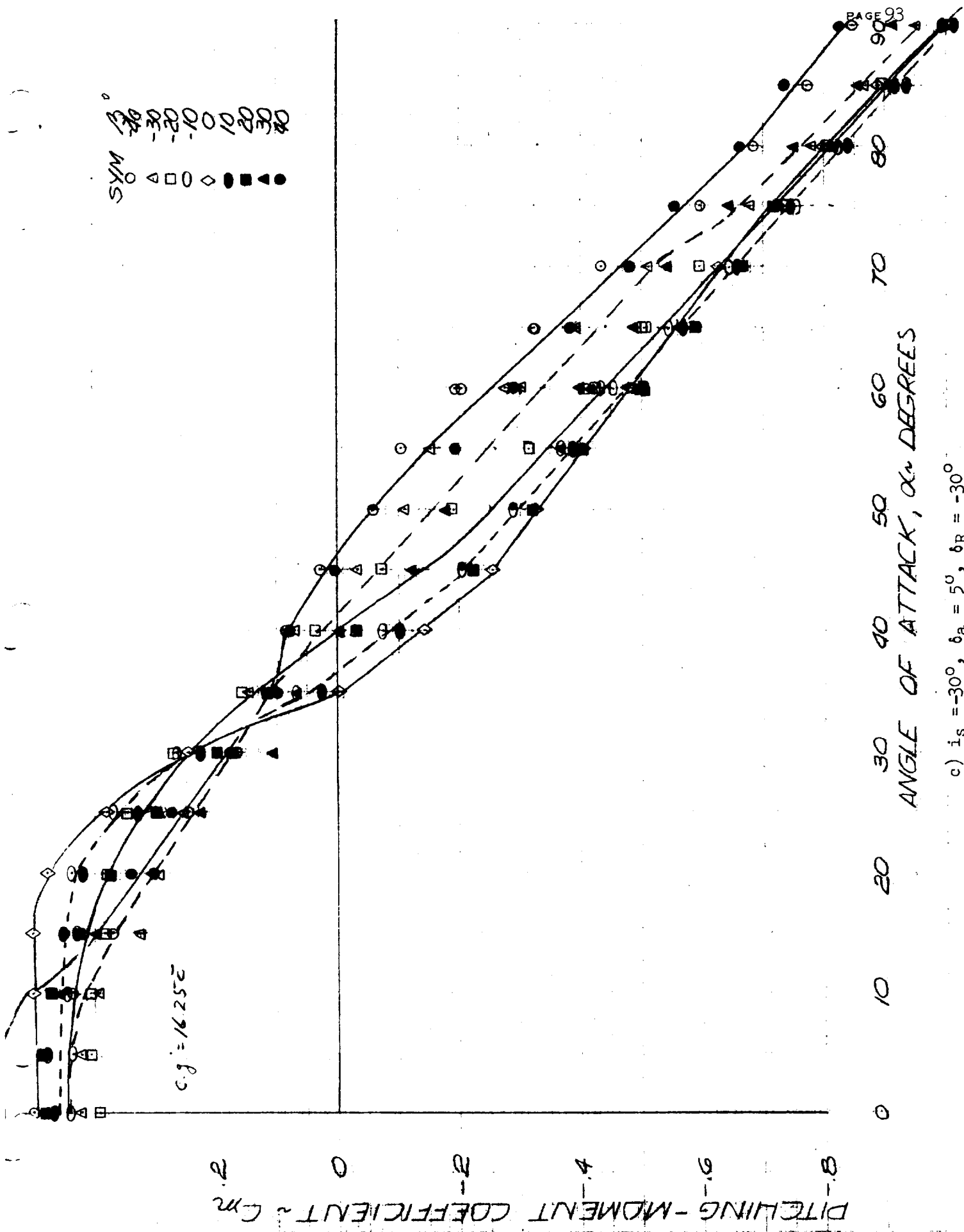


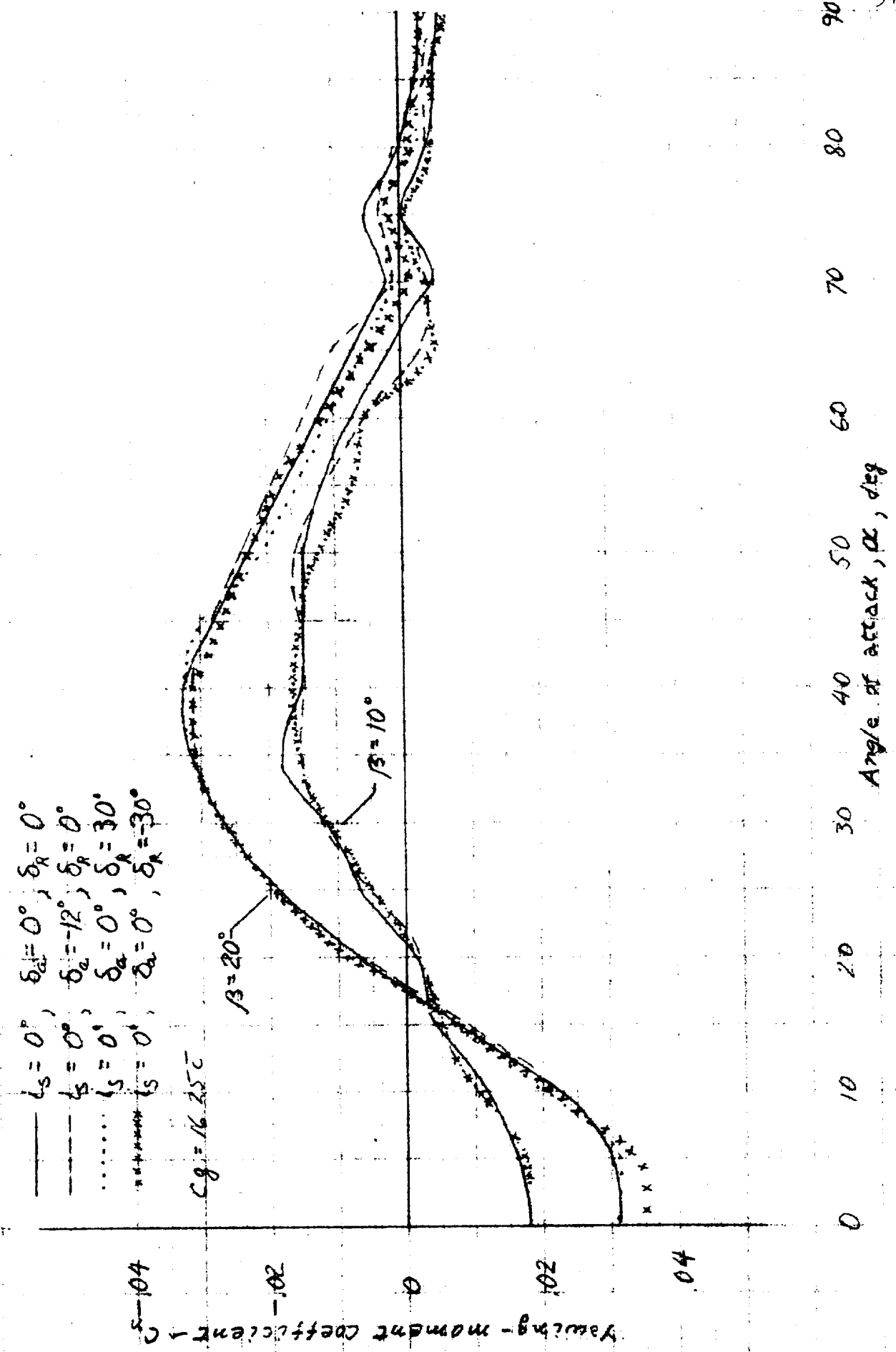
Figure D-3. Effect of sideslip angle on pitching-moment coefficient for various control configurations.



b) $i_s = -30^\circ$, δ_a , $\delta_R = 0^\circ$
 Figure D-3. Continued.



c) $i_s = -30^\circ$, $\delta_a = 5^\circ$, $\delta_R = -30^\circ$
 Figure D-3. Concluded.

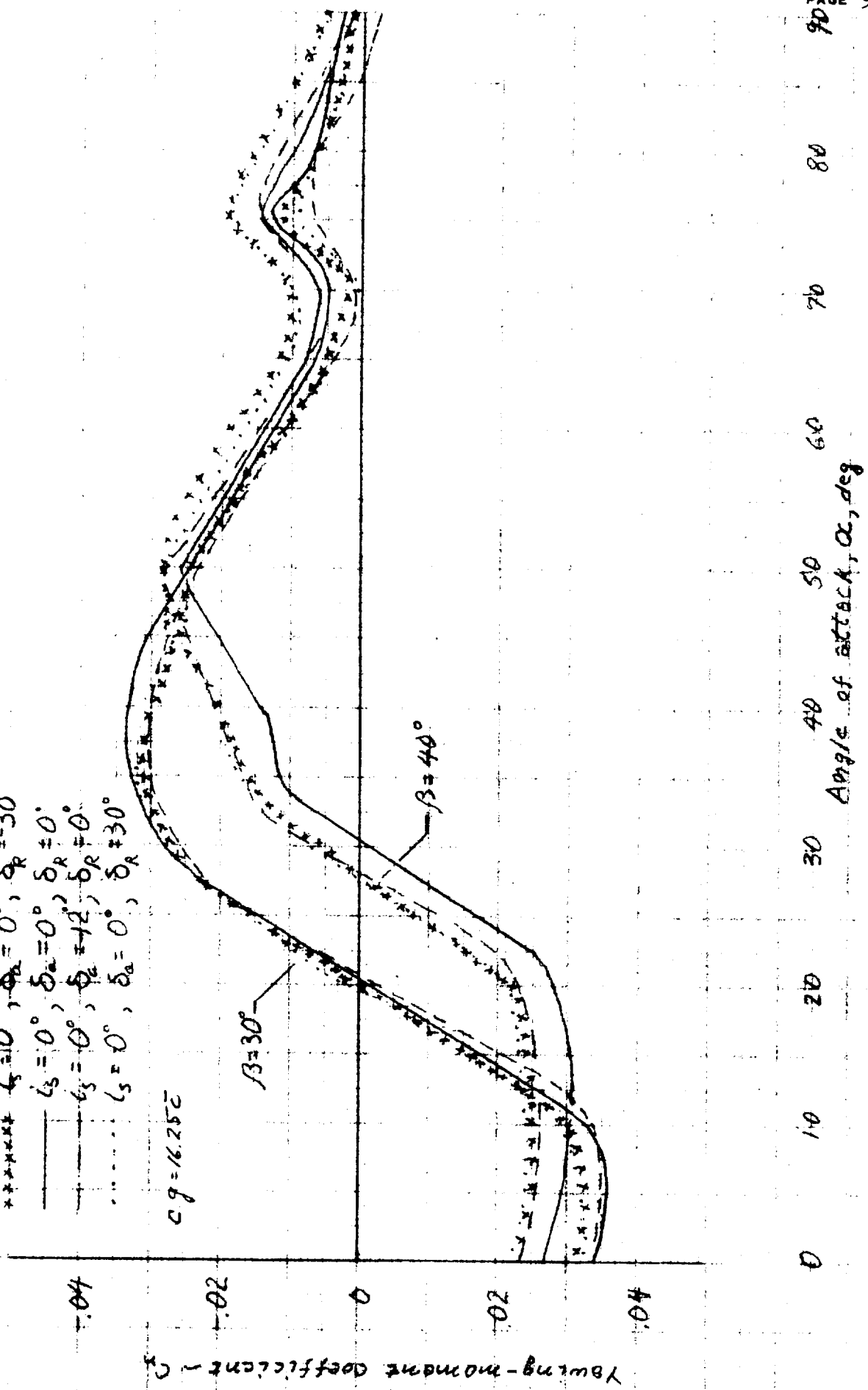


a) $\beta = 10^\circ, 20^\circ$

Figure D-4. Effect of $\delta_s=0^\circ$ control configurations on yawing-moment characteristics.

***** $\delta_a = 0^\circ, \delta_R = -30^\circ$
 ——— $\delta_a = 0^\circ, \delta_R = 0^\circ$
 - - - $\delta_a = +12^\circ, \delta_R = 0^\circ$
 $\delta_a = 0^\circ, \delta_R = 30^\circ$

$C_g = 16.25\bar{c}$



0 10 20 30 40 50 60 70 80 90

Angle of attack, α , deg

b) $\beta = 30^\circ, 40^\circ$
 Figure D-4. Concluded.

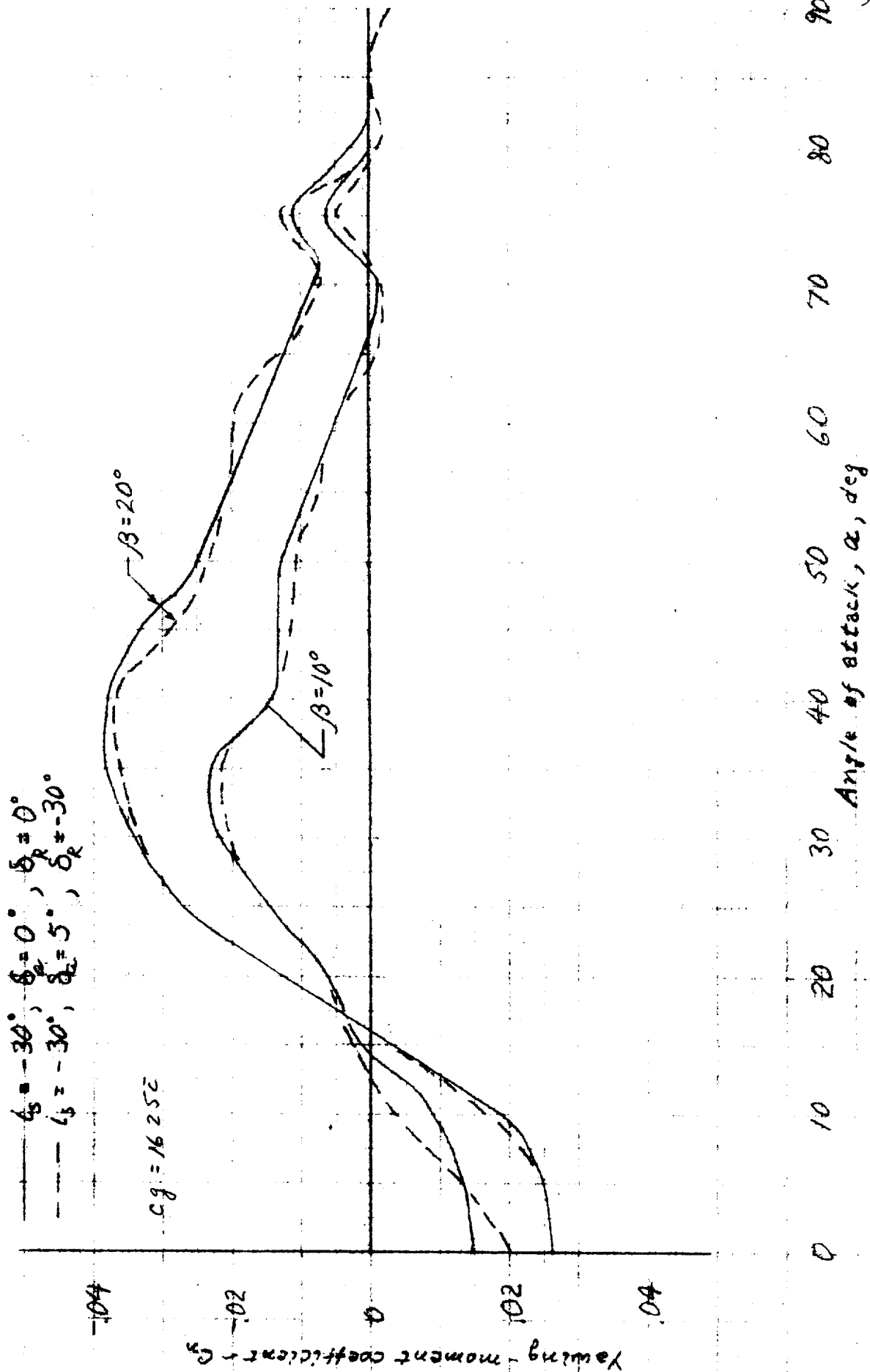
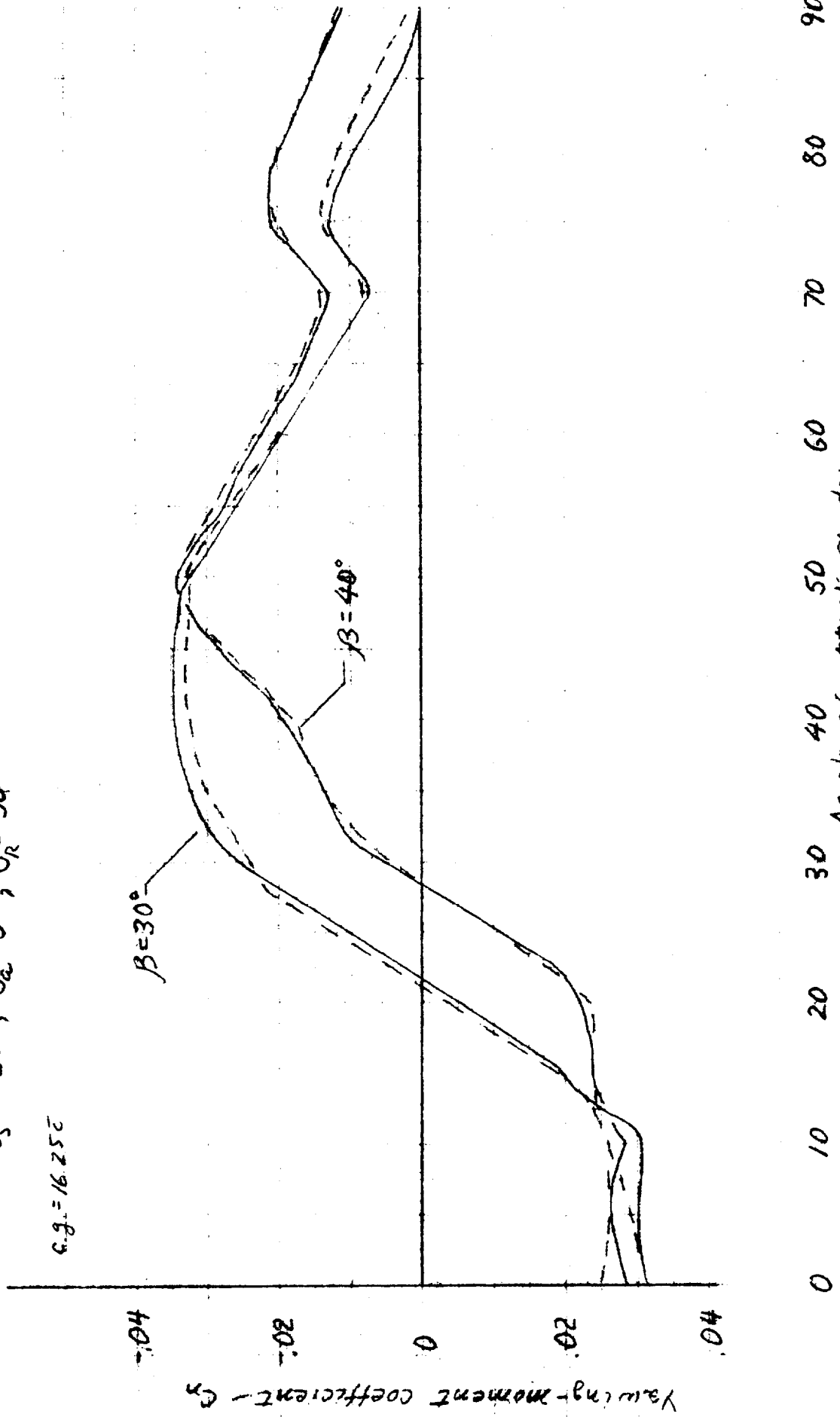


Figure D-5. Effect of $i_s = -30^\circ$ control configurations on yawing moment characteristics.
a) $\beta = 10^\circ, 20^\circ$

— $i_s = -30^\circ, \delta_a = 0^\circ, \delta_R = 0^\circ$
 - - - $i_s = -30^\circ, \delta_a = 5^\circ, \delta_R = -30^\circ$

c.g. = 16.25c



b) $\beta = 30^\circ, 40^\circ$
Figure D-5. Concluded.

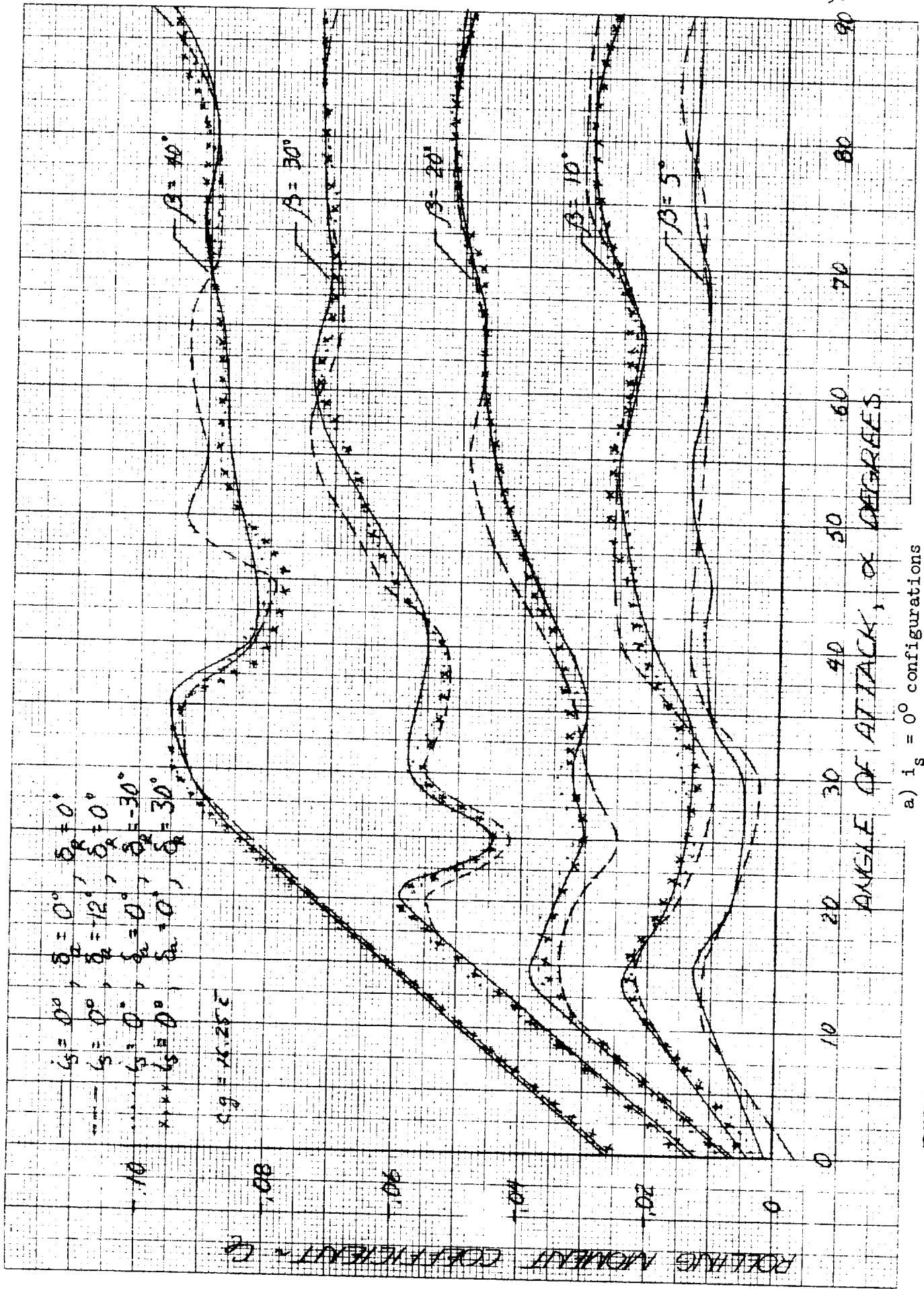
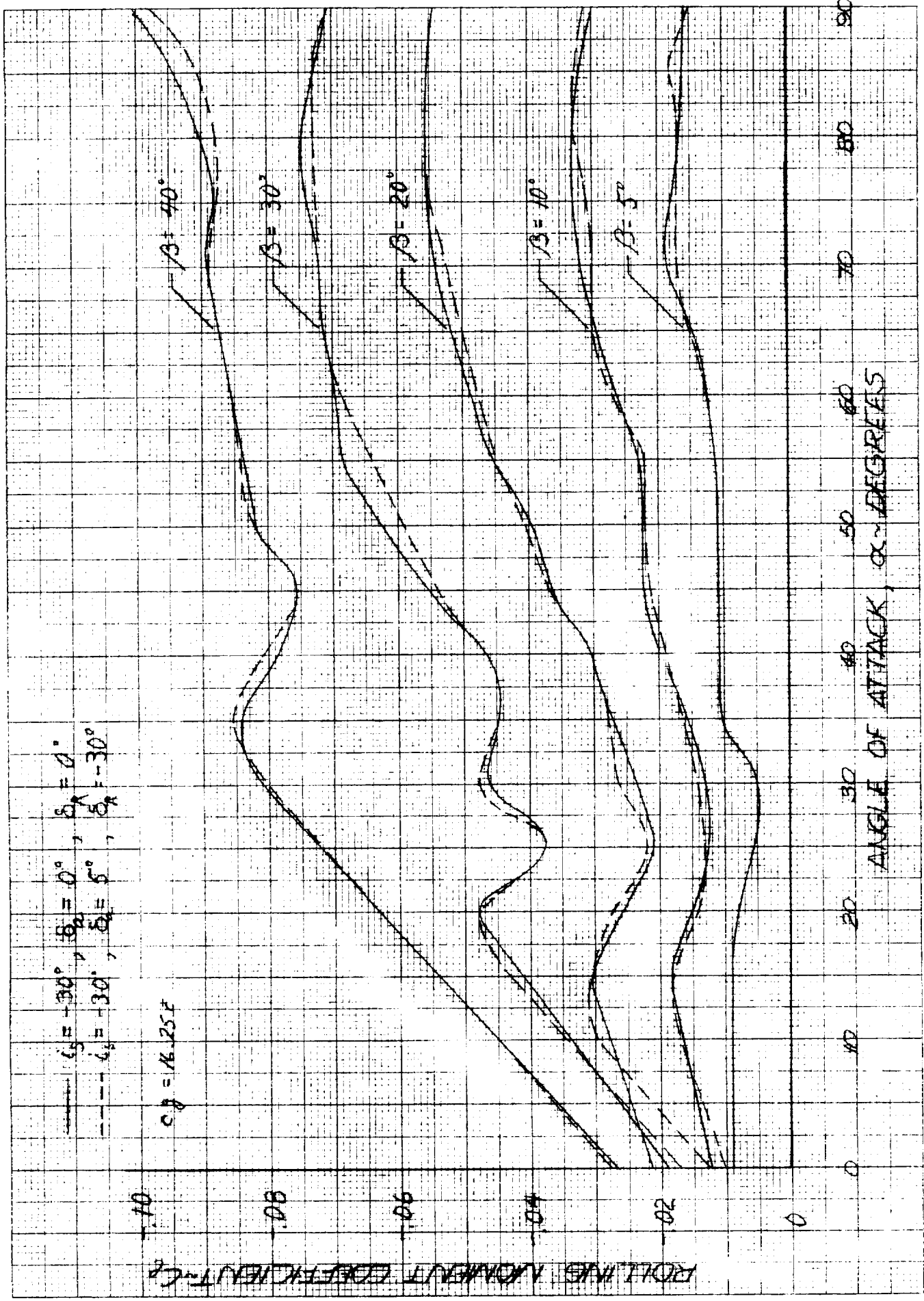
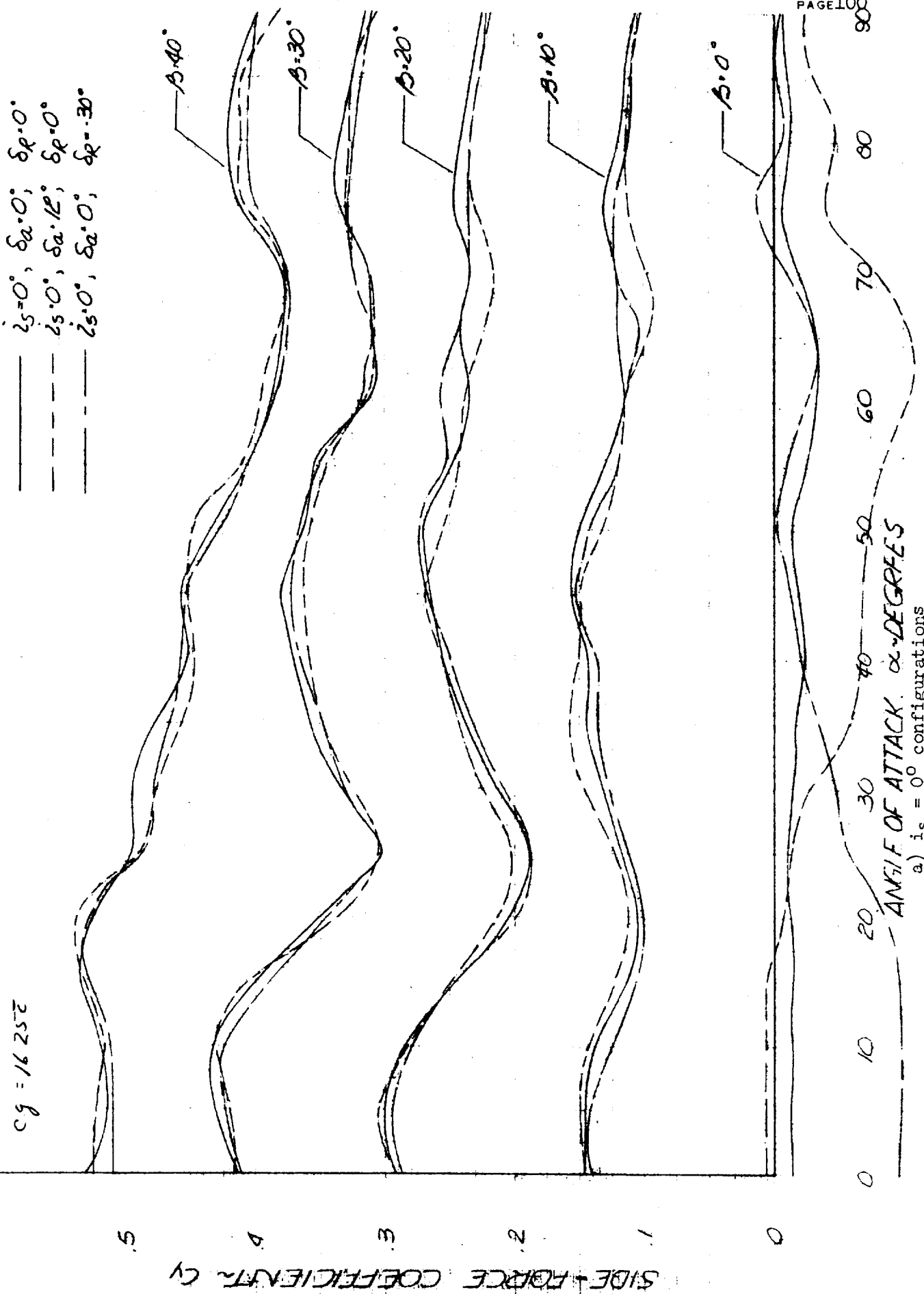


Figure n-1. Effect of control configuration on rolling-moment characteristics.



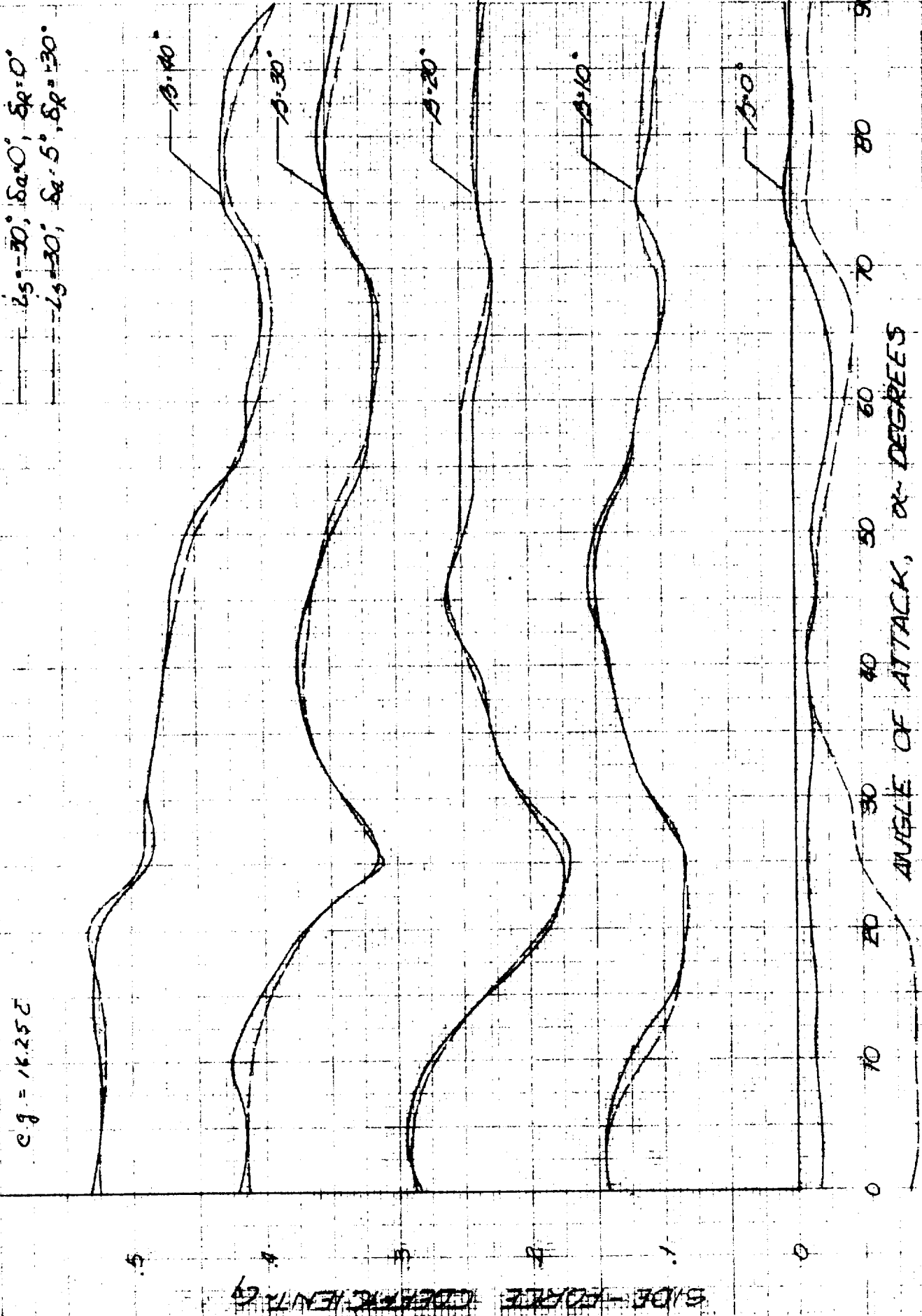
b) $i_{\beta} = -30^\circ$ configurations
Figure D-6. Concluded.

25291 = 85



a) $i_s = 0^\circ$ configurations

Effect of control configuration on side-force characteristics.



b) $i_s = -30^\circ$ configurations
Figure D-7. Concluded.

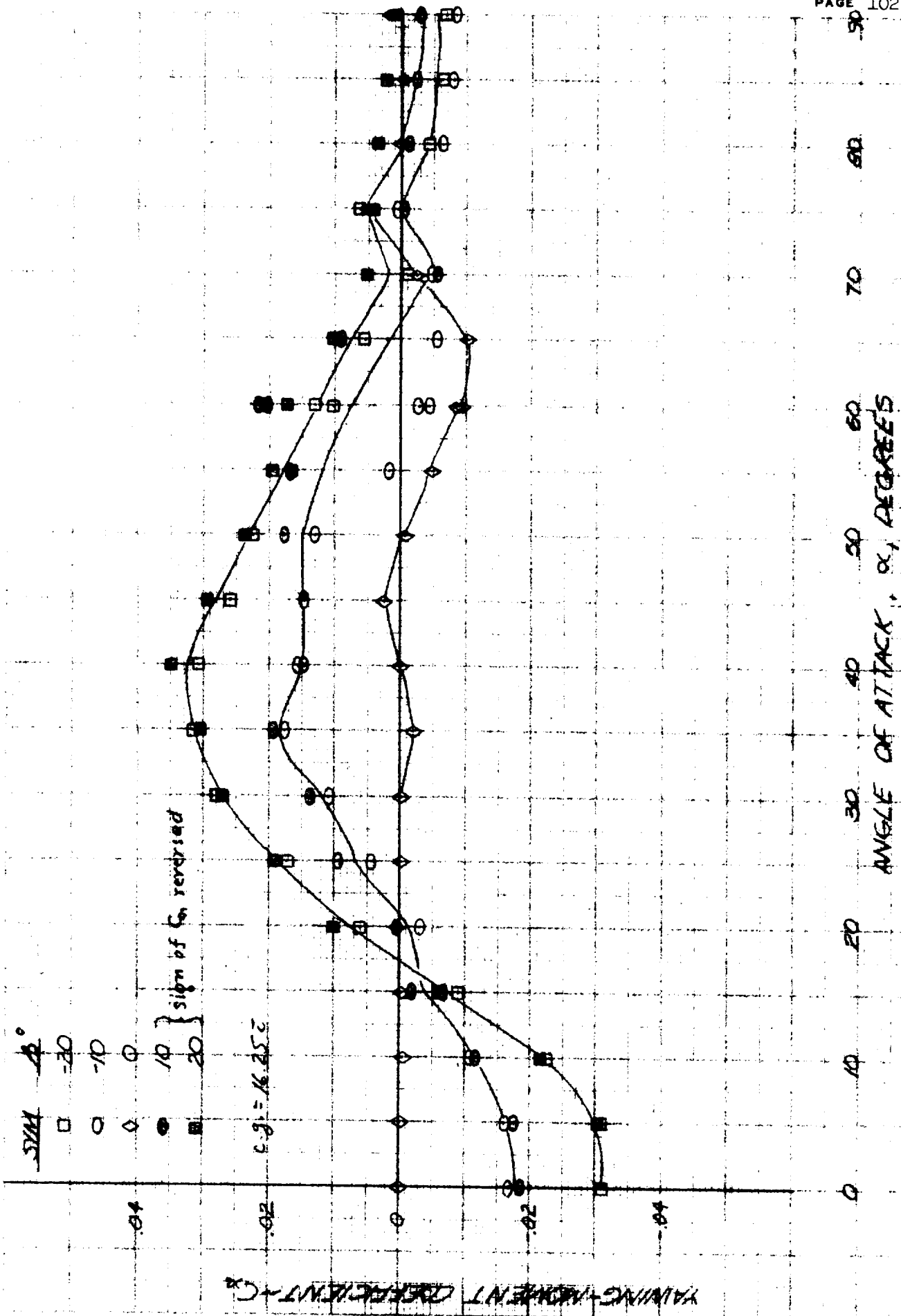
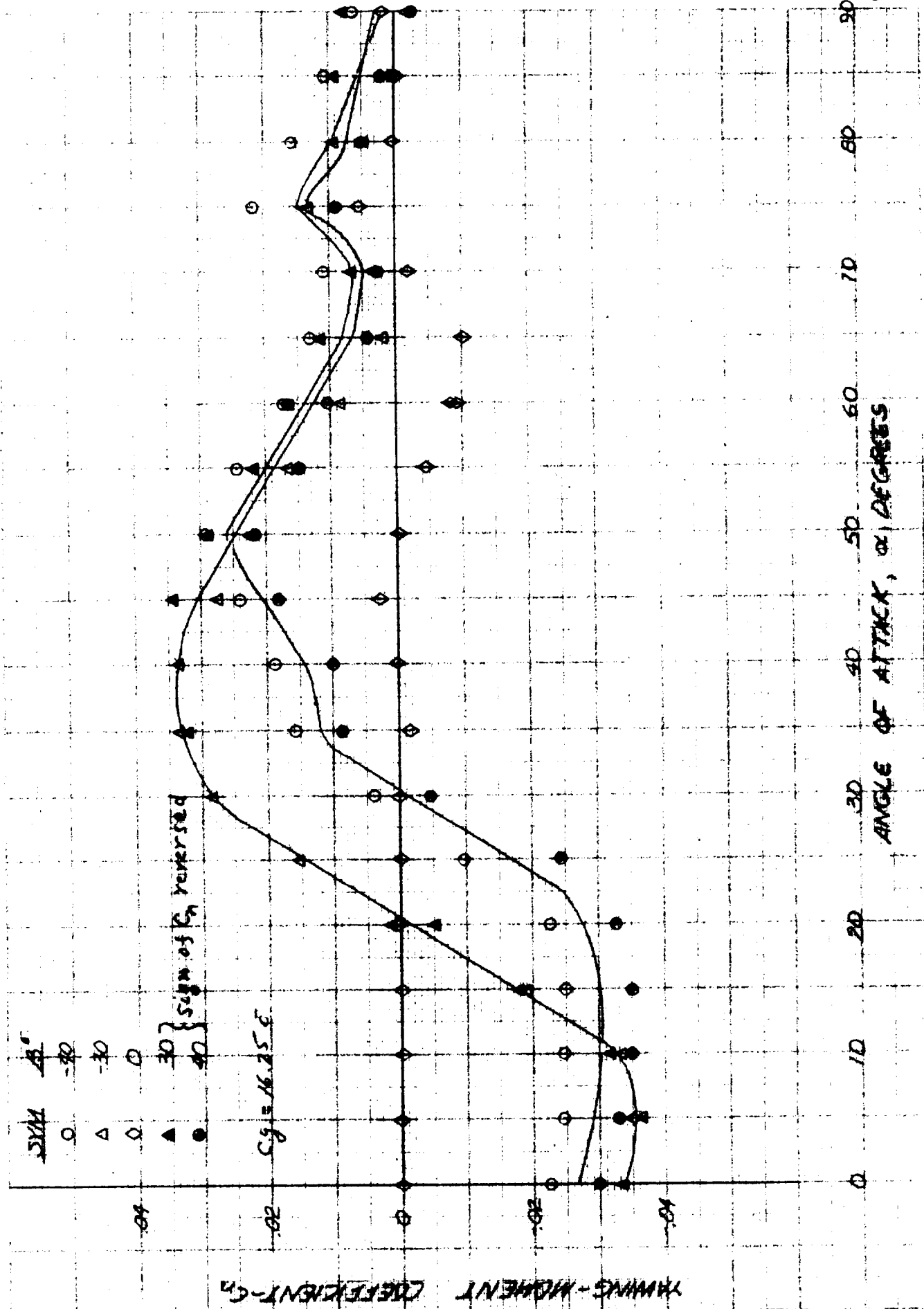
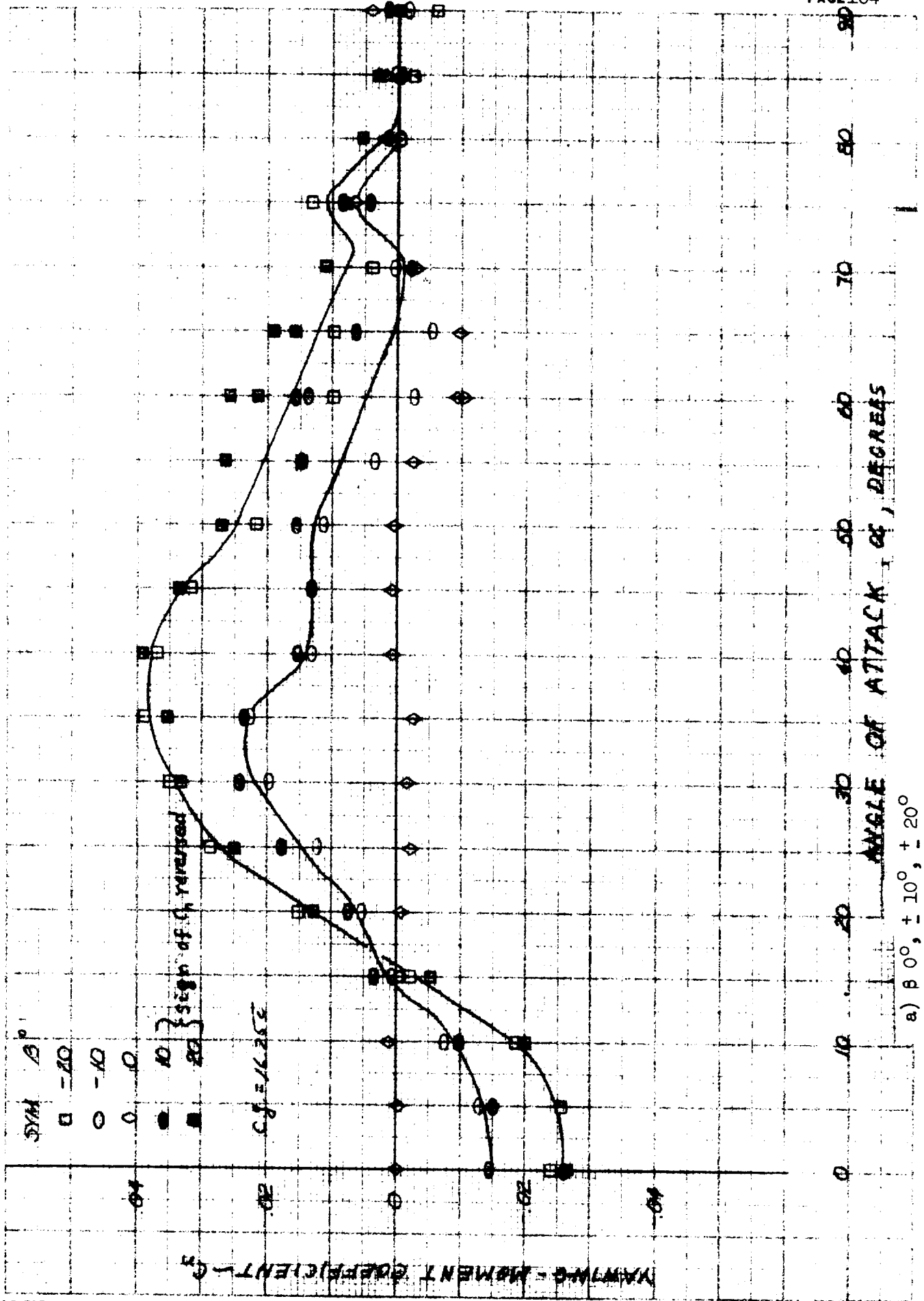


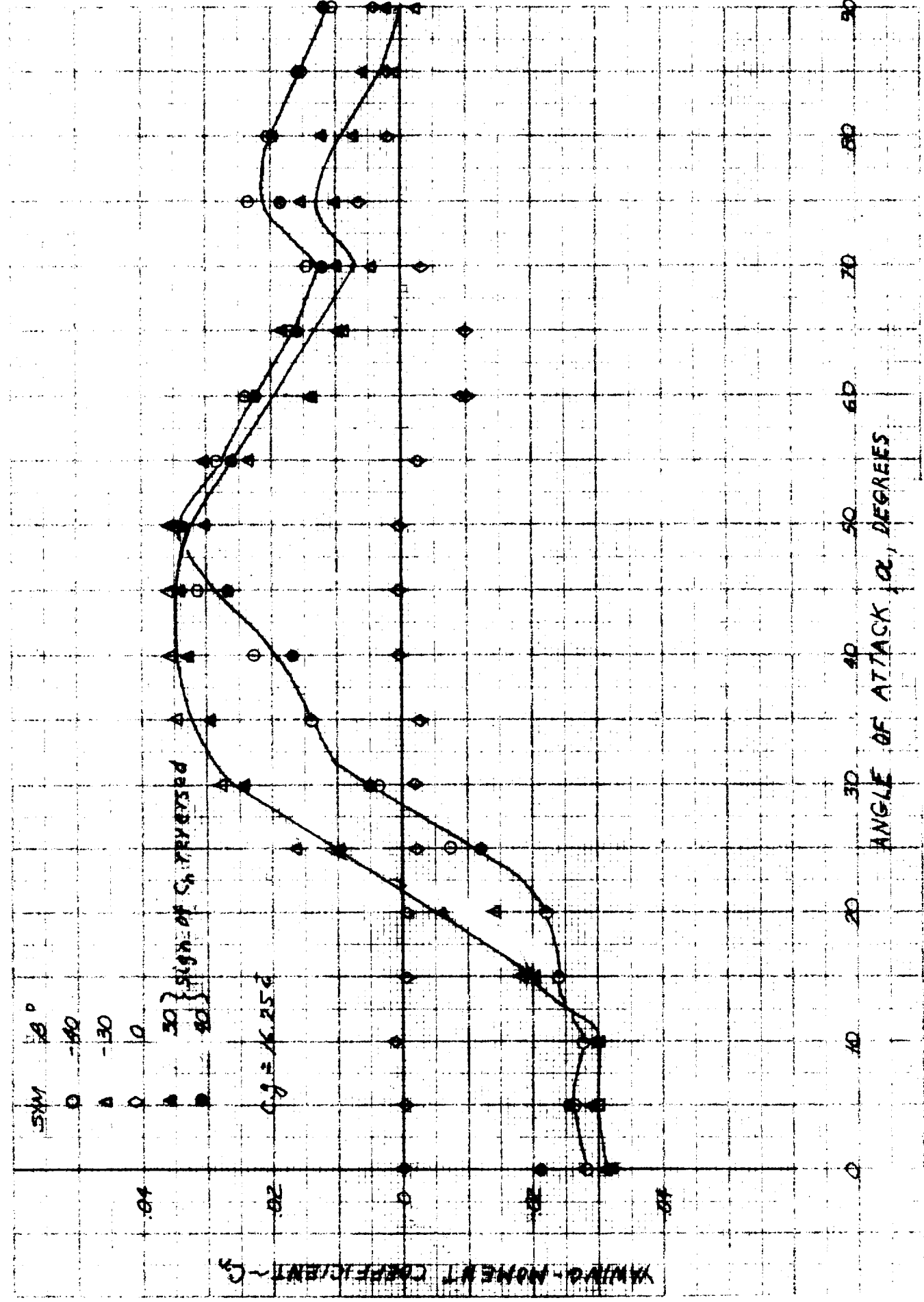
Figure D-8. Effect of angle of attack and sideslip angle on yawing-moment coefficient for configuration i_s , β_R , $\beta_P = 0^\circ$.
 a) $\beta = 0^\circ, \pm 10^\circ, \pm 20^\circ$



b) $\beta = 0^\circ, -30^\circ, -40^\circ$
Figure D-8. Concluded.



a) β 0° , $+10^\circ$, $+20^\circ$
 Figure D-9. Effect of angle of attack and sideslip angle on yawing -
 moment coefficient for configuration is $= -30^\circ$; δ_a , $\delta_R = 0^\circ$.



b) $\beta = 0^\circ, \pm 30^\circ, \pm 40^\circ$
Figure D-9. Concluded.

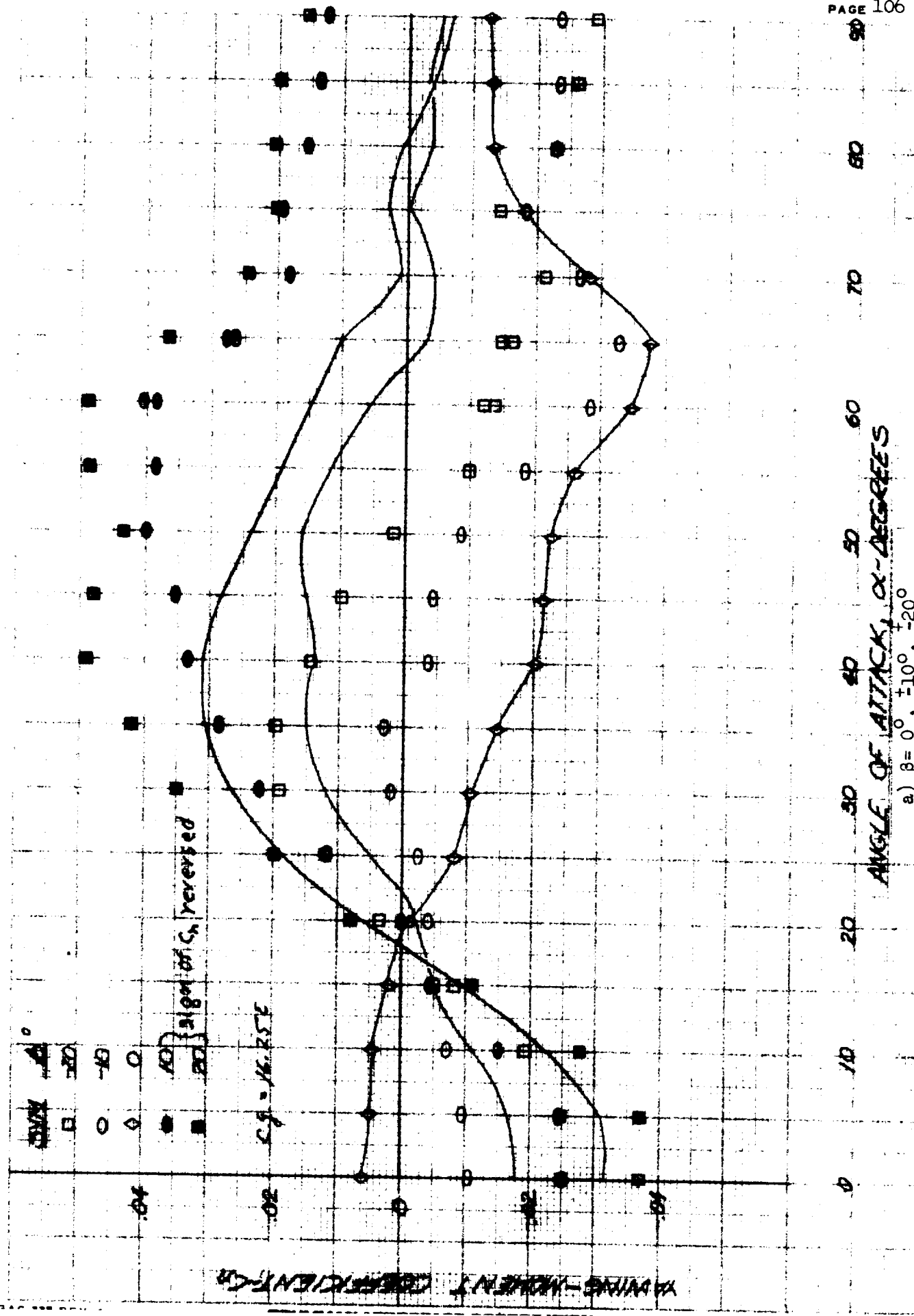
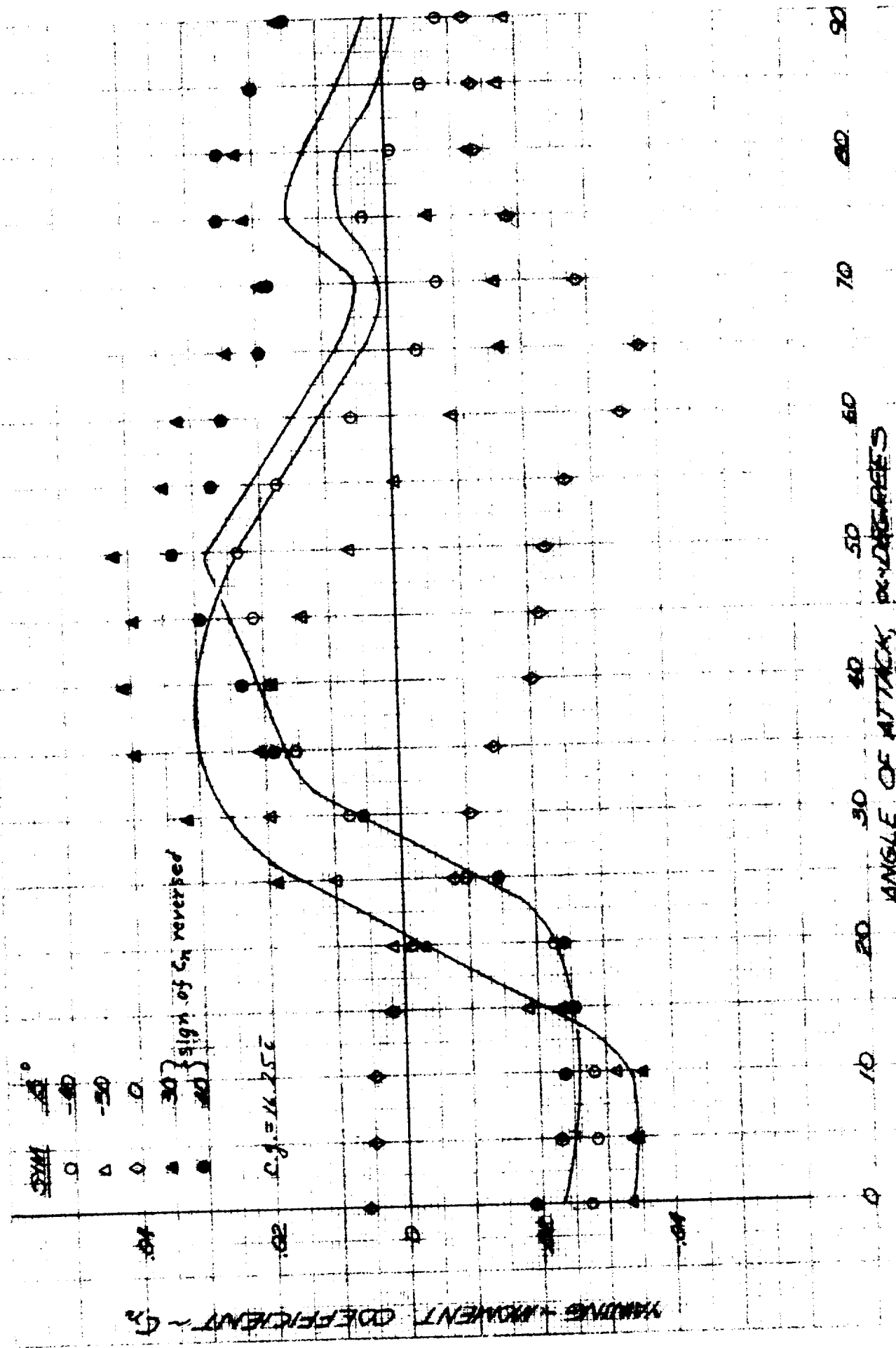
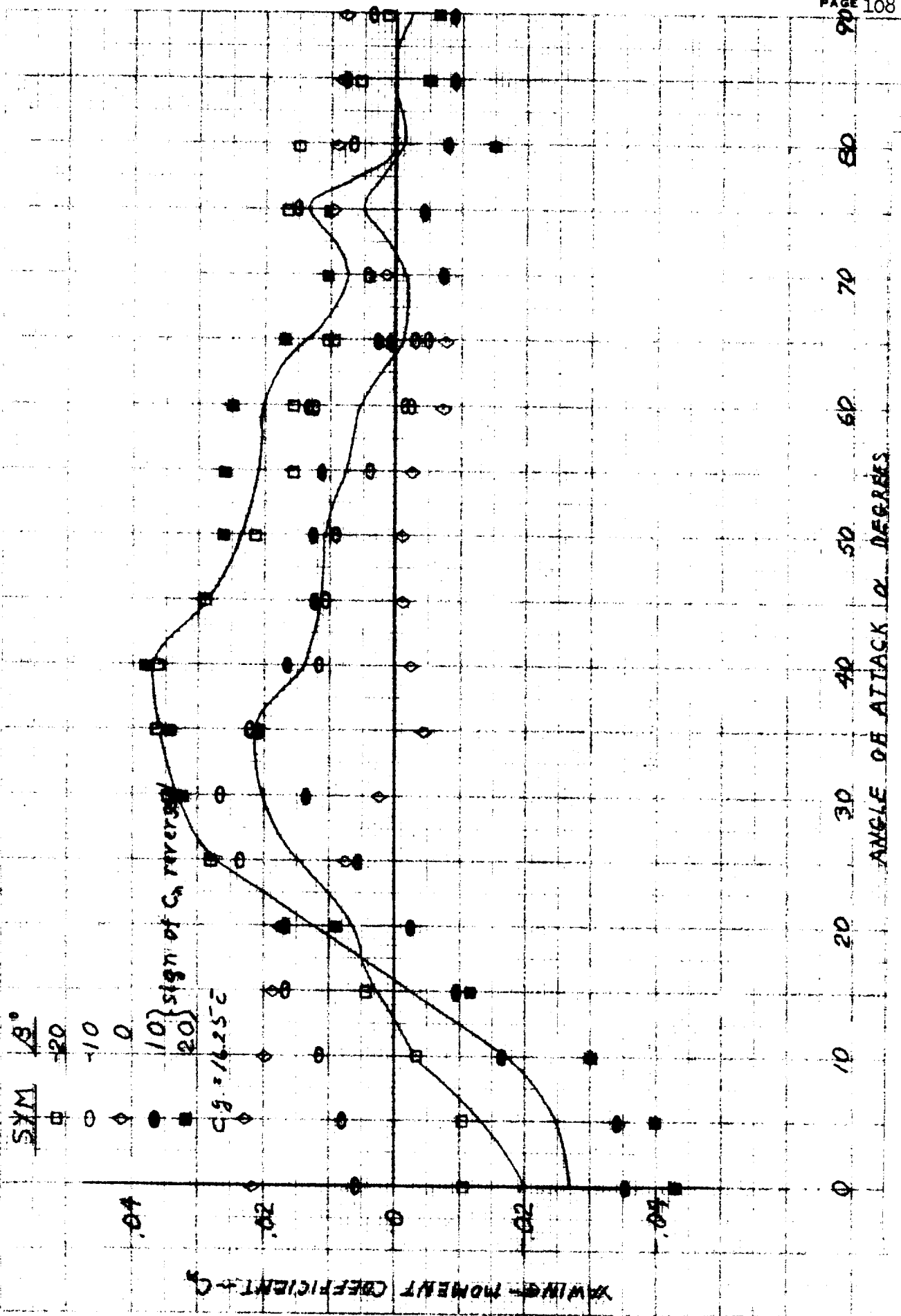


Figure D-10. Effect of angle of attack and sideslip angle on yawing-moment coefficient for configuration i_s , $\delta_R=0^\circ$; $\delta_a=-12^\circ$.
 a) $\beta = 0^\circ, \pm 10^\circ, -20^\circ$

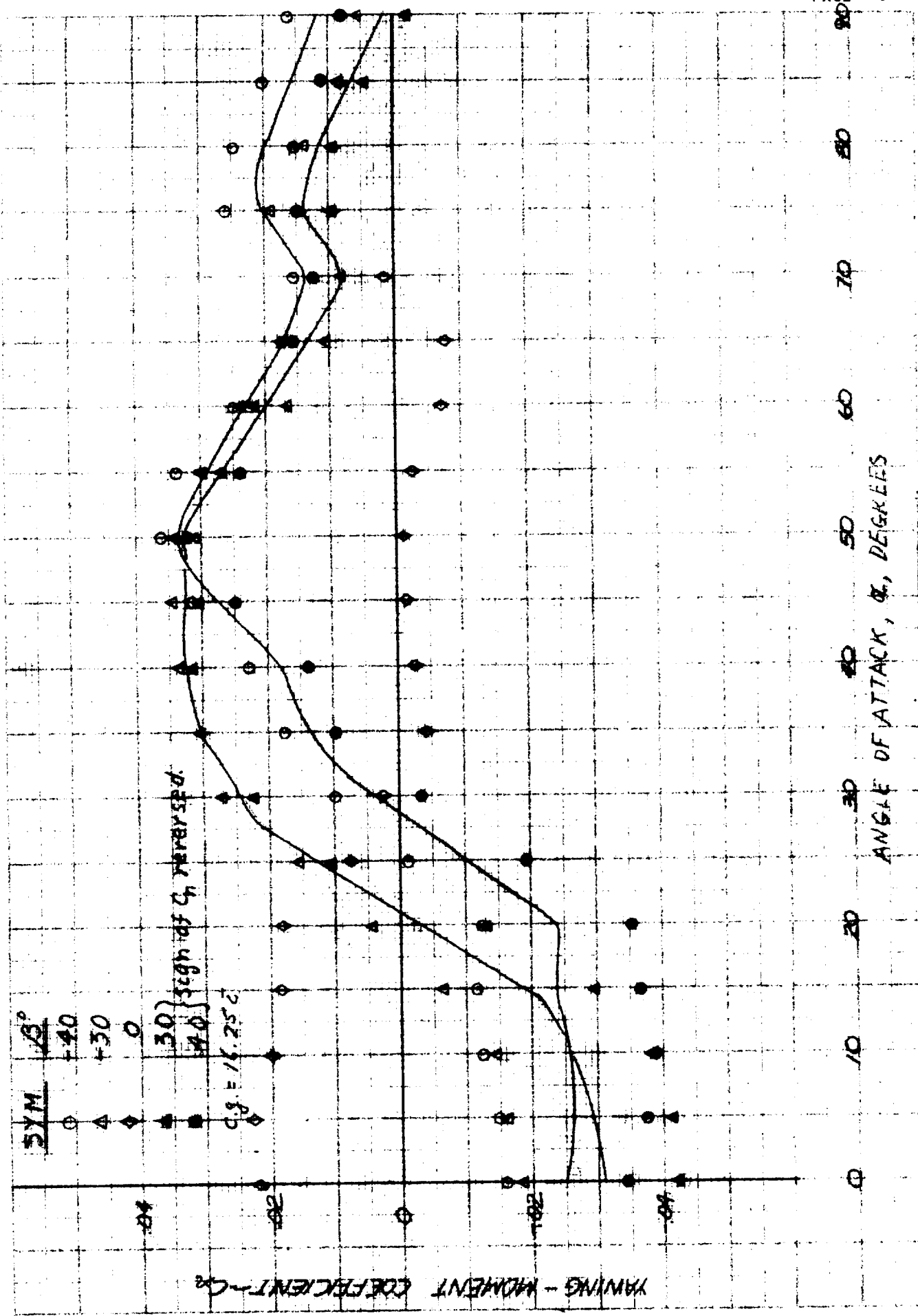


b) $\beta = 0^\circ, +30^\circ, -40^\circ$
 Figure D-10. Concluded.



a) $\beta = 0^\circ, 10^\circ, 20^\circ$
 Figure D-11. Effect of angle of attack and sideslip angle on yawing-
 moment coefficient for configuration is $\delta_a = 5^\circ, \delta_R = -30^\circ$.

DATE



b) $\beta = 0^\circ, \pm 30^\circ, \pm 40^\circ$
 Figure D-11. Concluded.

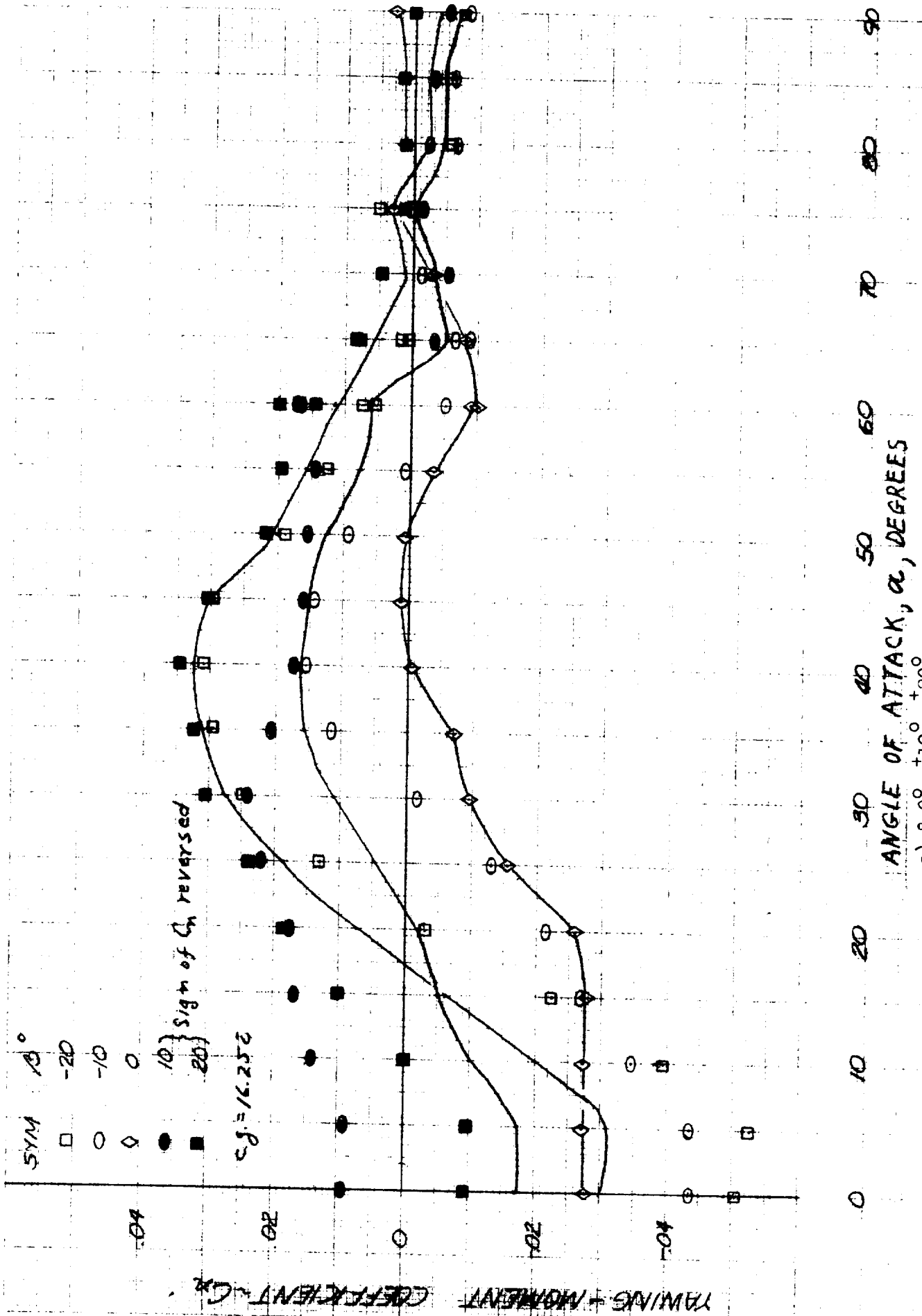
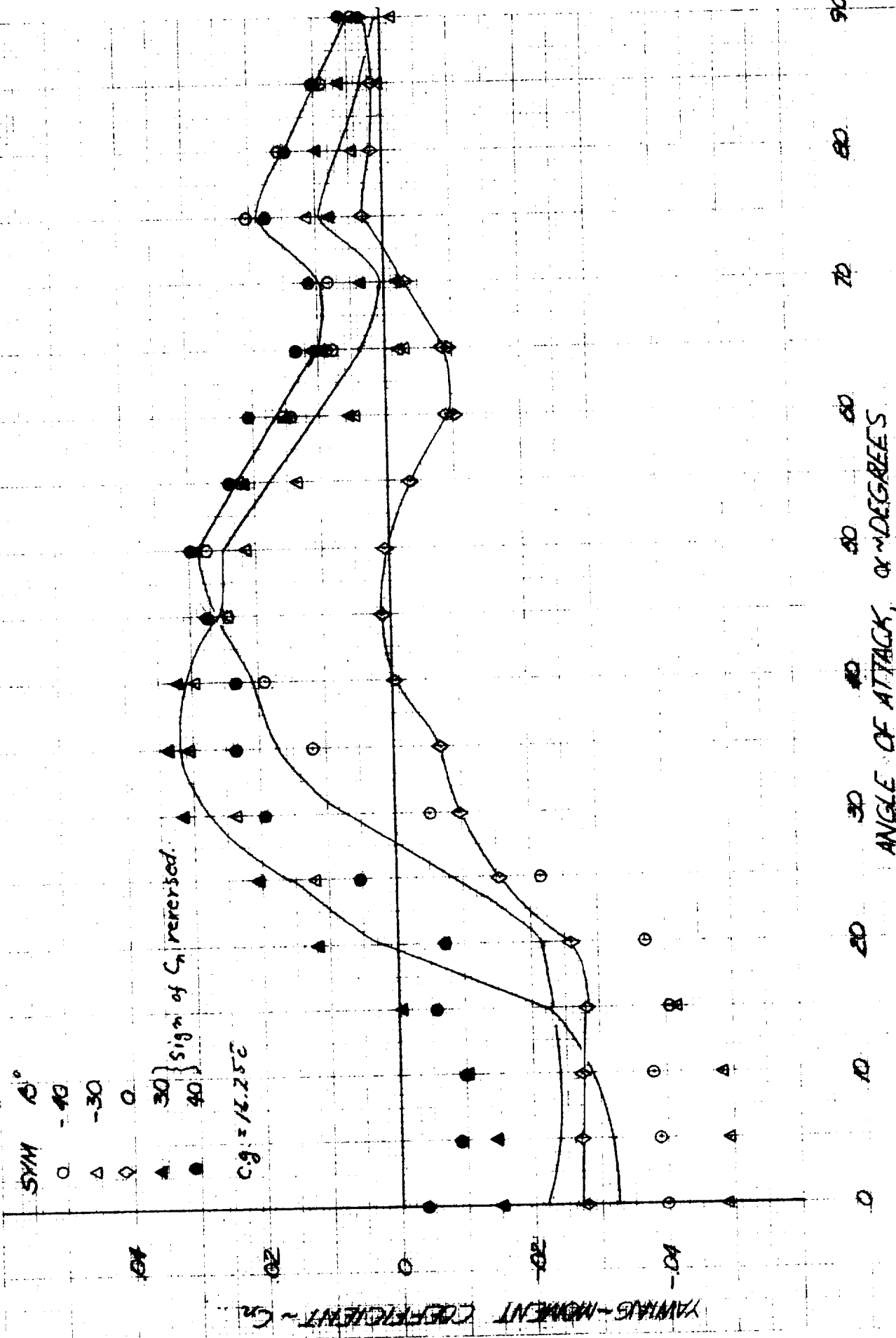


Figure D-12. Effect of angle of attack and sideslip angle on yawing-moment coefficient for configuration i.r. $\delta_r = 0^\circ$; $\delta_n = 30^\circ$



b) $\beta=0^\circ$, $+30^\circ$, -40°
Figure D-12, Concluded.

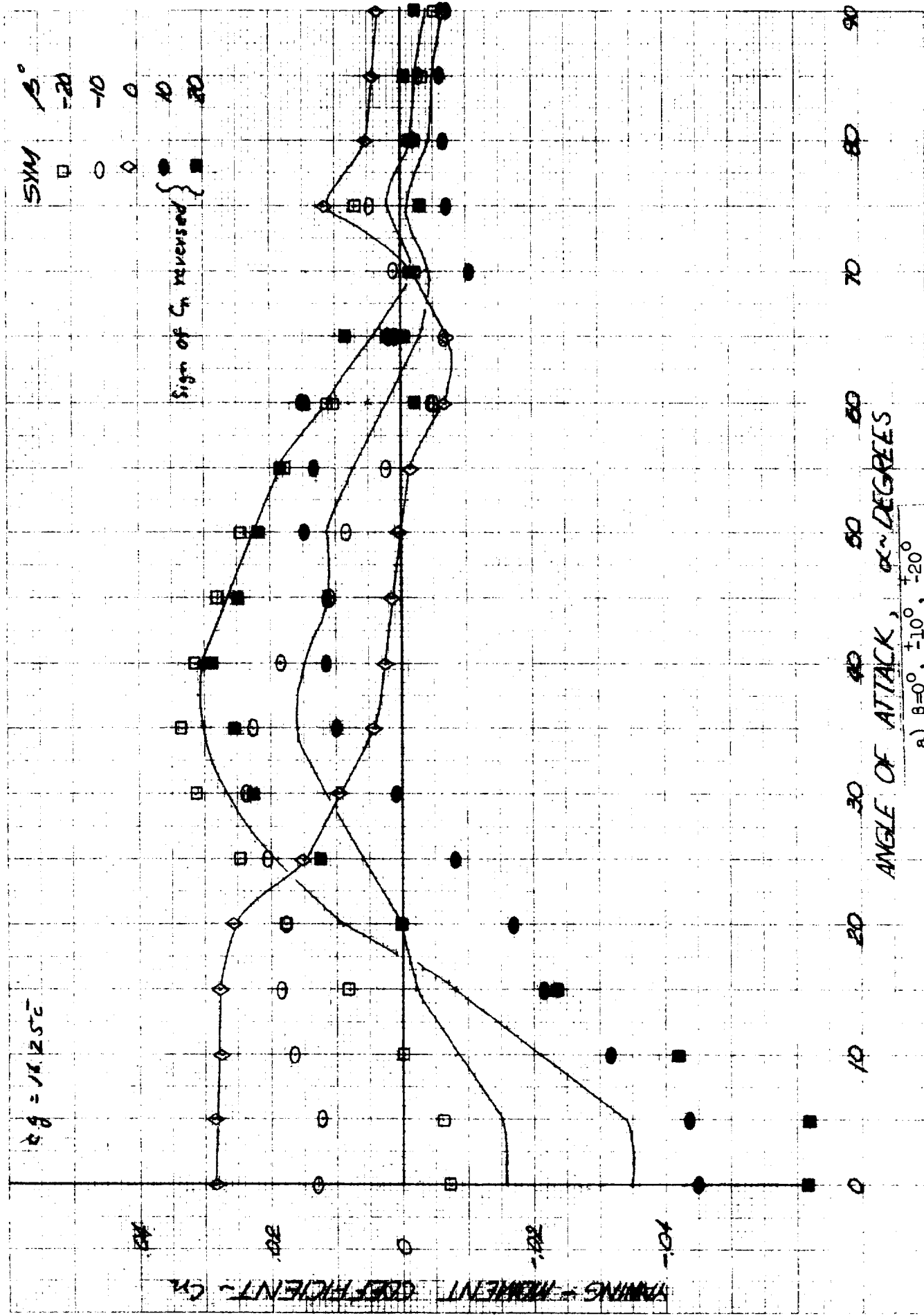
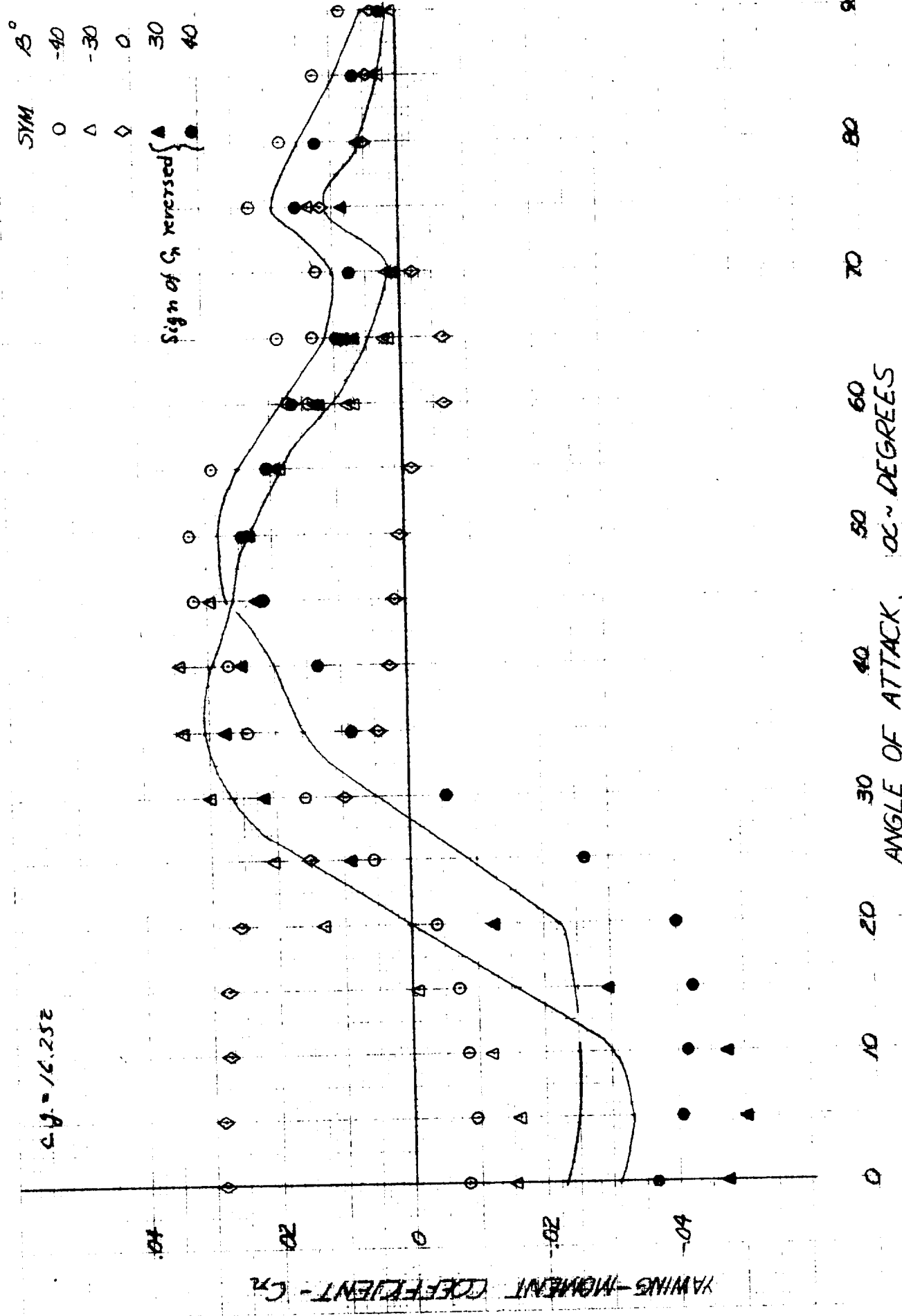


Figure D-13. Effect of angle of attack and sideslip angle on yawing-moment coefficient. a) $\beta = 0^\circ, \pm 10^\circ, \pm 20^\circ$. $\delta_a = 0^\circ; \delta_p = -30^\circ$.



b) $\beta=0^\circ, +30^\circ, +40^\circ$
Figure D-13. Concluded.

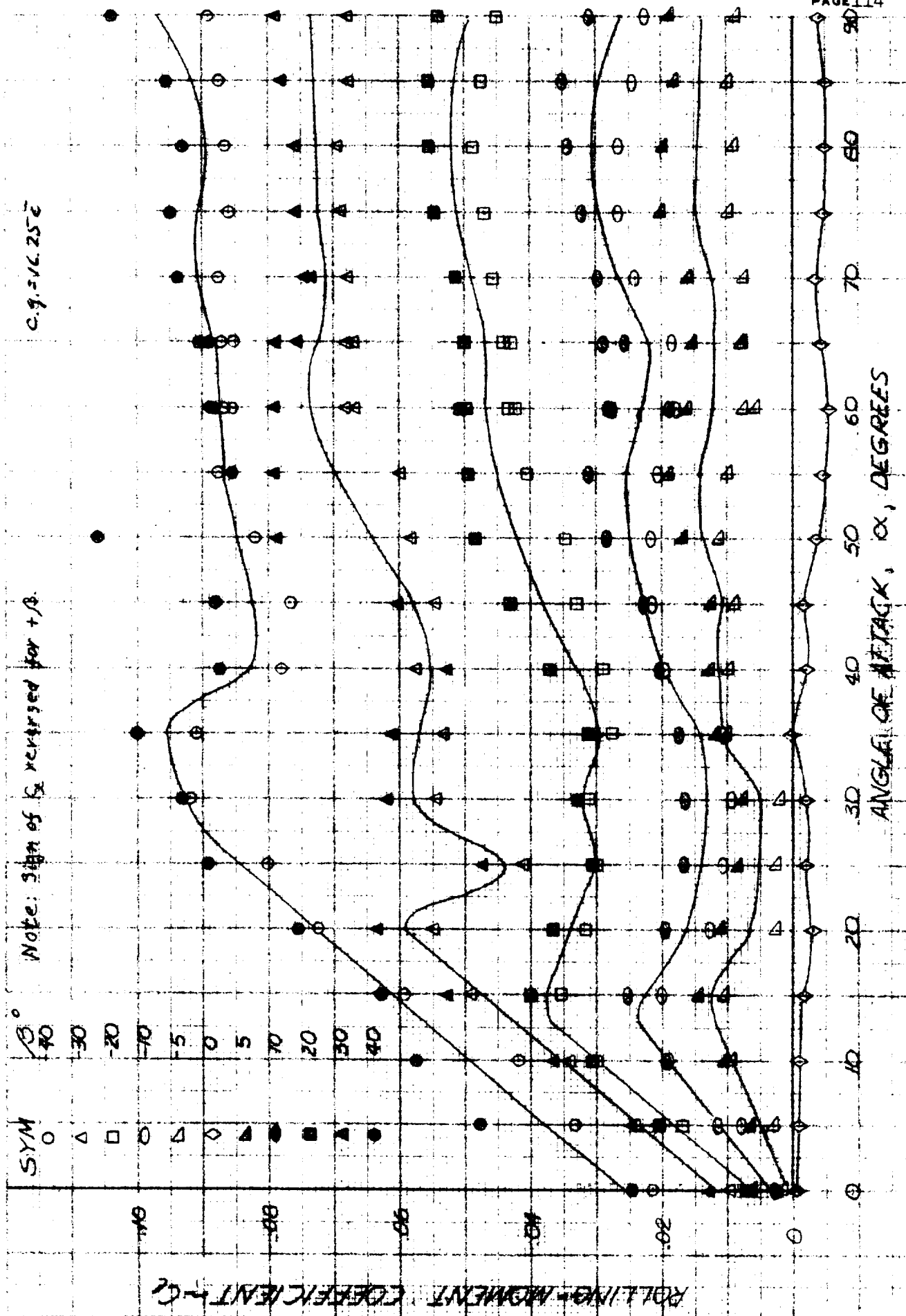
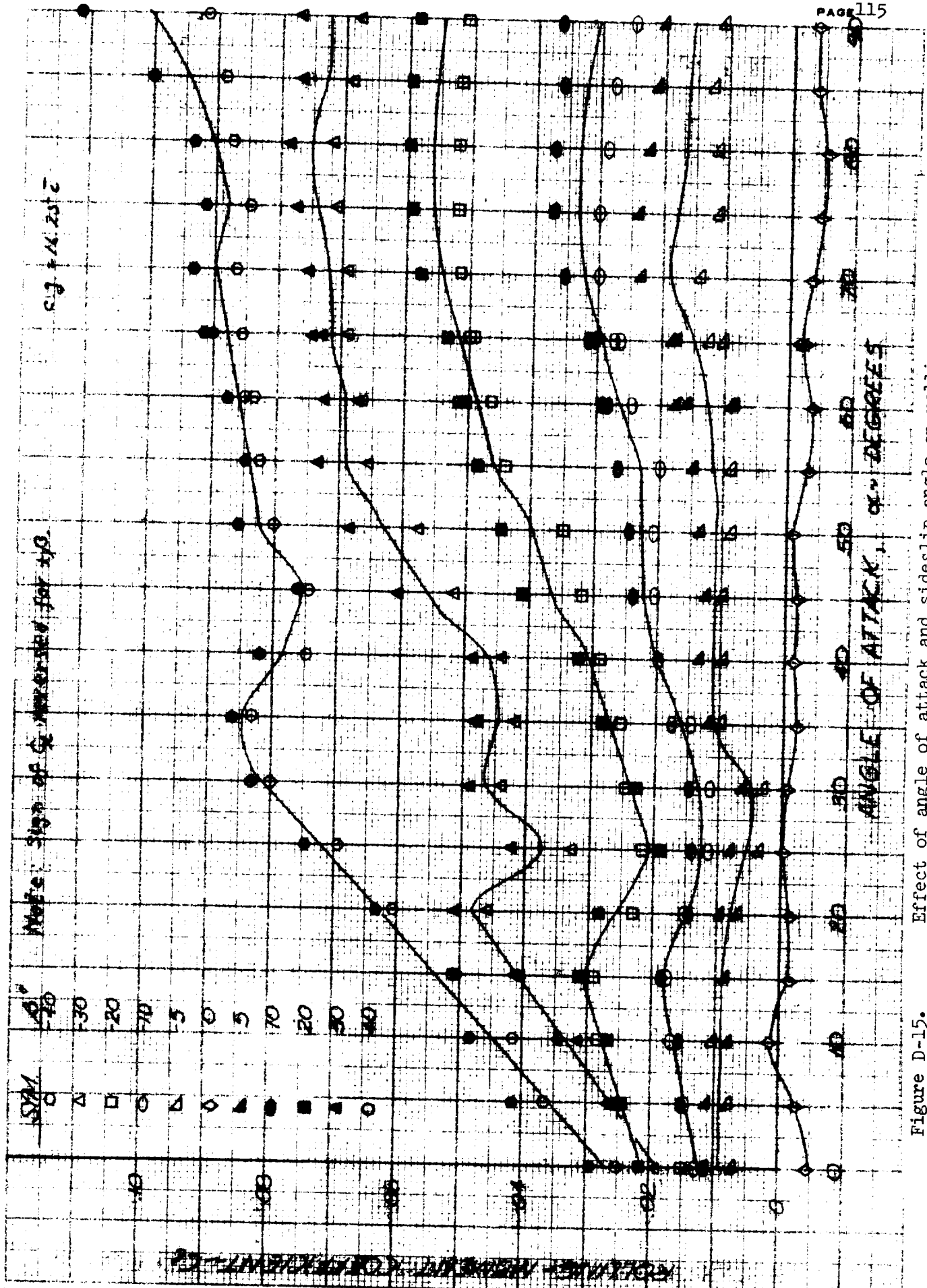


Figure D-14. Effect of angle of attack and sideslip angle on rolling-moment coefficient for configuration i_s , β_a , $\beta_R = 0^\circ$.



Effect of angle of attack and sideslip angle on rolling moment coefficient for configuration $i_s = -30^\circ$; $b_a, b_R = 0^\circ$.

Figure D-15.

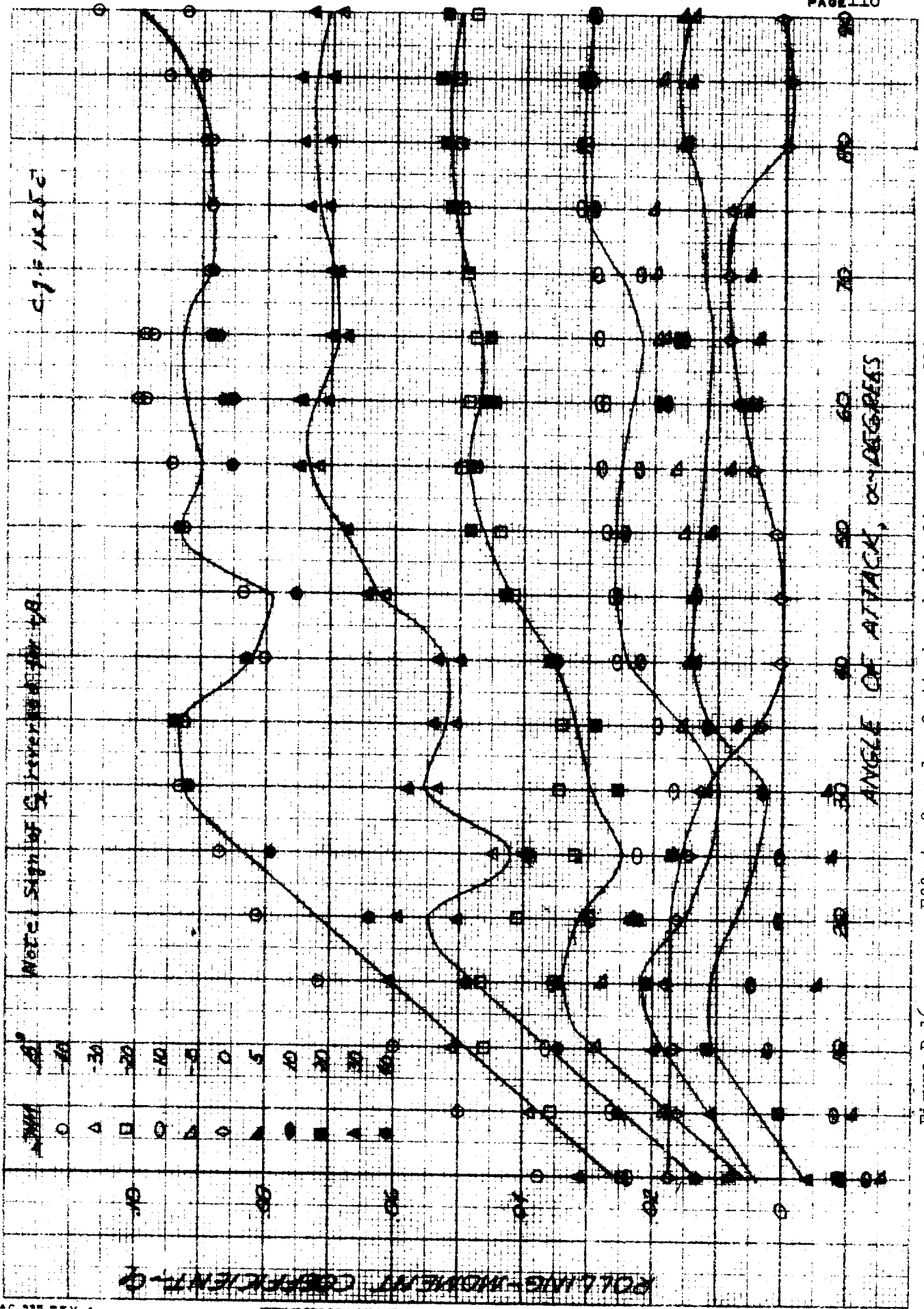


Figure D-16. Effect of angle of attack and sideslip angle on rolling-moment coefficient for configuration i_s , $\delta_{R0} = 0^\circ$; $\delta_a = -12^\circ$.

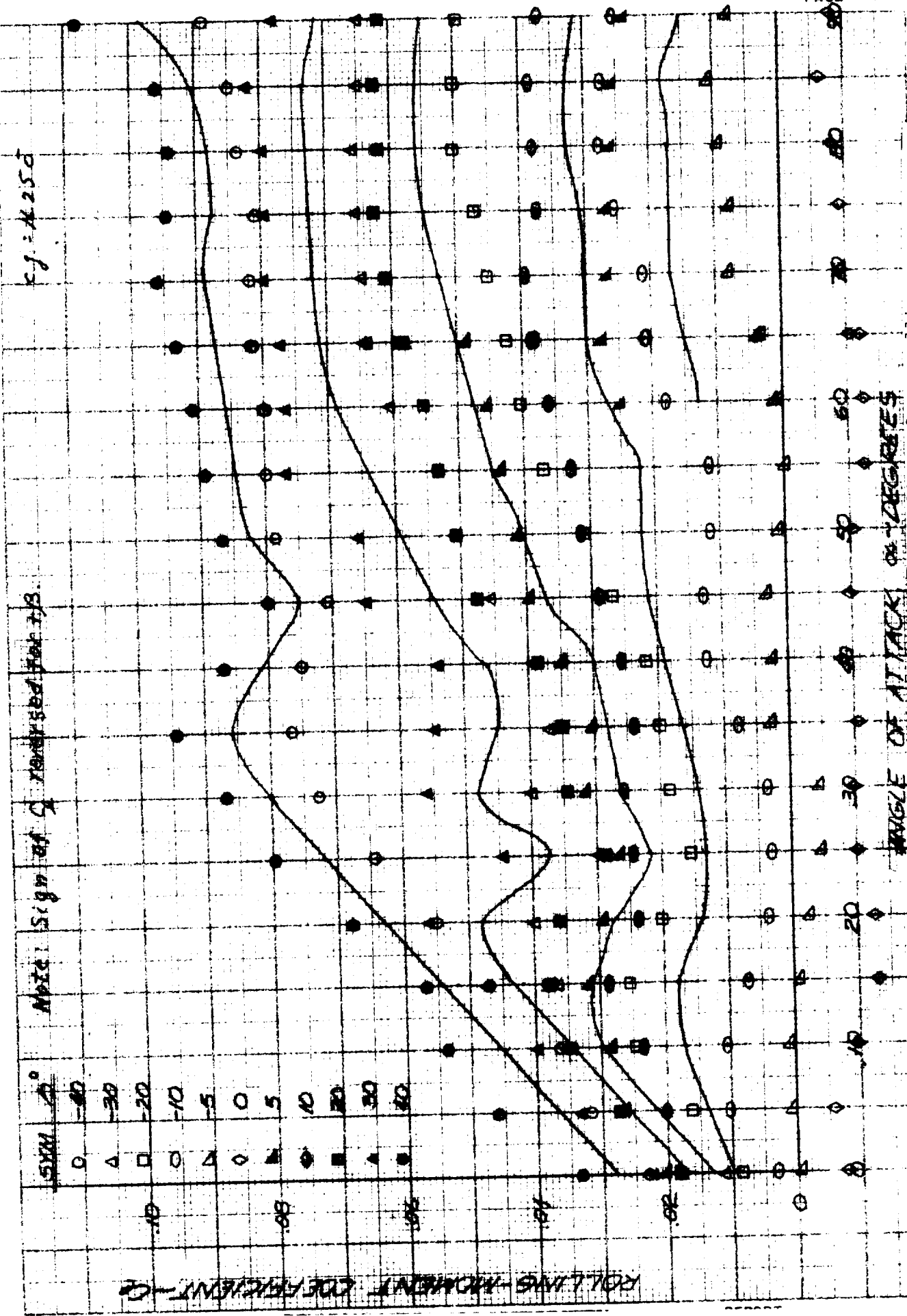


Figure D-17.
 Effect of angle of attack and sideslip angle on rolling-
 moment coefficient for configuration is $\alpha = -30^\circ$, $\beta = 5^\circ$,
 $b_R = -30^\circ$.

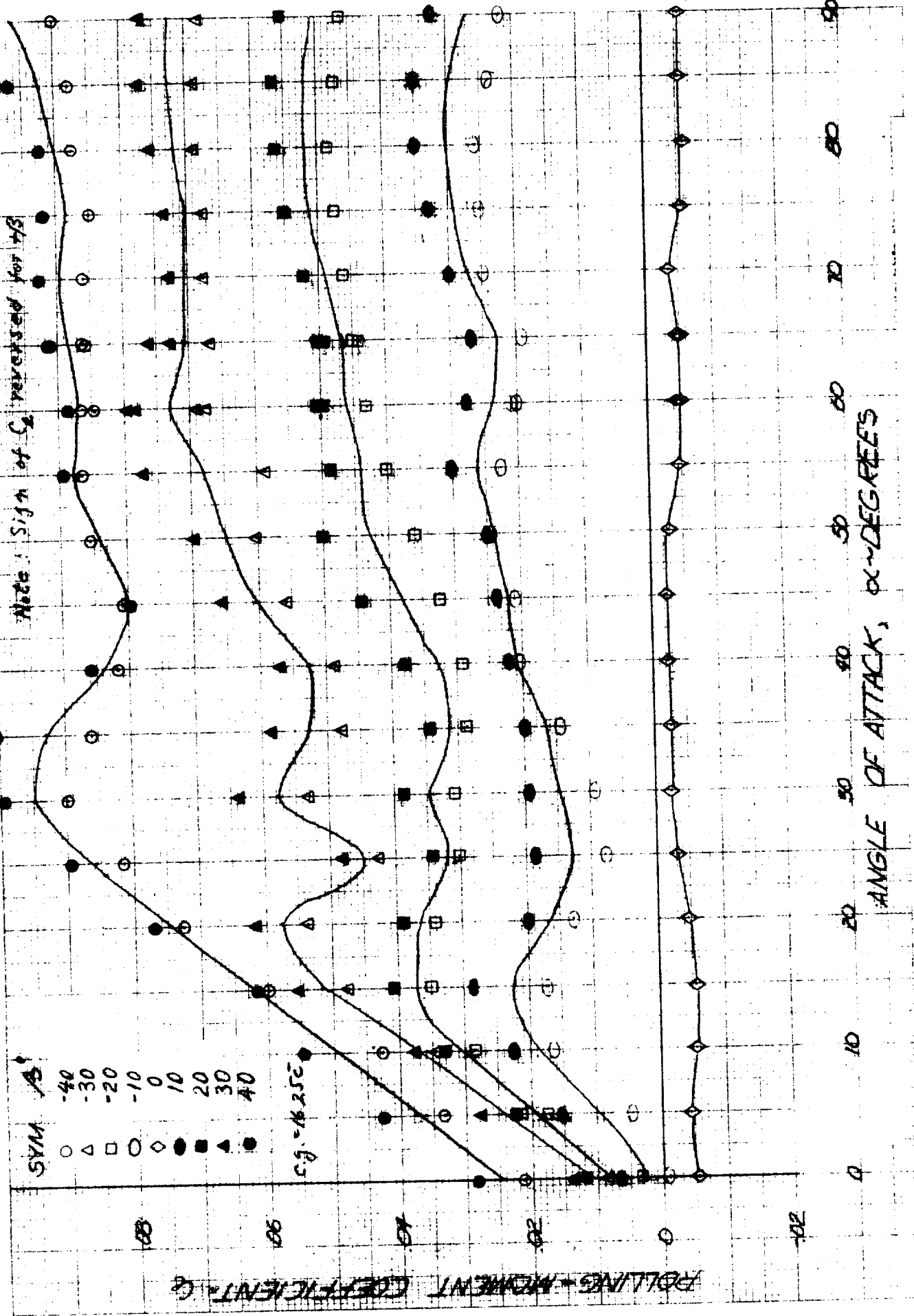


Figure D-19. Effect of angle of attack and sideslip angle on rolling-moment coefficient for configuration i_s , $\delta_a = 0^\circ$; $\delta_R = -30^\circ$.

Figure D-19.

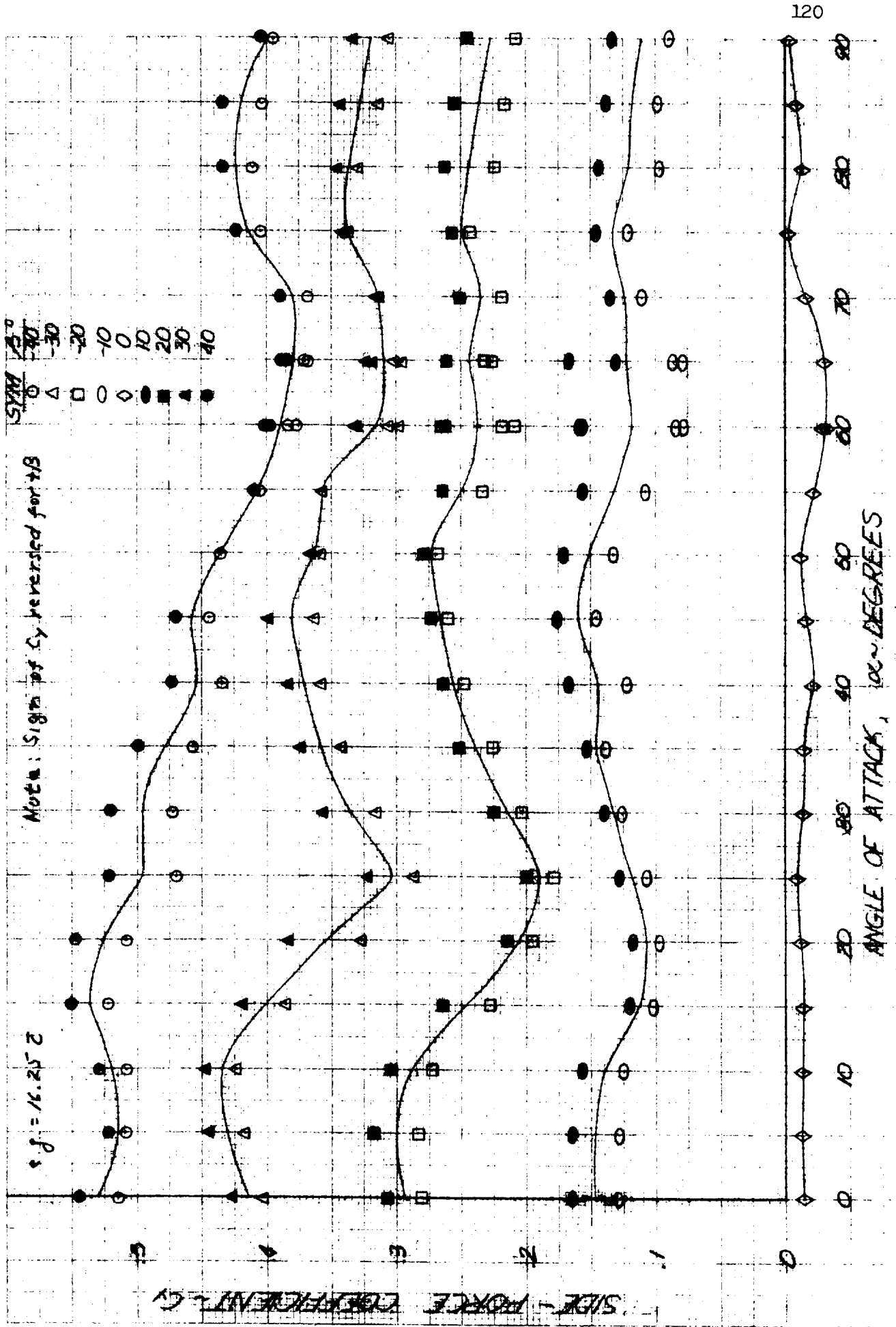


Figure D-20. Effect of angle of attack and sideslip angle on side-force coefficient for configuration i_s , θ_a , $\theta_R = 0^\circ$.

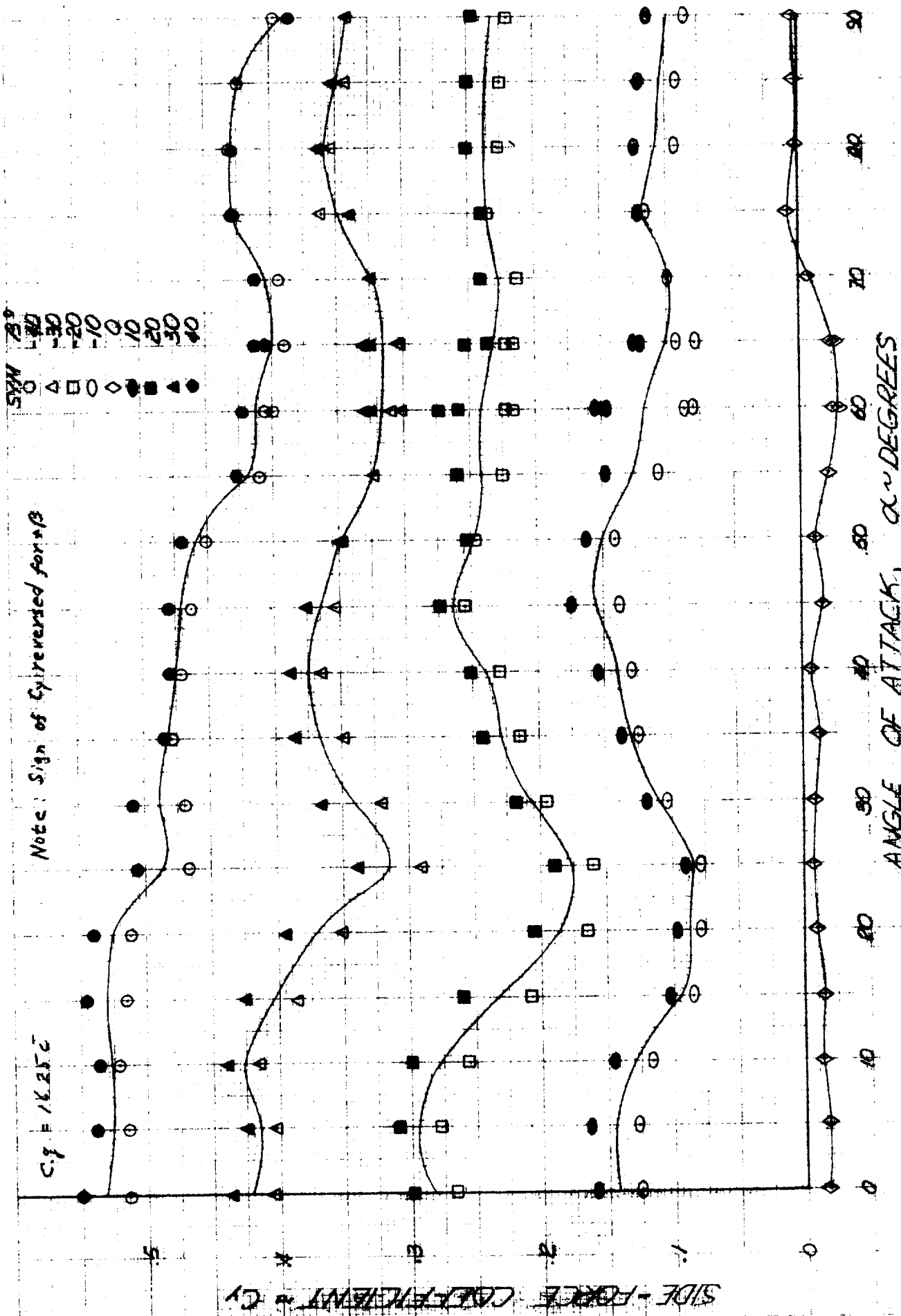


Figure D-21. Effect of angle of attack and sideslip angle on side-force coefficient for configuration is = -30°; β_a , $\beta_R = 0^\circ$.

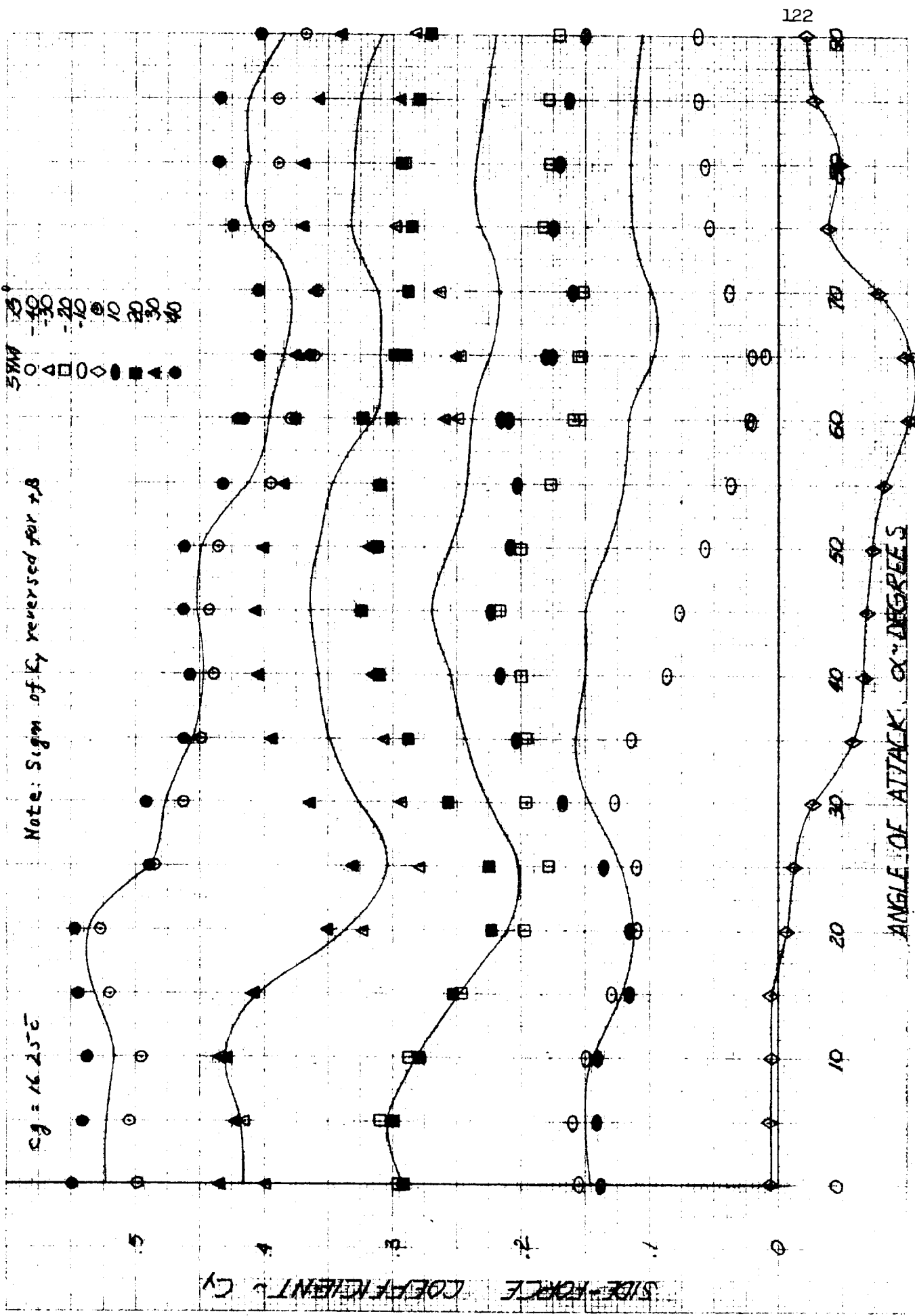


Figure D-22. Effect of angle of attack and sideslip angle on side-force coefficient for configuration is, $\delta_R = 0^\circ$; $\delta_a = 12^\circ$.

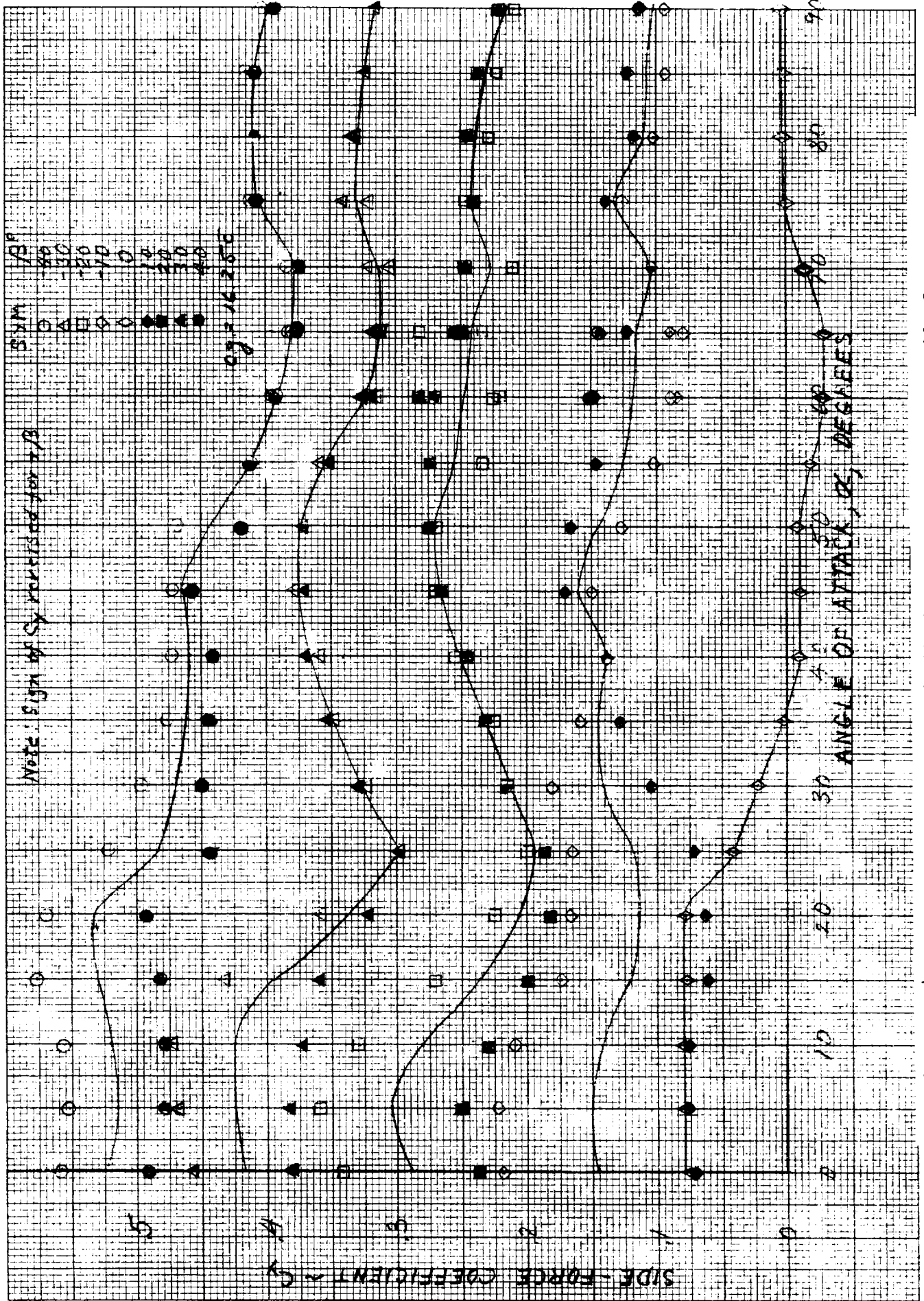


Figure D-24. Effect of angle of attack and sideslip angle on side-force

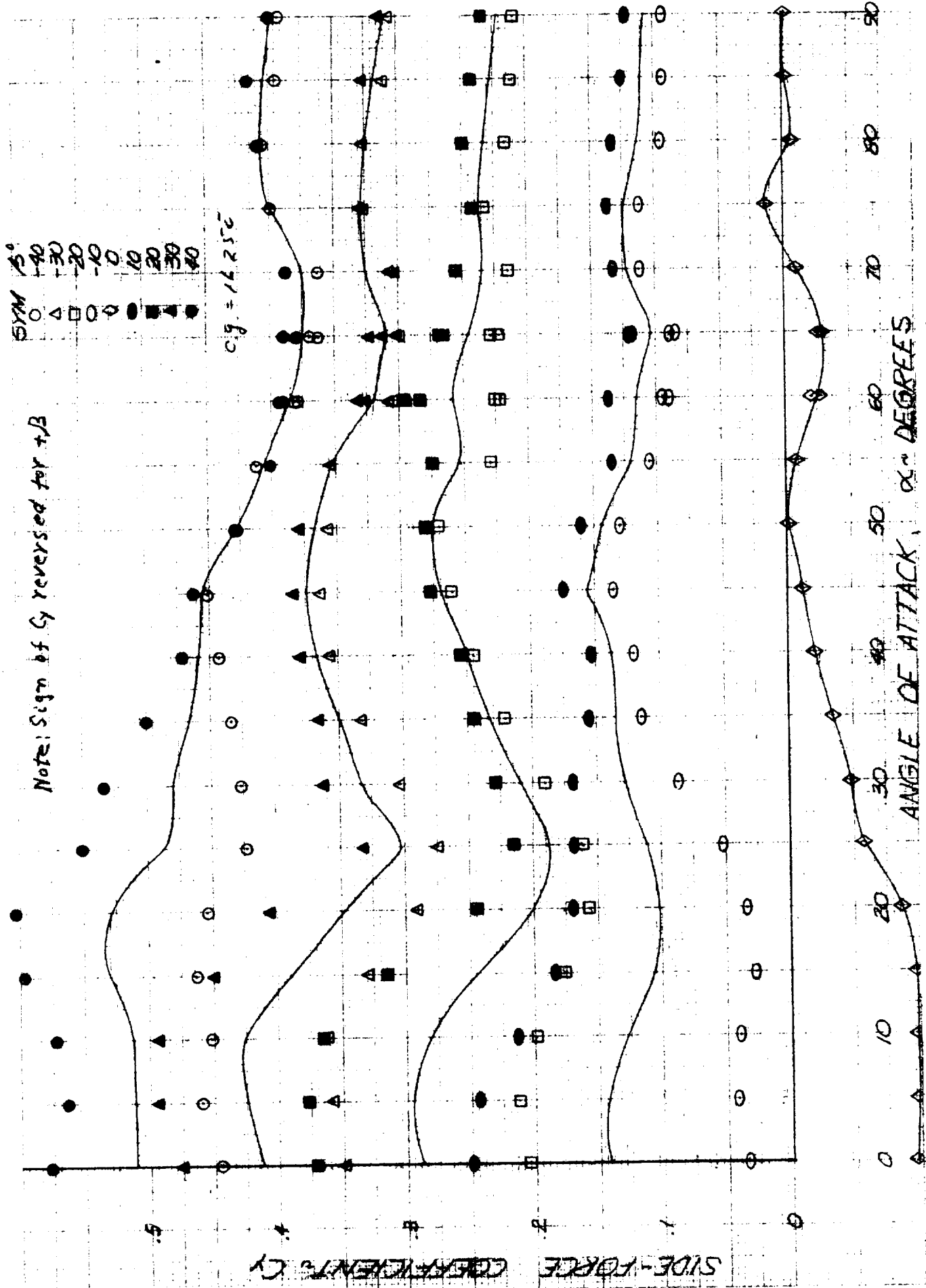
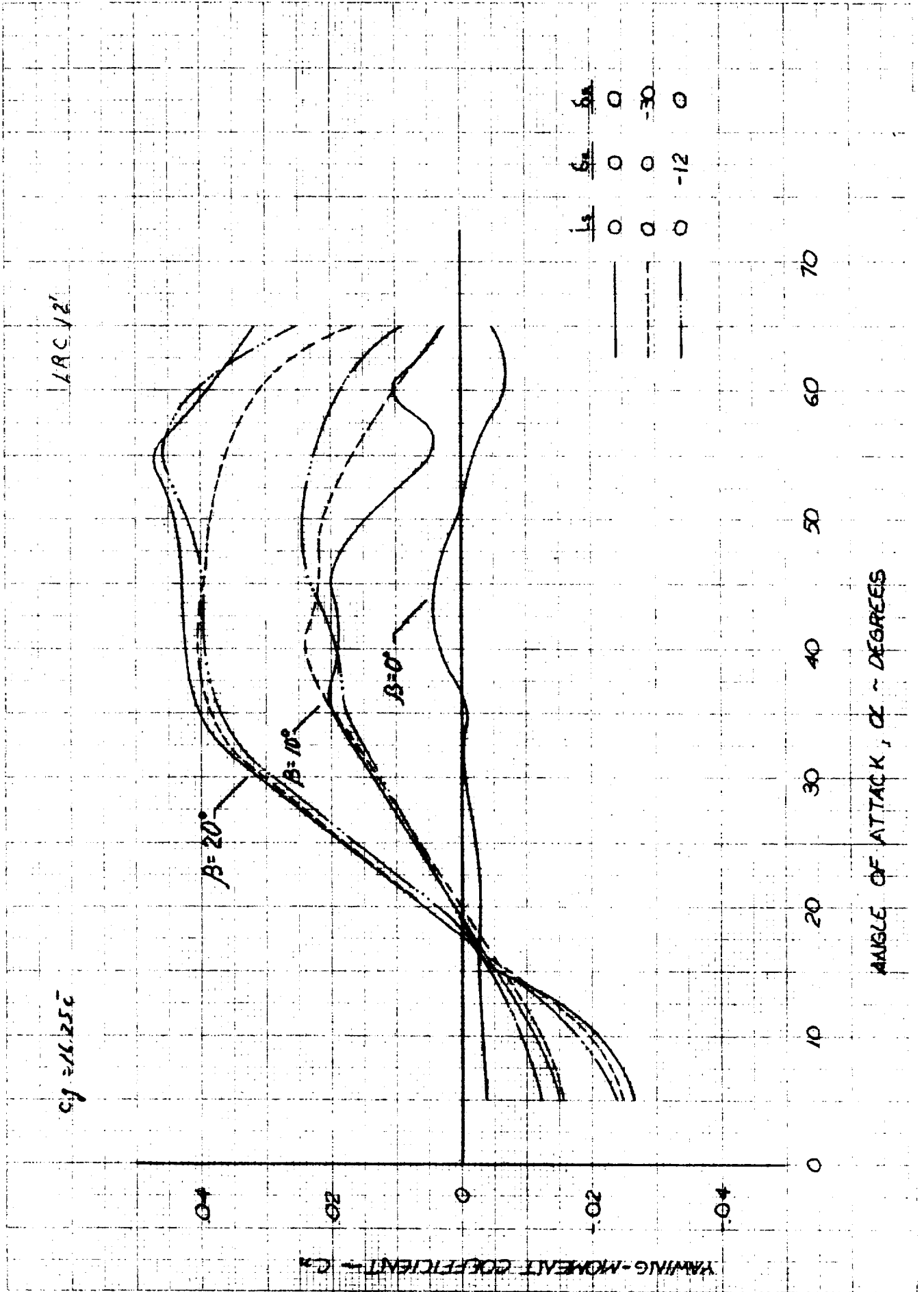
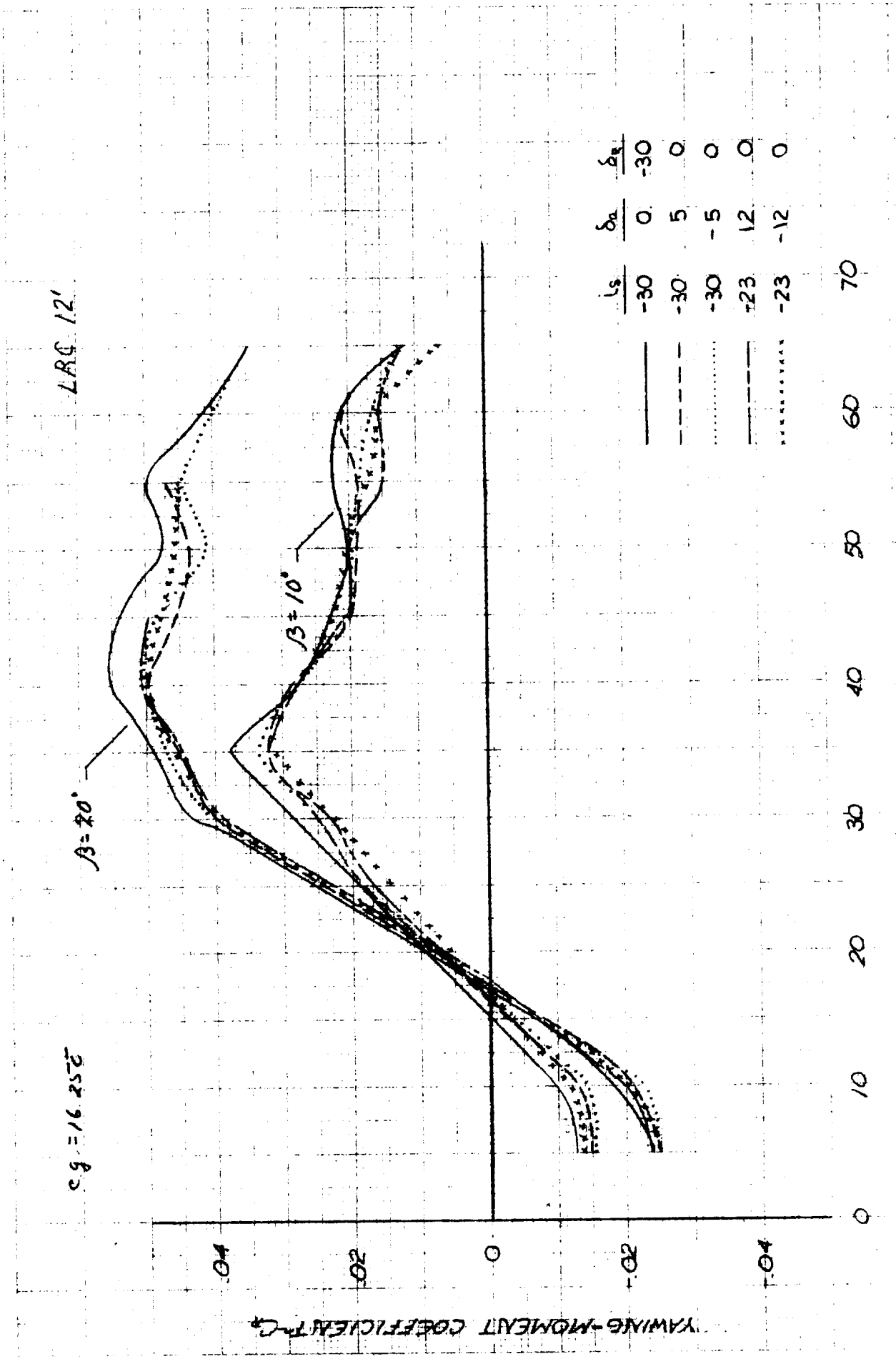


Figure D-25. Effect of angle of attack and sideslip angle on side-force coefficient for configuration i_s , $\delta_a = 0$; $\delta_R = -30^\circ$.



a) $i_s = 0^\circ$ configurations



LRC 12'

$c_g = 16.25\bar{E}$

$\beta = 20^\circ$

$\beta = 10^\circ$

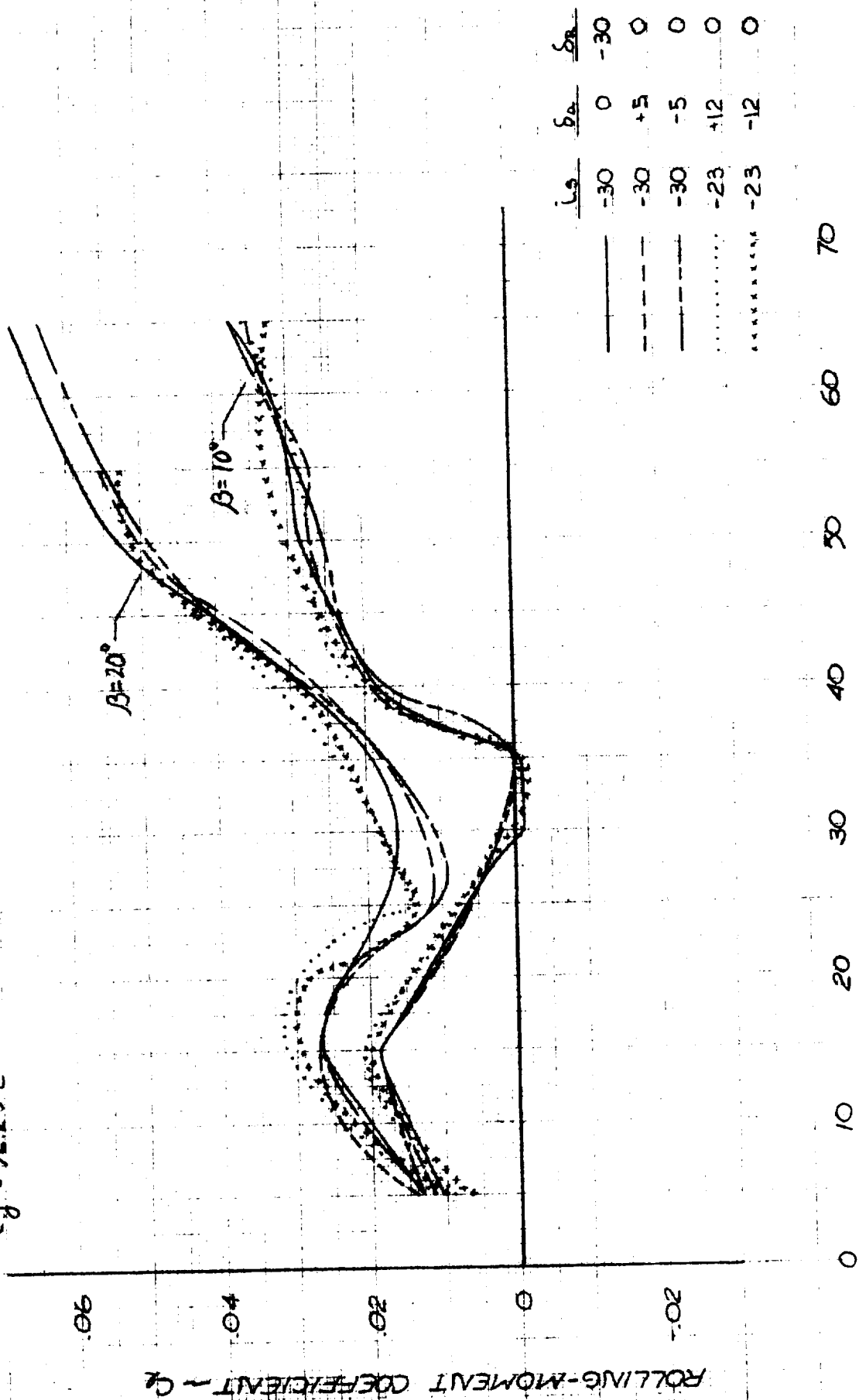
ANGLE OF ATTACK, $\alpha \sim$ DEGREES

YAWING-MOMENT COEFFICIENT C_y

b) i_s deflected configurations
Figure D-26. Concluded.

ARC. 12'

$R_g = 16.25 \bar{c}$



ANGLE OF ATTACK, α - DEGREES

b) is deflected configuration
Figure D-27. Concluded.

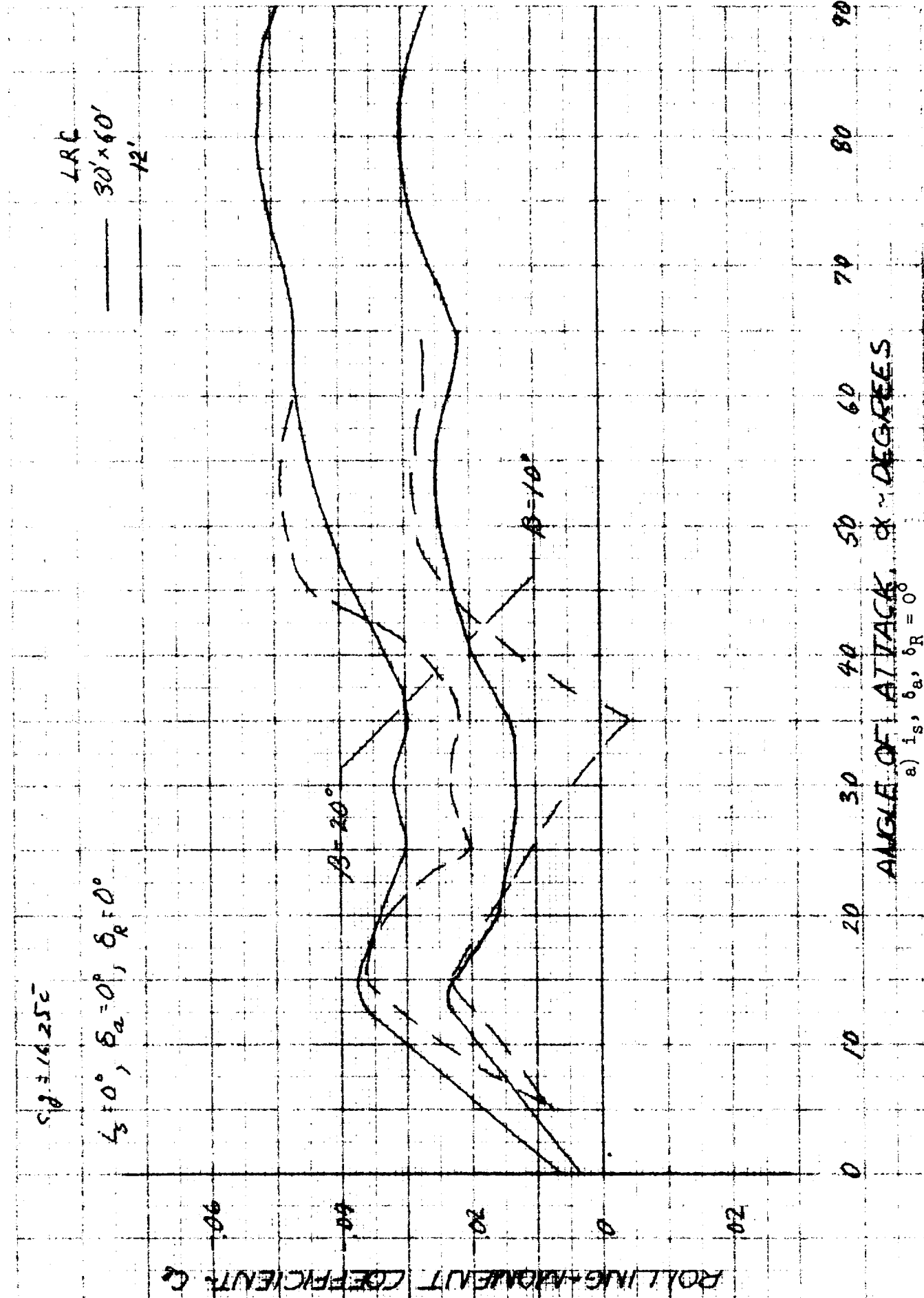
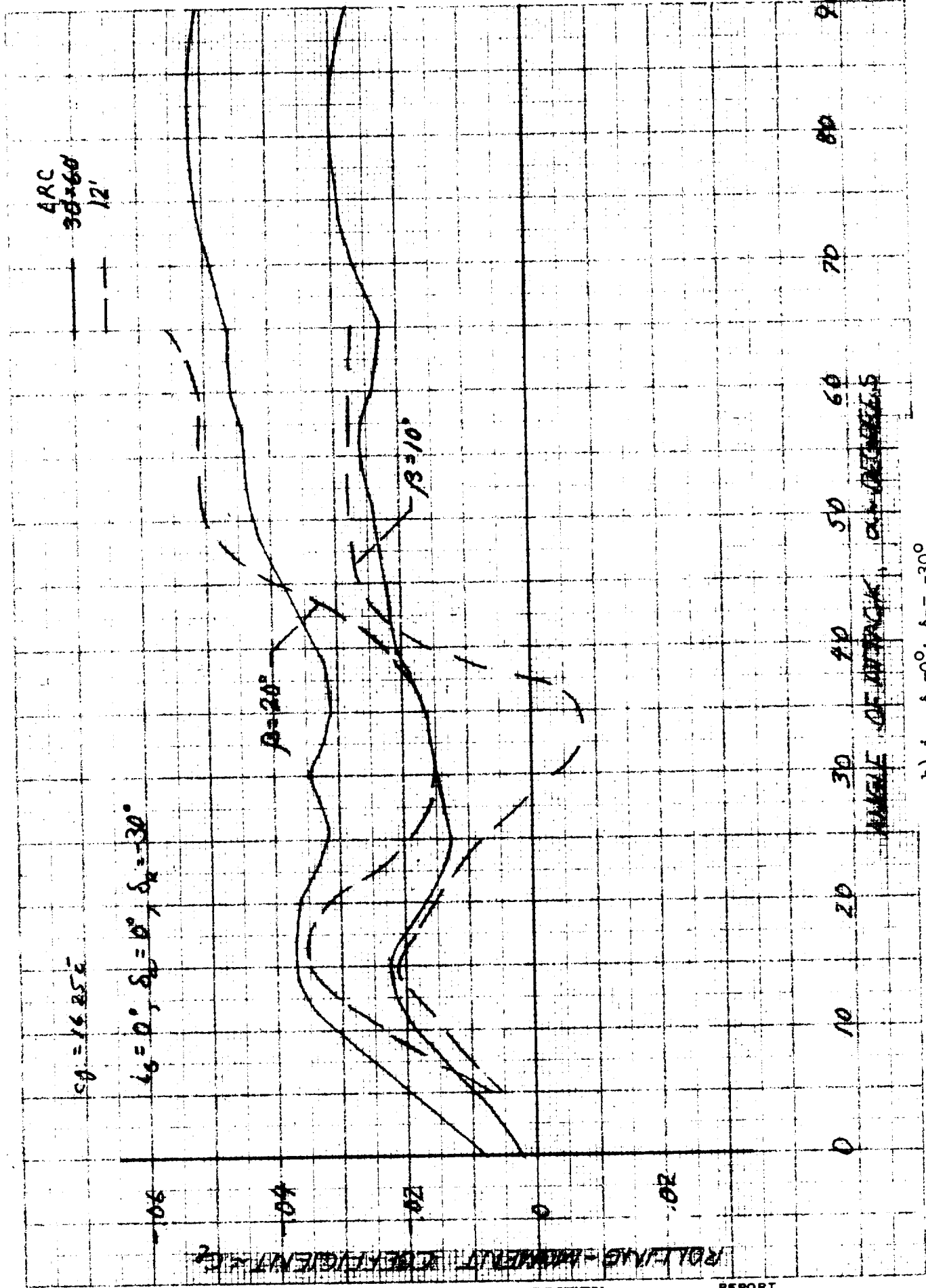
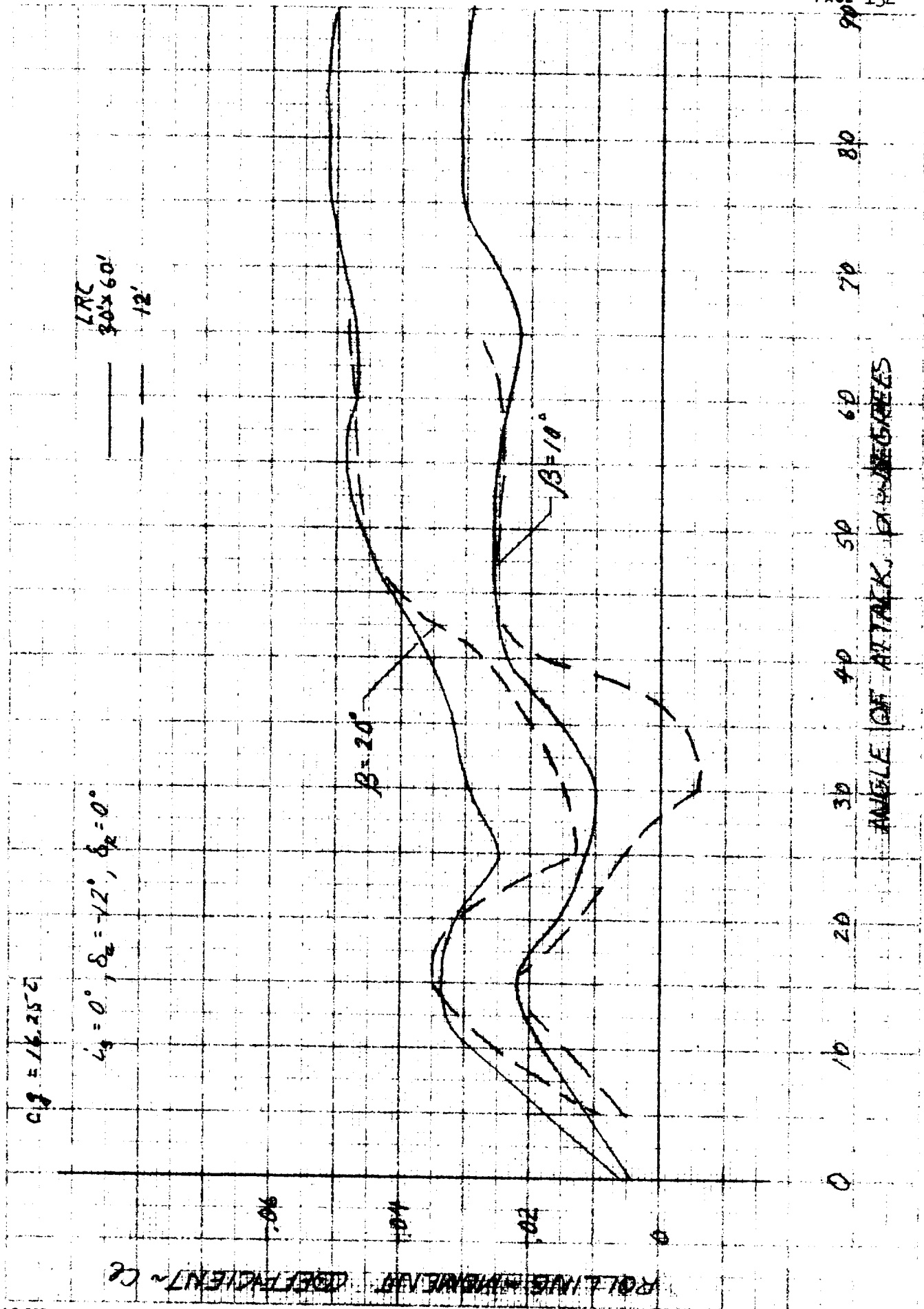


Figure D-28. Comparison between rolling-moment characteristics obtained in LRC 30' x 60' and 12' facilities for various control



b) $i_s, \delta_a = 0^\circ; \delta_R = -30^\circ$
Figure D-28. Continued.



c) $i_s = 0^\circ$, $\delta_a = -12^\circ$, $\delta_R = 0^\circ$
 Figure D-28. Concluded.

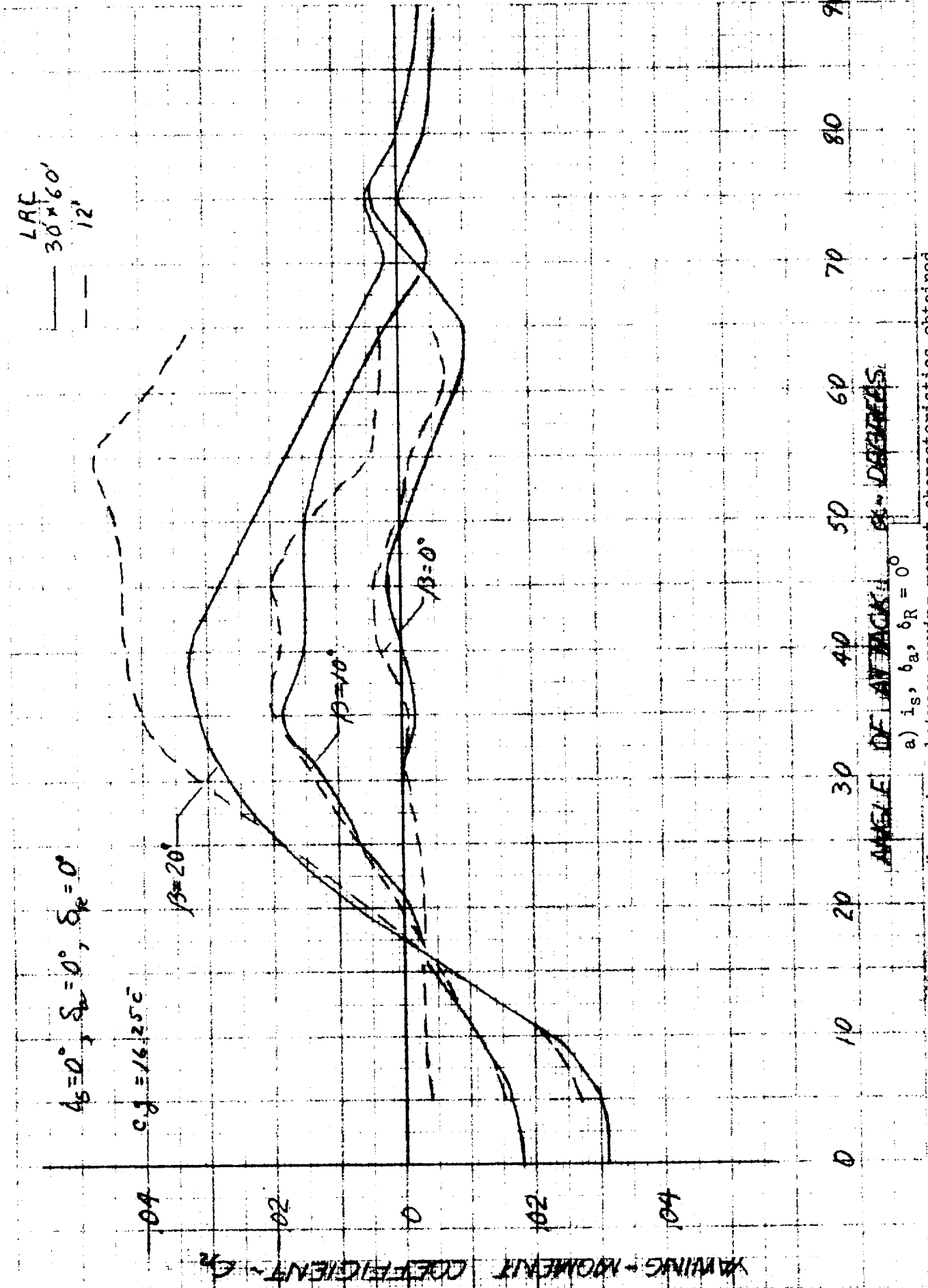


Figure D-29. Comparison between yawing-moment characteristics obtained in LRC 30' x 60' and 12' facilities for various control configurations.

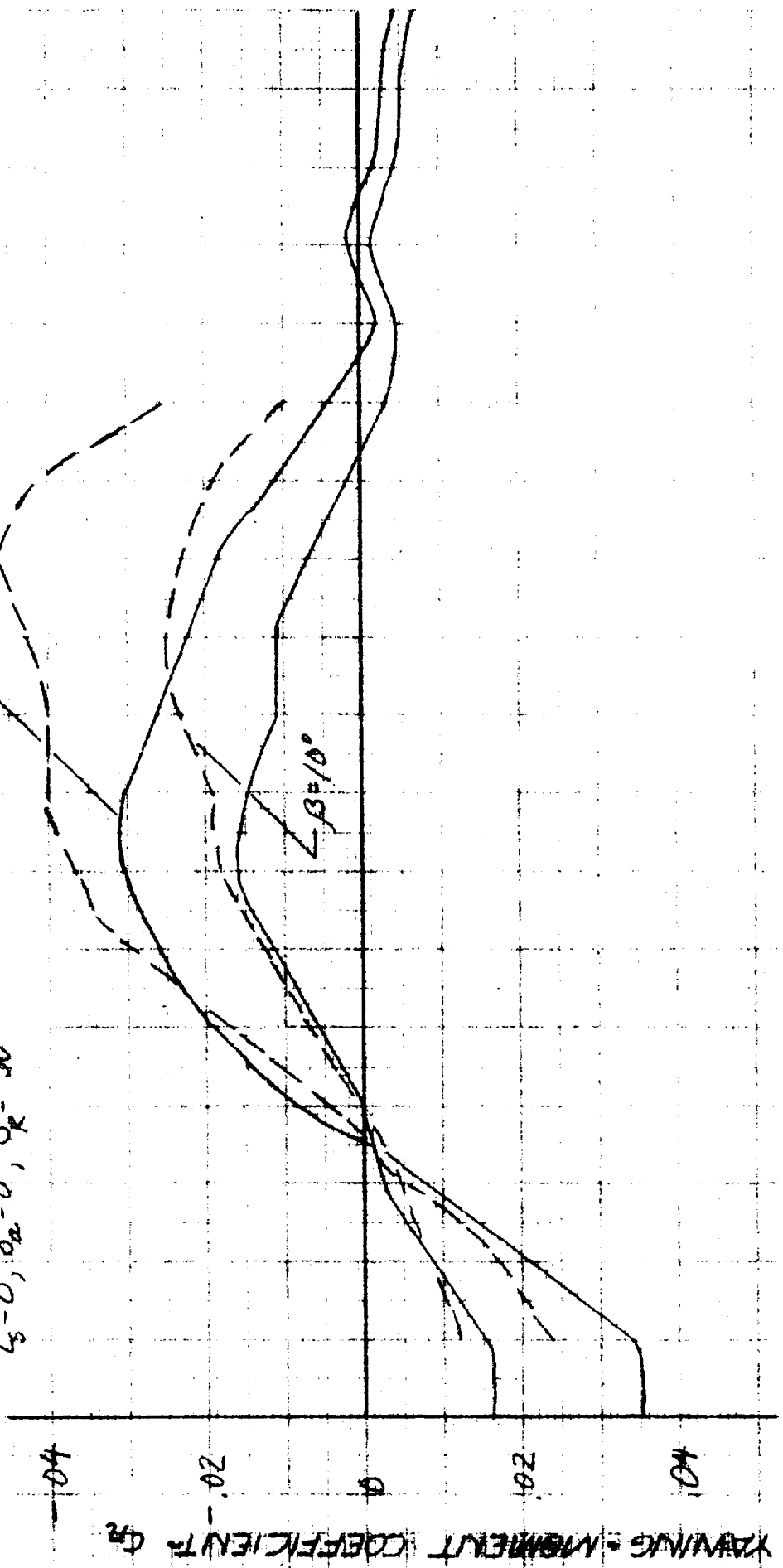
LRC
30' x 60'
12'

$c_g = 16.25\%$

$\delta_s = 0^\circ, \delta_a = 0^\circ, \delta_r = -30^\circ$

$\beta = 20^\circ$

$\beta = 10^\circ$

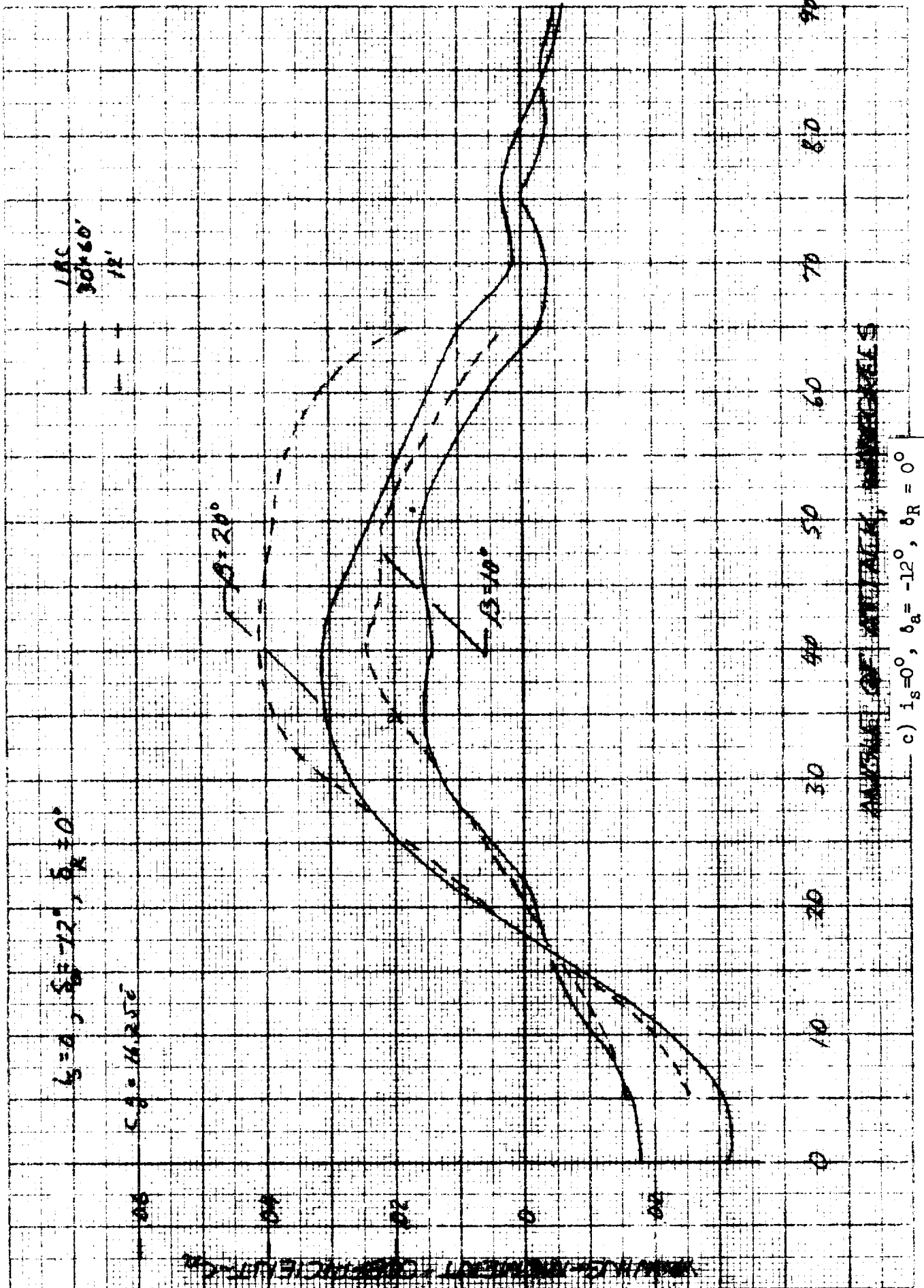


0 10 20 30 40 50 60 70 80 90

YAWING MOMENT COEFFICIENT C_m

ANGLE OF ATTACK, α DEGREES

b) $i_s, \delta_a = 0^\circ; \delta_r = -30^\circ$



c) $i_s = 0^\circ, \delta_a = -12^\circ, \delta_R = 0^\circ$

Figure D-29. Concluded.

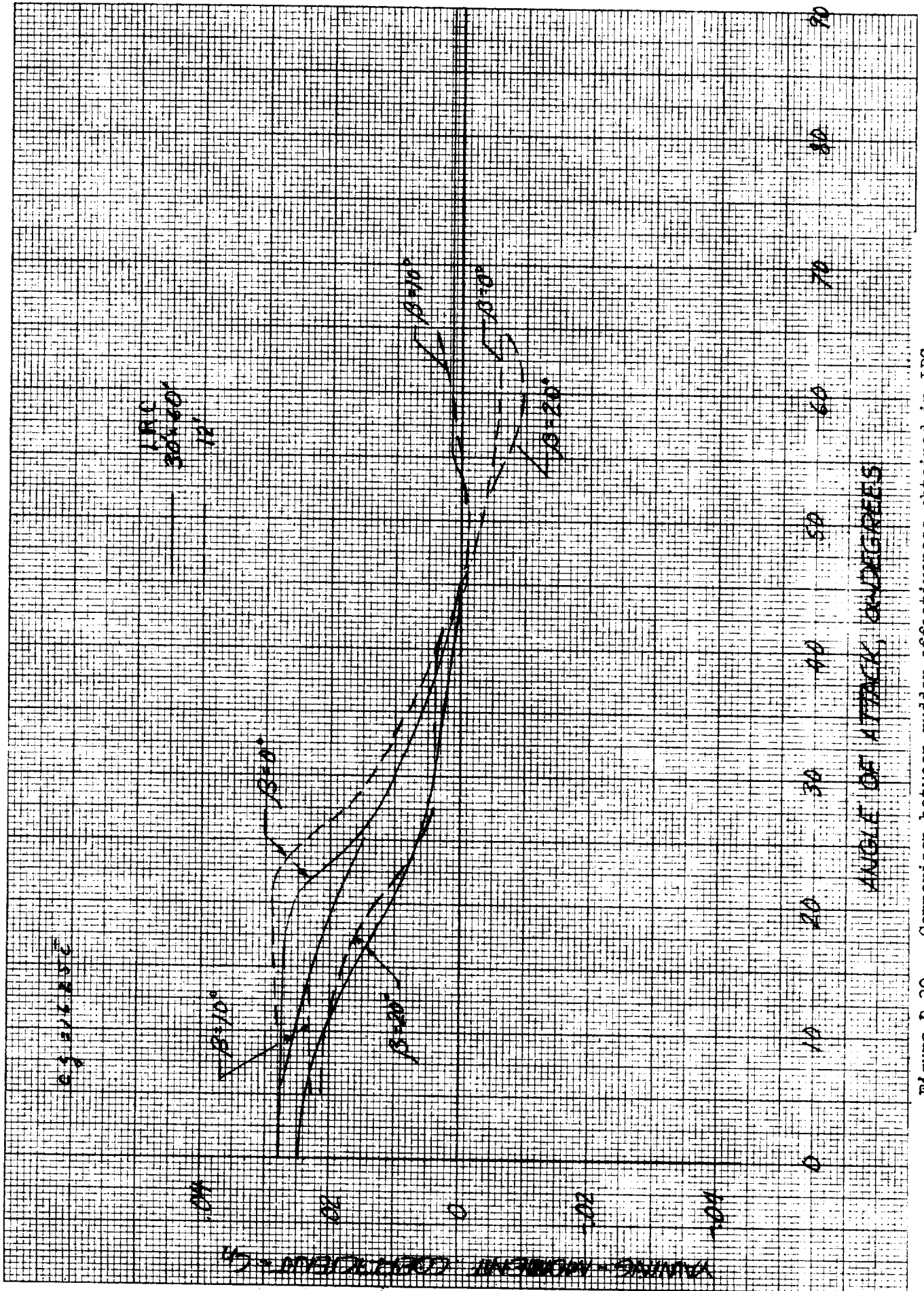


Figure D-30. Comparison between rudder effectiveness obtained in LRC

for ... facilities $\lambda_n = -200$

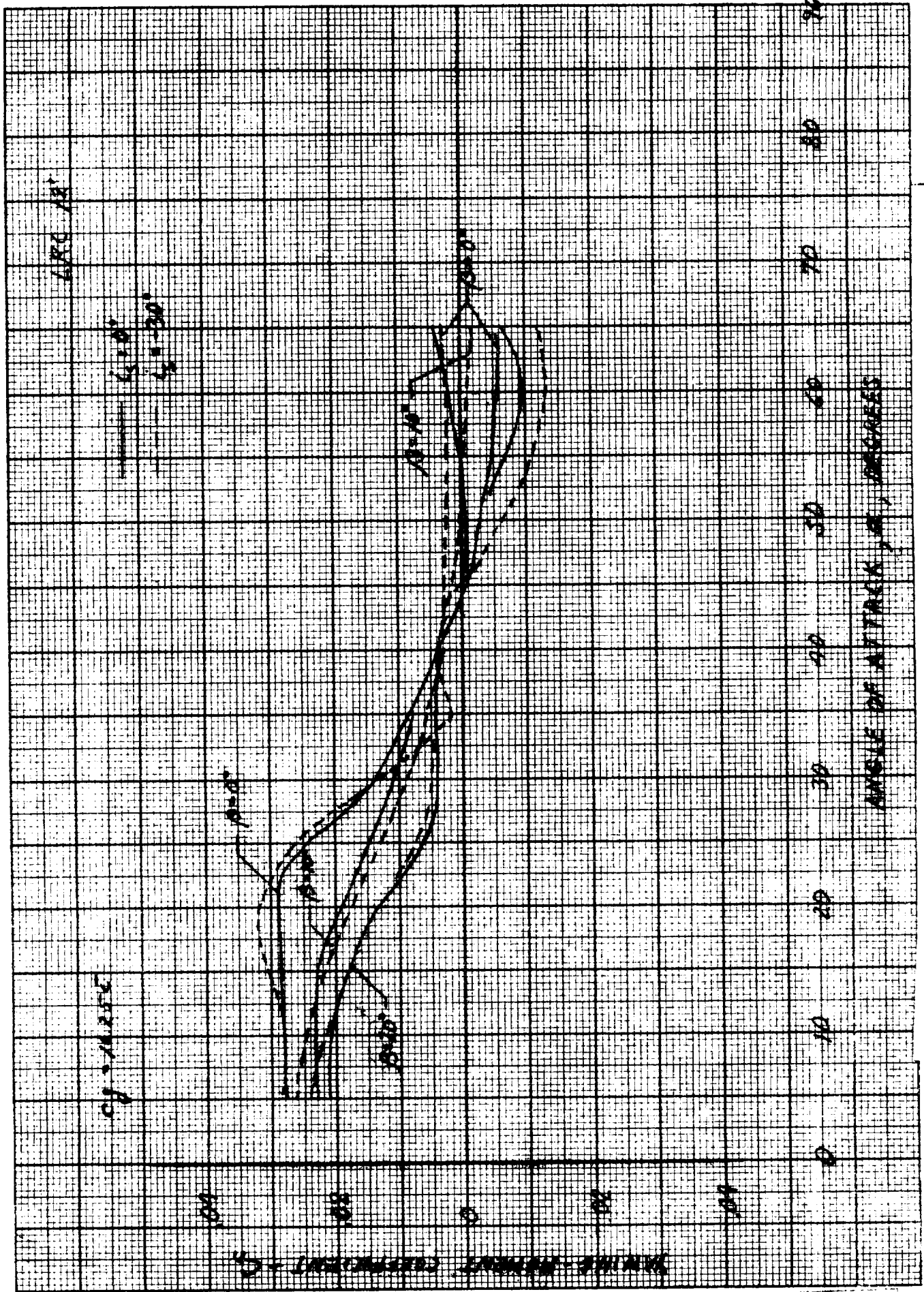


Figure D-31. Comparison between rudder effectiveness obtained at different stabilizer incidence in LRC 12' facility. $\delta_R = -30^\circ$.

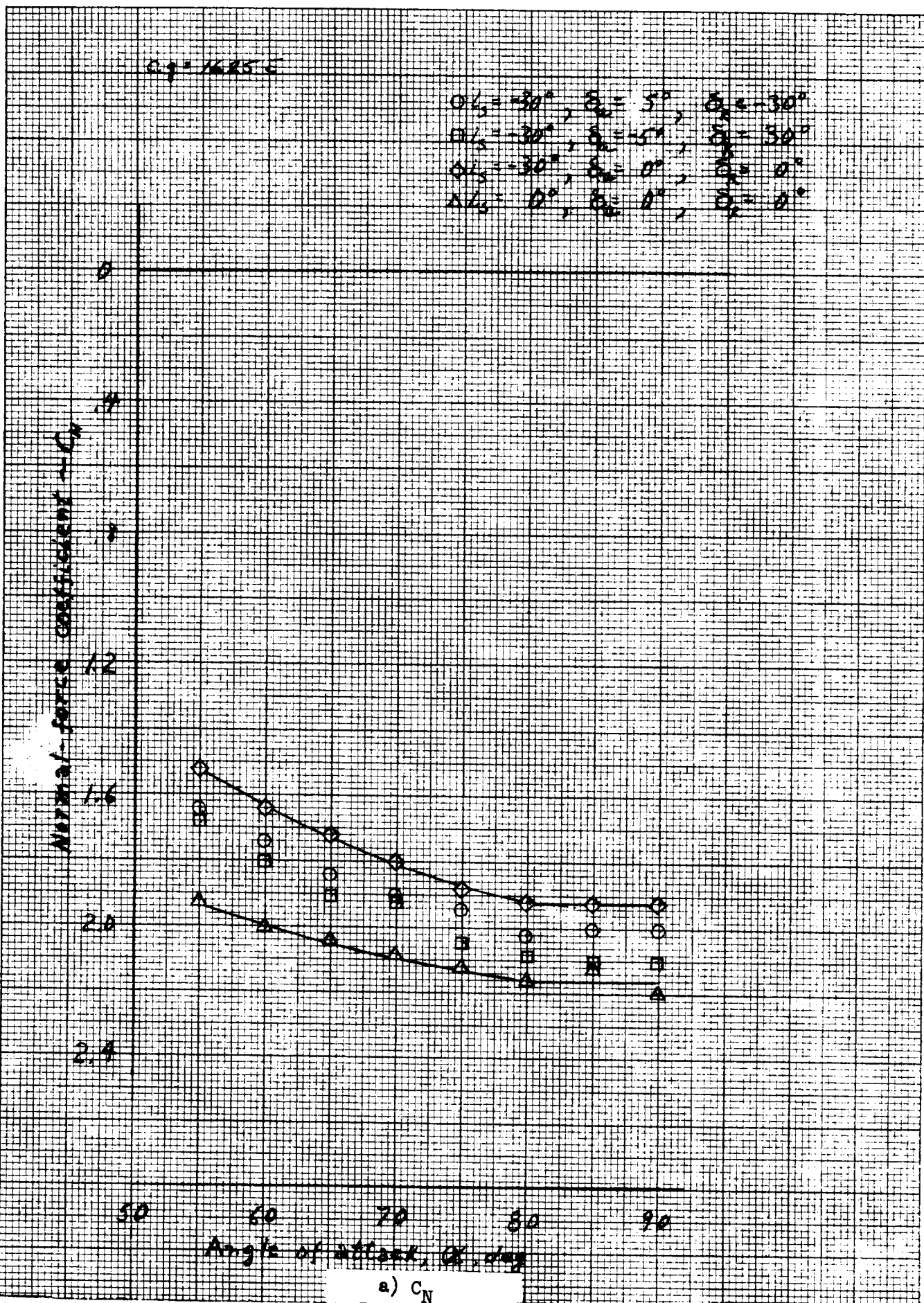
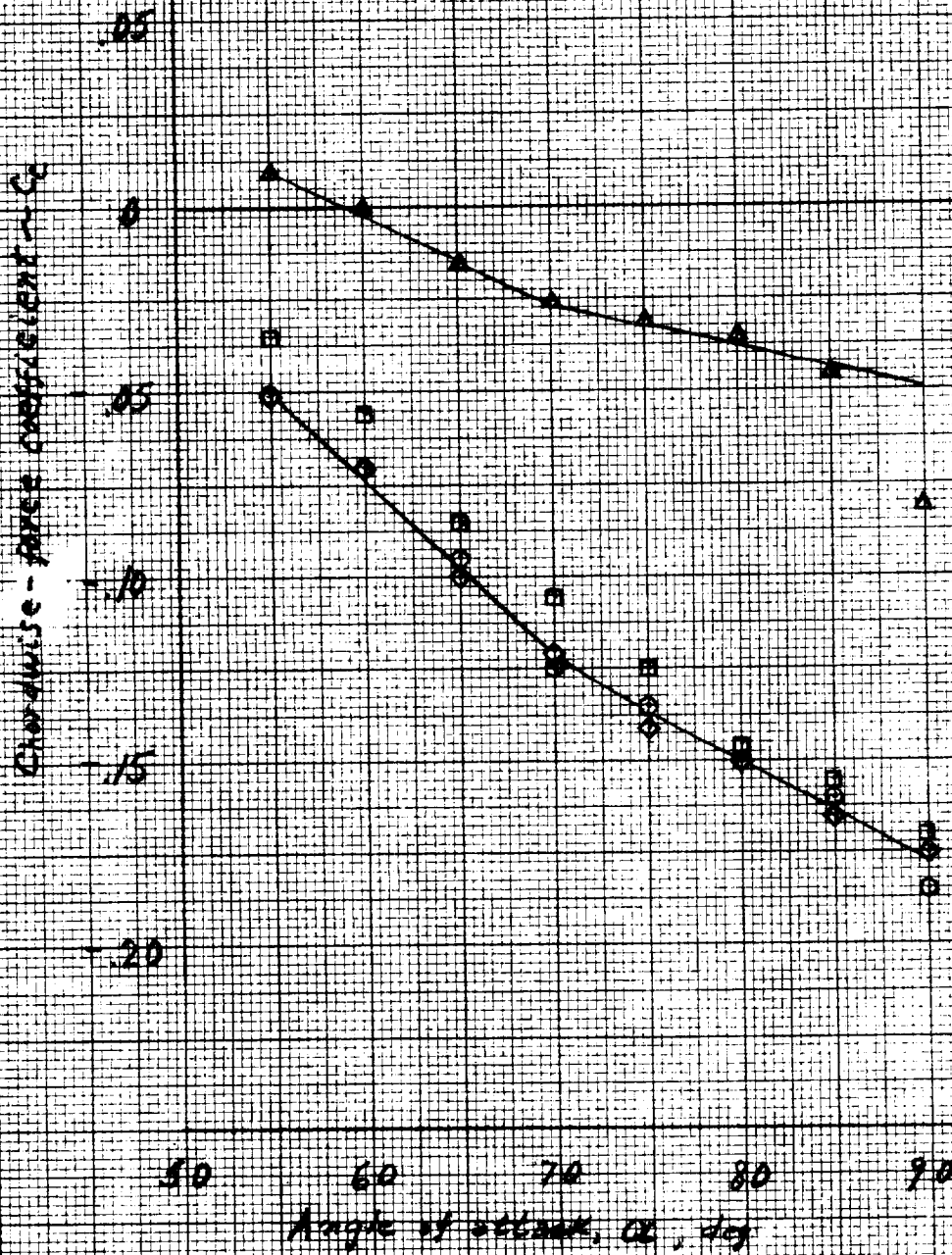


Figure D-32. Static longitudinal characteristics obtained from rotation balance data faired through $\dot{\alpha}_b = 0$ for various control configurations.

$c_g = 16.25^\circ$

$\circ \delta_s = -30^\circ, \delta_w = 5^\circ, \delta_r = -30^\circ$
 $\square \delta_s = -30^\circ, \delta_w = 5^\circ, \delta_r = 30^\circ$
 $\diamond \delta_s = -30^\circ, \delta_w = 0^\circ, \delta_r = 0^\circ$
 $\triangle \delta_s = 0^\circ, \delta_w = 0^\circ, \delta_r = 0^\circ$



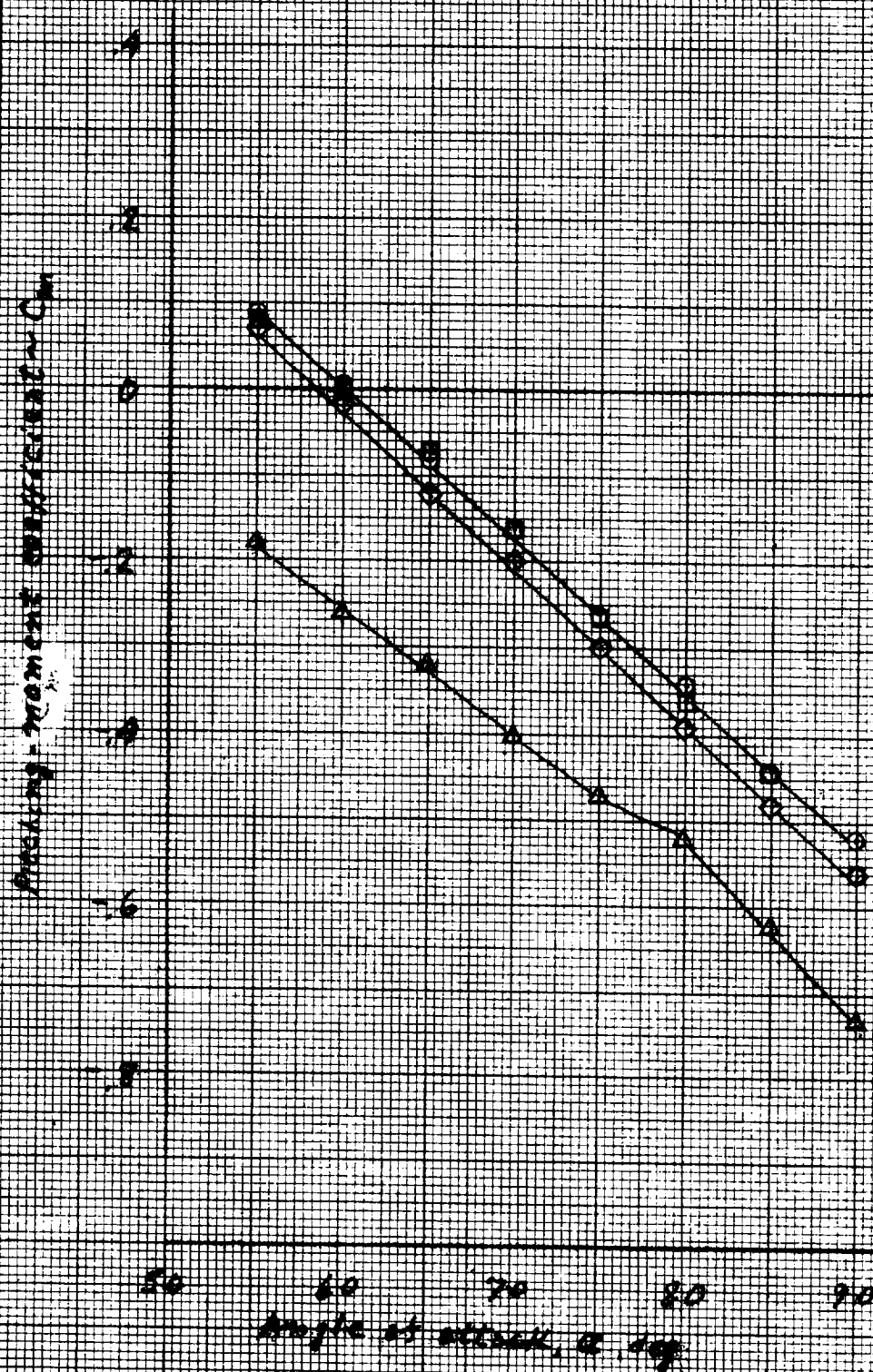
b) C_l

46 1327

K&E
 1/2 X 10 1/4 INCH
 KEUFFEL & ESSER CO. MADE IN U.S.A.

Fig. 11.23.6

$\alpha_1 = 30^\circ$	$\alpha_2 = 5^\circ$	$\alpha_3 = 30^\circ$
$\alpha_1 = 30^\circ$	$\alpha_2 = 5^\circ$	$\alpha_3 = 30^\circ$
$\alpha_1 = 30^\circ$	$\alpha_2 = 5^\circ$	$\alpha_3 = 0^\circ$
$\alpha_1 = 0^\circ$	$\alpha_2 = 0^\circ$	$\alpha_3 = 0^\circ$



c) C_m

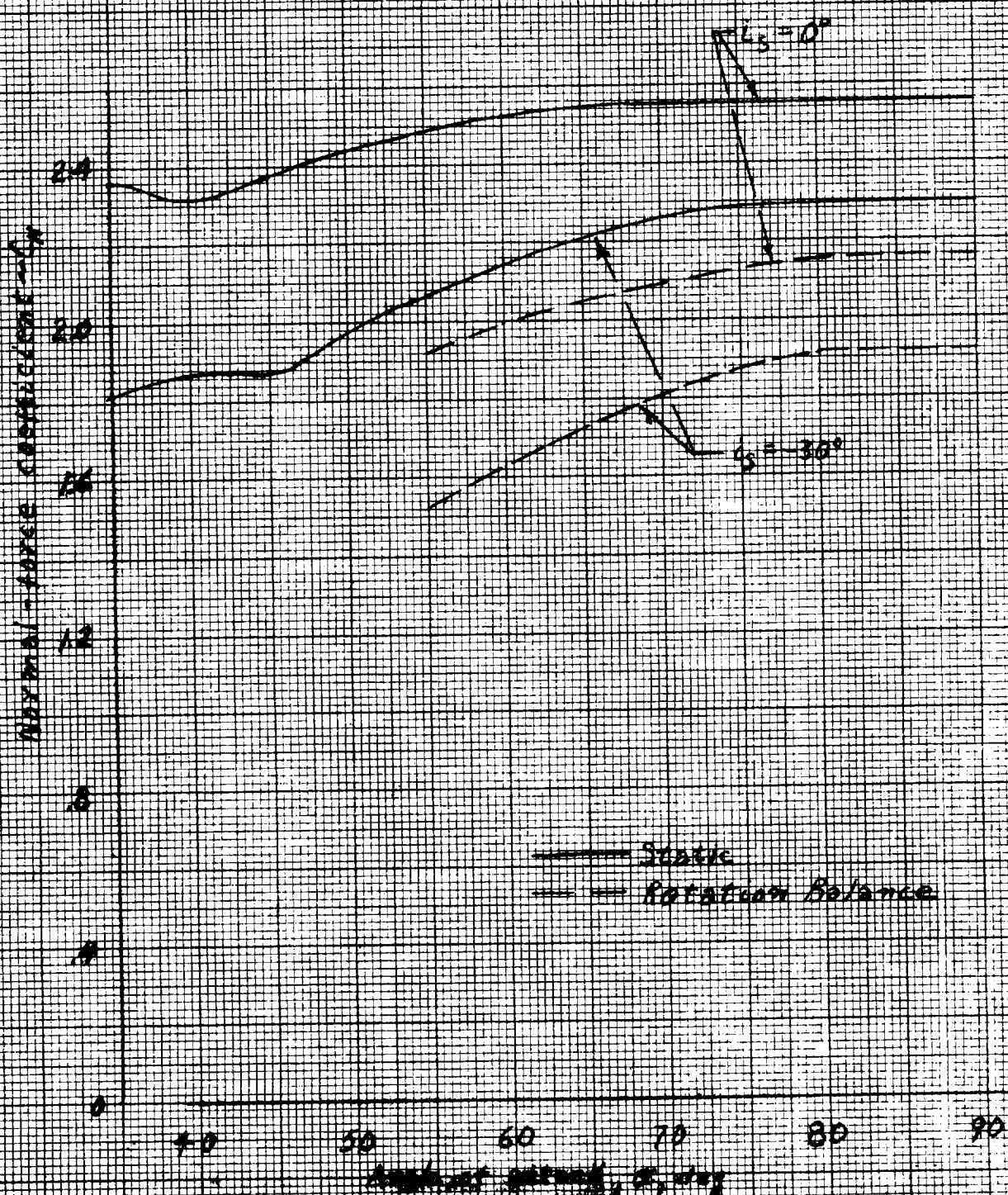
46 1327

K-E 1/2 X 10 TO 1/2 INCH KEUFFEL & ESSER CO. MADE IN U.S.A.

46 1327

THE RANDOLPH CORP. WASHINGTON, D.C. 20540

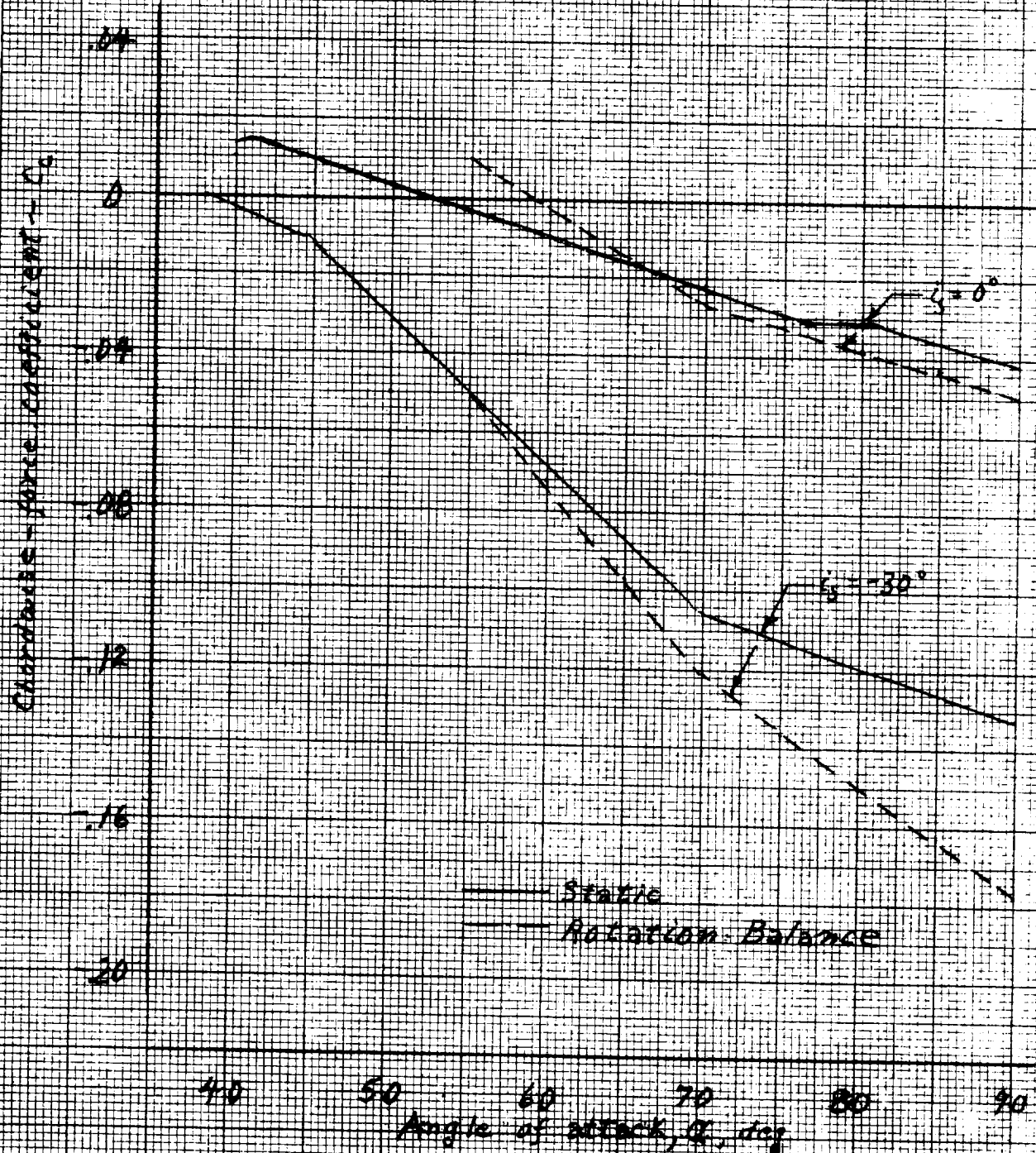
$C_{L_3} = 16.25^\circ$



a) C_N

Figure D-33. Comparison between static longitudinal characteristics obtained from static and rotation balance data at a stabilizer incidence

$C_g = 14.252$



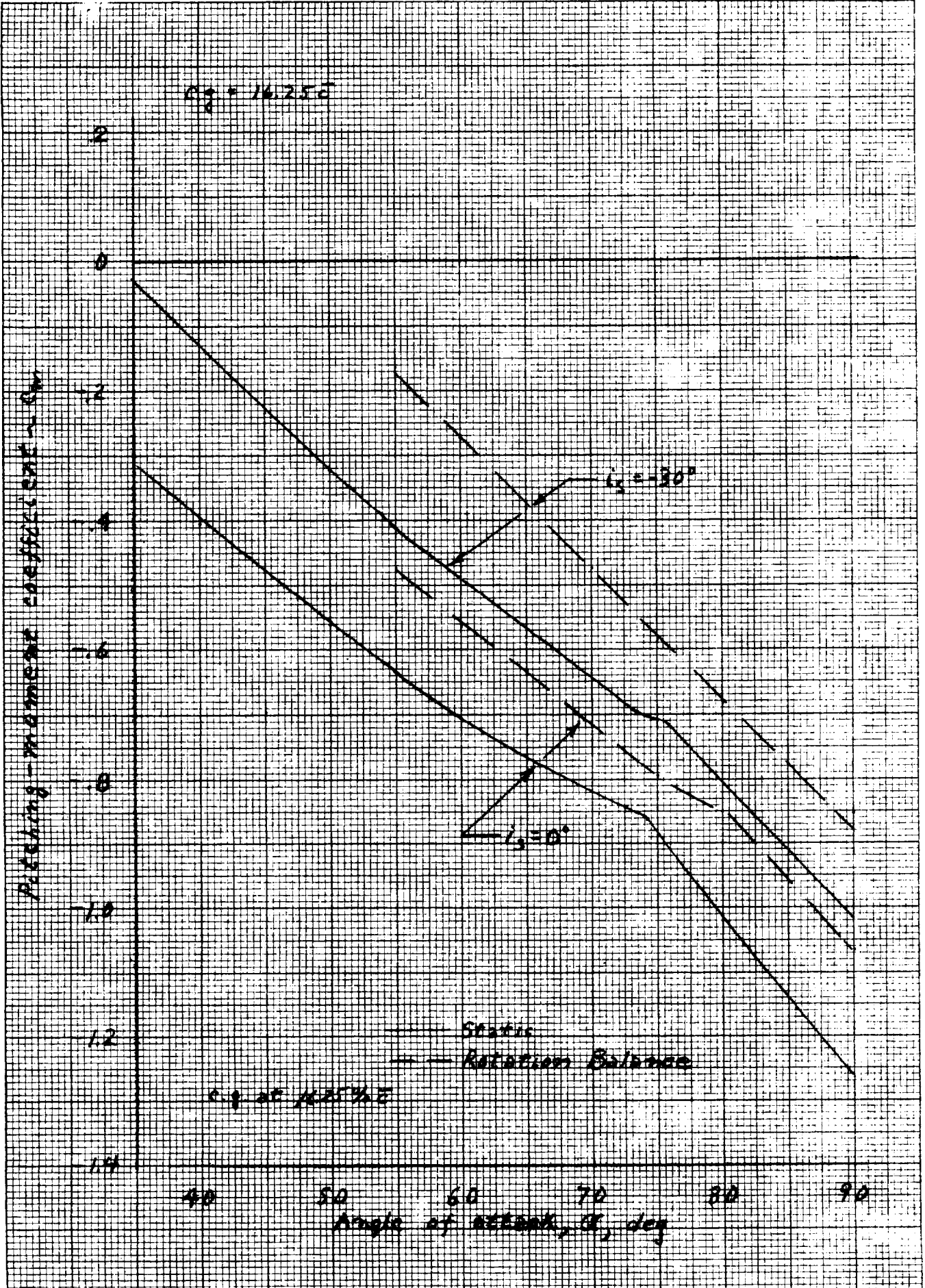
AC 1327

K-E 10 X 10 TO 1/4 INCH 7 X 10 INCHES
DUFFEL & LUBER CO. 4A - U.S.A.

b) C_c

16 1327

U.S. AIR FORCE REUFEL & ESSER CO. MIL. NUSA



c) C_m

Figure D-22 (continued)

46 1327

K·E 10 X 10 TO 1/4 INCH KEUFFEL & ESSER CO. MADE IN U.S.A.

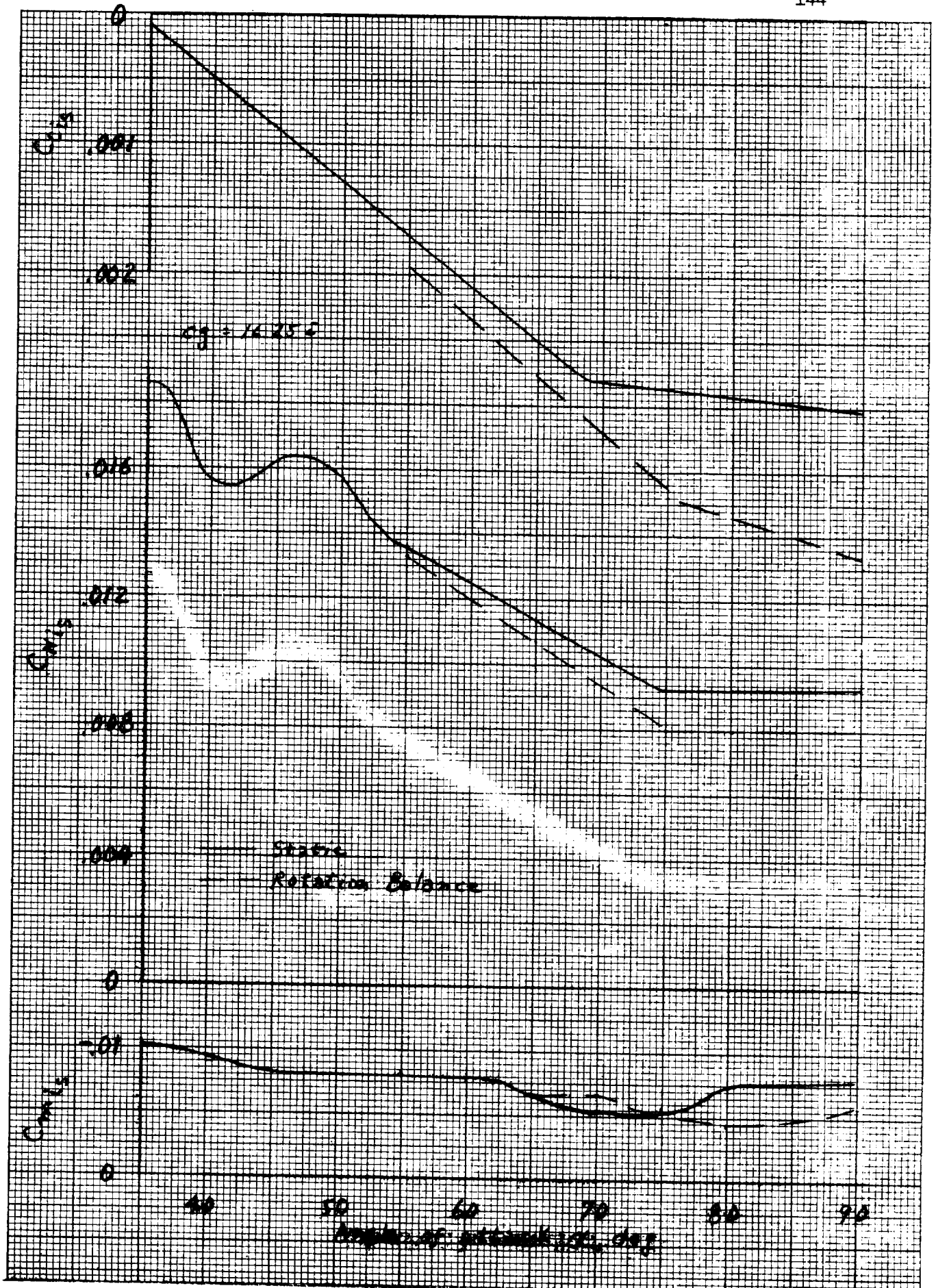


Figure D-34. Comparison between static longitudinal control power obtained from static and rotation balance data.

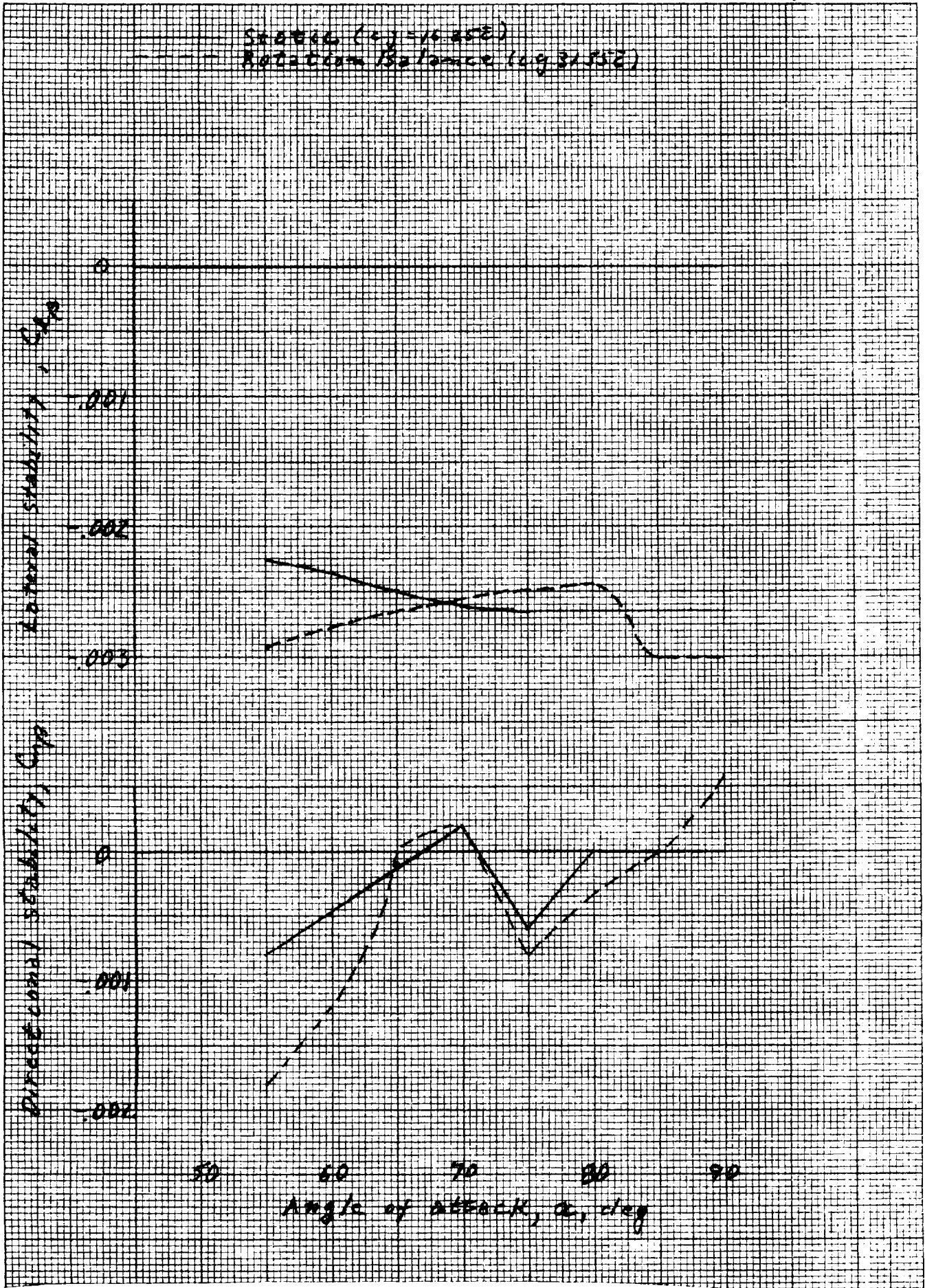


Figure D-35. Comparison between static lateral-directional characteristics obtained from static and ro-

